Restauration d'images dégradées par un bruit Poisson-Gauss

Anna Maria Jezierska

Université Paris-Est

Lab. Informatique Gaspard Monge

UMR CNRS 8049

THESIS

presented by

Anna Jezierska

31 July 2013, Paris

Image Restoration in the presence of Poisson-Gaussian noise

Reporter	Gabriel Peyré	CNRS researcher, Université Paris-Dauphine
Reporter	Gabriele Steidl	Prof. Technische Universität Kaiserslautern
Examiner	Eric Thiébaut	Prof. Centre de Recherche Astrophysique de Lyon
Examiner	Michaël Unser	Prof. École Polytechnique Fédérale de Lausanne
PhD co-supervisor	Caroline Chaux	CNRS researcher, Aix-Marseille Université
PhD supervisor	Jean-Christophe Pesquet	Prof. Université Paris-Est Marne-la-Vallée
PhD co-supervisor	Hugues Talbot	Prof. Université Paris-Est ESIEE

Resumé

Cette thèse porte sur la restauration d'images dégradées à la fois par un flou et par un bruit. Une attention particulière est portée aux images issues de la microscopie confocale et notamment celles de macroscopie.

Dans ce contexte, un modèle de bruit Poisson-Gauss apparaît bien adapté car il permet de prendre en compte le faible nombre de photons et le fort bruit enregistrés simultanément par les détecteurs. Cependant, ce type de modèle de bruit a été peu exploité car il pose de nombreuses difficultés tant théoriques que pratiques. Dans ce travail, une approche variationnelle est adoptée pour résoudre le problème de restauration dans le cas où le terme de fidélité exact est considéré. La solution du problème peut aussi être interprétée au sens du *Maximum A Posteriori* (MAP). L'utilisation d'algorithmes primaux-duaux récemment proposés en optimisation convexe permet d'obtenir de bons résultats comparativement à plusieurs approches existantes qui considèrent des approximations variées du terme de fidélité.

En ce qui concerne le terme de régularisation de l'approche MAP, des approximations discrète et continue de la pseudo-norme ℓ_0 sont considérées. Cette mesure, célèbre pour favoriser la parcimonie, est difficile à optimiser car elle est, à la fois, non convexe et non lisse. Dans un premier temps, une méthode basée sur les coupures de graphes est proposée afin de prendre en compte des *a priori* de type quadratique tronqué. Dans un second temps, un algorithme à mémoire de gradient de type Majoration-Minimisation, dont la convergence est garantie, est considéré afin de prendre en compte des *a priori* de type norme $\ell_2 - \ell_0$. Cet algorithme permet notamment d'obtenir de bons résultats dans des problèmes de déconvolution.

Néanmoins, un inconvénient des approches variationnelles est qu'elles nécessitent la détermination d'hyperparamètres. C'est pourquoi, deux méthodes, reposant sur une approche Espérance-Maximisation (EM) sont proposées, dans ce travail, afin d'estimer les paramètres d'un bruit Poisson-Gauss: (1) à partir d'une série temporelle d'images (dans ce cas, des paramètres de "bleaching" peuvent aussi être estimés) et (2) à partir d'une seule image.

De manière générale, cette thèse propose et teste de nombreuses méthodo-

logies adaptées à la prise en compte de bruits et de flous difficiles, ce qui devrait se révéler utile pour des applications variées, au-delà même de la microscopie.

Cette thèse est organisée comme suit:

Le Chapitre 1 a pour but d'introduire le lecteur aux problèmes inverses et aux outils mathématiques associés. Notre exposé se limite aux méthodes variationnelles appliquées aux modèles continus ou discrets. Ensuite, les méthodes d'optimisation associées sont discutées; une attention particulière est portée aux algorithmes de type Majoration-Minimisation, aux méthodes basées sur les coupures de graphes et enfin, aux algorithmes proximaux.

La quantification, définie comme le fait d'attribuer à une image un nombre fini de niveaux, est une opération fondamentale dans l'acquisition d'images et leur codage. Elle est également étroitement liée à de nombreuses tâches de traitement d'images, telles que le débruitage et la segmentation. Dans le Chapitre 2 nous étudions la quantification vectorielle combinée à des contraintes de régularité. Ce domaine encore peu étudié suscite un intérêt, en particulier, dans le contexte de la quantification en présence de bruit ou d'autres artefacts d'acquisition. Nous adoptons une approche d'optimisation afin de résoudre ce problème. La méthode proposée met en jeu à la fois des techniques d'optimisation convexe et combinatoire. Notre approche itérative comportant deux étapes entrelacées se révèle d'une grande souplesse. Nous illustrons l'efficacité de la méthode proposée sur des images monochromes et couleur. Nous montrons qu'en utilisant un petit nombre de niveaux de quantification, notre approche peut fournir des images de meilleure qualité que les méthodes classiques de quantification, optimales en termes de qualité d'approximation et d'entropie.

Dans de nombreux cas, le bruit lié au système d'imagerie n'est pas additif. En raison de la nature particulaire de la lumière, les images sont dégradées par le bruit quantique, tandis que bruit thermique peut jouer un rôle moins important. Bien qu'une approximation gaussienne soit tout à fait justifiée dans certains cas, on peut avoir besoin de considérer que la moyenne et/ou la variance du bruit dépendent de l'intensité de l'image. Par conséquent, la reconstruction d'image en présence de bruit dépendant du signal constitue un domaine de recherche actif. Le problème d'estimation des paramètres

d'un modèle de type Poisson-Gauss à partir de données expérimentales, a récemment suscité beaucoup d'intérêt dans diverses applications, en particulier pour les systèmes d'imagerie CCD. Dans ce contexte, un champ de variables aléatoires indépendantes est observé, qui est variable dans le temps et l'espace. Chaque variable est la somme de deux composantes: l'une suit une distribution de Poisson et l'autre une distribution gaussienne. Dans le Chapitre 3, une formulation générale est considérée lorsque le processus de Poisson est non stationnaire en espace et présente également une décroissance exponentielle dans le temps, alors que la composante gaussienne correspond à un bruit blanc stationnaire de moyenne arbitraire. Pour résoudre le problème d'estimation paramétrique considéré, un processus itératif de type Espérance-Maximisation (EM) est employé. Une attention est portée à l'initialisation de l'algorithme EM pour lequel une méthode de moments est appliquée. On réalise également une analyse des performances de la méthode mise en œuvre en calculant les bornes de Cramer-Rao sur les variables estimées. Des illustrations de la méthode d'estimation proposée sont fournies la fois sur des données synthétiques et réelles (correspondant à des séquences d'images de macroscopie confocale). On constate ainsi que l'algorithme produit des estimations fiables de la moyenne/variance du bruit gaussien et du paramètre d'échelle de la composante de Poisson, ainsi que des taux de décroissance exponentielle.

L'objectif du Chapitre 4 est encore l'estimation des paramètres de bruits de type Poisson-Gauss. Le problème est formulé dans un cadre d'optimisation mixte discrète-continue. L'approche proposée estime conjointement le signal d'intérêt et les paramètres du bruit. Ce résultat est obtenu par l'introduction d'un terme de régularisation adéquat associé à une terme d'attache aux données dans le critère à minimiser. La solution optimale est recherchée de manière itérative en alternant la minimisation d'un champ d'étiquettes et d'un vecteur de paramètres de bruit. L'algorithme proposé est inspiré de l'approche de régularisation spatiale pour la quantification vectorielle introduite dans le Chapitre 2, tandis que les paramètres de bruit sont estimés à chaque itération à l'aide des résultats établis au Chapitre 3. Nous illustrons l'utilité de notre approche sur des données synthétiques et des images de macroscopie confocale. Dans les résultats de simulation fournis, nous démontrons l'efficacité de notre approche.

Le Chapitre 5 marque le début de la partie centrale de notre travail lié à la restauration des données dégradées par un bruit de type Poisson-

Gauss. Comme nous l'avons déja souligné, un modèle Poisson-Gauss peut décrire avec précision le bruit présent dans une variété importante de systèmes d'imagerie. Cependant, la plupart des stratégies de restauration existantes reposent sur des approximations des statistiques du bruit Poisson-Gauss. Nous proposons un algorithme d'optimisation convexe pour la reconstruction des signaux dégradés par un opérateur linéaire et un bruit de type Poisson-Gauss. L'originalité de notre approche est liée à la prise en compte exacte du modèle continu-discret. Après avoir établi la Lipschitz-différentiabilité et la convexité de l'anti-log-vraisemblance Poisson-gaussienne, nous proposons un algorithme primal-dual permettant de minimiser le critère pénalisé associé. La méthode proposée est applicable à un large choix de termes de pénalisation convexes. Parmi ceux que nous considérons, un *a priori* hybride combinant un terme de variation totale et une pénalisation sur le hessien est démontré produire des résultats de haute qualité pour les images naturelles dans les problème de restauration de données en présence de bruit de Poisson-Gauss. La robustesse de notre méthode nous permet de gérer les difficultés liées au calcul de sommes infinies résultant du calcul du gradient du critère. L'approche proposée est validée sur des exemples de restauration d'images.

Le Chapitre 6 aborde le problème de la minimisation des énergies multi-labels associées à des *a priori* de type convexes tronqués. Ces *a priori* sont connus pour être performants mais également difficiles et lents à optimiser en raison de leur non-convexité. Nous proposons deux nouvelles méthodes basées sur les coupures de graphes, à savoir le *convex move* et le *quantized move*. Ces mouvements sont conçus pour être complémentaires l'un de l'autre mais peuvent aussi être utilisés indépendamment. Pour améliorer sensiblement l'efficacité de la méthode, la plage de labels est divisée en intervalles uniformes. Les *quantized move* ont tendance à affecter efficacement les labels des pixels aux intervalles appropriés pour l'énergie avec *a priori* convexe tronqué. Puis, le *convex move* affecte les labels plus précisément dans ces intervalles pour la même énergie. Le *quantized move* de type α-*expansion*, peut être intrerprété comme un *a priori* de type Potts généralisé, qui attribue une pénalité constante aux arguments au-dessus d'un certain seuil. Notre mouvement est une version coupures de graphes convexe de l'algorithme efficace de Murota. Nous ne traitons que les termes d'attache aux données convexes, puisque cette hypothèse est requise pour l'algorithme de Murota. Nous introduisons ensuite l'algorithme *Quantized-Convex Split Moves* qui minimise les énergies intégrant des *a priori* tronqués par alternance des deux mouvements. Cet algorithme est un solveur rapide pour des problèmes impliquant un grand

nombre de labels et des modèles de données convexes. Nous illustrons ses performances dans des problèmes de débruitage d'images.

Dans le Chapitre 7, nous considérons une classe de critères différentiables pour des problèmes parcimonieux en traitement d'images, où une régularisation non convexe est appliquée à une transformation linéaire arbitraire de l'image cible. Elle prend en compte, en particulier, les mesures préservant les contours mais aussi les trames couramment utilisées en traitement d'image. Comme le montrent nos résultats asymptotiques, la pénalisation $\ell_2 - \ell_0$ que nous considérons peut être utilisée pour fournir des solutions approchées aux problèmes d'optimisation incluant une pénalisation ℓ_0. Un des avantages de l'approche proposée est qu'elle nous permet de développer un algorithme de sous-espace de type Majoration-Minimisation. La convergence de l'algorithme est étudiée en utilisant des résultats récents en matière d'optimisation non convexe. Plus précisément, une nouvelle preuve de convergence de l'algorithme proposé est donnée en exploitant l'inégalité de Kurdyka-Łojasiewicz. Cette approche offre une alternative intéressante aux méthodes existantes en termes de qualité d'image reconstruite et de temps de calcul. La rapidité de convergence de cette méthode d'optimisation est illustrée au travers d'exemples en traitement d'image. En particulier, son efficacité est démontrée sur plusieurs problèmes de restauration de données.

Nous résumons nos contributions et dégageons quelques pistes pour des travaux futurs dans le Chapitre 8.

Abstract

This thesis deals with the restoration of images corrupted by blur and noise, with emphasis on confocal microscopy and macroscopy applications.

Due to low photon count and high detector noise, the Poisson-Gaussian model is well suited to this context. However, up to now it had not been widely utilized because of theoretical and practical difficulties. In view of this, we formulate the image restoration problem in the presence of Poisson-Gaussian noise in a variational framework, where we express and study the exact data fidelity term. The solution to the problem can also be interpreted as a Maximum A Posteriori (MAP) estimate. Using recent primal-dual convex optimization algorithms, we obtain results that outperform methods relying on a variety of approximations.

Turning our attention to the regularization term in the MAP framework, we study both discrete and continuous approximations of the ℓ_0 pseudo-norm. This useful measure, well-known for promoting sparsity, is difficult to optimize due to its non-convexity and its non-smoothness. We propose an efficient graph-cut procedure for optimizing energies with truncated quadratic priors. Moreover, we develop a majorize-minimize memory gradient algorithm to optimize various smooth versions of the $\ell_2 - \ell_0$ norm, with guaranteed convergence properties. In particular, good results are achieved on deconvolution problems.

One difficulty with variational formulations is the necessity to tune automatically the model hyperparameters. In this context, we propose to estimate the Poisson-Gaussian noise parameters based on two realistic scenarios: one from time series images, taking into account bleaching effects, and another from a single image. These estimations are grounded on the use of an Expectation-Maximization (EM) approach.

Overall, this thesis proposes and evaluates various methodologies for tackling difficult image noise and blur cases, which should be useful in various applicative contexts within and beyond microscopy.

Contents

Acknowledgments

I would like to acknowledge to my supervisors Caroline Chaux, Hugues Talbot and Jean-Christophe Pesquet for their support along the three years period of my PhD and the guidance on my research topic. It was a real pleasure to work with them, to share passion for optimization, to be enrolled into scientific discussions and to learn how to proceed from an idea to an article.

I would like also to gratefully acknowledge to ANR for founding the project DIAMOND. The project gave me an opportunity to participate into international conferences and work with great researchers from various disciplines. Our team was composed of 13 people including Gilbert Engler, Jean-Christophe Olivo-Marin, Josiane Zerubia, Laure Blanc-Feraud, Alain Dieterlen, Saima Ben Hadj, Praveen Pankajakshan, Bruno Colicchio, Elie Maalouf. Most particularly, I would like to thank to Gilbert Engler for providing me the data for my research and his expertise in biological imaging systems.

I would like to acknowledge to the members of my jury Gabriel Peyré, Gabriele Steidl, Eric Thiébaut and Michaël Unser for their time. It was a great honor for me to present my work to them.

I would like to acknowledge to the LIGM group for a great atmosphere at our Laboratory. I was lucky to meet there many friends and great, young scientists. I would like to thank to Nelly Pustelnik, Lotfi Chaari, Mounir Kaaniche, Pascal Vallet, Ilena Florian, Florian Dupuy, Olena Tankyevych, Camille Couprie, Roland Levillain, Mireille El Gheche, Emilie Chouzenoux, Mai Quyen Pham, Audrey Repetti and Frank Schmidt for their kind assistance. I would like also to thank two invited researchers at LIGM laboratory Olga Veksler and Yuri Boykow for their insight to the problems I studied and their expertise on Graph-Cut.

At last but not least, I would like to thank to my beloved Daniel Wesierski as without him I would not be strong enough to complete this thesis, to go through all the difficulties and to overcome them.

I dedicate this thesis to my beloved parents Krystyna and Adam.

Introduction

The recovery of a target function in the presence of perturbations (e.g. noise) is a problem studied in the literature over decades and is usually associated with the term inverse problem. In this thesis, we formulate novel solutions by studying probably the oldest image processing inverse problem i.e. image deconvolution.

Context

The human senses cooperate with the brain to gather information. Similarly, new imaging modalities combined with image processing algorithms allow us to retrieve information that is invisible to the human eyes. The study of astronomical objects and phenomena, human anatomy, basic cellular, biochemical, physiological and pathological processes benefit from new visualization tools. Imaging techniques have emerged in all areas of life sciences and are becoming increasingly relevant in the biomedical and pharmaceutical areas. Imaging based diagnostics and screening influence therapy design and drug development. Fast progress in biology would not be possible without new instruments and associated software. Rapid changes in optical acquisition techniques create opportunities and challenges for the image and video processing community. In this thesis, we face challenges related to confocal macroscopy.

Confocal macroscopy (i.e. large-area confocal microscopy) is an advanced fluorescence imaging system, grounded on the principle of confocal imaging introduced in 1957 by Marvin Minsky [Pawley, 2006, Chapter 1], [Minsky, 1957]. This innovation has had a huge impact on the development of biomedical research and on some areas of clinical practice, e.g. dermatopathology, ocularpathology. Examples in the area of medicine include a system for the early noninvasive diagnosis of skin cancer [Park et al., 2010], studies of drug delivery to the eye [Furrer and Gurny, 2010], analysis of single DNA damage in human cells [Fairbairn et al., 1993], examination of some diseases like schizophrenia [Sweet et al., 2010], Parkinson's [Tatton

and Rideout, 1999] and HIV [Hubner et al., 2009], ... Moreover it influences, among others, research on artificial eyes [Jeong et al., 2006], coral reef protection [Hawaii Institute of Marine Biology http://www.hawaii.edu/HIMB/] and geomaterials [Fredrich et al., 1995].

The popularity of confocal imaging systems stems from the high optical resolution of the produced images, particularly in the sample depth direction. This increased resolution is an important advantage of confocal over convential fluorescence imaging system, namely wide-field. The confocal light system produces 2D or 3D images of cells, tissues and microorganisms by measuring its optical or fluorescent properties within a large number of small, contiguous subvolumes. A collection of such image volumes over time results in time-series image. A complete image is acquired point-by-point, i.e. in the process of scanning. The basic idea behind confocal systems is to illuminate the object with a point source and to detect reflected signal through a pinhole at a conjugate position in the emission path (see Fig. 1). Consequently, fine specimen details, which are generally of most interest, become detectable.

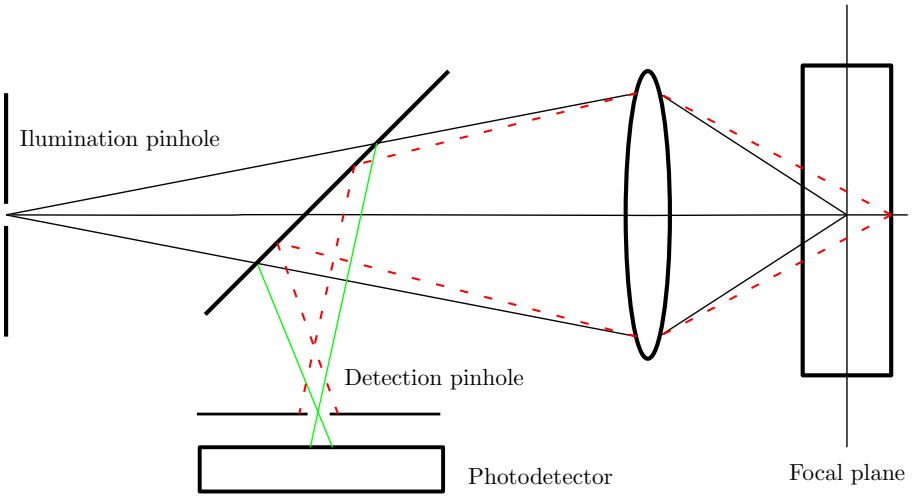

A system designed with confocal optics has the effect of eliminating much of the out-of-focus light from detection (red dotted line). The light originating from object features lying outside the focal plane is physically blocked by the detection pinhole and consequently does not reach a photodetector, while the light originating from object features lying in the focal plane (green line) is focused on the detection-pinhole.

Figure 1: *Principle of confocal imaging system*

However, until recently the maximum field of view of confocal systems was very small (typically less than 0.5×0.5 mm). Hence, visualization of large areas of tissue required merging of multiple images taken sequentially, using montage synthesis methods [Pawley, 2006, Chapter 15]. As an effect,

the quality of the resulting image had to be compromised. Macroscopy solves this problem by imaging a large area (up to a couple of centimeters) in confocal manner while maintaining the flexibility to zoom the smaller part of the object on demand (see Fig. 2). The confocal macroscopy is suited to illustrate complex biological samples, especially in multichannel mode (see Fig. 3).

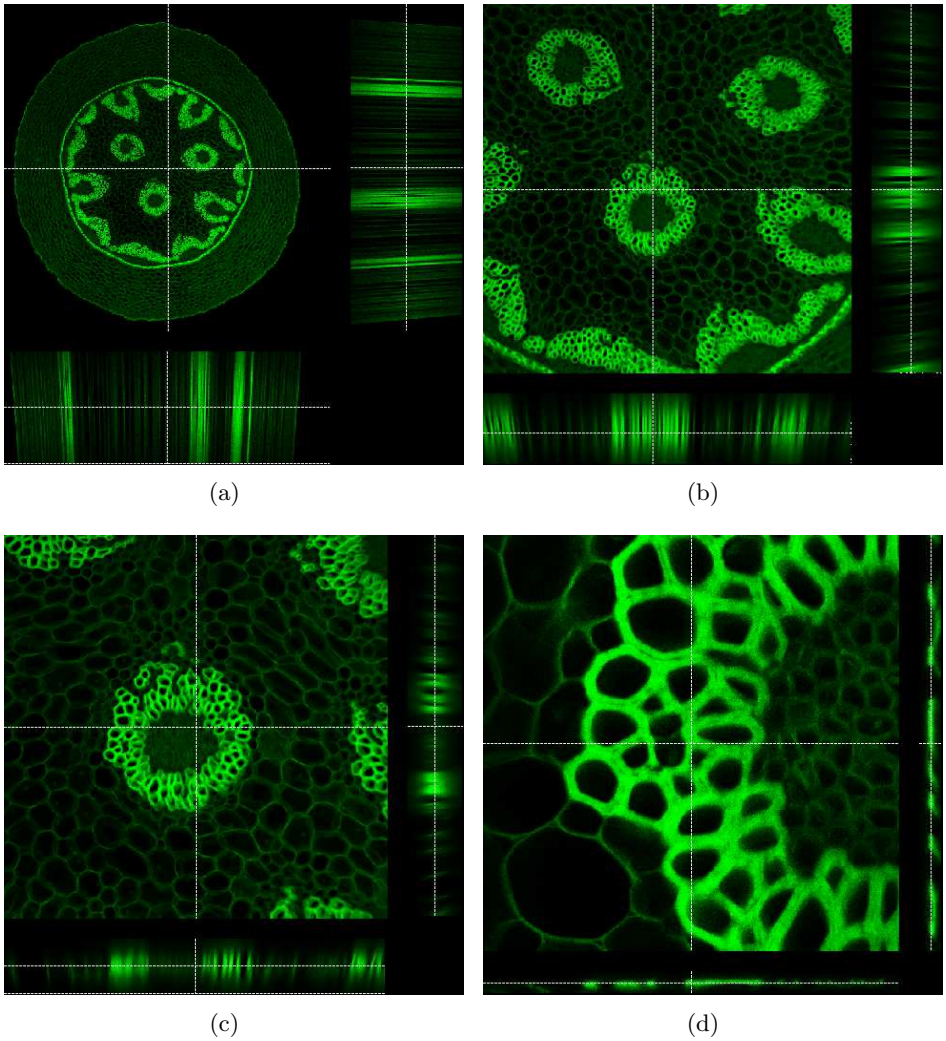

(a) (b)

(c) (d)

(a-d) illustrates Convallaria from a large to a finer scale (author: *Gilbert Engler*)

Figure 2: *An example illustrating zoom effect in confocal macroscopy*

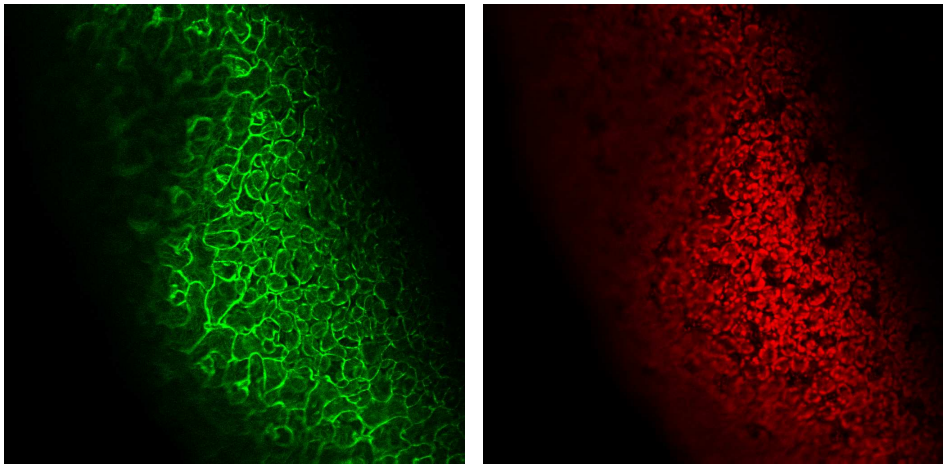

(a) Channel 1 (b) Channel 2

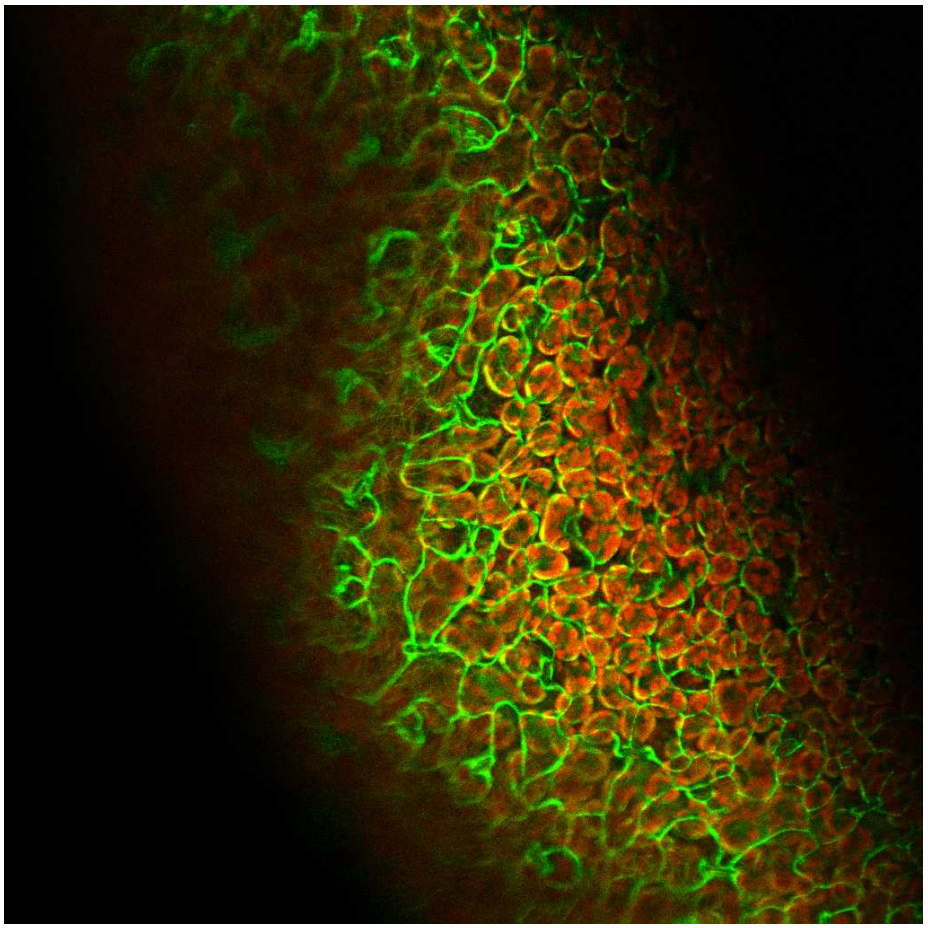

(c) Multichannel image composed of two channels presented above

Cortical leaf (author: *Gilbert Engler*)

Figure 3: *An example of multichannel confocal image*

Challenges

The challenges stem from the fact that confocal macroscopy suffers from various aberrations. Thus, an important goal is to improve the quality of the produced images. A major step toward achieving this goal is to understand how these artifacts are created, i.e. to determine the characteristics of the noise and the point spread function (PSF). A natural, simple strategy for PSF modeling would be to adopt a model established for confocal microscopy. However, first results presented in [Pankajakshan et al., 2011] indicate that it is not a good strategy. A full understanding of the PSF model requires further studies. They are particularly difficult due to the fact that precise information about the macroscope optics is not presently available. The second challenge is due to the noise characteristic and corresponding hyperparameters. Since in any confocal imaging system, increased resolution comes at the cost of decreased signal intensity (down to $8 - 12$ detectable photons per highest intensity pixel [Pawley, 2006, Chapter 2]) one can expect the noise to exhibit either Poisson or Poisson-Gaussian characteristics. Ideally, one wishes to identify this statistics and corresponding hyperparameters based on measured data.

Another difficulty is to establish distinctive features of high-quality images. Researchers in a variety of disciplines constantly push the frontiers of knowledge in order to improve the statistical description of images. As a result, the problems are formulated using more realistic models incorporating richer prior knowledge. However, achieved improvements are still limited. The true signal is estimated under various idealizations of its properties and using simplified assumptions about the degradation process. The produced results are accompanied by different artifacts (e.g. ringing, staircase effect). Some thin details of the object are not well retrieved.

In all these areas, the image processing community can contribute by formulating the related problems (noise identification, PSF modeling and deconvolution) in a solvable fashion. In this context, continuous and discrete optimization methods are particularly useful. For instance, the deconvolution results can be further improved by the design of a new prior term. In practice, this means the choice of appropriate signal representations and sparsity measure. The latter choice is most often limited to ℓ_1 function. However, one can search for other sparsity measures. Especially, algorithms originating from both domains, continuous and discrete, are continuously extended to be able to handle novel, more advanced models in an efficient way. Nevertheless, some of the considered problems are naturally formulated in a mixed discrete-continuous framework. Hence, an arising challenge is to develop appropriate methods featuring both of these worlds.

Contribution

The contribution of this thesis is developed along two axes. Firstly, we contribute to image optimization techniques and provide results concerning Poisson-Gaussian distribution, $\ell_2 - \ell_0$ sparsity measures, and associated algorithmic tools. Secondly, we contribute to the confocal macroscopy technique and develop tools for noise identification and image deconvolution. More precisely, the specific contributions are as follows:

Algorithms:

* We propose an optimization framework featuring both continuous and combinatorial techniques (Chapters 2 and 4). Our approaches address problems, in which all of the variables take values from an unknown discrete set. The discrete set is described by its cardinality and is known to be an inclusion of a given continuous set. We formulate the problem in a discrete-continuous framework, while attempting to bring together the best of both worlds.
* We address the same practical problem, namely image denoising with $\ell_2 - \ell_0$ sparsity measures, in discrete (Chapter 6) and continuous (Chapter 7) frameworks, which provide an opportunity to compare the two approaches with respect to the considered applications.
* We investigate $\ell_2 - \ell_0$ functions as a sparsity measures (Chapter 7).
* We develop an approximation for the Poisson-Gaussian neg log likelihood, and provide a bound on the involved error (Chapter 3). Building upon this result, the main contribution of Chapter 3 is a numerical method for computing a maximum likelihood estimate of Poisson-Gaussian distribution hyperparameters and its Cramer-Rao bounds.
* We propose a new algorithm designed in a combinatorial graph-cut framework for minimizing energies with truncated convex regularization function (Chapter 6).
* We show that Poisson-Gaussian neg log likelihood is an μ-Lipschitz differentiable convex function. This result provides us new opportunities to solve the related optimization problems, such as these offered by proximal splitting algorithms (Chapter 5).

Confocal macroscopy:

* We provide tools for a study of the noise characteristics, i.e. the shape of its probability distribution and values of the related hyper-parameters. Our tools allow us to identify the noise parameters from time series data (Chapter 3), as well as from single image (Chapter 4). This forms a backbone for calibration systems and constitutes a crucial preliminary step towards development of image restoration algorithms.

∗ We provide new tools for image deconvolution (Chapters 5 and 7). The method proposed in Chapter 5 incorporates a realistic noise model, but no PSF. Hence, it can be regarded as a preliminary work towards future restoration techniques.

Publications:

Journal papers:

1. Caroline Chaux, Anna Jezierska, Jean-Christophe Pesquet, and Hugues Talbot, A spatial regularization approach for vector quantization, Journal of Mathematical Imaging and Vision, vol 41, pages 23-38, 2011
2. Emilie Chouzenoux, Anna Jezierska, Jean-Christophe Pesquet, and Hugues Talbot, A Majorize-Minimize Subspace Approach for $\ell_2 - \ell_0$ Image Regularization , accepted to SIAM Journal on Imaging Science, 2011
3. Anna Jezierska, Caroline Chaux, Jean-Christophe Pesquet, Hugues Talbot and Gilbert Engler An EM Approach for Poisson-Gaussian Noise Modeling, submitted to IEEE Transactions on Signal Processing, 2012

Conference papers:

4. Anna Jezierska, Caroline Chaux, Hugues Talbot, and Jean-Christophe Pesquet Image quantization under spatial smoothness constraints, International Conference on Image Processing (ICIP), Honk Kong, 26-29 September 2010
5. Anna Jezierska, Hugues Talbot, Olga Veksler, and Daniel Wesierski A fast solver for truncated-convex priors: quantized-convex split moves, Energy Minimization Methods in Computer Vision and Pattern Recognition (EMMCVPR), Saint Petersburg, 25-27 July 2011
6. Anna Jezierska, Caroline Chaux, Jean-Christophe Pesquet, and Hugues Talbot An EM approach for Poisson-Gaussian noise modeling, European Signal Processing Conference (EUSIPCO), Barcelona, 29 August - 2 September 2011
7. Emilie Chouzenoux, Jean-Christophe Pesquet, Hugues Talbot, and Anna Jezierska A memory gradient algorithm for l2 - l0 regularization with applications to image restoration, International Conference on Image Processing (ICIP), Brussels, 11-14 September 2011
8. Anna Jezierska, Emilie Chouzenoux, Jean-Christophe Pesquet, and Hugues Talbot A primal-dual proximal splitting approach for restoring data corrupted with Poisson-Gaussian noise, International Conference on Acoustics, Speech, and Signal Processing (ICASSP), Kyoto, 25-30 March, 2012

9. Anna Jezierska, Hugues Talbot, Caroline Chaux, Jean-Christophe Pesquet, and Gilbert Engler Poisson-Gaussian noise parameter estimation in fluorescence microscopy imaging, International Symposium on Biomedical Imaging (ISBI), Barcelona, 2-5 May, 2012
10. Daniel Wesierski, Maher Mkhinini, Patrick Horain, and Anna Jezierska Fast Recursive Ensemble Convolution of Haar-like Features, Computer Vision and Pattern Recognition (CVPR), Providence, Rhode Island, 18-20 June, 2012

Organization and summary

The rest of this thesis is organized as follows. The next chapter serves to introduce the reader to the topic of inverse problems and associated mathematical tools, i.e. variational methods applied to either continuous or discrete models. We briefly discuss majorize-minimize, graph-cut and proximal optimization algorithms. Then, the subsequent Chapters 2-7 address various inverse problems. Each of them aims to provide a review of the state of the art, describe a problem, propose a solution and illustrate it with results. More precisely, in Chapter 2 we develop an optimization framework featuring both continuous and combinatorial techniques. In Chapter 3 we propose an Expectation-Maximization algorithm for Poisson-Gaussian noise parameters estimation from time series data. Then, in Chapter 4, using the results from the two previous Chapters, we develop a single image noise estimation approach. In Chapter 5, we study the problem of restoring data corrupted by Poisson-Gaussian noise using an exact continuous-discrete model. Chapters 6-7 provide an insight into the topic of minimizing objective function, which includes terms with $\ell_2 - \ell_0$ sparsity measure. Chapter 6 deals with a discrete problem formulation in the presence of truncated convex priors. In Chapter 7, we extend the work of [Chouzenoux et al., 2011] to minimize non necessarily convex functions. Finally, we draw some conclusions and perspectives in Chapter 8.

- Chapter 1 -

Background

An image is a realization of a stochastic signal which includes visual information about one or several objects. One says "A picture is worth a thousand words", which refers to the huge amount of information conveyed in a single image. Indeed, it is huge but also restricted in the following sense: the visual information about an object is acquired by imaging systems, which impose some limits on the amount of transmitted information. The question then arises if and how the lost information can be retrieved? There has been extensive research on this topic. In this chapter, we review some of the results relevant to our studies. Firstly, we provide an introduction to the topic of inverse problems and to the associated mathematical tools. In our context, the presentation is restricted to variational methods applied to either continuous or discrete models. Then, the related optimization methods are discussed, while a special attention is devoted to expectation-maximization, graph-cut and proximal optimization algorithms.

§ 1.1 Inverse problems

In signal theory, inverse problems refer to the principle of converting an observed signal into information about a physical object of interest, which is unobservable and inaccessible by direct measurements. Hence, the ideal solution usually cannot be computed exactly (an estimation is needed) and its computation may be highly unstable and sensitive to small changes in the data. There are many problems formulated within this framework. Examples in the area of image processing include segmentation, depth estimation, shape recognition, ...

In the following we study the problem of recovering information about an imaging system and an input signal. We consider an imaging system to be described by the distortion it introduces, which can be broadly divided into

deterministic and stochastic parts, usually a blur and a noise perturbation, where blurring is related to the process of image formation and noise to the process of image recording. This can be described by the following model:

$$y = z\left(H(x)\right) + w \tag{1.1}$$

where the operator $H : \mathcal{X} \mapsto \mathcal{Y}$ models blur, $\mathcal{X}$ and $\mathcal{Y}$ are subsets of finite dimensional real Hilbert spaces, and $z(H(x))$ and w are realizations of signal dependent and additive noise, respectively. Model (1.1) is a direct model i.e the opposite of an inverse problem. It relates vector of observations $y \in \mathcal{Y}$ with original signal $x \in \mathcal{X}$. In the context of image reconstruction, typical examples of $\mathcal{X}$ include: real matrix space $\mathbb{R}^{N\times M}$, real vector space $\mathbb{R}^N$, nonnegative integer matrix set $\mathbb{N}^{N\times M}$ or $\mathcal{L}^{N\times M}$, where $\mathcal{L}$ is any countable subset of real numbers. Signals $x = (x_i)_{i\in\mathbb{X}}$ and $y = (y_i)_{i\in\mathbb{Y}}$ are realizations of random vectors X and Y, respectively. In such settings $\mathbb{X}$ and $\mathbb{Y}$ denote the support of the signals associated with x and y, respectively, (i.e. their components in some basis of the underlying Hilbert spaces).

It is further assumed that statistical properties of the noise is known. More specifically, $z(H(x))$ and w are regarded as realizations of mutually independent random variables $Z(H(x))$ and W having independent components. The components of variables Z and W are scalar random variables defined by parametric probability measures P_{Z_i} and P_{W_i}, respectively. Additionally we assume that the families of distributions P_{Z_i} and P_{W_i} can be described by a finite number of parameters. They are collected together to form a single vector of parameters θ. We study the following associated inverse problems:

- Noise parameter estimation, where measurements are used to infer parameters in a mathematical model. This problem consists of searching θ and x under the assumption that y is known. In a denoising setting, the existence of H is neglected (see Fig. 1.1(a)).

- Signal recovery, where measurements are used to infer the original signal. This problem consists of searching x under the assumption that y, H and θ are known (see Fig. 1.1(b)).

Beyond these issues, one can consider blind restoration techniques, which are designed to simultaneously estimate the degradation kernel H and the original signal x. However, in the following, we assume that non-blind deblurring techniques can be efficiently used provided that the blur and noise models are accurate enough.

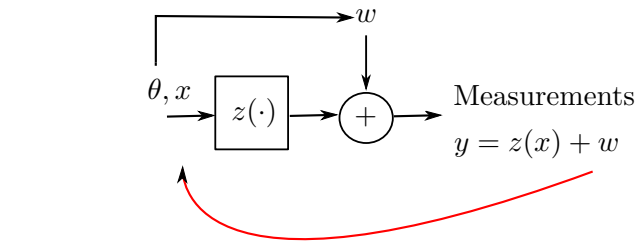

(a) Noise parameter identification

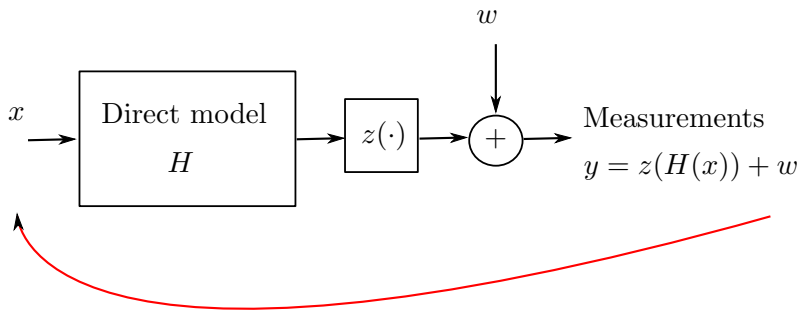

(b) Signal recovery

Figure 1.1: *Block diagrams of considered inverse problems*

The characteristic mathematical aspect of inverse problems is that they are usually ill-posed i.e. at least one of the properties of a well-posed problem is violated. According to the definition provided by Hadamard [Hadamard, 1902], well-posed problems respect the following conditions:

- a solution exists;
- the solution is unique;
- the solution is stable.

When a new problem is proposed, the first concern is to establish its well-posedness. The existence and uniqueness are usually addressed for a given class of functions e.g. the convex function class, while the stability is studied by verifying if the solution depends continuously on the data, i.e. $d(y-y') \rightarrow 0 \Rightarrow d(x-x') \rightarrow 0$ where d denotes a distance measure.

Example 1.1.1 A classical ill-posed inverse problem is the following. Let us consider the simple case when H is a linear operator and the problem is to restore signal $x \in \mathbb{R}^N$ in the presence of blur $H \in \mathbb{R}^{Q \times N}$ from observations $y \in \mathbb{R}^Q$. One can obtain the direct solution as $x = H^{-1}y$. This solution is computationally feasible if H is invertible i.e. H is a square matrix ($Q = N$) and $\text{Ker}\,(H) = \{0\}$. If the first condition fails, the solution x to the linear problem $Hx = y$ does not necessarily exist, while if the second condition fails

the solution x is not unique. The third Hadamard's condition is satisfied provided that H is well-conditioned, i.e. the stability of the solution can be evaluated in terms of condition number of H.

§ 1.2 Estimation of the solution

The solutions of inverse problems are the results of estimation problems. The goal of estimation is to find a solution $\widehat{x}$ which is reasonably close to the original signal x. Estimation techniques are often classified into two groups: deterministic or statistical. The difference stems from the assumptions made on the models. The statistical approach involves stochastic models, even the solution itself can be viewed as a random variable.

We adopt the following general definition of an estimator. An estimator $\widehat{X}$ is a rule by which we guess the value of unknown signal X on the basis of Y, where X and Y are vectors of random variables $(X_i)_{i\in\mathbb{X}}$ and $(Y_i)_{i\in\mathbb{Y}}$, respectively. Hence, $\widehat{X} : y \mapsto \widehat{X}(y)$ is a function. It is described by the following characteristics:

- $\text{bias}(\widehat{X}) = \left(\mathsf{E}\left[\widehat{X}_i(Y) - X_i\right]\right)_{i\in\mathbb{X}}$ (bias)
- $\text{cov}(\widehat{X}) = \left(\mathsf{E}\left[\left(\widehat{X_i}(Y) - \mathsf{E}(\widehat{X_i}(Y))\right)\left(\widehat{X_j}(Y) - \mathsf{E}(\widehat{X_j}(Y))\right)\right]\right)_{(i,j)\in\mathbb{X}}$ (covariance matrix)
- $\text{MSE} = \left(\mathsf{E}\left[(\widehat{X}_i(Y) - X_i)^2\right]\right)_{i\in\mathbb{X}}$ (mean square error vector).

An estimator calculates an estimate for particular observations $\{y_i\}_{i\in\mathbb{Y}}$. An unbiased estimator $\widehat{X}$ is called a minimum variance unbiased estimator (MVUE) if for every estimator X'

$$\text{trace}\left(\text{cov}(\widehat{X})\right) \leqslant \text{trace}\left(\text{cov}(\widehat{X'})\right) \tag{1.2}$$

where a lower bound on the variance of the components of $\widehat{X}$ is provided by the Cramer-Rao theorem [Rao, 1945], [Cramer, 1946].

Next we describe two classical estimators, namely the maximum likelihood estimator (MLE) and Bayesian estimators. The former is usually applied to well-posed problems while the latter one to ill-posed problems.

1.2.1 Maximum likelihood estimator

Let $p_Y(\cdot \mid X = x)$ be a probability measure i.e.

- a likelihood function in the continuous case
- a probability mass function in the discrete case

then the maximum likelihood estimate $\widehat{X}_{\text{MLE}}$ is defined as

$$\forall y \qquad \widehat{X}_{\text{MLE}}(y) \in \arg\max_{x} \; p_Y(y \mid X = x) \tag{1.3}$$

and for differentiable function $x \mapsto p_Y(y \mid X = x)$ it satisfies

$$\frac{\partial p_Y(y \mid X = x)}{\partial x} \; |_{\widehat{X}_{\text{MLE}}(y)} = 0. \tag{1.4}$$

In some cases, a maximum likelihood estimator is given as an explicit function of the observations. However, in many instances, no closed-form solution is available, and the MLE has to be found numerically using optimization methods. This can be illustrated with the example of the noise parameter estimation problem addressed in Chapter 3.

1.2.2 Bayesian estimators

Assuming that a desired property of a solution is known a priori, an ill-posed inverse problem can be replaced by a better-posed one, i.e. leading to solutions with a lower sensitivity to perturbations of the input data but not necessarily well-posed in the sense of Hadamard. For instance, the resulting problem can be non strictly convex or it can be discrete i.e. $\mathcal{X}$ is a discrete set. In both cases the solution is not guaranteed to be unique and all solutions are equally likely.

Bayesian estimators constitute a classical example of estimators incorporating prior belief. More recently, considerable interest has been drawn in empirical Bayesian approaches. For instance, there has been much attention devoted to Stein's unbiased risk estimate (SURE) [Stein, 1981],[Pesquet et al., 2009]. However, the discussion here is limited to classical Bayesian estimators. They are given as the solution of the following problem:

$$\text{Find} \quad \arg\min_{\widehat{x}} \mathsf{E}\left[C(\widehat{x}, X) \mid Y = y\right] \tag{1.5}$$

where C is a cost function and $\mathsf{E}\left[C(\widehat{X}(Y), X)\right]$ is called a risk function. A number of various estimators have been proposed which differ in the choice of a cost function. Among them we recall:

- MMSE: minimum mean square error estimator associated with a quadratic cost function. Then, rewriting Problem (1.5) yields:

$$\text{Find} \quad \arg\min_{\widehat{x}} \mathsf{E}\left[\|X - \widehat{x}\|^2 \mid Y = y\right] \tag{1.6}$$

  which results into

$$\widehat{X}_{\text{MMSE}}(y) = \mathsf{E}_{X|Y=y}\left[X\right]. \tag{1.7}$$

- MAP: maximum a posteriori estimator associated with hit or miss cost function defined as

$$\forall (u,v) \in \mathcal{X}^2,\ u = (u_i)_{i\in\mathbb{X}},\ v = (v_i)_{i\in\mathbb{X}},$$
$$C(u,v) = \begin{cases} 0 & \text{if } \forall i \in \mathbb{X} \ \ |u_i - v_i| < \Delta \\ 1 & \text{otherwise.} \end{cases} \tag{1.8}$$

  Assuming that $\Delta > 0$ and Δ tends to 0, Problem (1.5) results in

$$\widehat{X}_{\mathrm{MAP}}(y) \in \ \arg\max_x p_X(x \mid Y = y). \tag{1.9}$$

  By using Bayes rule, this can be simplified as follows:

$$\widehat{X}_{\mathrm{MAP}}(y) \in \arg\max_x p_X(x \mid Y = y) \Leftrightarrow$$
$$\widehat{X}_{\mathrm{MAP}}(y) \in \ \arg\max_x \left(p_Y(y \mid X = x)\, \frac{p_X(x)}{p_Y(y)} \right) \Leftrightarrow$$
$$\widehat{X}_{\mathrm{MAP}}(y) \in \ \arg\max_x \left(p_Y(y \mid X = x)\, p_X(x) \right). \tag{1.10}$$

  Due to the monotonicity of the logarithm function this can be rewritten as:

$$\widehat{x}_{\mathrm{MAP}} \in \ \arg\min_x \Phi(x) + \rho(x) \tag{1.11}$$

  where $\Phi(x) = -\log\left(p_Y(y \mid X = x)\right)$ and $\rho(x) = -\log\left(p_X(x)\right)$. The former function is called a data fidelity term, while the latter a regularization term.

The MMSE estimator can be regarded as an interesting choice. However, in general due to the involved high-dimensional integral, it is more difficult to compute. On the other hand the MAP estimator is computationally simple and consequently offers more flexibility in the choice of a prior.

1.2.2.1 Data fidelity term

In image reconstruction problems, the data fidelity term usually consists of the noise negative log likelihood or an approximation of it. The assumption of independence of the noise components translates into:

$$p_{Y|X=x}(x) = \prod_{i\in\mathbb{Y}} p_{Y_i|X=x}(y_i) \tag{1.12}$$

and consequently the data fidelity term is given by:

$$\Phi(x) = -\sum_{i\in\mathbb{Y}} \log\left(p_{Y_i|X=x}(y_i)\right) \tag{1.13}$$

Usually $p_{Y|X=x}(y)$ models simple types of noise. Among them the most popular are the uniform, Gaussian, Poisson and impulse (also known as salt-and-pepper) noises. Sometimes the Rayleigh and Gamma noise are considered. In the following, for brevity, we skip over the description of noise types other than Gaussian and Poisson.

A zero-mean Gaussian noise is additive and has a probability density function defined by the normal ($\mathcal{N}$) distribution i.e. for all $i \in \mathbb{Y}$

$$p_{Y_i|X=x}(y_i) = \frac{1}{\sqrt{2\pi\sigma^2}} e^{\frac{(y_i - [H(x)]_i)^2}{2\sigma^2}} \tag{1.14}$$

where σ^2 is a variance. This leads to

$$\Phi(x) = \frac{1}{2\sigma^2} \sum_{i \in \mathbb{Y}} (y_i - [H(x)]_i)^2. \tag{1.15}$$

The simple form of this data fidelity term makes the Gaussian noise assumption to be commonly encountered in imaging. By simple we mean that function (1.15) is convex, non negative and Lipschitz differentiable (provided that H is linear), which is desirable for solving estimation problems efficiently. However, nowadays, efficiency can also be guaranteed for more involved estimation problems. Hence, present studies are not limited to the simplest Gaussian case.

Poisson noise is signal dependent and can be analytically described by the following distribution ($\mathcal{P}$): for all $i \in \mathbb{Y}$

$$p_{Y_i|X=x}(y_i) = \frac{([H(x)]_i)^{y_i}}{y_i!} \exp(-[H(x)]_i) \tag{1.16}$$

The associated data fidelity term takes the form of a Kullback-Leibler divergence i.e.

$$\Phi(x) = \sum_{i \in \mathbb{Y}} \left(y_i \log(y_i) - y_i \log([H(x)]_i) + [H(x)]_i - y_i \right) \tag{1.17}$$

and by dropping the terms independent of x we can set

$$\Phi(x) = \sum_{i \in \mathbb{Y}} \left([H(x)]_i - y_i \log([H(x)]_i) \right). \tag{1.18}$$

Alternatively, one can resort to variance stabilization techniques, which are defined by a mapping ν_P replacing random variable Y by Y' such that $\mathrm{var}(Y')$ does not depend on x. For instance, in the case of Poisson noise it consists of finding ν_P such that $\mathrm{var}(Y')$ is a given constant value i.e. for all $i \in \mathbb{Y}$

$$Y_i \sim \mathcal{P}\big([H(X)]_i\big) \Leftrightarrow \nu_P(Y_i) \approx \mathcal{N}(\nu_P([H(X)]_i), 1) \tag{1.19}$$

Classical examples include:

- The Bartlett transform [Bartlett, 1936]: $\nu_P(x) = 2\left(\sqrt{x_i + c}\right)_{i\in\mathbb{Y}}$. For $c = \frac{3}{8}$ Anscombe transform [Anscombe, 1948] is recovered.

- The Wilson-Hilferty transform [Wilson and Hilferty, 1931]: $\nu_P(x) = \left(\sqrt[3]{x_i}\right)_{i\in\mathbb{Y}}$

- The Box - Cox transform [Box and Cox, 1964] : $\nu_P(x) = (\log(x_i))_{i\in\mathbb{Y}}$

- The Haar-Fisz transform [Fryzlewicz and Nason, 2004] where ν_P is defined in terms of Haar wavelet coefficients and it changes each detailed coefficient of x by normalizing it by the square root of the corresponding approximation coefficient.

This technique allows us to apply standard methods developed for Gaussian noise. In such settings, usually a three-step procedure is developed, i.e. forward transform followed by Gaussian data processing and inverse transform. However the simplicity of this procedure may compromise result quality. In fact, these approaches are known to provide poor numerical results for low-intensity signals. Nevertheless, some improvements have been achieved by providing a better inverse transform [Makitalo and Foi, 2011],[Sampathkumar and Arun, 2012]. Another possibility is to use the technique proposed in [Dupé et al., 2009]. In this work, the authors study the following data fidelity term:

$$\Phi(x) = \Phi_G \circ \nu_P(x) \tag{1.20}$$

where Φ_G is given by (1.15) and ν_P is defined by the Anscombe transform. This data fidelity term is shown to be a convex, non negative, Lipschitz differentiable function, which opens the possibility of employing variance stabilization techniques while not requiring an inverse transform.

Single noise analysis is attractive due to its simplicity. However many images are affected by a mixture of noise sources. A Poisson-Gaussian noise serves as a good example. In this case, $p_{Y|X=x}(y)$ models a weighted sum of a signal dependent Poisson noise and an additive Gaussian noise such that $Y = \alpha Z + W$, where $Z \sim \mathcal{P}(H(X))$, $W \sim \mathcal{N}(c, \sigma^2)$ and α is a Poisson noise scaling parameter.

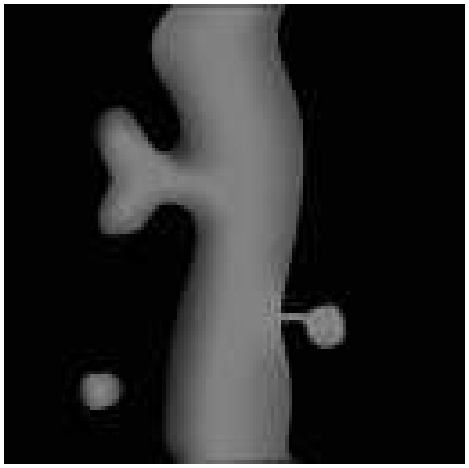

(a) Phantom of a 128 × 128 confocal microscopy image illustrating a neuron; Image intensities range between 0.25 and 17.25 (*Source: F.X. Dupe homepage* http://fxdupe.free.fr/software.html)

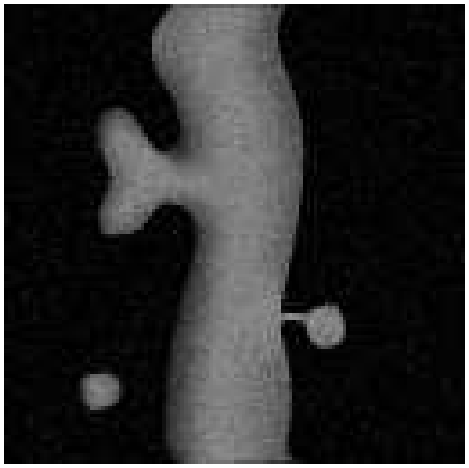

(b) Image corrupted by Gaussian noise ($c = 0, \sigma = 1$)

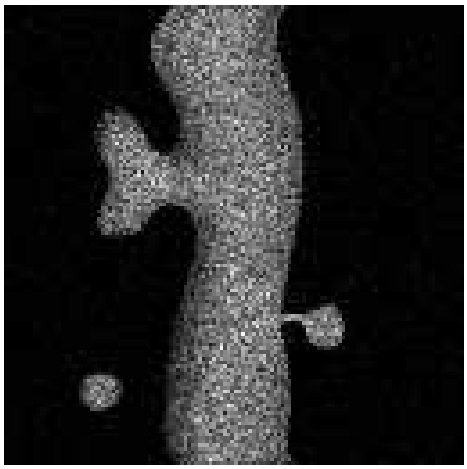

(c) Image corrupted by Poisson noise

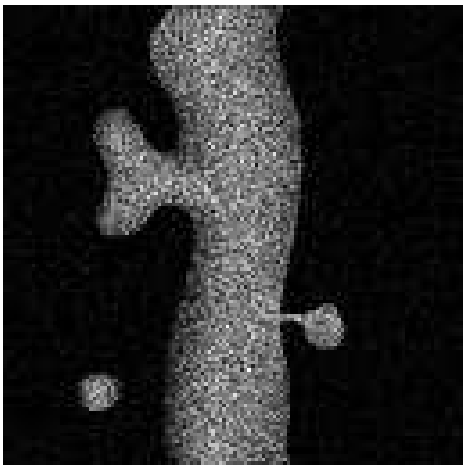

(d) Image corrupted by Poisson-Gaussian noise ($\alpha = 1$, $c = 0$, $\sigma = 1$)

Figure 1.2: *Influence of different noise types*

A related distribution is given by a discrete convolution of Gaussian and Poisson probability measure, i.e. for all $i \in \mathbb{Y}$:

$$p_{Y_i|X=x}(y_i) = \sum_{n=0}^{+\infty} \frac{e^{-[H(x)]_i}([H(x)]_i)^n}{n!} \frac{e^{-\frac{1}{2\sigma^2}(y_i - c - \alpha n)^2}}{\sqrt{2\pi\sigma^2}} \tag{1.21}$$

which leads to:

$$\Phi(x) = \sum_{i \in \mathbb{Y}} \left\{ [H(x)]_i - \log \left(\sum_{n=0}^{+\infty} \frac{([H(x)]_i)^n}{n!} \frac{e^{-\frac{1}{2\sigma^2}(y_i - c - \alpha n)^2}}{\sqrt{2\pi\sigma^2}} \right) \right\}. \quad (1.22)$$

Similarly to the Poisson case, approximations are often considered, e.g.:

- "Gaussianization" [Murtagh et al., 1995] by means of a variance stabilization transform ν_{PG} defined as: for all $i \in \mathbb{Y}$

$$Y_i \sim \alpha \mathcal{P}\big([H(X)]_i\big) * \mathcal{N}(c, \sigma^2) \Leftrightarrow \nu_{PG}(Y_i, \theta) \approx \mathcal{N}(\nu_{PG}([H(X)]_i, \theta), 1) \quad (1.23)$$

  where $*$ denotes the discrete convolution operator and $\theta = [\alpha, c, \sigma]^\top$.

- "Poissonization" procedure [Chakrabarti and Zickler, 2012], i.e. for all $i \in \mathbb{Y}$:

$$Y_i \sim \mathcal{P}\big([H(X)]_i\big) * \mathcal{N}(c, \sigma^2) \Leftrightarrow \big(Y_i - c + \sigma^2\big) \approx \mathcal{P}([H(X)]_i + \sigma^2) \quad (1.24)$$

- Approximations of gradient involving exponential functions:

$$\dot{\Phi}\,(x) = H^\top \left(\mathbf{1} - \exp\left(-\frac{\mathbf{1} + \mathbf{2}(\alpha\,[\mathbf{H(x)}]_\mathbf{i} + \mathbf{c} - \mathbf{y_i})}{\mathbf{2}(\alpha\,[\mathbf{H(x)}]_\mathbf{i} + \mathbf{c} + \boldsymbol{\sigma^2})} \right)_{\mathbf{i} \in \mathbb{Y}} \right) \quad (1.25)$$

  or

$$\dot{\Phi}\,(x) = H^\top \left(\mathbf{1} - \left(\frac{\mathbf{y_i} + \boldsymbol{\sigma^2}}{\alpha\,[\mathbf{H(x)}]_\mathbf{i} + \mathbf{c} + \boldsymbol{\sigma^2}} \right)_{\mathbf{i} \in \mathbb{Y}} \right) \quad (1.26)$$

  where Φ denotes the function defined in (1.22) and $\dot{\Phi}$ its gradient. These two approximations were proposed in [Benvenuto et al., 2008]. They apply only if y_i is sufficiently large i.e. according to authors greater than 30.

Among the listed above approximations, the most popular is Gaussianization using the generalized Anscombe transform (GAT) given by:

$$\nu_{PG}(x, \theta) = \frac{2}{\alpha} \left(\sqrt{\alpha x_i + \frac{3}{8}\alpha^2 + \sigma^2 - \alpha c} \right)_{i \in \mathbb{Y}} \quad (1.27)$$

The corresponding optimal inverse transform, proposed in [Makitalo and Foi, 2012], is relevant for three-step approaches. Instead, one can explore the fact that

$$\Phi(x) = \Phi_G \circ \nu_{PG}(x) \quad (1.28)$$

exhibits the same desirable properties as (1.20) i.e. it is non-negative, convex and Lipschitz differentiable. The influence of the described noises is illustrated on the example in Fig. 1.2.

1.2.2.2 Regularization term

The general objective of regularization terms consists of enforcing prior knowledge or assumptions about the solution. Additionally, a regularization term should meet the following criteria:

- good performance across a class of considered images
- robustness to the choice of parameters
- low computational cost.

Let the number of constraining terms be denoted by $R \in \mathbb{N}^*$. Then, the regularization combining different terms is called a hybrid regularization, i.e.

$$\rho(x) = \sum_{r=1}^{R} \psi_r(V_r(x)) \tag{1.29}$$

where $V_r : \mathcal{X} \mapsto \mathcal{V}_r$ is an operator, $\mathcal{V}_r$ is a subset of a finite dimensional real Hilbert space. If an operator V_r is parametrized by y we call $\psi_r(V_r(x))$ an image adaptive prior [Peyré, 2011]. Otherwise, it is called a non-adaptive prior.

In our context, the most common assumption is that the signal of interest x has a sparse representation with respect to preassigned operator V_r, i.e. $V_r(x)$ has a small number of large coefficients and zeros elsewhere. According to [Donoho et al., 1995], an ideal measure of sparsity ψ_r is the ℓ_0 measure, i.e.

$$\ell_0(x) = \sum_{j \in \mathbb{X}} \chi(x_j) \tag{1.30}$$

where

$$\chi(x_j) = \begin{cases} 0 & \text{if } x_j = 0 \\ 1 & \text{otherwise.} \end{cases} \tag{1.31}$$

However, due to the non-convexity of ℓ_0, different measures of sparsity have been proposed. Among them the ℓ_1 measure is the most popular, i.e.:

$$\ell_1(x) = \sum_{j \in \mathbb{X}} |x_j| \tag{1.32}$$

where $|\cdot|$ denotes absolute value. In this thesis we will examine the $\ell_2 - \ell_0$ measure. A detailed discussion is provided in Chapter 7. Next, we illustrate the sparsity concept with some examples of regularization terms often encountered in the context of image restoration.

Example 1.2.1 The first example concerns the sparsity of the gradient and higher order differences i.e. the case when V_r is either a gradient operator or a higher order difference operator. In both cases, depending on the choice of function ψ_r, the prior can be either isotropic or anisotropic. Isotropy is achieved by applying non-separable functions, for instance an ℓ_2 measure. In contrast, in anisotropic formulation, the differences in each direction contributes to the regularization cost independently, for instance using an ℓ_1 measure. The sparsity of the gradient is exploited in various image recovery application. It is enforced by the so-called total variation prior (TV), firstly introduced in imaging by Rudin, Osher and Fatemi [Rudin et al., 1992a]. In the classical settings, i.e. $\mathcal{X} = \mathbb{R}^N$, $\mathbb{X} = \{1, \ldots, N\}$ the total variation is defined by a collection of linear operators V_j, which for all $j \in \mathbb{X}$ are given by $V_j = [V_j^1, \ldots, V_j^O]^\top$, where O states for the number of considered orientations. Often for $2D$ images $O = 2$ while V_j^1 and V_j^2 denote the vertical and horizontal gradient operators, respectively. A similar concept was studied in the context of Markov Random Field (MRF) [Geman and Geman, 1984], [Geman and Reynolds, 1992]. In the latter formulation, the sparsity of the gradient is enforced by defining a pairwise clique potential depending on the gradient at each location j. The concept of total variation has been generalized to higher order differences. For instance, the Hessian based regularization was already discussed in the work by [Geman and Reynolds, 1992], [Li and Huttenlocher, 2008], where it is introduced by the MRF higher order clique model, while the authors in [Lefkimmiatis et al., 2012] provide a definition of operators V_r explicitly.

Example 1.2.2 The second example concerns the sparsity of differences across the directions defined by some image features. This prior is known as nonlocal total variation (NLTV) and was introduced by Gilboa and Osher [Gilboa and Osher, 2008]. It stems from the fact that the choice of directions pointed by local gradient is regarded as a drawback of TV prior. Hence, NLTV is associated with image-driven directions i.e. the directions are chosen for all $j \in \mathbb{X}$ independently, based on a similarity score between pixel intensity in a local neighborhood. Originally the patch based score [Buades et al., 2005] has been proposed. However different similarity measures can be employed. By analogy to TV, NLTV can be isotropic or anisotropic, which is related to the choice of sparsity measure ψ_r. NLTV requires a preprocessing step, which consists of computing weights and the number of orientations. In the setting from the previous example i.e. $\mathcal{X} = \mathbb{R}^N$ and $\mathbb{X} = \{1, \ldots, N\}$ NLTV is defined by a collection of linear operators V_j, which for all $j \in \mathbb{X}$ are given by $V_j = [\omega_j^1 V_j^1, \ldots, \omega_j^{O_j} V_j^{O_j}]^\top$, where the integers $(O_j)_{j \in \mathbb{X}}$ state for the number of orientations and $(\omega_j^o)_{o \in \{1,\ldots,O_j\}} \in [0, +\infty)^{O_j}$ is a vector of weights.

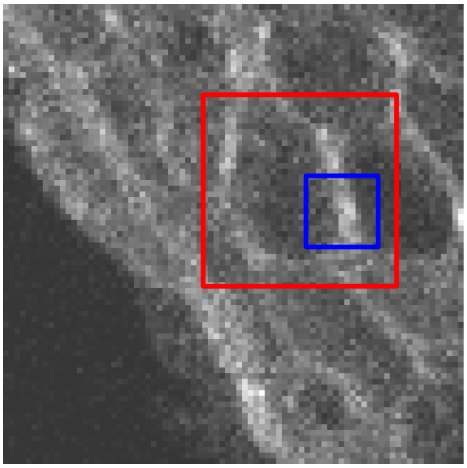

(a) Fragment of original macro confocal image (author: *Gilbert Engler*) Image parts highlighted by blue and red rectangles are illustrated in (b) and (c), respectively

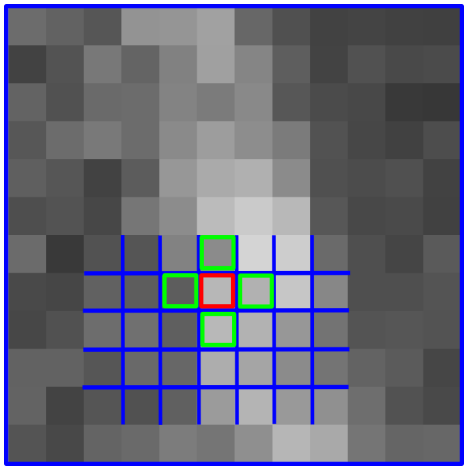

(b) Differences across horizontal and vertical gradient (TV). Local gradient at pixel (highlighted by red rectangle) is given by differences of its intensity and one of adjacent pixel. Green rectangles highlight horizontal and vertical neighbors.

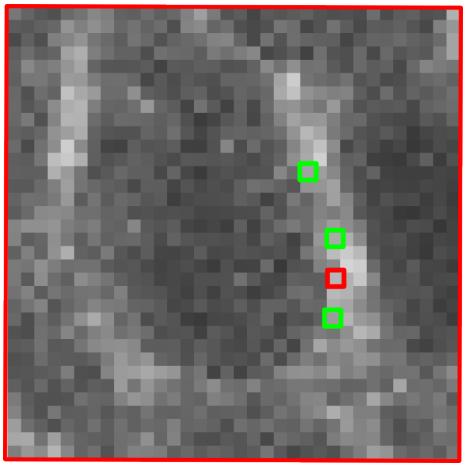

(c) Differences across the directions defined by some image features (NLTV). Gradient at pixel (highlighted by red rectangle) is given by differences of its intensity and one of pixel, chosen based on given similarity measure. Chosen neighboring pixels are highlighted by green rectangles.

Figure 1.3: *Illustration of idea behind local and nonlocal total variation.*

Example 1.2.3 The next example concerns sparsity in a frame domain. The frame approach consists of decomposing a signal into a dictionary of

"atoms". In general, the sparsity of the coefficients can be increased using an appropriate frame for the given class of signals. For convenience, let us assume that $\mathcal{X} = \mathbb{R}^N$, then a frame is a collection of vectors V_r, with $r \in \{1, \dots, R_F\}$, such that $\underline{v} \|x\|^2 \leqslant \sum_{r\in\{1,\dots,R_F\}} |\langle x, V_r\rangle|^2 \leqslant \overline{v} \|x\|^2$, where $\underline{v}, \overline{v}$ are two positive scalars in $(0, +\infty)$, $\langle \cdot, \cdot \rangle$ denotes the scalar product and $\|\cdot\| = \sqrt{\langle \cdot, \cdot \rangle}$ the norm of $\mathbb{R}^N$. It is worth noticing that in a finite dimensional case the upper bounds is always satisfied. An interesting special case is when the frame reduces to an orthonormal basis, i.e. when $\underline{v} = \overline{v} = 1$ and for all $r \in \{1, \dots, R_F\}, \|V_r\| = 1$. Some examples of orthonormal bases include: discrete Fourier transform, orthogonal wavelets [Mallat, 1999] ... However, often overcomplete representations are considered, e.g. Gabor transform, ridgelets [Candès, 1998]. The redundancy of frames is also typical for some image-adaptive frames, like Principal Component Analysis (PCA) bases [Yu et al., 2012], and Block Matching 3-D filtering (BM3D) [Danielyan et al., 2012]. One can also classify frames as tight-frames or non tight-frames. A frame is tight if and only if $\underline{v} = \overline{v}$. This classification stems from some mathematical requirements. Indeed, in some algorithms, computation of the pseudo-inverse of the frame analysis operator is required. This might be difficult, unless we have a tight frame. In such case, the pseudo-inverse of the frame analysis operator is given by its transpose (up to a multiplicative factor). Some examples of tight frames include: orthonormal basis union, shearlet tight frames [Hauser and Steidl, 2013] and curvelets [Candès and Donoho, 2001], while BM3D constitues an example of non-tight frame decomposition.

Another class of priors constitutes hard constraints. They are usually incorporated into the optimization problem by defining ψ_r as an indicator function $\iota_{\mathcal{C}}$, where

$$\iota_{\mathcal{C}}(x) = \begin{cases} 0 & \text{if } x \in \mathcal{C} \\ +\infty & \text{otherwise} \end{cases} \tag{1.33}$$

and $\mathcal{C}$ is a subset of $\mathcal{X}$.

Example 1.2.4 In the context of image restoration, especially when dealing with Poisson noise, a common assumption is that for all $j \in \mathbb{X}$, $x_j \geqslant 0$, which is known as a positivity constraint. Hence, in standard settings, i.e. $\mathcal{X} = \mathbb{R}^N$, the set $\mathcal{C}$ is given by the positive orthant $[0, +\infty)^N$.

1.2.3 Estimator quality

Different estimators yield various results on the same dataset. For a given amount of data, one estimator may prove to be the most attractive according to a given quality measure. The choice of quality measure is not unique. The superiority of one estimator over another depends on properties of the estimator we evaluate. Ideally, an estimator should carry at least the same

information about the unknown signal x as the observed data, be unbiased and have minimum variance.

In the context of image restoration, the estimation performance is often evaluated in terms of image quality assessment. Among various measures, the most standard ones are:

- SNR: Signal to noise ratio

$$\mathrm{SNR}(\widehat{x}, x) = 10 \log_{10} \left(\frac{\sum_{j \in \mathbb{X}} (x_j)^2}{\sum_{j \in \mathbb{X}} (\widehat{x}_j - x_j)^2} \right) \tag{1.34}$$

  SNR often serves as a gold standard. However its objectiveness is debatable. In [Cosman et al., 1994] the author writes that "*Common faults of squared error are that a slight spatial shift of an image causes a large numerical distortion but no visual distortion and, conversely, a small average distortion can result in a damaging visual artifact if all the error is concentrated in a small important region.*", and further " *The popularity of squared error is partly owed to the wealth of theory and numerical methods available for the analysis and synthesis of systems which are optimal in the sense of minimizing mean squared error*". SNR belongs to a family of quadratic error measures, which also includes, e.g. peak signal to noise ratio (PSNR) and improved signal to noise ratio (ISNR).

- MAE: Mean absolute error

$$\mathrm{MAE}(\widehat{x}, x) = \frac{\sum_{j \in \mathbb{X}} |\widehat{x}_j - x_j|}{\mathrm{card}\,(\mathcal{X})}. \tag{1.35}$$

  In the context of image restoration, MAE is used as an image quality assessment measure in the case of images corrupted by Poisson noise [Dupé et al., 2009].

- Threshold based quality measure

$$\mathrm{TQM}(\widehat{x}, x) = C(\widehat{x}, x), \tag{1.36}$$

  where C is the cost function defined in (1.8). TQM is less popular than SNR and MAE, but advocated, for instance in [Abrams et al., 2010]. It is closely related to the receiver operating characteristic (ROC), popular in signal detection theory, i.e. ROC is used to evaluate the performance of medical, biometric, and machine learning models, for instance described in the context of medical image compression in [Cosman et al., 1994]. TQM also naturally corresponds to MAP estimator (1.10).

These criteria owe popularity due to their simplicity. However, it was observed that they do not correlate well with human perceived quality measurement. Pioneering works related to this topic include [Budrikis, 1972], [Stockham, 1972]. However, a good model of human image perception is yet to be defined. Thus, the corresponding measures include various heuristics and usually are adjusted to a given data type [Wang et al., 2002]. Among them, the most popular are: a structural similarity measure (SSIM) [Wang et al., 2004], a visual information fidelity criterion (VIF) [Sheikh et al., 2005], a wavelet-based visual signal-to-noise ratio for natural images measure (VSNR) [Chandler and Hemami, 2007] and a multi-scale structural similarity measure (MS-SSIM) [Rouse and Hemami, 2008]. Most of the attention has been devoted to natural images, while to the best of our knowledge there is no measure designed for instance for confocal imaging data.

It is worth noticing that, in the area of image coding one additionally uses Shannon block entropy defined as:

$$\mathrm{SBE}(X) = -\frac{\sum_{b\in\mathbb{B}} P_b \log_2(P_b)}{B} \tag{1.37}$$

where b is a block symbol, $\mathbb{B}$ the considered set of symbols (codebook), B the block size, and P_b is the probability of symbol b. This measure provides an expected value of information contained in a signal. The entropy reaches its maximum value for signals for which block symbols are uniformly distributed. The entropy reaches its minimum for signals for which a given block symbol arises almost surely.

§ 1.3 Algorithms

An estimate of the original image can be computed in several ways, i.e. via different algorithms. Hence, selecting the best algorithm to solve a given inverse problem is a challenge by itself [Smith-Miles, 2008], [Kadioglu et al., 2011]. The question then arises which algorithm is better. Let us recall a quote by Paul Erdös *"Why are numbers beautiful? It's like asking why is Beethoven's Ninth Symphony beautiful. If you don't see why, someone can't tell you"*. By an analogy to algorithms, it is often very difficult to compare them objectively. In the following, we recall some basic criteria for algorithm evaluation.

Firstly, an algorithm can be analyzed in terms of its produced solution. Generally, for iterative algorithms the solution needs to be guaranteed by algorithm convergence properties and can be either local or global with respect to a given solution set. In some cases, the convergence is further classified, for instance as monotone or non-monotone. Additionally, in an infinite dimensional Hilbert space, one considers convergence to be weak or strong while in discrete optimization, it is a common practice to show that

the solution obtained is within some bounded distance to the global optimum. The solution of an optimization problem can also be computed by non-iterative procedures. In such case a theoretical justification of optimality is still desired.

Secondly, an algorithm can be evaluated in terms of its limitation i.e. the number of assumptions it requires. Due to some strong assumptions, some algorithms may only be applicable to a very restricted class of problems. In the worst case this class may only include problems of little practical use. We refer to an algorithm with strong assumptions as a demanding algorithm. An algorithm producing valid results irrespective of data uncertainty is called robust [Bertsimas et al., 2010].

An algorithm can be also evaluated in terms of its effectiveness, by its capacity to produce quickly high quality but not necessarily optimal solutions to complex optimization problems. Usually computational complexity and memory consumption are regarded as objective measures of effectiveness [Drepper, 2007]. In the case of iterative algorithms one can additionally estimate efficiency by inspecting a number of iterations before convergence, a predisposition to parallelization, and processing time.

Finally, the significance of an algorithm needs to be analyzed. The practical value of an algorithm can be judged based on its usefulness either in a broad spectrum of applications or for a problem which has never been addressed before. Significance of an algorithm can also result from its theoretical originality.

A digital image is naturally discrete, i.e. each pixel takes a value in a finite set. Nevertheless, imaging problems are often formulated in a continuous framework, by allowing pixels to take value from a continuous set. Consequently, in the context of image processing, the continuous and discrete optimization fields are increasingly intertwined. Often approaches cross the boundaries between discrete and continuous optimization. Examples include convex relaxation techniques [Pock et al., 2010], [Zach and Kohli, 2012]. In the following:

- we propose an optimization framework featuring both continuous and combinatorial techniques (Chapters 2 and 4). Our approaches address problems, in which all of the variables take values from an unknown discrete set. The discrete set is described by its cardinality and is known to be an inclusion of a given continuous set. We formulate the problem in a discrete-continuous framework, while attempting to bring together the best of both worlds.

- We address the same practical problem, i.e. image denoising with $\ell_2 - \ell_0$ sparsity measures, in discrete (Chapter 6) and continuous (Chapter 7) frameworks, which provide an opportunity to compare the two approaches with respect to the considered applications.

The description of mathematical tools used in this thesis can be found in books on convex optimization [Boyd and Vandenberghe, 2004], [Bauschke and Combettes, 2011], combinatorial optimization [Papadimitriou and Steiglitz, 1982], [Graham and Lovász, 1995] and incremental gradient methods [Lange, 2010]. Hence in the following we only provide basic ideas behind these methods and survey some of their properties.

1.3.1 Continuous optimization

We present two strategies for deriving a continuous optimization algorithm. The first relies on majorize-minimize the principle (MM), while the second on proximal minimization. Based on these general concepts, many algorithms have been derived, within them some focus on image reconstruction problem. Generally these algorithms prove to be useful for high-dimensional problems. In such a context, Model (1.1) is formulated in Hilbert spaces i.e. $\mathcal{X}$ and $\mathcal{Y}$ are finite dimensional real Hilbert spaces.

1.3.1.1 Majorize-Minimize Framework

MM strategy consists of substituting a difficult problem into a series of simple ones. Usually in optimization routines, simplicity is highly rated. Difficulties can be evaded by e.g. separating variables involved in optimization problem and avoiding matrix inversion. More precisely, in the MM framework one minimizes at each iteration a carefully chosen surrogate function g instead of the original one f. This function is called a tangent majorant and needs to satisfy the following conditions at $x' \in \mathcal{X}$:

$$\forall\, x \in \mathcal{X}, \quad g(x, x') \geqslant f(x) \tag{1.38}$$

and

$$g(x', x') = f(x'). \tag{1.39}$$

MM strategy guarantees that a function value sequence $\left(f(x^{(\ell)})\right)_{\ell\in\mathbb{N}}$ is monotonically nonincreasing, where $x^{(\ell+1)}$ minimizes the tangent majorant function $g\left(\cdot, x^{(\ell)}\right)$ and ℓ denotes the current iteration index. Indeed (1.38) and (1.39) imply that, for every ℓ:

$$f(x^{(\ell+1)}) \leqslant g\left(x^{(\ell+1)}, x^{(\ell)}\right) \leqslant g\left(x^{(\ell)}, x^{(\ell)}\right) = f(x^{(\ell)}). \tag{1.40}$$

For the sake of illustration, consider a simple case when $\mathcal{X} = \mathbb{R}$ (Fig. 1.4).

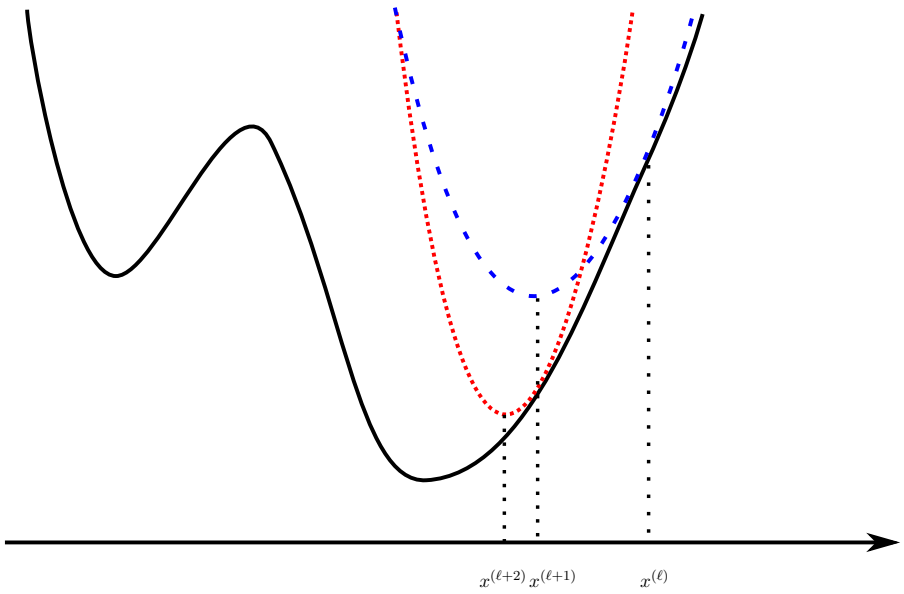

The function sequence $\left(f(x^{(\ell)})\right)_{\ell\in\mathbb{N}}$ is monotonically nonincreasing, where $x^{(\ell+1)}$ and $x^{(\ell+2)}$ are the minimum of tangent majorant functions at $x^{(\ell)}$ and $x^{(\ell+1)}$ denoted in blue and red, respectively. The majorants are associated with the original function f denoted in black.

Figure 1.4: *Illustration of idea behind Majorize-Minimize methods*

The design of an algorithm in the MM framework consists of a choice of a sequence of tangent majorant functions. Generally, the sequence of majorant functions can be iteration dependent [Jacobson and Fessler, 2007], e.g. adapted based on an observed progress in the previous iterations. They can also be block alternating, i.e. at each iteration a domain of tangent majorant function can be restricted to a given subset of $\mathcal{X}\times\mathcal{X}$ [Fessler and Hero, 1994]. Regardless of which modeling technique is used, minimization of majorizing function needs to be computationally simpler than the original function. Many standard methods of constructing majorizing functions are summarized in [Lange, 2010, Chapter 12.3].

Among others, they include a quadratic strategy adapted to the problem considered in Chapter 7, which applies to Lipschitz differentiable functions. The basic idea consists of majorizing the second-order Taylor expansion of f, i.e. if f is a twice differentiable function, $\forall\,(x,x')\in\mathcal{X}^2$:

$$\begin{aligned} f(x) &= f(x') + \nabla f(x')^\top (x-x') + \frac{1}{2}(x-x')^\top \nabla^2 f(x'')\,(x-x') \\ &\leqslant f(x') + \nabla f(x')^\top (x-x') + \frac{1}{2}(x-x')^\top A\,(x-x') \\ &= g(x,x') \end{aligned} \tag{1.41}$$

where x'' lies in the line segment from x to x' and A is a positive definite matrix satisfying the following condition: for every $x \in \mathcal{X}$, matrix $A - \nabla^2 f(x)$ is positive definite.

In the context of this thesis, it is worth noticing that Expectation - Maximization (EM) algorithms can be regarded as a special case of MM methods with a Jensen's inequality based majorant [Lange, 2010, Chapter 12.4], [Jacobson and Fessler, 2007]. More precisely, the direct consequence of Jensen's inequality is that the following holds. Let f be given by $-\log p_{Y|X}(y)$ and Z be some hidden random variable in a discrete set $\mathcal{Z}$, then, for $\forall\,(x, x') \in \mathcal{X}^2$:

$$
\begin{aligned}
f(x) &= -\log\left(p_{Y|X=x}(y)\right) \sum_{z\in\mathcal{Z}} p_{Z|Y=y,X=x'}(z) \\
&= -\sum_{z\in\mathcal{Z}} p_{Z|Y=y,X=x'}(z) \log\left(\frac{p_{Y,Z|X=x}(y,z)}{p_{Z|X=x,Y=y}(z)}\right) \\
&= -\sum_{z\in\mathcal{Z}} p_{Z|Y=y,X=x'}(z) \log\left(p_{Y,Z|X=x}(y,z)\right) \\
&\qquad\qquad + \sum_{z\in\mathcal{Z}} p_{Z|Y=y,X=x'}(z) \log\left(p_{Z|X=x,Y=y}(z)\right) \\
&= -\sum_{z\in\mathcal{Z}} p_{Z|Y=y,X=x'}(z) \log\left(p_{Y,Z|X=x}(y,z)\right) \\
&\qquad\qquad + \sum_{z\in\mathcal{Z}} p_{Z|Y=y,X=x'}(z) \log\left(\frac{p_{Z|X=x,Y=y}(z)}{p_{Z|X=x',Y=y}(z)}\right) \\
&\qquad\qquad + \sum_{z\in\mathcal{Z}} p_{Z|Y=y,X=x'}(z) \log\left(p_{Z|Y=y,X=x'}(z)\right) \\
&\leqslant -\sum_{z\in\mathcal{Z}} p_{Z|Y=y,X=x'}(z) \log\left(p_{Y,Z|X=x}(y,z)\right) \\
&\qquad\qquad + \log\left(\sum_{z\in\mathcal{Z}} p_{Z|X=x',Y=y}(z) \frac{p_{Z|X=x,Y=y}(z)}{p_{Z|X=x',Y=y}(z)}\right) \\
&\qquad\qquad + \sum_{z\in\mathcal{Z}} p_{Z|Y=y,X=x'}(z) \log\left(p_{Z|Y=y,X=x'}(z)\right) \\
&= \underbrace{-\sum_{z\in\mathcal{Z}} p_{Z|Y=y,X=x'}(z) \log\left(p_{Y,Z|X=x}(y,z)\right)}_{\text{EM term}} + \\
&\qquad\qquad \underbrace{\sum_{z\in\mathcal{Z}} p_{Z|Y=y,X=x'}(z) \log\left(p_{Z|Y=y,X=x'}(z)\right)}_{\text{Entropy term}} \\
&= g(x, x'). \qquad (1.42)
\end{aligned}
$$

In the above derivation, we have adopted a unified notation for the probability density functions, discrete probabilities and mixed discrete-continuous

probability measures. In practice one just needs to minimize the EM term. This is equivalent to computing a conditional expectation and maximizing the obtained result. Hence, the first part of the tangent majorant in (1.42) is equal to $\mathsf{E}\left[\log\left(p_{Y,Z}(y, Z \mid X = x)\right) \mid Y = y, X = x'\right]$. The EM concept is illustrated by the algorithm derived in Chapter 3.

There are also many others algorithms that fit into the MM framework. For instance the concave-convex procedure (CCCP) [Yuille and Rangarajan, 2003] can be regarded as an MM algorithm with a linear majorant. Hence, often the properties of MM types of algorithms were established independently, for a given majorant. In this thesis, we recall some of the results related to the general MM framework and EM algorithm. The global convergence of MM types of algorithms is ensured for strictly convex, coercive and differentiable f [Lange, 2004, Chapter 10.3]. The local convergence result of the EM algorithm under the joint continuity assumption was presented in [Wu, 1983], i.e. under the assumption that the majorant function is continuous in terms of x and x'. These results were generalized to a wider class of MM procedures in [Fessler and Hero, 1995], i.e. iteration dependent MM. Then, in [Jacobson and Fessler, 2007] the authors relax the continuity assumption in favor of the requirement that the tangent majorant functions are locally upper bounded around x'. Further studies and convergence results for non-convex functions f are provided in Chapter 7. Besides their convergence guaranties and their simplicity, MM-type algorithms offer a great efficiency in some instances [Chouzenoux et al., 2011]. However, this does not generalizes to the EM case, whose convergence rate can be quite slow, depending on the amount of missing information. This justifies an extensive research focusing on accelerating the EM algorithm [Lange, 1995], [Liu et al., 1998],[Fischer and Kersting, 2003].

1.3.1.2 Parallel-Proximal Splitting algorithms

Proximal splitting strategy consists of decomposing f into a sum of simpler functions $(f_r)_{1 \leqslant r \leqslant R}$ such that either an element of the sum f_r, e.g. f_1, is μ-Lipschitz differentiable with $\mu \in (0, +\infty)$, i.e.

$$\forall (x, x') \in \mathcal{X}^2, \quad \left\| \nabla f_1(x) - \nabla f_1\left(x'\right) \right\| \leqslant \mu \left\| x - x' \right\| \tag{1.43}$$

or the closed form solution of the associated proximity operator exists. Provided that this is possible, the proximal algorithm iterations can become more efficient than alternative methods, i.e. subgradient iterations. Both subgradient and parallel-proximal splitting algorithms are particularly attractive due to their capability to deal with nonsmooth problems. However, proximal methods are often considered to be more stable [Bertsekas, 2011]. The presentation here features these algorithms. Among them, we discuss primal-dual proximal splitting algorithm, which retains i) the simplicity of iterative projection algorithms while retaining the capacity to handle non

differentiable functions f_r and ii) the flexibility of forward-backward iterations together with the capacity of handling the problem corresponding to the minimization of a sum of more than two functions. Most of the presented results are valid under the assumption that $f \in \Gamma_0(\mathcal{X})$.

Definition 1.3.1 $\Gamma_0(\mathcal{X})$ is the class of lower semicontinuous convex functions $f : \mathcal{X} \mapsto (-\infty, +\infty]$ such that their domain $\operatorname{dom} f$ is nonempty.

The splitting procedure results in an additive cost problem of the following form:

$$\forall x \in \mathcal{X}, \quad f(x) = \sum_{r=1}^{R} f_r(x), \tag{1.44}$$

which is often encountered in practice. For instance, it arises naturally in the context of MAP estimator (1.11), where the component functions f_r are defined by the data fidelity and the regularization term, possibly hybrid in (1.29). If at least one function f_r is nondifferentiable on at least one point, the problem (1.44) is called nonsmooth. The optimization algorithms associated with nonsmooth problems are often related with a concept generalizing the gradient, namely the subdifferential.

Definition 1.3.2 The subdifferential [Rockafellar and Wets, 2004] of a function $f \in \Gamma_0(\mathcal{X})$ at $x \in \mathcal{X}$, denoted by $\partial f(x)$, is defined as:

$$\partial f(x) := \left\{ x' \in \mathcal{X} \mid \forall x'' \in \mathcal{X}, \quad f(x) + x'^{\top} \left(x'' - x\right) \leqslant f(x'') \right\} \tag{1.45}$$

It admits the following geometric interpretation: $x' \mapsto f(x) + x'^{\top} (x'' - x)$ is a lower bounding tangent function of f at x. ∂f is set-valued and $\partial f(x)$ is nonempty for any x in the relative interior of $\operatorname{dom}(f)$.

The usefulness of this concept becomes clearer in view of the following classical result relating subgradient and optimality. For any function f, x is a minimizer of f if

$$0 \in \partial f(x) \tag{1.46}$$

This inclusion principle is essential in developing nonsmooth optimization algorithms. More precisely the non-differentiability is handled via the subdifferential or via the closely related concept of proximity operator.

Definition 1.3.3 The proximity operator [Rockafellar, 1976] of a function $f \in \Gamma_0(\mathcal{X})$ at x, denoted by $\operatorname{prox}_f : \mathcal{X} \mapsto \mathcal{X}$, is defined as:

$$\forall x \in \mathcal{X}, \quad \operatorname{prox}_f(x) := \underset{p \in \mathcal{X}}{\arg\min}\ f(p) + \frac{1}{2} \|x - p\|^2 \tag{1.47}$$

The proximity operator is non-expansive, i.e. $\left\|\operatorname{prox}_f(x) - \operatorname{prox}_f(x')\right\| \leqslant \|x - x'\|$ for every $(x, x') \in \mathcal{X}^2$.

In the following, a proximal algorithm is defined as one involving the computation of proximity operators. The proximity operator was introduced in [Moreau, 1965] as a generalization of orthogonal projections. The fundamental result about this operator is the one relating the proximity operator and the subdifferential:

$$\forall x \in \mathcal{X}, \quad p = \operatorname{prox}_f(x) \;\Leftrightarrow\; x - p \in \partial f(p) \tag{1.48}$$

which implies that $\operatorname{prox}_f(x) = x$ if and only if $0 \in \partial f(x)$, i.e. the fixed point set of proximity operator of f is precisely the set of minimizers of f. Hence, one can find the optimal x by testing the condition $\operatorname{prox}_f(x) = x$, which is the key to the Rockafellar's proximal point algorithm [Rockafellar, 1976], i.e.

$$\forall \ell \in \mathbb{N}, \quad x^{(\ell+1)} = \operatorname{prox}_{\gamma^{(\ell)} f}\left(x^{(\ell)}\right), \tag{1.49}$$

where $(\gamma^{(\ell)})_{\ell \in \mathbb{N}}$ is a sequence of positive, possibly varying stepsizes. The above algorithm can be described as follows: an update is based on the minimization of function f in the neighborhood of a current $x^{(\ell)}$. There are several extensions of this method, which differ in the update scheme, assumptions about the number of involved functions R and the presence of smooth terms. In this thesis, we use proximal methods, which incorporate each functions f_r via proximity operator, i.e. PPXA+ [Pustelnik et al., 2011] in Chapter 2 and Douglas-Rachford [Lions and Mercier, 1979] in Chapter 3. These algorithms are related to the alternating-direction method of multipliers [Fortin and Glowinski, 1985]. We refer to [Combettes and Pesquet, 2011] for a survey. Moreover, motivated by the problem addressed in Chapter 5, we use primal-dual splitting algorithms, which incorporate functions $(f_r)_{1 \leqslant r \leqslant R}$ either via their proximity operators or via their gradients.

The presence of a smooth term becomes important if: 1) at least one of the component functions f_r is differentiable, 2) computing gradient of differentiable f_r presents some advantages over computing its proximity operator, e.g. it is more efficient. This can be illustrated with the example of image restoration in the presence of Poisson-Gaussian noise addressed in Chapter 5. However, not all proximal methods offer the required flexibility. More precisely, in the case when $R = 2$, one can employ either the forward-backward algorithm [Lions and Mercier, 1979], [Bach et al., 2012, Chapter 3]:

$$\forall \ell \in \mathbb{N}, \quad x^{(\ell+1)} = \operatorname{prox}_{\gamma^{(\ell)} f_1}\left(x^{(\ell)} - \gamma^{(\ell)} \nabla f_2\left(x^{(\ell)}\right)\right) \tag{1.50}$$

or the forward-backward-forward algorithm [Tseng, 2000]:

$$\begin{aligned} \forall \ell \in \mathbb{N}, \quad x^{(\ell+1)} =& \operatorname{prox}_{\gamma^{(\ell)} f_1}\left(x^{(\ell)} - \gamma^{(\ell)} \nabla f_2\left(x^{(\ell)}\right)\right) \\ & - \gamma^{(\ell)} \nabla f_2\left(\operatorname{prox}_{\gamma^{(\ell)} f_1}\left(x^{(\ell)} - \nabla f_2\left(x^{(\ell)}\right)\right)\right), \end{aligned} \tag{1.51}$$

where $f_1 \in \Gamma_0(\mathcal{X})$ and $f_2 \in \Gamma_0(\mathcal{X})$ are assumed to be μ-Lipschitz differentiable. The important, well known special case of algorithm (1.50) is the projection gradient algorithm [Polyak, 1987], which is recovered for f_1 given by an indicator function (1.33). In the case of $R > 2$ one can resort to primal-dual techniques proposed in [Combettes and Pesquet, 2012] and [Vu, 2011],[Condat, 2012], where the former one can be regarded as an extension of forward-backward-forward algorithm (1.51), while the latter one is an extension of forward-backward algorithm (1.50). We should also mention the Chambolle-Pock algorithm [Chambolle and Pock, 2011], which can be viewed as a special case of the algorithm by Vu. These algorithms are designed to jointly solve the primal and dual formulations of an optimization problem by use of the Fenchel duality theorem.

Definition 1.3.4 The Fenchel-Rockafellar duality [Bauschke and Combettes, 2011, Chapter 15] theorem states that for any convex functions $f_1 : \mathcal{X} \mapsto \mathbb{R}$ and $f_2 : \mathcal{V} \mapsto \mathbb{R}$:

$$\underbrace{\inf_{x \in \mathcal{X}} \{f_1(x) + f_2(Vx)\}}_{\text{Primal problem}} = \underbrace{\sup_{v \in \mathcal{V}} \{-f_1^\star(V^\star v) - f_2^\star(-v)\}}_{\text{Fenchel-Rockafellar dual problem}} \tag{1.52}$$

where $f^\star : \mathcal{X} \mapsto \mathbb{R}$ is the convex-conjugate of $f : \mathcal{X} \mapsto \mathbb{R}$ [Bauschke and Combettes, 2011, Chapter 13] i.e.

$$\forall v \in \mathcal{X}, \quad f^\star(v) = \sup_{x \in \mathcal{X}} \left(\langle x, v \rangle - f(x) \right), \tag{1.53}$$

$V : \mathcal{X} \mapsto \mathcal{V}$ is a linear operator and $V^\star$ is its adjoint. In such settings, primal and dual variables refer to x and v, respectively.

In a primal-dual scheme, the dual variable is used in the derivation of an update of the primal variable. From a practical point of view, the considered primal-dual algorithms [Combettes and Pesquet, 2012], [Vu, 2011] have the great advantage of avoiding a computationally expensive inversion of the linear operators involved into some optimization problems and that they are error-tolerant. More precisely, they are robust to an error resulting from inexact computation of a gradient or a proximity operator, provided that this error is absolutely summable.

In the context of our work, it is worth noticing that the EM algorithm, discussed previously in the context of MM methods, can also be recast as a proximal point algorithm with a Kullback information penalty. This interpretation was firstly presented in [Chretien and Hero, 1998] and then further results were presented in [Tseng, 2004], [Chretien and Hero, 2008].

In general, proximity methods are known for their good convergence properties. However, most of the results are established for convex functions, while there exist very few results related to the non-convex case [Kaplan

and Tichatschke, 1998], [Attouch et al., 2011], [Sra, 2012]. In the following, we apply mostly proximal methods to convex problems, apart of Douglas-Rachford in Chapter 3. The proximal methods are also considered to be efficient, provided that the computation of the proximity operator is relatively simple. Ideally, from the efficiency point of view, they should admit a closed-form expression. Examples of such proximity operators are provided in [Combettes and Pesquet, 2011], [Bach et al., 2012, Chapter 3]. For further properties of proximity operator we refer to [Bauschke and Combettes, 2011, Chapter 23].

1.3.2 Discrete optimization

Similarly to continuous optimization, discrete optimization is a vast field offering mathematical methods to challenging problems, some of them often encountered in image processing and computer vision. Examples of discrete methods include among others iterated conditional mode [Besag, 1986], dynamic programming [Amini et al., 1990], [Felzenszwalb and Huttenlocher, 2005], message passing [Felzenszwalb and Huttenlocher, 2004], [Kolmogorov, 2006] and graph-cut algorithms. For a survey, we refer to [Felzenszwalb and Zabih, 2011]. We focus on graph-cut methods, which has had a significant and lasting impact on image processing and computer vision. Ideas on the use of graph-cuts in image processing go back at least to the work by [Greig et al., 1989], where they were employed for denoising binary images. Later, these algorithms were shown to be useful for various image processing problems, e.g. stereo-vision [Woodford et al., 2008], multiview reconstruction [Sinha et al., 2007], motion analysis [Xiao and Shah, 2007], segmentation [Boykov and Jolly, 2001] and image restoration [Darbon and Sigelle, 2006]. In such a context, Model (1.1) is formulated in a discrete space i.e. $\mathcal{X}$ is a discrete subset of finite dimensional real Hilbert spaces while $\mathcal{Y}$ can be either a finite dimensional real Hilbert spaces or one of its subsets.

1.3.2.1 Graph-cut framework

Graph-cut strategy consists of presenting an optimization problem on a directed graph, and then solving it by applying efficient max-flow/min-cut algorithms. The global convergence of these methods is guaranteed in the binary case, i.e $\mathcal{X} = \{0,1\}^N$. A number of discrete problems have been shown to be equivalent to a "binary" min-cut problem, e.g. closure/selection problem [Balinski, 1970], [Picard, 1976], [Hochbaum, 2004]. Hence, firstly our discussion is limited to this scenario.

Definition 1.3.5 A directed graph $\mathcal{G}$ is defined by a set of nodes $\mathbb{X}$ and a collection of ordered pairs of elements of $\mathbb{X}$, i.e. a set of edges $\mathbb{E}$.

Alternatively, one defines a graph by $\mathbb{X}$ and a node-arc incident-matrix E. It is defined as follows [Papadimitriou and Steiglitz, 1982, Definition 3.3]: let $N = \text{card}(\mathbb{X})$ and $M = \text{card}(\mathbb{E})$, then the node-arc incidence-matrix E is the $N \times M$ matrix such that: $\forall k \in \{1, \dots, N\}$, $\forall e \in \{1, \dots, M\}$

$$E(k,e) = \begin{cases} 1 & \text{if } \mathbb{E}(e) = (i,j) \text{ and } i = k \\ -1 & \text{if } \mathbb{E}(e) = (i,j) \text{ and } j = k, \\ 0 & \text{otherwise} \end{cases} \tag{1.54}$$

where $\mathbb{E}(e)$ denotes the e-th element of $\mathbb{E}$. In the graph-cut routine, there is a variable x_i associated with each node $i \in \mathbb{X}$. Moreover, one assumes $\mathbb{X}$ to include two special nodes $\{s, t\}$ with assigned values $x_s = 0$ and $x_t = 1$. Nodes s and t are called the source and sink, respectively. An example of directed graph is provided in Fig. 1.5.

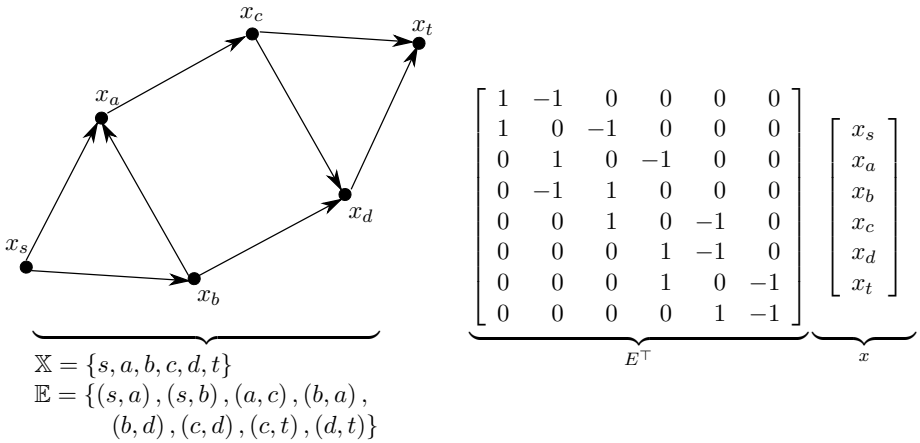

Figure 1.5: *An example of a directed graph*

The problem then is to find an optimal solution $(\mathbb{X}_0, \mathbb{X}_1)$ such that $\mathbb{X} = \mathbb{X}_0 \cup \mathbb{X}_1$, $\mathbb{X}_0 \cap \mathbb{X}_1 = \emptyset$, $s \in \mathbb{X}_0$ and $t \in \mathbb{X}_1$ to an associated objective function f, which assigns to each edge $(i,j) \in \mathbb{E}$ the cost $\omega_{i,j} \in (0, +\infty]$. The cost $\omega_{i,j}$ is usually called the capacity of the edge (i,j). A collection of $\omega_{i,j}$ forms a vector $\omega \in (0, +\infty]^M$. Given sets $\mathbb{X}_0$ and $\mathbb{X}_1$ one finds x using the following relation:

$$\forall i \in \mathbb{X}, \ , \quad x_i = \begin{cases} 0 & \text{if } i \in \mathbb{X}_0 \\ 1 & \text{if } i \in \mathbb{X}_1. \end{cases} \tag{1.55}$$

A graph $\mathcal{G} = (\mathbb{X}, \mathbb{E})$ can be partitioned into two disjoint sub-graphs $\mathcal{G}_0 = (\mathbb{X}_0, \mathbb{E}_0)$ and $\mathcal{G}_1 = (\mathbb{X}_1, \mathbb{E}_1)$ by removing the edges connecting the two parts, i.e. by a cut. The capacity of the cut is defined as the sum of the capacities

of its forward part, i.e

$$\mathrm{cut}\,(\mathbb{X}_0, \mathbb{X}_1) = \sum_{\substack{i \in \mathbb{X}_0, j \in \mathbb{X}_1 \\ (i,j) \in \mathbb{E}}} \omega_{i,j} \tag{1.56}$$

An example illustrating a cut with its forward and backward part is provided in Fig. 1.6.

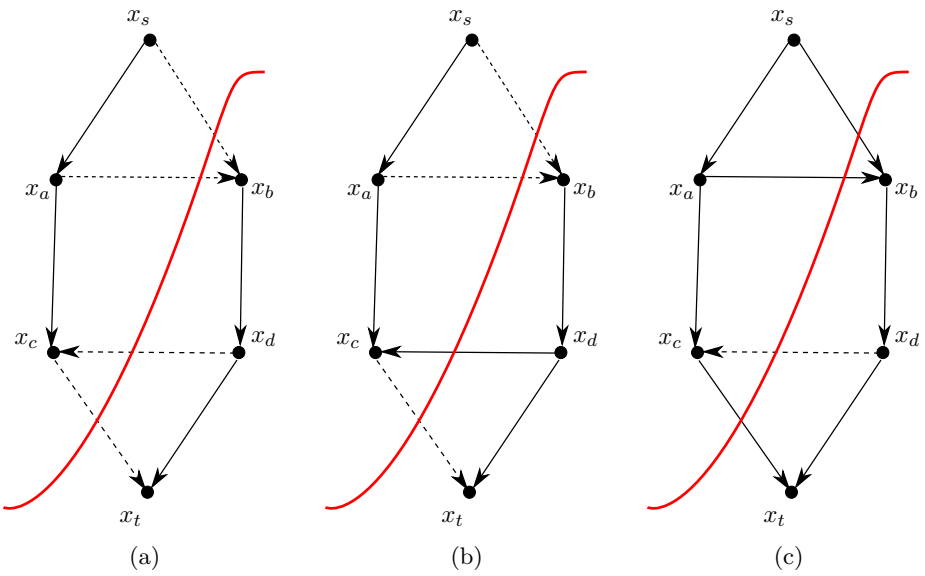

(a,b,c) illustrate separating edges, edges involved in the cost of the cut (forward ones) and edges omitted in the cost of the cut (backward ones), respectively. Edges of interest are denoted with dashed arrows.

Figure 1.6: *A cut*

Definition 1.3.6 The min-cut problem takes the following form. Given the graph $\mathcal{G}(\mathbb{X}, \mathbb{E})$ and ω, find

$$\min_{\mathbb{X}_0, \mathbb{X}_1} \ \mathrm{cut}\,(\mathbb{X}_0, \mathbb{X}_1) \tag{1.57}$$

such that $s \in \mathbb{X}_0$ and $t \in \mathbb{X}_1$.

The graph-cut problem defined above admits also the following formulation:

$$\min_{x \in \mathcal{X}} \sum_{(i,j) \in \mathbb{E}} \omega_{i,j}\,(1 - x_i)\,x_j \quad \text{such that} \quad x_s = 0,\ x_t = 1. \tag{1.58}$$

Introducing the binary variable $d_{i,j} = (1 - x_i)\,x_j$ transforms (1.58) into the minimization of a linear functional over a finite set of vectors. Alternatively,

one can attempt to minimize over the convex hull of this finite vector set, i.e. a convex polytope [Graham and Lovász, 1995, Chapter 30]. In this fashion, Problem (1.58) can be rewritten as

$$\min_{x\in\mathcal{X},\, d\in\{0,1\}^M} \omega^\top d \quad \text{such that} \quad E^\top x + d \geqslant 0,\ d \geqslant 0,\ x_s = 0,\ x_t = 1, \tag{1.59}$$

which is a standard Integer Linear Program. Moreover, the total unimodularity [1] of matrix E implies that the solutions of the linear programming (LP) relaxation of the Problem (1.59) has integral solutions. Hence, one can resort to LP techniques for solving this problem. However, in some instances discrete algorithms are considered to be more efficient. These algorithms use often a dual formulation to min-cut problem (as defined in 1.3.6), namely the max-flow problem. The max-flow problem is defined over the dual variable to x, i.e. v. The $v_{i,j} \in [0, +\infty)$ associated with each $(i, j) \in \mathbb{E}$ is called flow, while a collection of all $v_{i,j}$ forms a vector $v \in [0, +\infty)^M$. If additionally v satisfies the flow conservation constraint, i.e.

$$\forall\ i \in \mathbb{X} \setminus \{s, t\}, \quad \sum_{(i,j)\in\mathbb{E}} v_{i,j} - \sum_{(j,i)\in\mathbb{E}} v_{j,i} = 0 \tag{1.60}$$

and the capacity constraint, i.e.

$$\forall\ (i, j) \in \mathbb{E}, \qquad 0 \leqslant v_{i,j} \leqslant \omega_{i,j} \tag{1.61}$$

then it is called s-t flow. The max-flow problem is related to the concept of an s-t flow polytope C_{flow} , i.e. the set of all vectors $v \in \mathbb{R}^M$ satisfying constraints (1.60) and (1.61).

Definition 1.3.7 The max-flow problem [Papadimitriou and Steiglitz, 1982, Chapter 5.6] consists of finding the maximum value of total flow v_s from the source node s to the sink node t through the graph $\mathcal{G}(\mathbb{X}, \mathbb{E})$, subject to the flow conservation (1.60) and the capacity (1.61) constraints, i.e.

$$\max_{v\in C_{\text{flow}}} v_s \tag{1.62}$$

where $v_s = \sum_{(s,i)\in\mathbb{E}} v_{s,i}$.

Similarly like in the case of min-cut problem, by the total modularity of incidence matrix E, if ω is integral, then the s-t flow polytope has integral vertices [Graham and Lovász, 1995, Chapter 30]. More precisely, the max-flow problem defined above admits the following linear formulation:

$$\max\ v_s \quad \text{such that} \quad Ev + v_s z \leqslant 0,\ v \leqslant \omega,\ -v \leqslant 0 \tag{1.63}$$

[1] Each column of matrix E is a vector for which all elements are equal to 0 except one equal to -1 and one equal to 1.

where $z = (z_i)_{i \in \mathbb{X}}$ is a vector in $\mathbb{R}^N$ such that

$$z_i = \begin{cases} -1 & \text{if } i = s \\ 1 & \text{if } i = t \\ 0 & \text{otherwise.} \end{cases} \tag{1.64}$$

The strong duality between min-cut and max-flow problems was proved in [Elias et al., 1956], [Ford and Fulkerson, 1962]. This classical result is known as the max-flow/min-cut theorem.

Definition 1.3.8 The max-flow/min-cut theorem [Papadimitriou and Steiglitz, 1982, Chapter 6.1] states that the value v_s of any s-t flow is no greater than the capacity cut $(\mathbb{X}_0, \mathbb{X}_1)$ of any s-t cut. Furthermore the value of the maximum flow equals the capacity of the minimum cut, and a flow v and a cut $(\mathbb{X}_0, \mathbb{X}_1)$ are jointly optimal if and only if

$$\forall (i,j) \in \mathbb{E},\ i \in \mathbb{X}_1,\ j \in \mathbb{X}_0, \qquad v_{i,j} = 0 \tag{1.65}$$

$$\forall (i,j) \in \mathbb{E},\ i \in \mathbb{X}_0,\ j \in \mathbb{X}_1, \qquad v_{i,j} = \omega_{i,j}. \tag{1.66}$$

Hence, the optimal set of edges separating $\mathbb{X}_0$ and $\mathbb{X}_1$ includes the saturated ones in the forward direction and the empty ones in the backward direction.

The max-flow/min-cut theorem is a special case of linear programming duality. For further discussion, we refer to [Graham and Lovász, 1995].

Several algorithms solving min-cut/max-flow problem have been proposed. For a brief review in the context of image processing we refer to [Boykov and Kolmogorov, 2004]. Classical examples include Ford and Fulkerson [Ford and Fulkerson, 1962] and Push-Relabel [Goldberg and Tarjan, 1988] algorithms, whereas the former is the first polynomial time algorithm for globally optimal solution [Papadimitriou and Steiglitz, 1982, Theorem 6.3]. Parallel algorithms with some restrictions were studied in [Delong and Boykov, 2008], [Strandmark et al., 2011].

1.3.2.2 Graph-cut algorithms in imaging

The theory of graph cuts was first applied to image processing in [Greig et al., 1989], where the authors consider a problem of binary image denoising, i.e. $\forall j \in \mathbb{X},\ x_j \in \{0,1\}$. The author proposed to rewrite Problem (1.58) in the following fashion: let $x_s = 0,\ x_t = 1$,

$$\arg\min_{x \in \mathcal{X}} \sum_{(s,i) \in \mathbb{E}} \omega_{s,i} x_i + \sum_{(i,t) \in \mathbb{E}} \omega_{i,t}(1 - x_i) \quad + \sum_{\substack{(i,j)\ \in\ \mathbb{E} \\ i \neq s, j \neq t}} \omega_{i,j}(1 - x_i) x_j \tag{1.67}$$

and on the one hand to view the sums involving $\omega_{s,i}$ and $\omega_{i,t}$ as a data fidelity term; and on the other hand the sum with $\omega_{i,j}, i \neq s, j \neq t$ as a

regularization. More generally, in the graph cut framework, one usually considers an additive cost problem with the objective function:

$$f(x) = \sum_{(i,j)\in\mathbb{E}} f_{i,j}\left(x_i, x_j\right). \tag{1.68}$$

The function $f_{i,j}$ can be represented on the graph provided that it is submodular [Kolmogorov and Zabih, 2004]. The submodularity was originally defined for functions of subsets of $\mathbb{X}$ [Murota and Tamura, 2004]. However, in the following, we adopt the equivalent definition proposed in [Kolmogorov and Zabih, 2004], which is more popular in the image processing community.

Definition 1.3.9 A function $f_{i,j} : \{0,1\}^2 \mapsto \mathbb{R}$ is submodular if the following condition holds:

$$f_{i,j}\left(0,0\right) + f_{i,j}\left(1,1\right) \leqslant f_{i,j}\left(0,1\right) + f_{i,j}\left(1,0\right) \tag{1.69}$$

This condition generalizes to a multilabel case [Kolmogorov and Rother, 2007] i.e. $f_{i,j} : \mathcal{L}^2 \mapsto \mathbb{R}$, where $\mathcal{L}$ is a finite set of real values with cardinality greater than two and:

$$f_{i,j}\left(l_\beta, l_\gamma\right) + f_{i,j}\left(l_\alpha, l_\alpha\right) \leqslant f_{i,j}\left(l_\beta, l_\alpha\right) + f_{i,j}\left(l_\alpha, l_\gamma\right), \tag{1.70}$$

for any $(l_\alpha, l_\beta, l_\gamma) \in \mathcal{L}$.

Most of the image processing problems are multilabel, i.e. $\forall j \in \mathbb{X} \setminus \{s,t\}$, $x_j \in \mathcal{L}$. Despite of the multi-label character of most image processing problems, in the graph-cut framework, they are still represented as binary ones. The goal is to find a new problem representation, which can be formulated as a maximum flow or a minimum cut problem. Hence, graph-cut algorithms may be regarded as method for minimizing quadratic and cubic submodular pseudo-boolean functions [Boros and Hammer, 2002], [Kohli et al., 2008], [Strandmark and Kahl, 2012]. In such settings, usually either a multiple binary decision problem or a single binary problem is considered. More specifically, we present an iteration of a multilabel graph-cut algorithm as a three-step procedure, i.e. forward transform ν_B followed by binary data processing and inverse transform ν_B^{-1} i.e, $\nu_B : \{0,1\} \times \mathcal{L}^{N-2} \times \{0,1\} \mapsto \{0,1\}^{(N-2)K+2}$ such that the new additive data cost function is

$$f'(x') = \sum_{(i,j)\in\mathbb{E}'} f'_{i,j}(x'_i, x'_j), \tag{1.71}$$

where for a given positive integer K

$$\begin{aligned} x' &= \nu_B(x) \\ &= \left(x'_j\right)_{j\in\mathbb{X}'} \\ &= \left(x_s, \left(x_{j,k}\right)_{k=\{1,\ldots,K\}, j\in\mathbb{X}\setminus\{s,t\}}, x_t\right) \end{aligned} \tag{1.72}$$

is a vector in $\{0,1\}^{N'}$, where $N' = (N-2)K+2$. Ideally, given a function f one needs to find ν_B such that for all $(i,j) \in \mathbb{E}'$, $f'_{i,j}$ is submodular. This is illustrated in the case study in Chapter 6, where the quantized-convex split moves algorithm is discussed in the context of function f with truncated-convex terms. Next, we illustrate the presented above general idea behind multilabel graph-cut algorithms with classical examples.

Example 1.3.10 The first example concerns the Ishikawa method [Ishikawa, 2003]. Let $\mathcal{L}$ be an ordered set of evenly spaced labels, i.e. $\forall k,\ l_k - l_{k-1} = l_{k+1} - l_k,\ l_k \in \mathbb{R}$. The author proposes to associate $\forall j \in \mathbb{X} \setminus \{s,t\}\ x_j$ with binary variables $(x_{j,k})_{k\in\{1,\dots,L\}}$, where L denotes the cardinality of $\mathcal{L}$ and to define ν_B^{-1} such that for all $j \in \mathbb{X}$ it returns $x_j = l_i$ where $i = L - \sum_{k=1}^{L} x_{j,k}$. One deduces that the resulting graph $\mathcal{G}(\mathbb{X}', \mathbb{E}')$ related with binary variables has $(N-2)L+2$ nodes, i.e. $\operatorname{card}(\mathbb{X}') = (N-2)L+2$, where $N = \operatorname{card}(\mathbb{X})$ (2 is due to the special nodes $\{s,t\}$). We discuss the details of a graph construction (the edge set $\mathbb{E}'$ and a vector ω') in Chapter 2. The method proposed by Ishikawa is known for its global convergence properties in the case of some non-convex objective functions, i.e. in the presence of a non-convex data fidelity and a convex regularization term.

Example 1.3.11 The second example concerns the moves framework. This strategy consists of solving a graph-cut problem iteratively. Hence, it can be regarded as a multiple binary decision problem. The resulting function value sequence $\left(f\left(x^{(\ell)}\right)\right)_{\ell\in\mathbb{N}}$ is monotone nonincreasing. At each iteration, $\forall j \in \mathbb{X} \setminus \{s,t\}$ a binary variable $x_{j,b}^{(\ell)}$ is assigned to $x_j^{(\ell)}$, i.e. $\operatorname{card}(\mathbb{E}') = \operatorname{card}(\mathbb{E})$. The moves algorithms differ in the choice of ν_B^{-1}. Often in the case of $x_{j,b}^{(\ell+1)} = 0$, the associated signal $x_j^{(\ell+1)}$ remains unchanged with respect to previous iteration, i.e. $x_j^{(\ell+1)} = \nu_B^{-1}(0) = x_j^{(\ell)}$. However, in the case of $x_{j,b}^{(\ell+1)} = 1$ the mapping ν_B^{-1} varies depending on the choice of move algorithm. The examples of moves algorithms include α-expansion [Boykov et al., 2001], $\alpha-\beta$ swap [Boykov et al., 2001] and the Murota gradient algorithm [Murota, 2004]. Some moves algorithms, e.g. the α-expansion move and $\alpha-\beta$ swap are appropriate for computing approximate solutions of non-convex problems, while for the other the optimality is guaranteed, e.g. Murota gradient descent algorithm for convex functions. The graph construction (the set of edges $\mathbb{E}'$ and the definition of ω') for α-expansion algorithm is discussed in Chapter 2, while Murota gradient move algorithm is discussed in Chapter 6.

It is worth noticing that some works in convex optimization were inspired by min-cut/max-flow results. In the continuous domain, the min-cut/max-flow problem was studied among others in [Strang, 1983], [Nikolova et al.,

2006], [Appleton and Talbot, 2006], [Pock et al., 2010], [Strang, 2010], [Yuan et al., 2010], [Couprie et al., 2011] and [Zach and Kohli, 2012].

- Chapter 2 -

Discrete-continuous framework for vector quantization

Quantization, defined as the act of attributing a finite number of levels to an image, is an essential task in image acquisition and coding. It is also intricately linked to many image analysis tasks, such as denoising and segmentation. In this chapter[1], we investigate vector quantization combined with regularity constraints. This is a little-studied area which is of interest, in particular, when quantizing in the presence of noise or other acquisition artifacts. We present an optimization approach to the problem involving a novel two-step, iterative, flexible, joint quantizing-regularization method featuring both convex and combinatorial optimization techniques. We show that when using a small number of levels, our approach can yield lower entropy and better quality images in terms of SNR, than conventional optimal quantization methods.

§ 2.1 Introduction

Quantization is a fundamental task in digital image processing and information theory [Gersho and Gray, 1992]. It plays a prominent role in early processing stages such as image digitization, and it is essential in lossy coding. It bears close resemblance to high level tasks such as denoising, segmentation, and data classification. In particular, quantizing a grey scale image in Q levels can be viewed as a classification or segmentation of the image in Q areas following an intensity homogeneity criterion. Each segmented area then corresponds to a decision class of the quantizer.

A classical solution for designing an optimal quantizer of a monochrome image is provided by the celebrated Lloyd-Max (LM) algorithm [Max, 1960],

[1] Published in JMIV, 2011

[Lloyd, 1982]. An extension to the general vector case is the Linde–Buzo–Gray(LBG) algorithm [Linde et al., 1980]. The LBG algorithm proceeds iteratively by alternatively optimizing codevectors and decision classes so as to minimize a flexible quantization error measure. It is known to present good convergence properties in practice [Wu, 1992b], [Du et al., 2006]. However, one drawback is the lack of spatial regularity of the quantized image. Spatially smooth properties may be useful in low-rate compression when using advanced coding algorithms (e.g based on run length, differential or multi-resolution techniques), especially in the context of medical and low bit-rate video compression applications like compression of confocal laser scanning microscopy image sequences [Arya et al., 2005] or mobile television [Kawada et al., 2006]. It may also be of interest for quantizing images featuring noise. In the latter case, quantization can be viewed as a means for denoising discrete-valued images that are piecewise constant.

Since the LBG algorithm is closely related to K-means, which are widely used in data classification, a possibility to enforce spatial smoothness of the quantized image would be to resort to fuzzy C-means clustering techniques and their extensions [Chuang et al., 2006]. These algorithms are however based on local measures of smoothness. The C-means with total-variation global smoothness constraint is discussed in [He et al., 2012]. Furthermore, an interesting approach was proposed by Alvarez *et al.* [Alvarez and Esclarín, 1997]. However, this method is based on reaction-diffusion PDEs and it addresses the quantization of grey-scale images, while our approach is more general and applicable to multicomponent images.

In this chapter, we propose a quantization method that enforces some global spatial smoothness. This is achieved by introducing an adjustable regularization term in the minimization criterion, in addition to a quantization error measure. Similarly to the LBG algorithm, the optimal design of the quantizer is performed iteratively by alternating the minimization of a label field $i_{\mathcal{P}}$ and of a codebook $\boldsymbol{r}$. The latter minimization reduces to a convex optimization problem whereas the former is carried out by efficient combinatorial optimization techniques.

Section 2.2 describes the background of the work. The considered regularization approach is formulated in Section 2.3. Section 2.4 describes the proposed quantizer design algorithm. Section 2.5 provides more details on the combinatorial optimization step. Finally, some simulation results are provided in Section 2.6 before a conclusion is drawn in Section 2.7.

§ 2.2 Background

We consider the vector quantization of a multichannel image $f = \big(f(n,m)\big)_{(n,m)\in\mathbb{X}}$ where $\mathbb{X} = \{1,\ldots,N\} \times \{1,\ldots,M\}$ is the image support

and, for every $(n,m) \in \mathbb{X}$,

$$f(n,m) = \big(f_1(n,m), \ldots, f_D(n,m)\big)^\top \in \mathbb{R}^D. \tag{2.1}$$

A similar notation will be used for the D-channel fields defined throughout the chapter. Example of such multivariate data are complex-valued images ($D = 2$), color images ($D = 3$), multispectral images (D usually less than 10), hyperspectral images (D usually more than 10),... In the following, the vector quantizer will operate on each D-dimensional vector of pixel values. The case when $D = 1$ corresponds to a scalar quantization of a monochannel image.

In order to define such a vector quantizer, we introduce the following variables: Q is a positive integer, $\mathcal{P} = (\mathbb{D}_k)_{1 \leq k \leq Q}$ is a partition of $\mathbb{X}$ and $\boldsymbol{r} = (r_1, \ldots, r_Q)$ is a matrix belonging to a nonempty closed convex subset C of $\mathbb{R}^{D \times Q}$. The role of this constraint set will be made more explicit in the next sections. The partition $\mathcal{P}$ can be characterized by the label image $\big(i_{\mathcal{P}}(n,m)\big)_{(n,m)\in\mathbb{X}} \in \{1, \ldots, Q\}^{N \times M}$, defined as: for every $(n,m) \in \mathbb{X}$ and $k \in \{1, \ldots, Q\}$,

$$i_{\mathcal{P}}(n,m) = k \quad \Leftrightarrow \quad (n,m) \in \mathbb{D}_k. \tag{2.2}$$

A vector quantized image over Q codevectors $r_1, \ldots, r_Q$ and associated with the partition $\mathcal{P}$ is then given by

$$q_{i_{\mathcal{P}},\boldsymbol{r}} = (r_{i_{\mathcal{P}}(n,m)})_{(n,m)\in\mathbb{X}} \in \{r_1, \ldots, r_Q\}^{N \times M}. \tag{2.3}$$

A numerical example is given below to better explain the relation between variables Q,$\boldsymbol{r}$, $i_{\mathcal{P}}$ and $q_{i_{\mathcal{P}},\boldsymbol{r}}$, which play a prominent role in the rest of the chapter. For instance, if a quantization over 2 bits of a 3×3 monochannel image is performed, we have $N = M = 3$, $D = 1$, $Q = 4$, and we may have $\boldsymbol{r} = (1, 4, 9, 10)$ and $i_{\mathcal{P}} = \begin{bmatrix} 1 & 2 & 3 \\ 1 & 4 & 1 \\ 3 & 2 & 3 \end{bmatrix}$, then $q_{i_{\mathcal{P}},\boldsymbol{r}} = \begin{bmatrix} 1 & 4 & 9 \\ 1 & 10 & 1 \\ 9 & 4 & 9 \end{bmatrix}$. Note that the $i_{\mathcal{P}}$ matrix values belong to the set $\{1, 2, 3, 4\}$ which corresponds to the set of labels and $q_{i_{\mathcal{P}},\boldsymbol{r}}$ matrix values belong to $\boldsymbol{r}$.

An "optimally" quantized image $q_{i_{\overline{\mathcal{P}}},\overline{\boldsymbol{r}}}$ of f is usually obtained by looking for $(i_{\overline{\mathcal{P}}}, \overline{\boldsymbol{r}}) \in \{1, \ldots, Q\}^{N \times M} \times C$ solution to the following problem:

$$\underset{(i_{\mathcal{P}},\boldsymbol{r})\in\{1,\ldots,Q\}^{N\times M}\times C}{\text{minimize}} \quad \Phi(q_{i_{\mathcal{P}},\boldsymbol{r}}, f) \tag{2.4}$$

where $\Phi \colon (\mathbb{R}^D)^{N \times M} \times (\mathbb{R}^D)^{N \times M} \to (-\infty, +\infty]$ is some measure of the quantization error.

Standard choices for Φ are separable functions of the form

$$\big(\forall g = \big(g(n,m)\big)_{(n,m)\in\mathbb{X}} \in (\mathbb{R}^D)^{N\times M}\big)$$
$$\Phi(g,f) = \sum_{n=1}^{N} \sum_{m=1}^{M} \varphi_{n,m}\big(g(n,m), f(n,m)\big) \tag{2.5}$$

where, for every $(n,m) \in \mathbb{X}$, $\varphi_{n,m} \colon \mathbb{R}^D \times \mathbb{R}^D \to (-\infty, +\infty]$. For example, one can use:

- the matrix weighted quadratic norm

$$\varphi_{n,m}\big(g(n,m), f(n,m)\big) = \|g(n,m) - f(n,m)\|^2_{\Gamma_{n,m}} \tag{2.6}$$

  where $\Gamma_{n,m} \in \mathbb{R}^{D\times D}$ is a symmetric definite positive matrix and we have used the notation

$$(\forall a \in \mathbb{R}^D) \quad \|a\|_{\Gamma_{n,m}} = (a^\top \Gamma_{n,m} a)^{1/2}; \tag{2.7}$$

- the weighted ℓ_p norm measure ($p \in [1, +\infty[$)

$$\varphi_{n,m}\big(g(n,m), f(n,m)\big) = \sum_{d=1}^{D} \omega_d(n,m) |g_d(n,m) - f_d(n,m)|^p \tag{2.8}$$

  where $\omega_d(n,m) \in [0, +\infty[$. As a special case, a mean absolute error criterion is found when $p = 1$.

- the generalized Kullback-Leibler divergence

$$\varphi_{n,m}\big(g(n,m), f(n,m)\big) = \sum_{d=1}^{D} \kappa\big(g_d(n,m), f_d(n,m)\big) \tag{2.9}$$

  where

$$\big(\forall (u,v) \in \mathbb{R}^2\big)$$
$$\kappa(u,v) = \begin{cases} -v \ln(u/v) + u - v & \text{if } (u,v) \in (0,+\infty)^2 \\ u & \text{if } u \in [0,+\infty) \text{ and } v = 0 \\ +\infty & \text{otherwise.} \end{cases} \tag{2.10}$$

Maximum error measures may also be useful, which are expressed as

$$\big(\forall g = \big(g(n,m)\big)_{(n,m)\in\mathbb{X}} \in (\mathbb{R}^D)^{N\times M}\big)$$
$$\Phi(g,f) = \max_{\substack{1\le n\le N \\ 1\le m\le M}} \varphi_{n,m}\big(g(n,m), f(n,m)\big) \tag{2.11}$$

where, for every $(n,m) \in \mathbb{X}$, $\varphi_{n,m} \colon \mathbb{R}^D \times \mathbb{R}^D \to (-\infty, +\infty]$. For example, we can use the sup norm:

$$\varphi_{n,m}\big(g(n,m), f(n,m)\big) = \max_{1\le d\le D} |g_d(n,m) - f_d(n,m)|. \tag{2.12}$$

In this context, a numerical solution to problem (2.4) when $C = \mathbb{R}^{D\times Q}$ is provided by the LBG algorithm, the general form of which is recalled below.

Algorithm 1 LBG Algorithm

Fix $Q \in \mathbb{N}^*$ and $\boldsymbol{r}^{(0)} \in \mathbb{R}^{D\times Q}$.
For $\ell = 0, 1, \ldots$
$\quad i_{\mathcal{P}}^{(\ell)} \in \arg\min_{i_{\mathcal{P}}\in\{1,\ldots,Q\}^{N\times M}} \Phi(q_{i_{\mathcal{P}},\boldsymbol{r}^{(\ell)}}, f)$
$\quad \boldsymbol{r}^{(\ell+1)} \in \arg\min_{\boldsymbol{r}\in\mathbb{R}^{D\times Q}} \Phi(q_{i_{\mathcal{P}}^{(\ell)},\boldsymbol{r}}, f)$

For separable and maximum error measures (see (2.5) and (2.11)), the optimization of the label field at iteration ℓ then amounts to applying a nearest neighbour rule, i.e. finding $i_{\mathcal{P}}^{(\ell)}$ such that, for every $(n, m) \in \mathbb{X}$ and, for every $k \in \{1, \ldots, Q\}$, $i_{\mathcal{P}}^{(\ell)}(n, m) = k$ only if

$$(\forall k' \in \{1, \ldots, Q\}) \quad \varphi_{n,m}\big(r_k, f(n, m)\big) \leq \varphi_{n,m}\big(r_{k'}, f(n, m)\big). \tag{2.13}$$

Note that, in general, $i_{\mathcal{P}}^{(\ell)}(n, m)$ is not uniquely defined since there may exist $k' \in \{1, \ldots, Q\} \setminus \{k\}$ such that $\varphi_{n,m}\big(r_k, f(n, m)\big) = \varphi_{n,m}\big(r_{k'}, f(n, m)\big)$.

On the other hand, updating of the codebook at iteration ℓ is performed by computing the centroid of each region $\mathbb{D}_k^{(\ell)}$, $k \in \{1, \ldots, Q\}$. For the matrix weighted quadratic norm ((2.5) and (2.6)), we thus obtain the classical center of mass of $\mathbb{D}_k^{(\ell)}$:

$$r_k^{(\ell+1)} = \Big(\sum_{(n,m)\in\mathbb{D}_k^{(\ell)}} \Gamma_{n,m} \Big)^{-1} \Big(\sum_{(n,m)\in\mathbb{D}_k^{(\ell)}} \Gamma_{n,m} f(n, m) \Big). \tag{2.14}$$

For the mean absolute value criterion ((2.5) and (2.8) with $p = 1$ and equal weights), $r_k^{(\ell+1)}$ is the vector median of the pixel values located in $\mathbb{D}_k^{(\ell)}$:

$$r_k^{(\ell+1)} = \big(\text{median} \big\{ f_d(n, m) \;\big|\; (n, m) \in \mathbb{D}_k^{(\ell)} \big\} \big)_{1\leq d\leq D}. \tag{2.15}$$

For the generalized Kullback-Leibler divergence ((2.5), (2.9) and (2.10)), we get

$$r_k^{(\ell+1)} = \frac{1}{\operatorname{card} \mathbb{D}_k^{(\ell)}} \sum_{(n,m)\in\mathbb{D}_k^{(\ell)}} f(n, m) \tag{2.16}$$

provided that $f \in ([0, +\infty)^D)^{N\times M}$. For the sup norm ((2.11) and (2.12)), we have

$$r_k^{(\ell+1)} = \Big(\frac{\beta_{d,k} + \gamma_{d,k}}{2} \Big)_{1\leq d\leq D} \tag{2.17}$$

where

$$\beta_{d,k} = \min \big\{ f_d(n, m) \;\big|\; (n, m) \in \mathbb{D}_k^{(\ell)} \big\} \tag{2.18}$$

and

$$\gamma_{d,k} = \max \big\{ f_d(n, m) \;\big|\; (n, m) \in \mathbb{D}_k^{(\ell)} \big\}. \tag{2.19}$$

When a closed form expression of $r_k^{(\ell+1)}$ is not available, one may resort to numerical optimization algorithms [Boyd and Vandenberghe, 2004] to compute centroids.

It can also be noticed that an alternative to the LBG algorithm is the dynamic programming approach proposed in [Bruce, 1965] (see also [Wu and Rokne, 1989], [Wu, 1991] for more recent extensions) which features better global convergence properties. Generally, if LBG is used, the final solution is sub-optimal.

§ 2.3 Considered design criterion

One drawback of the approach described in the previous section is that it does not guarantee any spatial homogeneity of the resulting quantized image. To alleviate this shortcoming, we propose to solve the following problem:

$$\underset{(i_{\mathcal{P}},\boldsymbol{r})\in\{1,\dots,Q\}^{N\times M}\times C}{\text{minimize}} \quad \Phi(q_{i_{\mathcal{P}},\boldsymbol{r}},f)+\rho(i_{\mathcal{P}}) \tag{2.20}$$

where $\rho\colon \{1,\dots,Q\}^{N\times M}\to(-\infty,+\infty]$ is some penalty function which is used to promote the spatial regularity of the label image. Note that an alternative approach for ensuring the smoothness of the quantized image would be to solve a problem of the form

$$\underset{(i_{\mathcal{P}},\boldsymbol{r})\in\{1,\dots,Q\}^{N\times M}\times C}{\text{minimize}} \quad \Phi(q_{i_{\mathcal{P}},\boldsymbol{r}},f)+\widetilde{\rho}(q_{i_{\mathcal{P}},\boldsymbol{r}}) \tag{2.21}$$

where the regularization term $\widetilde{\rho}$ is now a function from $(\mathbb{R}^D)^{N\times M}$ to $(-\infty,+\infty]$. The latter problem appears however more difficult to solve than (2.20) since the regularization term in (2.21) is a multivariate function depending both on $i_{\mathcal{P}}$ and $\boldsymbol{r}$.

The existence of a solution to problem (2.20) is secured by the following result:

Proposition 2.3.1 *Assume that $\Phi(\cdot,f)$ is a lower-semicontinuous function and that one of the following conditions holds:*

1. *$\Phi(\cdot,f)$ is coercive;*[2]
2. *C is bounded.*

Then, problem (2.20) has a solution.

Proof. Let $i_{\mathcal{P}}$ be any given label field in $\{1,\dots,Q\}^{N\times M}$. According to (4.1), $\boldsymbol{r}\mapsto q_{i_{\mathcal{P}},\boldsymbol{r}}$ is a linear operator, and consequently $\boldsymbol{r}\mapsto\Phi(q_{i_{\mathcal{P}},\boldsymbol{r}},f)$ is a lower-semicontinuous function. As a direct consequence of Weierstrass theorem

[2] This means that $\lim_{\|g\|\to+\infty}\Phi(g,f)=+\infty$.

[Rockafellar and Wets, 2004], under Assumption 1 or 2, there exists $\overline{\boldsymbol{r}}_{\mathcal{P}} \in C$ such that

$$\Phi(q_{i_{\mathcal{P}},\overline{\boldsymbol{r}}_{\mathcal{P}}}, f) = \min_{\boldsymbol{r}\in C} \Phi(q_{i_{\mathcal{P}},\boldsymbol{r}}, f). \tag{2.22}$$

Problem (2.20) can thus be reexpressed as

$$\underset{i_{\mathcal{P}}\in\{1,\ldots,Q\}^{N\times M}}{\text{minimize}} \quad \Phi(q_{i_{\mathcal{P}},\overline{\boldsymbol{r}}_{\mathcal{P}}}, f) + \rho(i_{\mathcal{P}}). \tag{2.23}$$

The latter minimization can be performed by a search among a finite number of candidate values, so leading to an optimal label field $i_{\overline{\mathcal{P}}}$. Hence, $(i_{\overline{\mathcal{P}}}, q_{i_{\overline{\mathcal{P}}},\overline{\boldsymbol{r}}_{\overline{\mathcal{P}}}})$ is a solution to problem (2.20). □

Typical choices for ρ in (2.20) that can be made are the following:

- isotropic variation functions

$$\rho(i_{\mathcal{P}}) = \mu \sum_{n=1}^{N-1} \sum_{m=1}^{M-1} \psi(\|\nabla i_{\mathcal{P}}(n,m)\|), \quad \mu \geq 0 \tag{2.24}$$

  where $\nabla i_{\mathcal{P}}(n,m) = \big(i_{\mathcal{P}}(n+1,m) - i_{\mathcal{P}}(n,m), i_{\mathcal{P}}(n,m+1) - i_{\mathcal{P}}(n,m)\big)$ is the discrete gradient of $i_{\mathcal{P}}$ at location (n,m).

- anisotropic variation functions

$$\rho(i_{\mathcal{P}}) = \mu\Big(\sum_{n=1}^{N-1} \sum_{m=1}^{M} \psi(|i_{\mathcal{P}}(n+1,m) - i_{\mathcal{P}}(n,m)|) + \sum_{n=1}^{N} \sum_{m=1}^{M-1} \psi(|i_{\mathcal{P}}(n,m+1) - i_{\mathcal{P}}(n,m)|)\Big), \quad \mu \geq 0. \tag{2.25}$$

In the above two examples, ψ is a function from $[0,+\infty)$ to $(-\infty,+\infty]$. When ψ is the identity function, the classical isotropic or anisotropic total variations are obtained. A more flexible form is given by the truncated linear function [Veksler, 1999] defined as

$$(\forall x \in [0,+\infty)) \qquad \psi(x) = \begin{cases} x & \text{if } x < \zeta \\ \zeta & \text{otherwise} \end{cases} \tag{2.26}$$

where $\zeta > 0$ is the limiting constant. If $\psi = (\cdot)^2$, then a Tikhonov-like regularization is performed. Another interesting choice of ψ is the binary cost function (also named ℓ_0 criterion).

$$(\forall x \in [0,+\infty)) \qquad \psi(x) = \begin{cases} 0 & \text{if } x = 0 \\ 1 & \text{otherwise.} \end{cases} \tag{2.27}$$

When ψ is a (strictly) increasing function, higher local differences of the label values entail a stronger penalization. For this behaviour to be consistent with the quantized image values, some ordering relation should typically exist between the codevectors. Hence, if $D = 1$, a natural choice is to constrain the vector $\boldsymbol{r}$ to belong to the closed convex cone:

$$C = \big\{(s_1, \ldots, s_Q) \in \mathbb{R}^Q \;\big|\; s_1 \leq \cdots \leq s_Q\big\}. \tag{2.28}$$

When $D > 1$, the definition of C becomes more debatable since there exists no total order on $\mathbb{R}^D$. A possibility is to impose an artificial total order. In mathematical morphology, authors have proposed various lexicographic orderings [Vertan et al., 1996], [Talbot et al., 1998] or bit-mixing [Chanussot and Lambert, 1997] along space-filling (Peano-like) curves.

A possible choice for C is the closed convex cone:

$$C = \big\{(s_1, \ldots, s_Q) \in \mathbb{R}^{D \times Q} \;\big|\; \theta(s_1) \leq \cdots \leq \theta(s_Q)\big\} \tag{2.29}$$

where

$$(\forall u \in \mathbb{R}^D) \qquad \theta(u) = \eta^\top u \tag{2.30}$$

and $\eta \in \mathbb{R}^D$. For example, for color images, by an appropriate choice of $\eta \in \mathbb{R}^3$ (possibly depending on the considered color system [Hill et al., 1997]), the function θ may serve to extract the luminance component of the codevectors.

More generally, the parameter vector $\eta \in \mathbb{R}^D$ may be obtained through a principal component analysis [Eckart and Young, 1936] of the original multichannel data. Note that, when the binary function in (2.27) is employed, the magnitudes of the local differences of the label fields have no influence as soon as they are nonzero. This means that ordering the codevectors does not appear useful in this case, and that one can set $C = \mathbb{R}^{D \times Q}$.

In addition to these considerations, when the regularization constant μ in (2.24) or (2.25) takes large values, solving (2.20) under the constraints modeled by (2.28) may lead to very close or even equal values of codevectors. As a consequence, the readibility of the quantized image may be affected. In some applications, it may therefore be beneficial to redefine the constraint C in order to prevent this effect. When $D = 1$, the closed convex set C can thus be given by

$$C = \{(s_1, \ldots, s_Q) \in \mathbb{R}^Q \mid (\forall k \in \{1, \ldots, Q-1\})\; s_{k+1} - s_k \geq \delta\} \tag{2.31}$$

where $\delta \geq 0$. Similarly, when $D > 1$, we propose to set

$$C = \{(s_1, \ldots, s_Q) \in \mathbb{R}^{D \times Q} \mid (\forall k \in \{1, \ldots, Q-1\})\; \theta(s_{k+1} - s_k) \geq \delta\} \tag{2.32}$$

where $\delta \geq 0$ and θ is the function given by (2.30). Penalization of quantization values for being too close to each other was previously introduced in the energy model proposed in [Alvarez and Esclarín, 1997].

§ 2.4 Proposed optimization method

Even if $\Phi(\cdot, f)$ and ρ are convex functions, problem (2.20) is a nonconvex optimization problem due to the fact that $i_{\mathcal{P}}$ belongs to a (nonconvex) set of discrete values. In order to solve numerically this problem, we propose to use the following alternating optimization algorithm:

Algorithm 2 Proposed algorithm for solving (2.20)

Fix $Q \in \mathbb{N}^*$ and $\boldsymbol{r}^{(0)} \in C$.
For $\ell = 0, 1, \ldots$
$$\left\lfloor \begin{array}{l} i_{\mathcal{P}}^{(\ell)} \in \underset{i_{\mathcal{P}} \in \{1,\ldots,Q\}^{N\times M}}{\arg\min} \Phi(q_{i_{\mathcal{P}},\boldsymbol{r}^{(\ell)}}, f) + \rho(i_{\mathcal{P}}) \\ \boldsymbol{r}^{(\ell+1)} \in \underset{\boldsymbol{r}\in C}{\arg\min}\, \Phi(q_{i_{\mathcal{P}}^{(\ell)},\boldsymbol{r}}, f) \end{array} \right.$$

It is worth noticing that this algorithm constitutes an extension of the LBG algorithm (see Algorithm 1) which would correspond to the case when ρ is the null function and $C = \mathbb{R}^{D\times Q}$. Similarly to the LBG algorithm, under the assumptions of proposition 2.3.1, Algorithm 2 generates a sequence $(i_{\mathcal{P}}^{(\ell)}, \boldsymbol{r}^{(\ell+1)})_{\ell\in\mathbb{N}}$ such that $\big(\Phi(q_{i_{\mathcal{P}}^{(\ell)},\boldsymbol{r}^{(\ell+1)}}, f) + \rho(i_{\mathcal{P}}^{(\ell)})\big)_{\ell\in\mathbb{N}}$ is a convergent decaying sequence. At each iteration ℓ, the determination of $i_{\mathcal{P}}^{(\ell)}$ given $\boldsymbol{r}^{(\ell)}$ is a combinatorial optimization problem for which there exist efficient solutions for particular choices of Φ and ρ, as explained in the next section.

In turn, if $\Phi(\cdot, f)$ is a convex function, the determination of $\boldsymbol{r}^{(\ell+1)}$ given $i_{\mathcal{P}}^{(\ell)}$ is a constrained convex optimization problem the solution of which can be determined numerically. For any given $i_{\mathcal{P}} \in \{1, \ldots, Q\}^{N\times M}$, let $L_{i_{\mathcal{P}}}$ be the linear operator defined as

$$\begin{aligned} L_{i_{\mathcal{P}}} \colon \mathbb{R}^{D\times Q} &\to (\mathbb{R}^D)^{N\times M} \\ \boldsymbol{r} &\mapsto q_{i_{\mathcal{P}},\boldsymbol{r}} \end{aligned} \tag{2.33}$$

the adjoint of which is

$$\begin{aligned} L_{i_{\mathcal{P}}}^* \colon (\mathbb{R}^D)^{N\times M} &\to \mathbb{R}^{D\times Q} \\ g &\mapsto \Big(\sum_{(n,m)\in\mathbb{D}_1} g(n,m), \ldots, \sum_{(n,m)\in\mathbb{D}_Q} g(n,m) \Big) \end{aligned} \tag{2.34}$$

(with the convention $\sum_{(n,m)\in\varnothing} \cdot = 0$). Then,

$$\begin{aligned} L_{i_{\mathcal{P}}}^* L_{i_{\mathcal{P}}} \colon \mathbb{R}^{D\times Q} &\to \mathbb{R}^{D\times Q} \\ \boldsymbol{r} &\mapsto \boldsymbol{r}\, \mathrm{Diag}(\mathrm{card}\,\mathbb{D}_1, \ldots, \mathrm{card}\,\mathbb{D}_Q). \end{aligned} \tag{2.35}$$

In addition, let Θ be the linear operator defined as

$$\begin{aligned}\Theta\colon \mathbb{R}^{D\times Q} &\to \mathbb{R}^{Q-1}\\ (s_1,\ldots,s_Q) &\mapsto \big(\theta(s_2-s_1),\ldots,\theta(s_Q-s_{Q-1})\big)\end{aligned} \tag{2.36}$$

where θ is given by (2.30) (with $\eta=1$ when $D=1$). The set C defined in (2.31) or (2.32) is thus equal to $\Theta^{-1}([\delta,+\infty[^{Q-1})$. Hence, the problem of minimization of $\boldsymbol{r}\mapsto\Phi(q_{i_\mathcal{P}},\boldsymbol{r},f)$ over C can be reexpressed as

$$\underset{\boldsymbol{r}\in\mathbb{R}^{D\times Q}}{\text{minimize}} \quad \Phi(L_{i_\mathcal{P}}\boldsymbol{r},f)+\iota_{[\delta,+\infty[^{Q-1}}(\Theta\boldsymbol{r}) \tag{2.37}$$

where ι_S denotes the indicator function of a set S, which is zero on S and equal to $+\infty$ on its complement. If we assume that $\Phi(\cdot,f)$ belongs to $\Gamma_0\big((\mathbb{R}^D)^{N\times M}\big)$, the class of lower-semicontinuous proper convex functions from $(\mathbb{R}^D)^{N\times M}$ to $(-\infty,+\infty]$, (2.37) can be solved through existing convex optimization approaches [Boyd and Vandenberghe, 2004], [Combettes and Pesquet, 2011], [Hiriart-Urruty and Lemaréchal, 1993]. One possible solution is to employ the method proposed in [Pesquet and Pustelnik, 2012] (hereafter called PPXA+) which constitutes an extension of the parallel proximal algorithm (PPXA) developed in [Combettes and Pesquet, 2008] and of the simultaneous direction of multipliers method proposed in [Setzer et al., 2010] (see also [Goldstein and Osher, 2009], [Afonso et al., 2010b], [Afonso et al., 2010a]).

Algorithm 3 PPXA+ for solving (2.37)

Initialization:

$(\omega_1,\omega_2,\omega_3)\in(0,+\infty)^3$

$t^{(1,0)}\in(\mathbb{R}^D)^{N\times M}, t^{(2,0)}\in\mathbb{R}^{Q-1}, \boldsymbol{s}^{(0)}\in\mathbb{R}^{D\times Q}$

$R=(\omega_1 L_{i_\mathcal{P}}^* L_{i_\mathcal{P}}+\omega_2\Theta^*\Theta+\omega_3 I)^{-1}$

$\boldsymbol{r}^{(0)}=R\,(\omega_1 L_{i_\mathcal{P}}^* t^{(1,0)}+\omega_2\Theta^* t^{(2,0)}+\omega_3\boldsymbol{s}^{(0)})$

Main loop:

For $\ell=0,1,\ldots$

$p^{(1,\ell)}=\operatorname{prox}_{\frac{1}{\omega_1}\Phi(\cdot,f)}\big(t^{(1,\ell)}\big)$

$p^{(2,\ell)}=P_{[\delta,+\infty[^{Q-1}}\big(t^{(2,\ell)}\big)$

$\boldsymbol{c}^{(\ell)}=R\,(\omega_1 L_{i_\mathcal{P}}^* p^{(1,\ell)}+\omega_2\Theta^* p^{(2,\ell)}+\omega_3\boldsymbol{s}^{(\ell)})$

$\lambda_\ell\in\,]0,2[$

$t^{(1,\ell+1)}=t^{(1,\ell)}+\lambda_\ell\big(L_{i_\mathcal{P}}(2\boldsymbol{c}^{(\ell)}-\boldsymbol{r}^{(\ell)})-p^{(1,\ell)}\big)$

$t^{(2,\ell+1)}=t^{(2,\ell)}+\lambda_\ell\big(\Theta(2\boldsymbol{c}^{(\ell)}-\boldsymbol{r}^{(\ell)})-p^{(2,\ell)}\big)$

$\boldsymbol{s}^{(\ell+1)}=\boldsymbol{s}^{(\ell)}+\lambda_\ell(2\boldsymbol{c}^{(\ell)}-\boldsymbol{r}^{(\ell)}-\boldsymbol{s}^{(\ell)})$

$\boldsymbol{r}^{(\ell+1)}=\boldsymbol{r}^{(\ell)}+\lambda_\ell(\boldsymbol{c}^{(\ell)}-\boldsymbol{r}^{(\ell)}).$

In the above algorithm, $\operatorname{prox}_{\frac{1}{\omega_1}\Phi(\cdot,f)}$ is the proximity operator of $\omega_1^{-1}\Phi(\cdot,f)$ [Moreau, 1965] and $P_{[\delta,+\infty[^{Q-1}}$ is the projector onto $[\delta,+\infty[^{Q-1}$. Expressions

of proximity operators for usual convex functions are listed in [Chaux et al., 2007]. The convergence of the PPXA+ algorithm is guaranteed under weak assumptions.

Proposition 2.4.1 *Assume that*

1. *there exists* $\underline{\lambda} \in]0, 2[$ *such that* $(\forall \ell \in \mathbb{N})\ \underline{\lambda} \leq \lambda_{\ell+1} \leq \lambda_\ell$.
2. *There exists* $\overline{\boldsymbol{r}} \in \mathbb{R}^{D\times Q}$ *such that*

$$L_{i_{\mathcal{P}}}\overline{\boldsymbol{r}} \in \operatorname{ri}\operatorname{dom}\Phi(\cdot, f) \quad \text{and} \quad \Theta\overline{\boldsymbol{r}} \in]\delta, +\infty[^{Q-1} \tag{2.38}$$

where $\operatorname{dom}\Phi(\cdot, f)$ *is the domain of* $\Phi(\cdot, f)$ *and* $\operatorname{ri}\operatorname{dom}\Phi(\cdot, f)$ *is its relative interior.*

Then, the sequence $(\boldsymbol{r}^{(\ell)})_{\ell\in\mathbb{N}}$ *generated by Algorithm 3 converges to a solution to problem* (2.37).

Proof. See [Pesquet and Pustelnik, 2012]. □

§ 2.5 Combinatorial partitioning

We now consider two combinatorial optimization methods for finding

$$i_{\widehat{\mathcal{P}}} \in \underset{i_{\mathcal{P}}\in\{1,\ldots,Q\}^{N\times M}}{\arg\min}\ \Phi(q_{i_{\mathcal{P}},\boldsymbol{r}}, f) + \rho(i_{\mathcal{P}}) \tag{2.39}$$

for a given value of $\boldsymbol{r} \in C$. Here we seek to use standard methods in combinatorial optimization which have proved to be useful in applications to image processing. In this context, a common form for regularization problems is the following:

$$\underset{i_{\mathcal{P}}\in\{1,\ldots,Q\}^{N\times M}}{\text{minimize}}\ \widetilde{\Phi}(i_{\mathcal{P}}, f) + \rho(i_{\mathcal{P}}), \tag{2.40}$$

where $\widetilde{\Phi}\colon \{1,\ldots,Q\}^{N\times M} \times (\mathbb{R}^D)^{N\times M} \to (-\infty, +\infty]$ is a data fidelity function, ρ a regularization function, f the initial image and $i_{\mathcal{P}}$ the target discrete one. To formulate our problem in this framework, we need to introduce the auxiliary function

$$\begin{aligned} \chi_{\boldsymbol{r}}\colon \{1,\ldots,Q\}^{N\times M} &\to \{r_1,\ldots,r_Q\}^{N\times M} \\ i_{\mathcal{P}} &\mapsto q_{i_{\mathcal{P}},\boldsymbol{r}}. \end{aligned}$$

Then, our problem becomes

$$\underset{i_{\mathcal{P}} \in \{1,\dots,Q\}^{N\times M}}{\text{minimize}} \Phi(\chi_{\boldsymbol{r}}(i_{\mathcal{P}}), f) + \rho(i_{\mathcal{P}}). \tag{2.41}$$

Note that $\chi_{\boldsymbol{r}}$ is monotonic but nonlinear. Note further that the set $\{r_1, \dots, r_Q\}$ changes at each iteration of the complete algorithm. However, during the regularization step, this set is fixed.

In this section, we use graph-cut based algorithms briefly introduced in Chapter 1.3.2.

2.5.1 Method I - convex regularization term

Here we describe a way to formulate the problem as a globally optimal graph cut, inspired by the approach of Ishikawa *et al.* [Ishikawa and Geiger, 1999]. In this approach, we build a discrete graph that will allow us to represent the quantized and regularized version of our original image. Let us define the oriented, edge-weighted graph $\mathcal{G} = (\mathcal{V}, \mathcal{E})$ as follows:

1. $\mathcal{V} = \mathbb{X} \times \{1, \dots, Q\} \cup \{s, t\}$ the set of vertices quantized over Q levels, where $\mathbb{X}$ is the image support as defined in section 2.2. We add two special vertices, the *source* s and the *sink* t.

2. $\mathcal{E} = \mathcal{E}_D \cup \mathcal{E}_C \cup \mathcal{E}_P$, the set of edges. In the following we denote an oriented edge by $[a, b]$, with a and b the vertices it joins in the direction from a to b. We have :

   (a) $\mathcal{E}_D = \bigcup_{v\in\mathbb{X}} \mathcal{E}_D^v$ the upward columns of the graph. For all $v \in \mathbb{X}$, let $h_{v,k}$ denote the node in column v and row k. A single column associated with pixel v is defined as
   $$\mathcal{E}_D^v = \{[s, h_{v,1}]\} \cup \{[h_{v,k}, h_{v,k+1}] \mid k \in \{1, ..., Q-1\}\} \cup \{h_{v,Q}, t\},$$

   (b) $\mathcal{E}_C = \bigcup_{v\in\mathbb{X}} \mathcal{E}_C^v$ the downward columns of the graph, with
   $\mathcal{E}_C^v = \{[h_{v,k}, h_{v,k+1}] \mid k \in \{1, ..., Q-1\}\}$,

   (c) and the penalty edges of the graph are thus defined as
   $$\mathcal{E}_P = \{[h_{v,k}, h_{w,k}] \mid v, w \in \mathbb{X},\ \{v, w\} \text{ neighbours}, k \in \{1, ..., Q\}\}.$$

The above graph is depicted in Fig. 2.1. In this figure, for simplicity we assume each pixel has only two neighbours, which allows us to represent the graph in a 2D planar layout. For actual 2D images, there exist many more penalty edges between all neighbours in $\mathbb{X}$. The graph layout is then non-planar, but remains similar. For 2D images, it is best to see the arrangement of v vertices as in the original images, with the column of penalty edges in an extra dimension.

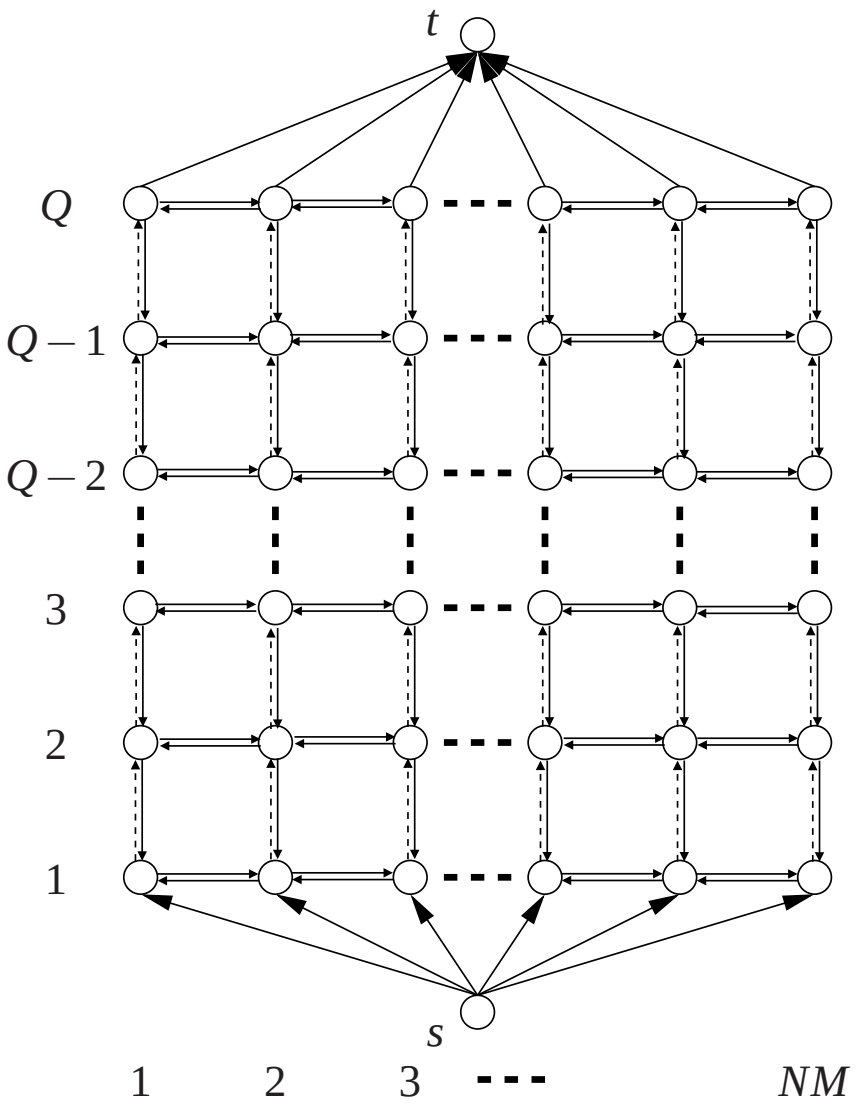

Arrows represent the edges $\mathcal{E}$ and circles the nodes in $\mathcal{V}$. Horizontal edges are in $\mathcal{E}_P$, the dotted upward vertical edges are in $\mathcal{E}_D$ and the plain downward vertical edges are in $\mathcal{E}_C$. Vertices s and t are respectively the source and the sink. All pixels in the image from 1 to NM are represented in the columns. In actual 2D images, there exist many more penalty edges $\mathcal{E}_P$ than depicted here: all those between neighbours in $\mathbb{X}$.

Figure 2.1: *Construction of the Ishikawa-like optimization graph.*

If Φ is the separable function defined in (2.5) and ρ is the anisotropic TV in (2.25) where ψ is the identity function, we define the capacities (or weights) c of edges $[a, b] \in \mathcal{E}$ as follows:

1. Links to the source have infinite capacity:
   $\forall v \in \mathbb{X}, c([s, h_{v,1}]) = +\infty$.
2. Data fidelity terms for any pixel $v \in \mathbb{X}$ is
   $\forall k \in \{1, \dots, Q-1\}, c([h_{v,k}, h_{v,k+1}]) = \varphi_v(r_k, f(v)),\ c([h_{v,Q}, t]) = \varphi_v(r_Q, f(v))$.
3. The capacity of downward columns is infinite to constrain a single cut per column:
   $\forall v \in \mathbb{X}, \forall k \in \{1 \dots Q-1\}, c([h_{v,k+1}, h_{v,k}]) = +\infty$.
4. The regularization term along the penalty edges of the graph is:
   for every $v, w \in \mathbb{X}$, and $\{v, w\}$ neighbours
   $\forall k \in \{1, \dots, Q\}, c([h_{v,k}, h_{w,k}]) = \mu$

The above graph $\mathcal{G}$ has the same topology as the one proposed by Ishikawa and it can be extended to any convex function ψ [Ishikawa and Geiger, 1999]. The capacities of $\mathcal{E}$ are adjusted in such a way that a cut of $\mathcal{G}$ corresponds to the solution of (2.41), granted by the following result:

Proposition 2.5.1 *If ρ is the anisotropic TV in (2.25) where ψ is the identity function, then the min cut of $\mathcal{G} = (\mathcal{V}, \mathcal{E})$ is the globally optimal solution to (2.41).*

Proof. This result is derived from the construction of the graph. First note that we build here a binary flow network with one source and one sink. Following Ishikawa, relying on the celebrated discrete maxflow/mincut theorem of Ford and Fulkerson [Ford and Fulkerson, 1962], any binary cut that separates s and t along a series of edges, that can be interpreted as a solution $i_{\mathcal{P}}$. Indeed, the infinite capacity of the downward edges ensure a single cut edge in each column of the graph, and the infinite capacity of the upward $[s, h_{v,1}]$ edges for all v ensures that, in all columns, this cut will be located above one of the nodes corresponding to a level $k \in \{1, \dots, Q\}$. We can therefore associate the cut in column v with the value of the level immediately below the cut, and associate this with $i_{\mathcal{P}}(v)$. Recalling that all labels below the cut will have the same label as s, and all that above the cut the same label as t, the value of $i_{\mathcal{P}}$ at pixel v is the highest level l in column v of the graph that is labelled like the source s. Here, by convention, the source is labelled with 1 and the sink with 0. We can then write $i_{\mathcal{P}}(v) = \max\{k, h_{v,k} = 1\}$.

Now, the computation of the maxflow/mincut on this graph minimizes the energy of the cut, interpreted as the sum of two terms:

1. since the downward constraint edges ensure a single cut edge along each column of the graph, this corresponds to contribution of the data fidelity term $\varphi_v(r_Q, f(v))$ to the total energy.

2. Similarly, we note that each penalty edges in $\mathcal{E}_P$ with capacity μ can be cut at most once. Let u and v be two neighbouring pixels in the graph. The cut along penalty edges between $i_{\mathcal{P}}(u)$ and $i_{\mathcal{P}}(v)$ crosses exactly as many penalty edges as there are quantization level differences between u and v. We note that this correspond to a contribution of $\mu|i_{\mathcal{P}}(u) - i_{\mathcal{P}}(v)|$ to the total energy.

Hence, the computation of the maxflow/mincut on this graph solves (2.41) exactly, in the case of (2.25), when ψ is the identity. □

Remark 2.5.2

1. It is also possible to solve this problem exactly in the case when ψ is convex and not necessarily the identity, by adding non-horizontal penalty edges [Ishikawa, 2003], but we do not consider this case here, as $\psi = Id$ is favorable when discontinuities exist in the original image.

2. In the case when the number of quantized levels Q is small (say between 1 and 32), the Ishikawa framework is very efficient.

3. As the dimensionality of the problem increases, so does the number of penalty edges in the graph. The cut is always an hypersurface of codimension 1.

4. Ishikawa recommends solving the maxflow/mincut by using a push-relabel algorithm, which makes perfect sense as the dimensionality increases, because these algorithms have an asymptotic complexity independent of the number of edges.

2.5.2 Method II - submodular regularization term

Since the method proposed in Section 2.5.1 works only for a convex function ψ, we propose to solve the general problem defined in (2.39) with the α-expansion algorithm [Boykov et al., 2001], which has been proven to be very effective for some non-convex functions ψ such as the Potts model of (2.27). Though only a local minimum is then guaranteed, the resulting energy will be within a known factor of the global minimum energy [Boykov et al., 2001]. Here we reintroduce the standard notation of α-expansions as we need to specify the capacities on the corresponding edges in the context of this chapter. Following Kolmogorov *et al.* [Kolmogorov and Zabih, 2004], we build a directed graph for each quantization level, called α-expansion graph $\mathcal{G}_\alpha = (\mathcal{V}, \mathcal{E})$, defined as follows:

1. $\mathcal{V} = V \cup \{\alpha, \overline{\alpha}\}$ is the set of vertices, with α and $\overline{\alpha}$ two special term nodes and $V = \{1, ..., NM\}$ is the set of image nodes ;

2. $\mathcal{E} = \mathcal{E}_V \cup \mathcal{E}_{\mathcal{N}}$ is the set of edges, defined as follows :

   (a) $\mathcal{E}_V = \bigcup_{v \in V} \{[\alpha, v], [v, \overline{\alpha}]\}$ is the set of edges between special term nodes and image nodes ;

   (b) $\mathcal{E}_{\mathcal{N}} = \bigcup_{\{u,v\} \text{ neighbours}}$ is the set of edges between neighbours and $\mathcal{N}$ is the set of neighbours pairs containing only ordered pairs u, v, i.e. such that $u < v$.

   (c) The capacity for all edges are given in Table 2.1.

Computing the max-flow/min-cost cut of $\mathcal{G}_\alpha$ separates vertices α and $\overline{\alpha}$ in such a way that the α region can only expand, hence the name of the algorithm. The value of the function associating new values to $i_{\mathcal{P}}$, based on cut of $\mathcal{G}_\alpha$, is called *"α-move of $i_{\mathcal{P}}$"* [Veksler, 1999]. The algorithm is as follows:

Algorithm 4 α-expansion algorithm

Fix $i_{\mathcal{P}}^{(0)}$.
For $\ell = 0, 1, \ldots$
$\quad \widetilde{\alpha}^{(\ell)} \in \arg\min_{\alpha \in \{1,\ldots,Q\}} \left\{ \Phi(\chi_{\boldsymbol{r}}(\widehat{i}_{\mathcal{P}}), f) + \rho(\widehat{i}_{\mathcal{P}}) \;\middle|\; \widehat{i}_{\mathcal{P}} = \alpha\text{-move of } i_{\mathcal{P}}^{(\ell)} \right\}$
$\quad i_{\mathcal{P}}^{(\ell+1)} = \widetilde{\alpha}^{(\ell)}\text{-move of } i_{\mathcal{P}}^{(\ell)}$

Proposition 2.5.3 *If* (2.39) *is submodular then it can be solved with the α-expansion algorithm.*

Proof. It is shown in [Kolmogorov and Zabih, 2004] that in order to employ the α-expansion algorithm, (2.39) has to satisfy the following conditions at iteration ℓ:

1. (2.39) has a binary representation of the form:

$$\begin{array}{ll} \text{minimize} & \sum_{u \in V} B_1^{(\ell)}(b_{(n_u, m_u)}) + \\ & \sum_{\{u,v\} \text{neighbours}} B_2^{(\ell)}(b_{(n_u,m_u)}, b_{(n_v,m_v)}), \end{array} \tag{2.42}$$

   where b is a binary field while $B_1^{(\ell)}$ and $B_2^{(\ell)}$ have binary arguments.

2. The binary representation b is graph-representable, which can be verified by testing if term $B_2^{(\ell)}$ satisfies the submodular inequality:

$$B_2^{(\ell)}(0,0) + B_2^{(\ell)}(1,1) \leqslant B_2^{(\ell)}(1,0) + B_2^{(\ell)}(0,1)\,. \tag{2.43}$$

We now propose the following binary formulation of (2.39) by defining :

$$B_1^{(\ell)}(b_{(n_u,m_u)}) = \varphi_{n_u,m_u}(r_{\widehat{i}_{\mathcal{P}}(n_u,m_u)}, f(n_u, m_u)) \tag{2.44}$$

and

$$B_2^{(\ell)}(b_{(n_u,m_u)}, b_{(n_v,m_v)}) = \psi(|\widehat{i}_{\mathcal{P}}(n_u, m_u) - \widehat{i}_{\mathcal{P}}(n_v, m_v)|) \tag{2.45}$$

where

$$\widehat{i}_{\mathcal{P}}(n_u, m_u) = \begin{cases} i_{\mathcal{P}}^{(\ell)}(n_u, m_u) & \text{if } b_{(n_u,m_u)} = 0 \\ \alpha & \text{if } b_{(n_u,m_u)} = 1. \end{cases} \tag{2.46}$$

More standard graph-cut formulations would only allow us to optimize (2.40). These formulations would be problematic because we would not be able to separate the two steps in the inner loop of Algorithm 2, and therefore no convergence property could be derived.

Assuming (2.39) submodular, then the terms of its binary representation defined in (2.45) satisfy (2.43). Furthermore, it is shown in [Veksler, 1999] that for ψ defined as Potts model of (2.27) or the truncated linear function in (2.26), and when ρ is the anisotropic TV of (2.25), then this type of energy is indeed submodular. Consequently (2.39) can be solved with α-expansions. □

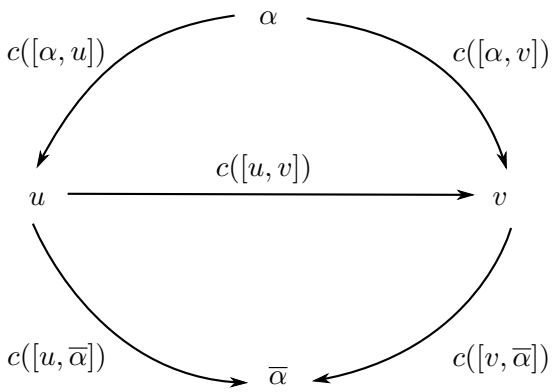

Notations for the α-expansion graph, following Kolmogorov *et al.* [Kolmogorov and Zabih, 2004]. Here we took a simplified 2-pixel neighbourhood. The cost (or capacity) between u and v is labelled as $c([u, v])$ for instance, and so on for all edges. The expressions for the capacity for all edges are given in Table 2.1.

Figure 2.2: *Construction of the α-expansion graph.*

Figure 2.2 provides an illustration of the notation for edge weights in a simplified situation. In order to solve problem (2.39) with the α-expansion

algorithm, we propose to define the capacities c of edges $\mathcal{E}$ in the graph $\mathcal{G}_\alpha$ for all $\{u, v\}$ pairs of neighbours, as described in Table 2.1.

Table 2.1: *Capacities for the α-expansion graph of Fig 2.2.*

edge	capacity [a]
$c([u,\overline{\alpha}])$	$\mathcal{R}\ (K_u) + \sum_{(u,v)\in\mathcal{N}} \mathcal{R}(A_{u,v} - C_{u,v}) + \sum_{(v,u)\in\mathcal{N}} C_{v,u}$
$c([\alpha,u])$	$\mathcal{R}(-K_u) + \sum_{(u,v)\in\mathcal{N}} \mathcal{R}(C_{u,v} - A_{u,v})$
$c([u,v])$	$\sum_{(u,v)\in\mathcal{N}} (B_{u,v} + C_{u,v} - A_{u,v})$

[a] The following notation is used:
$\mathcal{R}$ denotes the ramp function, i.e. $\mathcal{R}(x) = 0$ if $x \in (-\infty, 0)$ and $\mathcal{R}(x) = x$ if $x \in [0, +\infty)$
$K_u = \varphi_{n_u,m_u}(r_{i_\mathcal{P}(n_u,m_u)}, f(n_u,m_u)) - \varphi_{n_u,m_u}(r_\alpha, f(n_u,m_u))$
$A_{u,v} = \psi(|i_\mathcal{P}(n_u,m_u) - i_\mathcal{P}(n_v,m_v)|)$
$B_{u,v} = \psi(|i_\mathcal{P}(n_u,m_u) - \alpha|)$
$C_{u,v} = \psi(|\alpha - i_\mathcal{P}(n_v,m_v)|)$

2.5.3 Other methods

Other combinatorial optimization methods might also be used. For instance, when minimizing *isotropic* TV as in (2.24), one might want to use Chambolle's algorithm [Chambolle, 2004]. Similarly to the Ishikawa framework, we would obtain the global optimum in this case also. Moreover *isotropic* TV minimization was recently discussed among others by Lellmann *et al.* [Lellmann et al., 2009], Trobin *et al.* [Trobin et al., 2008] and Zach *et al.* [Zach et al., 2009]. One other possibility is the use of α - β generalized range moves algorithm, which is shown in [Veksler, 2007] to be able to optimize a wider range of combinatorial energies than α-expansion method presented in Section 2.5.2. Furthermore, similar properties are held by the FastPD [Komodakis et al., 2008] and the PD3$_a$ [Komodakis and Tziritas, 2007] algorithms, both introduced by Komodakis *et al.*. Also worth mentioning is the Darbon and Sigelle method for levelable energies, introduced in [Darbon and Sigelle, 2006], the Kolmogorov and Shioura primal and primal-dual algorithms and Zalesky's MSFM algorithm [Zalesky, 2003], since they are all faster than Ishikawa's approach, while still providing an exact solution for a similar class of functions. Our method can be also improved using higher order cliques, which already has been proven to provide effective filtering results [Ishikawa, 2009]. It might be also possible to extend the quantization techniques proposed by Chambolle and Darbon in [Chambolle and Darbon, 2009]. Also of interest would be to explore variants of anisotropic diffusion, and other combinatorial optimizers such as generalized Dirichlet solvers, which are naturally multi-label [Couprie et al., 2009] and could provide much simpler algorithms.

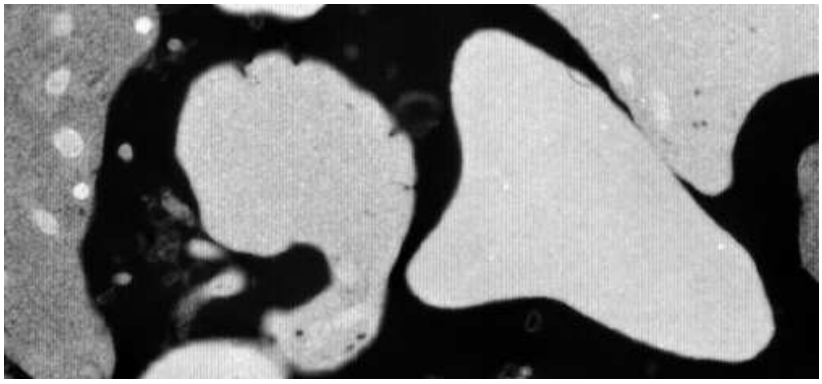

(a) Fragment of the original image

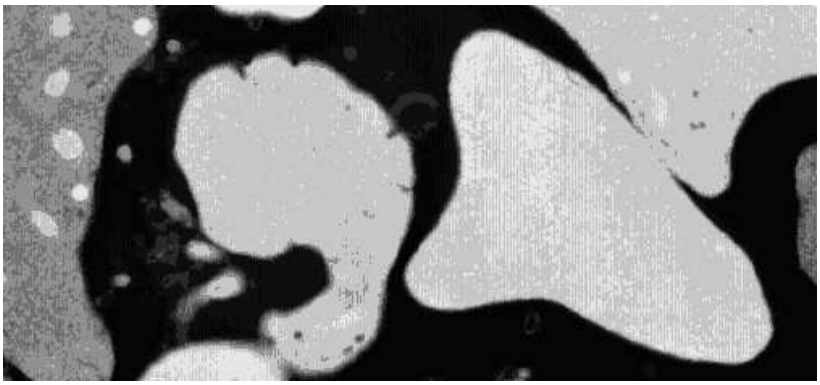

(b) Fragment of LM result

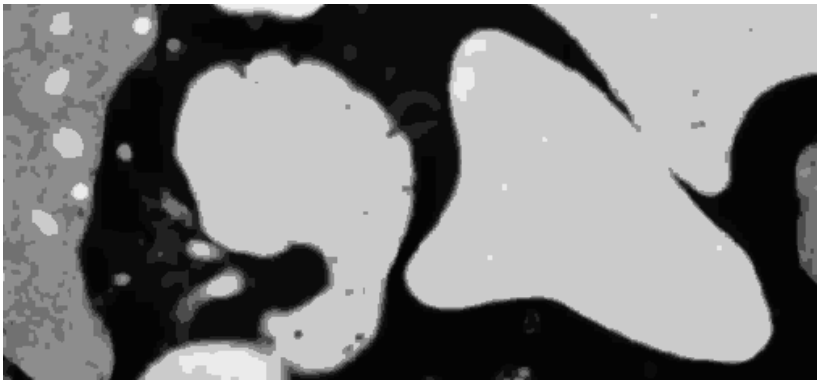

(c) Fragment of our result

Note that LM retained acquisition vertical artifacts, which are absent in our result.

Figure 2.3: *Low resolution quantization (grey scale image)*

§ 2.6 Simulation examples

In this section we present four experiments in order to demonstrate the performance of our method in various scenarii. Both color and grey scale images are considered. For grey scale images, our approach is confronted with the LM method [Lloyd, 1982]. It is a fair comparison, since the same function Φ is used for both algorithms. Although sophisticated initialization procedures [Wu, 1990; Peric and Nikolic, 2007], [Katsavounidis et al., 1994] can be employed for LM and our approach, the methods presented in the following were simply initialized with either uniform or cumulative histograms based decision levels.

In the case of color images, we compared our method with: i) special case of LBG algorithm with Φ defined as ℓ_2 norm (K-means), ii) median cut [Heckbert, 1982] and iii) Wu's method [Wu, 1992a]. Ximagic (http://www.ximagic.com) quantization package was used to generate results of K-means, Wu and median cut algorithms. Their performance is measured in terms of SNR between the original and quantized images and also by the Shannon entropy of order $(2, 2)$ (that is the entropy over image blocks of size 3×3). Note that, in all the following experiments, regularization functions are used corresponding to a 4-pixel neighbourhood (2 pixels in horizontal and 2 in vertical direction) in the employed graph cut techniques. They were implemented with the help of the publicly available library described in [Boykov and Kolmogorov, 2004]. When running experiments using Algorithm 3, there are 4 parameters to set. We have set $\omega_1 = \omega_2 = \omega_3 = 1/3$ and λ_ℓ was fixed and equaled 1.5. The appropriate choice of parameter μ depends on the ratio between maximum values of Φ and ρ codomain, the level of noise in original image and prior knowledge about the desired entropy of output images.

2.6.1 Low resolution quantization

First, we consider grey scale image quantization over $Q = 8$ levels. The combinatorial method described in Section 2.5.1 was used to find the global optimum of convex criterion (2.20) with function Φ defined as the ℓ_1 norm and function ρ defined by (2.25) where ψ is the identity. It was applied to 8 bit microscopy image of size 512×512, the fragment of which is shown in Fig. 2.3(a) (from public domain, http://www.remf.dartmouth.edu). Regularization parameter μ was hand-optimized to 10. Both methods, LM and ours, were initialized with uniform decision levels. In order to solve (2.37), Algorithm 3 was used. The convex set C is defined by (2.31), where $\delta = 12$. As expected, our results provide the best spatial smoothness among the considered methods, which is confirmed by the entropy equal to 0.58 bpp, while in case of LM it is equal to 0.84 bpp. In this example, it is shown that, in case of quantization with high level reduction, our method provides smaller

entropy rate while maintaining the desired fidelity.

In the second example, we show that a similar behaviour is obtained for different choices of Φ, regularity criterion and combinatorial method. This time, the number of quantization levels is $Q = 32$, function (2.20) is specified by Φ defined as the squared ℓ_2 norm and ρ defined by (2.25) where ψ is the binary cost-function (2.27). It is applied to the color-image of size 256×256, which is shown in Fig. 2.4(a). Fig. 2.4(e) presents the results when μ is set to 25 and in Fig. 2.4(f), when it is set to 50. The difference between the two presented images (Fig. 2.4(e) and Fig. 2.4(f)) is not significant but highlights the visual influence of parameter μ. The criterion (2.20) was minimized by using the modified α-expansion graph described in Section 2.5.2, which was initialized with $\boldsymbol{r}^{(0)}$ obtained by median cut algorithm. Image pixels were mapped into the XYZ image space [Ohno, 2000]. Similarly to the previous example, Fig. 2.4 shows that a better spatial smoothness is obtained with the proposed approach. This is also verified by inspecting the entropy value, which in our case is equal to 1.06 bpp for $\mu = 25$, and 1.00 bpp for $\mu = 50$, whereas in the case of Wu, K-means and Median-cut the entropies are equal to 1.18 bpp, 1.14 bpp, 1.19 bpp, respectively.

2.6.2 Quantization in the presence of noise

Next, we present the performance of our method in the presence of noise. Note that here function Φ is chosen based on two noise models, i.e. ℓ_2 for Gaussian and ℓ_1 for Laplacian noise. Firstly, the problem of grey scale image quantization over 16 levels is investigated. The image of size 256×256, shown in Fig. 2.5(b), is corrupted by zero-mean i.i.d. Laplacian noise with standard deviation 9. Quantization is performed using Algorithm 2. The method described in Section 2.5.2 is used to minimize energy (2.20), where Φ is defined as the ℓ_1 norm and ρ is given by (2.25) with ψ taken as the truncated linear function (2.26), where the limiting constant is set to $\zeta = 3$. The associated regularization parameter μ was experimentally chosen equal to 6. Both methods, LM and ours, were initialized with cumulative histogram based decision levels. Problem (2.37) was solved by using Algorithm 3. The convex set C is defined by (2.31), where $\delta = 1$. The proposed approach shows satisfactory results when dealing with Laplacian noise: i) the visual effect of the noise is reduced (see Fig. 2.5(d)), ii) the SNR, which was equal to 22.7 dB for the noisy image increases to 24.6 dB, and iii) the entropy is only 0.96 bpp. In case of LM (see Fig. 2.5(c)), the SNR is equal 22.4 dB and the entropy is 1.41 bpp. In this example, we show that, in case of quantization in the presence of noise, our method reconstructs the original image, while performing image quantization.

Similar properties have been observed for $D > 1$. To illustrate this fact, the quantization over 16 quantization levels of a 300×300 color image is presented in Fig. 2.6. Zero-mean Gaussian noise with standard deviation 20

(a) Original

(b) Wu result

(c) K-means result

(d) Median-cut result

(e) Ours result with μ equal 25

(f) Ours result with μ equal 50

Note that there are many isolated small regions in (b,c,d), while both (e) and (f) feature only smooth large regions, retaining global aspect nonetheless.

Figure 2.4: *Low resolution quantization (color image)*

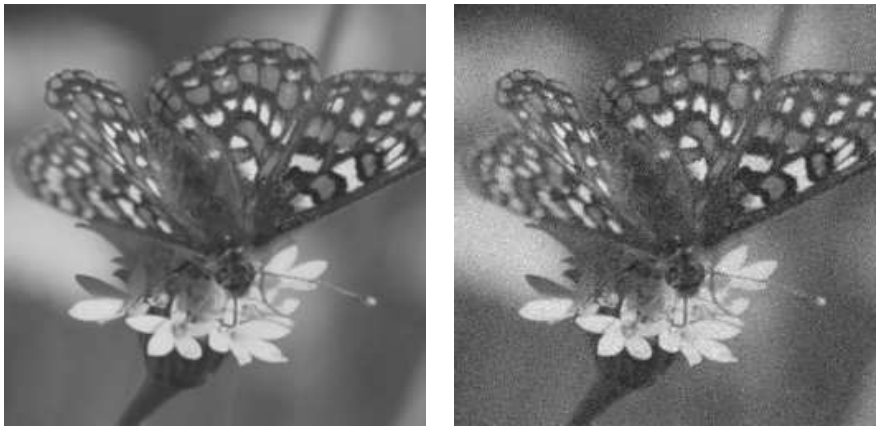

(a) Original (b) Noisy

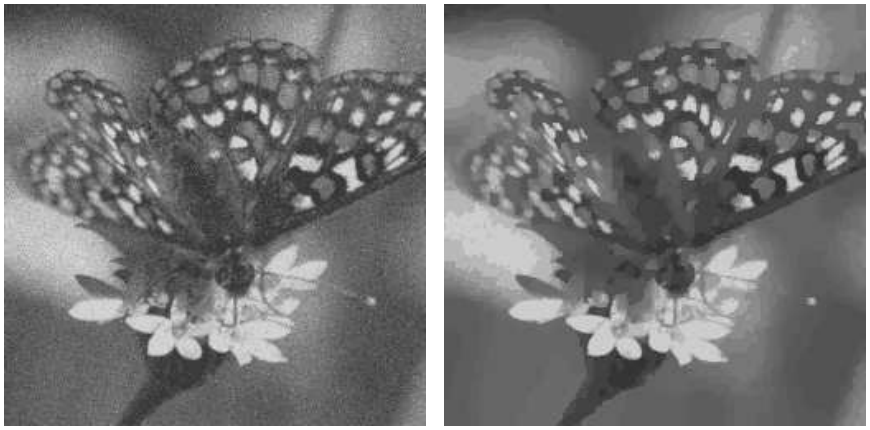

(c) LM result (d) Ours result

Figure 2.5: *Quantization in the presence of noise (grey scale image)*

was added to the image presented in Fig. 2.6(a) (source: photo by Neon JA, colored by Richard Bartz / Wikimedia Commons). This image was transformed from the RGB space into a more appropriate one, using the linear transformation defined by the matrix of its PCA (Principal Component Analysis) components. Then, the total order of quantization levels along the principal component is chosen, which corresponds to $\eta^\top = \begin{bmatrix} 1 & 0 & 0 \end{bmatrix}$. The convex set C is defined by (2.31). Since the probability of merging codevectors is negligible in three-channel color space, the associated parameter δ was set to 0. The resulting image (see Fig. 2.6(f)) was obtained by minimizing energy (2.20), which was initialized with decision levels computed by the median cut method. Function Φ was defined by (2.6) and ρ by (2.25) where ψ is identity and μ is equal to 250. The algorithm described in Section 2.5.1 was used for computing $i_{\mathcal{P}}^{(\ell)}$. One can observe that the noise has been highly reduced in our result (Fig. 2.6(f)), while the K-means method (Fig. 2.6(d))

preserved noise in the images. This is also verified by SNR values which is equal to 13.8 dB for our method and 10.6 dB, 10.4 dB and 9.8 dB for the K-means, Wu and median-cut, respectively. The difference is even greater in terms of entropy: our method led to 0.79 bpp and the other ones to 1.48 bpp. Additionally, the quantization result for the original image is presented. Our result (Fig. 2.6(e)) was obtain with the same algorithm settings as described above except μ, which here is equal to 30 and of course the PCA parameters, which were computed from the original image. Our method performs the required quantization and provides an interesting tradeoff between precision and smoothness, which is validated with an SNR of 18.5 dB and an entropy of 0.9 bpp. In contrast, K-means (Fig. 2.6(c)) achieved a SNR = 20.2 dB and an entropy = 1.1 bpp.

2.6.3 Note about computation time

The time complexity of Algorithm 2 is equal to the product of the complexity of each iteration and the complexity of the number of iterations ℓ. The bound on ℓ is not known a priori. Our observation suggests that it is a function of the weight of smoothness term μ, number of quantization levels Q, and the spatial entropy of original image f. Moreover, there may be small differences in the number of iterations, depending on the choice of the combinatorial optimization method. For instance, the first problem described in Section 2.6.1, which was solved with an Ishikawa-like graph, converges in 18 iterations. In contrast, using the α-expansion algorithm (Algorithm 4), it converges in only 16. In practice the number of iterations never seems to exceed 50 for grey-scale and 200 for color images. By analyzing the inner loop of Algorithm 2, one can observe that the complexity of step 1 is greater than the one of step 2. Thus, the computation time of each iteration is strongly dominated by the cost of step 1, namely finding $i_{\mathcal{P}}^{(\ell)}$. Note that Algorithm 3 is run only if matrix $\boldsymbol{r}$ derived from a centroid rule does not belong to C, so usually its influence on the overall time complexity of Algorithm 2 is small for grey-scale images. It becomes more important for multi-channel images. Generally, the cost of combinatorial graph-cut based methods depends on $\mathrm{card}(\mathbb{X})$ and on the number of quantization levels Q. More precisely, the relabeling algorithm finds solution for single graphs in polynomial time $O((\mathrm{card}(\mathcal{V}))^3)$, where $\mathrm{card}(\mathcal{V})$ is equal to $Q \times \mathrm{card}(\mathbb{X})$ for the method described in Section 2.5.1 and to $\mathrm{card}(\mathbb{X})$ for the method described in Section 2.5.2. However, Algorithm 4 (in Section 2.5.2) requires solving many different graphs independently, so its computation cost increases linearly with the number of quantization levels Q. It is worth noting that some recently published extensions of the α-expansion algorithm are faster. In particular, Lipitsky *et al.* presented the LogCut and Fusion move methods that lead to nearly logarithmic growth [Lempitsky et al., 2010], e.g. for $Q = 256$ the algorithm converges approximately 10 times faster.

A similar acceleration was obtained by the FastPD algorithm introduced by Komodakis *et al.* [Komodakis et al., 2008] and analyzed by Kolmogorov in [Kolmogorov, 2007]. Likewise, recently introduced primal and primal-dual algorithms by Kolmogorov *et al.* in [Kolmogorov and Shioura, 2009] may be an alternative for the method described in Section 2.5.1. They offer a significant improvement in terms of time efficiency. For instance, our first problem described in Section 2.6.1 solved with the method described in Section 2.5.1 takes 37 seconds, while using Kolmogorov's primal only algorithm, it takes only 12 seconds. As an alternative to the methods presented in Section 2.5, one may adopt these novel methods. Constant progress in the efficiency of graph-cut algorithms makes our approach increasingly competitive with the ones that do not feature a smoothness constraint. Nonetheless, our method may take significantly more time than the use of basic quantization methods (for details see Table 2.2). The tests were performed single-threaded, on a computer with a 2.5GHz Intel Xeon processor, in the RedHat Enterprise Linux 5.5 environment, using the GCC compiler version 4.1 in 64-bit mode.

	Ex1	Ex2 [a]	Ex3	Ex4 [b]
No. of iter.	18	183 (113)	6	51 (42)
Time $[s]$	37	1618 (1015)	27	808 (625)

Table 2.2: *Iteration number and computation time*

[a] The values in and without brackets correspond to $\mu = 50$, and $\mu = 25$, respectively.
[b] The values in and without brackets concerns case without and with noise, respectively.

§ 2.7 Conclusion

In this chapter, we have proposed a new quantization method based on a two-step procedure combining a convex optimization algorithm for the selection of quantization levels, and a combinatorial regularization procedure. Unlike classical methods, the proposed approach allows us to enforce a tunable spatial regularity in the quantized image. We have also shown that both grey scale and color images can be processed. As shown by our simulation results, the proposed approach leads to promising results, in particular in the presence of noise. As future work, we plan to explore isotropic regularization methods, to adapt and implement faster combinatorial algorithms and to take advantage of this method in various applications such as image compression and multispectral/hyperspectral imaging. Moreover, since in the context of segmentation TV was shown to be outperformed by other regularization strategies [Hauser and Steidl, 2013], we plan to extend the list of considered priors, e.g. with Non Local TV.

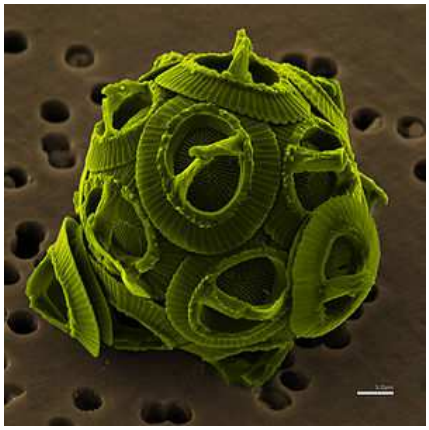

(a) Original

(b) Noisy

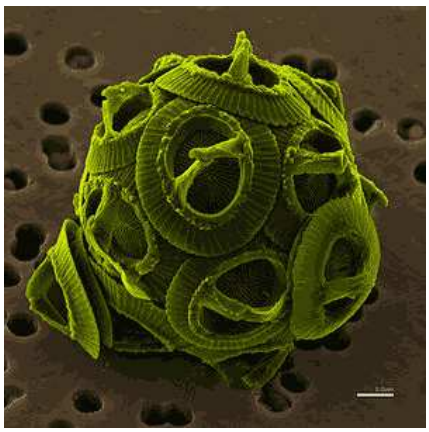

(c) K-means result for original image

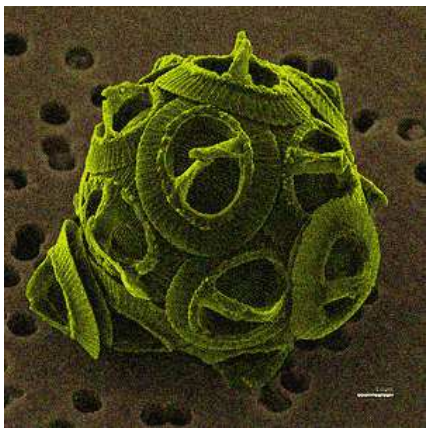

(d) K-means result for noisy image

(e) Ours result for original image

(f) Ours result for noisy image

Figure 2.6: *Quantization in the presence of noise (color image)*

- Chapter 3 -

Noise estimation from time series data

The problem of estimating the parameters of a Poisson-Gaussian model from experimental data has recently raised much interest in various applications, especially for CCD imaging systems. In this context, a field of independent random variables is observed, which is varying both in time and space. Each variable is a sum of two components, one following a Poisson and the other a Gaussian distribution. In this chapter[1], a general formulation is considered where the associated Poisson process is nonstationary in space and also exhibits an exponential decay in time, whereas the Gaussian component corresponds to a stationary white noise with arbitrary mean. To solve the considered parametric estimation problem, an iterative Expectation-Maximization (EM) approach is proposed. Much attention is paid to the initialization of the EM algorithm for which an adequate moment-based method using recent optimization tools is proposed. In addition, a performance analysis of the proposed approach is carried out by computing the Cramer-Rao bounds on the estimated variables. The performance of the proposed estimation procedure is illustrated on both synthetic data and real fluorescence microscopy image sequences. The algorithm is shown to provide reliable estimates of the mean/variance of the Gaussian noise and of the scale parameter of the Poisson component, as well as of its exponential decay rate.

§ 3.1 Introduction

Estimating the parameters of a probability distribution constitutes a fundamental task in many statistical signal processing problems. This estimation problem becomes more challenging when the observed data are distributed according to some mixture of given probability laws [Redner and Walker, 1984]. Most existing works are focused on Gaussian mixture models [Roberts

[1]Published in part in Proc. of EUSIPCO, 2011 and Proc. of ISBI, 2012

et al., 1998]. However, due to their importance in signal/image recovery problems, there has been recently a growing interest in Poisson-Gaussian probabilistic models. The Poisson component is often related to the quantum nature of light and accounts for photon-counting principles in signal registration, whereas the Gaussian component is typically related to thermal noise present in the electronic part of the imaging system. Despite constant improvements in data acquisition devices, electronic noise usually cannot be neglected. Among existing works dealing with Poisson-Gaussian noise, a number of methods have addressed noise identification problems [Healey and Kondepudy, 1994], [Starck and Murtagh, 1998], [Zhang, 2007], [Foi et al., 2008], [Boulanger et al., 2008], [Abramov et al., 2010], [Acito et al., 2011], as well as denoising [Delpretti et al., 2008], [Boulanger et al., 2008], [Foi, 2009a], [Bosco et al., 2010], [Luisier et al., 2011], [Begovic et al., 2011] and reconstruction [Snyder et al., 1993], [Lantéri and Theys, 2005], [Benvenuto et al., 2008], [Gil-Rodrigo et al., 2011], [Chakrabarti and Zickler, 2012], [Li et al., 2012], [Jezierska et al., 2012a]. The developed algorithms are useful in various areas such as digital photography [Foi et al., 2008], medicine [Nichols et al., 2002], biology [Pawley, 1994] and astronomy [Lantéri and Theys, 2005].

A brief overview of published works primarily directed towards the problem of parameter estimation of Poisson-Gaussian densities is useful. It reveals that most existing methods assume a zero-mean Gaussian noise component. Furthermore, they are usually grounded on some approximations based on variance stabilization techniques [Healey and Kondepudy, 1994], [Foi et al., 2008], [Boulanger et al., 2008], [Abramov et al., 2010], [Acito et al., 2011]. Only a few publications differ. Zhang, in [Zhang, 2007], proposes a cumulant-based approach. A method estimating solely the Gaussian component was also proposed in [Starck and Murtagh, 1998]. Although methods based on maximum likelihood are very popular in parametric estimation [Fessler and Hero, 1994], [Stein, 1994], they have not been extensively investigated in the context of Poisson-Gaussian distribution yet.

In the following, we propose a new framework dealing with Poisson-Gaussian noise parameter estimation from multidimensional time series. We first discuss the properties of the observation model. The versatility of the considered non-stationary model allows us to take into account an exponential decay of the intensity of the Poisson component. Analysis of time series including such an exponential decay covers a broad range of application areas, e.g. nuclear magnetic resonance (NMR) spectroscopy [Ernst et al., 1991], magnetic resonance imaging (MRI) [Hornak, 2008] and fluorescence imaging systems [Pawley, 2006, Chapter 2].

For mixed probability distributions, one must usually resort to some iterative estimation procedure. In the Poisson-Gaussian case, we propose to employ an Expectation-Maximization (EM) [Dempster et al., 1977] approach. In Chapter 1.3.1.1 we presented EM algorithm as a special case of

MM algorithmic framework. In this chapter we show that the development of our EM algorithm is nontrivial in the sense that it requires tackling some numerical problems. Also a sufficiently accurate initialization procedure is required. In this work, the initialization is performed through a Douglas-Rachford [Lions and Mercier, 1979], [Eckstein and Bertekas, 1992], [Combettes and Pesquet, 2007] method which aims at optimizing a moment-based estimate of the unknown parameters.

The chapter is organized as follows. We provide a description of the considered parameter estimation problem in Section 3.2. Then, we interpret it as an incomplete data problem and derive the associated EM algorithm in Section 3.3. The numerical issues raised by the implementation of the algorithm are investigated in Section 3.4 as well as the proposed moment-based initialization. In addition, in Section 3.5, we derive the Fisher Information matrix and the Cramer-Rao bounds for the estimation problem. Section 3.6 illustrates the algorithm performance on both synthetic data and real confocal image sequences. Finally, Section 3.7 concludes the chapter.

§ 3.2 Problem

Of interest here is a parametric model arising in the case of random variables modeled as a weighted sum of Poisson and Gaussian components. The problem is to estimate the vector of parameters θ characterizing the associated mixed continuous-discrete probability distribution from available observations $r = (r_{s,t})_{1\leq s\leq S, 1\leq t\leq T}$, which are realizations of a random field $R = (R_{s,t})_{1\leq s\leq S, 1\leq t\leq T}$. Here, s corresponds to a location index (e.g. locating pixel (x, y) in 2D or voxel (x, y, z) in 3D) and t is the time index.

More precisely, the considered stochastic model reads :

$$\forall (s,t) \in \mathbb{S} \qquad R_{s,t} = \alpha Q_{s,t} + W_{s,t} \tag{3.1}$$

where $\mathbb{S} = \{1, \ldots, S\} \times \{1, \ldots, T\}$, $\alpha \in (0, +\infty)$ is a scaling parameter, and, for every $(s,t) \in \mathbb{S}$, $Q_{s,t}$ is a random variable following a Poisson distribution, and $W_{s,t}$ is a normally distributed random variable, which are expressed as

$$Q_{s,t} \sim \mathcal{P}\big(v_{s,t}\big), \qquad W_{s,t} \sim \mathcal{N}(c, \sigma^2) \tag{3.2}$$

where $v = (v_{s,t})_{1\leq s\leq S, 1\leq t\leq T} \in [0, +\infty)^{ST}$ is the vector of intensities of the Poisson distribution and $c \in \mathbb{R}$ (resp. $\sigma > 0$) is the mean value (resp. standard-deviation) of the Gaussian distribution.

Our goal is to estimate the vector of unknown parameters (v, α, c, σ^2) under the following assumptions:

- $Q = (Q_{s,t})_{1\leq s\leq S, 1\leq t\leq T}$ and $W = (W_{s,t})_{1\leq s\leq S, 1\leq t\leq T}$ are mutually statistically independent;

- the components of Q (resp. W) are independent.

Note that some special instances of this model have been studied in the literature, in the case when, for example, $v_{s,t}$ is no longer depending on t, thus reducing to

$$\forall (s,t) \in \mathbb{S} \qquad v_{s,t} = u_s. \tag{3.3}$$

Most existing works [Foi et al., 2008], [Abramov et al., 2010], [Uss et al., 2011] assume that $c = 0$, whereas in [Jezierska et al., 2011a] we considered a Gaussian noise with non-zero mean. The motivation of these works was to identify noise parameters, the knowledge of which is required in many algorithms used for denoising [Luisier et al., 2011] or restoration [Benvenuto et al., 2008], [Gil-Rodrigo et al., 2011]. These parameters are usually not known in advance and their values may depend on experimental conditions, for instance in the case of imaging systems on camera settings, temperature, vibrations, ... Gaussian approximations [Foi et al., 2008], [Abramov et al., 2010] of the Poisson distribution are sometimes performed in the identification process, which often rely on the use of variance stabilization methods like the Anscombe transform [Anscombe, 1948] in the subsequent data recovery tasks [Delpretti et al., 2008].

Variable	Definition
s	location index, $1 \leq s \leq S$
t	time index, $1 \leq t \leq T$
$r = (r_{s,t})_{1 \leq s \leq S, 1 \leq t \leq T}$	observed signal in $\mathbb{R}^{ST}$
$R_{s,t}$	random variable following a Poisson-Gaussian distrib.
$q = (q_{s,t})_{1 \leq s \leq S, 1 \leq t \leq T}$	the numbers of occurrences in $\mathbb{N}^{ST}$
$Q_{s,t}$	random variable following a Poisson distrib.
$\alpha > 0$	scaling parameter
$v = (v_{s,t})_{1 \leq s \leq S, 1 \leq t \leq T}$	mean values in $(\mathbb{R}_+)^{ST}$ of the Poisson distrib.
$u = (u_s)_{1 \leq s \leq S} \in (\mathbb{R}_+^*)^S$	initial values of the exponential change rate
$k = (k_s)_{1 \leq s \leq S} \in (\mathbb{R}_+^*)^S$	Poisson distrib. decay rates
$x = (x_s)_{1 \leq s \leq S} \in (\mathbb{R}_+^*)^S$	Poisson distrib. exponential decays $x_s = e^{-k_s}$
$a = (a_s)_{1 \leq s \leq S} \in (\mathbb{R}_+^*)^S$	mean values of Poisson distrib. for $t = 1$, $a_s = u_s x_s$
$W_{s,t}$	normally distributed random noise variable
$c \in \mathbb{R}$	mean value of the Gaussian distribution
$\sigma > 0$	standard-deviation of the Gaussian distribution
$\theta = [u^\top, k^\top, \alpha, c, \sigma^2]^\top$	vector of unknown parameters

Table 3.1: *Notations of Chapter 3*

In this chapter, we consider a more challenging case than (3.3), when

$$\forall (s,t) \in \mathbb{S} \qquad v_{s,t} = u_s e^{-k_s t} \tag{3.4}$$

with $u = (u_s)_{1\leq s\leq S} \in (0,+\infty)^S$ and $k = (k_s)_{1\leq s\leq S} \in (0,+\infty)^S$. In this case, the $2S+3$-dimensional vector of unknown noise parameters becomes $\theta = [u^\top, k^\top, \alpha, c, \sigma^2]^\top$ where $(\cdot)^\top$ denotes the transpose operator. Some results concerning time series data decaying exponentially in time in the presence of additive noise can be found in [Lawunmi, 1997], [Lawunmi, 2004] but they cannot deal with the considered Poisson model. The notations used in the chapter are summarized in Table 3.1.

§ 3.3 EM APPROACH

Under the considered statistical assumptions, for every $s \in \{1,\ldots,S\}$ and $t \in \{1,\ldots,T\}$, the mixed continuous-discrete distribution of $(R_{s,t}, Q_{s,t})$ is obtained by applying Bayes rule:

$$\begin{aligned}(\forall r_{s,t}\in\mathbb{R})(\forall q_{s,t}\in\mathbb{N}) \quad & p_{R_{s,t},Q_{s,t}}(r_{s,t},q_{s,t}\mid\theta)\\ =& f_{R_{s,t}|Q_{s,t}=q_{s,t}}(r_{s,t}\mid\alpha,c,\sigma)\mathsf{P}(Q_{s,t}=q_{s,t}\mid u_s,k_s)\\ =& f_{W_{s,t}}(r_{s,t}-\alpha q_{s,t}\mid c,\sigma)\mathsf{P}(Q_{s,t}=q_{s,t}\mid u_s,k_s)\\ =& \frac{\exp\left(-\frac{(r_{s,t}-\alpha q_{s,t}-c)^2}{2\sigma^2}\right)}{\sqrt{2\pi}\sigma}\frac{(u_s e^{-k_s t})^{q_{s,t}}}{q_{s,t}!}\exp(-u_s e^{-k_s t}),\end{aligned} \tag{3.5}$$

where $f_{R_{s,t}|Q_{s,t}=q_{s,t}}(\cdot\mid\alpha,c,\sigma)$ is the conditional probability density function (pdf) of $R_{s,t}$ knowing that $Q_{s,t}=q_{s,t}$ and $f_{W_{s,t}}(\cdot\mid c,\sigma)$ is the pdf of $W_{s,t}$. Using the spatial and time independence properties, the associated likelihood takes the following intricate form:

$$\begin{aligned}&\left(\forall r=(r_{s,t})_{1\leq s\leq S,1\leq t\leq T}\in\mathbb{R}^{ST}\right)\\ &\qquad f_R(r\mid\theta)=\prod_{s=1}^{S}\prod_{t=1}^{T}\sum_{q_{s,t}=1}^{+\infty}p_{R_{s,t},Q_{s,t}}(r_{s,t},q_{s,t}\mid\theta).\end{aligned} \tag{3.6}$$

Deriving the maximum likelihood estimate of the unknown parameter vector θ from this expression appears to be analytically intractable. To circumvent this difficulty, we propose to resort to an EM approach. Then, R is viewed as an incomplete random vector and the chosen completed vector is $[R^\top, Q^\top]^\top$. This formulation allows us to estimate θ by using the following EM iterations:

$$(\forall n\in\mathbb{N}) \qquad \theta^{(n+1)} = \underset{\theta}{\operatorname{argmax}}\ J(\theta\mid\theta^{(n)}) \tag{3.7}$$

where

$$J(\theta\mid\theta^{(n)}) = \mathsf{E}_{Q|R=r,\theta^{(n)}}[\ln p_{R,Q}(R,Q\mid\theta)] \tag{3.8}$$

and

$$\big(\forall r = (r_{s,t})_{1\le s\le S, 1\le t\le T} \in \mathbb{R}^{ST}\big) \quad \big(\forall q = (q_{s,t})_{1\le s\le S, 1\le t\le T} \in \mathbb{N}^{ST}\big)$$
$$p_{R,Q}(r, q \mid \theta) = \prod_{s=1}^{S}\prod_{t=1}^{T} p_{R_{s,t},Q_{s,t}}(r_{s,t}, q_{s,t} \mid \theta) \quad (3.9)$$

is the mixed continuous-discrete probability distribution of (R, Q). The complete data log-likelihood can now be rewritten as:

$$\begin{aligned}\ln p_{R,Q}(R, Q \mid \theta) = &-\frac{1}{2\sigma^2}\sum_{s=1}^{S}\sum_{t=1}^{T}(R_{s,t} - \alpha Q_{s,t} - c)^2 \\ &- \frac{ST}{2}\ln(2\pi\sigma^2) - \sum_{s=1}^{S} u_s e^{-k_s}\frac{1 - e^{-Tk_s}}{1 - e^{-k_s}} \\ &+ \sum_{s=1}^{S}\ln u_s \sum_{t=1}^{T} Q_{s,t} - \sum_{s=1}^{S} k_s \sum_{t=1}^{T} tQ_{s,t} - \sum_{s=1}^{S}\sum_{t=1}^{T}\ln(Q_{s,t}!). \quad (3.10)\end{aligned}$$

By dropping the terms that are independent of θ and via a change of sign, we see that the EM algorithm reduces to:

$$(\forall n \in \mathbb{N}) \qquad \theta^{(n+1)} = \operatorname*{argmin}_{\theta} \ \widetilde{J}(\theta \mid \theta^{(n)}) \quad (3.11)$$

where

$$\begin{aligned}\widetilde{J}(\theta \mid \theta^{(n)}) = &\frac{1}{2\sigma^2}\sum_{s=1}^{S}\sum_{t=1}^{T}\mathsf{E}_{Q|R=r,\theta^{(n)}}[(r_{s,t} - \alpha Q_{s,t} - c)^2] \\ &+ \sum_{s=1}^{S} k_s \sum_{t=1}^{T} t\mathsf{E}_{Q|R=r,\theta^{(n)}}[Q_{s,t}] + \sum_{s=1}^{S} u_s e^{-k_s}\frac{1 - e^{-Tk_s}}{1 - e^{-k_s}} \\ &- \sum_{s=1}^{S}\ln u_s \sum_{t=1}^{T}\mathsf{E}_{Q|R=r,\theta^{(n)}}[Q_{s,t}] + ST\ln\sigma. \quad (3.12)\end{aligned}$$

The EM algorithm alternates between expectation and maximization steps, guaranteeing that the likelihood is increased at each iteration [Dempster et al., 1977], [Fessler and Hero, 1995].

The update rules are found by differentiating (3.12). The obtained relations lead us to the following operations to be performed at iteration n:

1. For every $s \in \{1, \dots, S\}$, find $k_s^{(n+1)}$ satisfying:

$$\begin{aligned}&\frac{1 + Te^{-(T+1)k_s^{(n+1)}} - (T+1)e^{-Tk_s^{(n+1)}}}{(1 - e^{-k_s^{(n+1)}T})(1 - e^{-k_s^{(n+1)}})}\sum_{t=1}^{T}\mathsf{E}_{Q|R=r,\theta^{(n)}}[Q_{s,t}] \\ &\qquad = \sum_{t=1}^{T} t\mathsf{E}_{Q|R=r,\theta^{(n)}}[Q_{s,t}]. \quad (3.13)\end{aligned}$$

2. For every $s \in \{1, \dots, S\}$ compute

$$u_s^{(n+1)} = \frac{1 - e^{-k_s^{(n+1)}}}{e^{-k_s^{(n+1)}}(1 - e^{-Tk_s^{(n+1)}})} \sum_{t=1}^{T} \mathsf{E}_{Q|R=r,\theta^{(n)}}[Q_{s,t}]. \tag{3.14}$$

3. Determine $c^{(n+1)}$ and $\alpha^{(n+1)}$ by solving the following system of linear equations:

$$\begin{bmatrix} ST & \sum_{(s,t)\in\mathbb{S}} \mathsf{E}_{Q|R=r,\theta^{(n)}}[Q_{s,t}] \\ \sum_{(s,t)\in\mathbb{S}} \mathsf{E}_{Q|R=r,\theta^{(n)}}[Q_{s,t}] & \sum_{(s,t)\in\mathbb{S}} \mathsf{E}_{Q|R=r,\theta^{(n}}[Q_{s,t}^2] \end{bmatrix} \begin{bmatrix} c^{(n+1)} \\ \alpha^{(n+1)} \end{bmatrix}$$
$$= \begin{bmatrix} \sum_{(s,t)\in\mathbb{S}} r_{s,t} \\ \sum_{(s,t)\in\mathbb{S}} r_{s,t} \mathsf{E}_{Q|R=r,\theta^{(n)}}[Q_{s,t}] \end{bmatrix}. \tag{3.15}$$

4. Set $(\sigma^2)^{(n+1)}$ to

$$\frac{1}{ST} \sum_{(s,t)\in\mathbb{S}} \mathsf{E}_{Q|R=r,\theta^{(n)}}[(r_{s,t} - \alpha^{(n+1)} Q_{s,t} - c^{(n+1)})^2] =$$
$$\frac{1}{ST} \sum_{(s,t)\in\mathbb{S}} r_{s,t} \left(r_{s,t} - \alpha^{(n+1)} \mathsf{E}_{Q|R=r,\theta^{(n)}}[Q_{s,t}] - c^{(n+1)} \right). \tag{3.16}$$

As discussed in the next section, the procedure however raises a number of numerical issues which need to be carefully addressed.

§ 3.4 Implementation issues of the EM algorithm

3.4.1 Computation of the required conditional means

According to (3.12), the expectation step requires to compute the conditional expectations $\mathsf{E}_{Q_{s,t}|R_{s,t}=r_{s,t},\theta}[Q_{s,t}]$ and $\mathsf{E}_{Q_{s,t}|R_{s,t}=r_{s,t},\theta}[Q_{s,t}^2]$, for every $(s,t) \in \mathbb{S}$. These are expressed as follows

$$\mathsf{E}_{Q_{s,t}|R_{s,t}=r_{s,t},\theta}[Q_{s,t}] = \sum_{q_{s,t}=1}^{+\infty} q_{s,t} \mathsf{P}(Q_{s,t} = q_{s,t} \mid R = r, \theta^{(n)}) \tag{3.17}$$

$$\mathsf{E}_{Q_{s,t}|R_{s,t}=r_{s,t},\theta}[Q_{s,t}^2] = \sum_{q_{s,t}=1}^{+\infty} q_{s,t}^2 \mathsf{P}(Q_{s,t} = q_{s,t} \mid R = r, \theta^{(n)}) \tag{3.18}$$

where, for every $q_{s,t} \in \mathbb{N}$,

$$\mathsf{P}(Q_{s,t} = q_{s,t} \mid R = r, \theta) = \frac{p_{R_{s,t},Q_{s,t}}(r_{s,t}, q_{s,t} \mid \theta)}{f_{R_{s,t}}(r_{s,t} \mid \theta)}, \tag{3.19}$$

$p_{R_{s,t},Q_{s,t}}(\cdot,\cdot \mid \theta)$ is given by (3.5) and

$$(\forall r_{s,t} \in \mathbb{R}) \qquad f_{R_{s,t}}(r_{s,t} \mid \theta) = \sum_{q_{s,t}=0}^{+\infty} p_{R_{s,t},Q_{s,t}}(r_{s,t}, q_{s,t} \mid \theta). \tag{3.20}$$

Hence, one can reexpress (3.17) and (3.18) as

$$\mathsf{E}_{Q_{s,t}|R_{s,t}=r_{s,t},\theta}[Q_{s,t}] = \frac{\zeta_{s,t}(\theta)}{\eta_{s,t}(\theta)} \tag{3.21}$$

$$\mathsf{E}_{Q_{s,t}|R_{s,t}=r_{s,t},\theta}[Q_{s,t}^2] = \frac{\xi_{s,t}(\theta)}{\eta_{s,t}(\theta)} \tag{3.22}$$

where

$$\zeta_{s,t}(\theta) = \sum_{q_{s,t}=0}^{+\infty} \Pi_{s,t}(\theta, 1, q_{s,t}) \tag{3.23}$$

$$\eta_{s,t}(\theta) = \sum_{q_{s,t}=0}^{+\infty} \Pi_{s,t}(\theta, 0, q_{s,t}) \tag{3.24}$$

$$\xi_{s,t}(\theta) = \sum_{q_{s,t}=0}^{+\infty} \Pi_{s,t}(\theta, 1, q_{s,t}) + \sum_{q_{s,t}=0}^{+\infty} \Pi_{s,t}(\theta, 2, q_{s,t}) \tag{3.25}$$

and, for every $(d, q_{s,t}) \in \mathbb{N}^2$,

$$\Pi_{s,t}(\theta, d, q_{s,t}) \;=\; \exp\left(-\frac{(r_{s,t} - \alpha(q_{s,t} + d) - c)^2}{2\sigma^2}\right) \frac{(u_s e^{-k_s t})^{q_{s,t}+d}}{q_{s,t}!}. \tag{3.26}$$

The computation of a ratio of two infinite sums is not always an easy task when these sums do not have closed form expressions. Next a method allowing us to get a reliable approximation of the series given by (3.23), (3.24) and (3.25) while simultaneously limiting the required computational time is described.

Let $(s,t) \in \mathbb{S}$ and let $d \in \mathbb{N}$. The presented here results are based on the following upper bound for function $\Pi_{s,t}$ obtained through Stirling's formula:

$$\left(\forall q_{s,t} \in \mathbb{N}^*\right) \qquad \Pi_{s,t}(\theta, d, q_{s,t}) \leq \widehat{\Pi}_{s,t}(\theta, d, q_{s,t}) \tag{3.27}$$

where $(\forall \tau \in (0, +\infty))$

$$\widehat{\Pi}_{s,t}(\theta, d, \tau) = \exp\left(-\frac{(r_{s,t} - \alpha(\tau + d) - c)^2}{2\sigma^2}\right) \frac{(u_s e^{-k_s t})^{\tau+d}}{\sqrt{2\pi}\tau^{\tau} e^{-\tau}}. \tag{3.28}$$

Lemma 3.4.1 *Function $\widehat{\Pi}_{s,t}(\theta, d, \cdot)$ has a unique maximizer*

$$q^*_{s,t} = \frac{\sigma^2}{\alpha^2} \mathsf{W}\left(\frac{\alpha^2}{\sigma^2} u_s e^{\frac{\alpha}{\sigma^2}(r_{s,t}-c-d\alpha)-tk_s}\right) \tag{3.29}$$

where W *denotes the Lambert* W *function. In addition,* $\left(\forall q_{s,t} \in \mathbb{N}^*\right)$

$$\Pi_{s,t}(\theta, d, q_{s,t}) \leq \widehat{\Pi}_{s,t}(\theta, d, q^*_{s,t}) \exp\left(-\frac{\alpha^2}{2\sigma^2}\left(q_{s,t} - q^*_{s,t}\right)^2\right). \tag{3.30}$$

Proof. For every $\tau \in (0, +\infty)$, we have

$$\begin{aligned}\ln\left(\widehat{\Pi}_{s,t}(\theta, d, \tau)\right) = &-\frac{(r_{s,t} - \alpha(\tau + d) - c)^2}{2\sigma^2} - tk_s(\tau + d) \\ &+ (\tau + d)\ln u_s - \tau \ln \tau + \tau - \frac{1}{2}\ln(2\pi).\end{aligned} \tag{3.31}$$

This allows us to deduce that

$$\frac{\partial\left(\ln \widehat{\Pi}_{s,t}(\theta, d, \tau)\right)}{\partial \tau} = -\ln \tau - \frac{\alpha^2}{\sigma^2}\tau + \ln u_s + \frac{\alpha}{\sigma^2}(r_{s,t} - c - \alpha d) - tk_s.$$

Hence, any extremum value $q^*_{s,t}$ of $\widehat{\Pi}_{s,t}(\theta, d, \cdot)$ must satisfy the following equation:

$$\ln q^*_{s,t} + \frac{\alpha^2}{\sigma^2} q^*_{s,t} - \ln u_s - \frac{\alpha}{\sigma^2}(r_{s,t} - c - \alpha d) + tk_s = 0. \tag{3.32}$$

There exists a unique solution to this equation which is given by (3.29) [Cranmer, 2004]. It is easy to check from (3.32) that

$$\frac{\partial\left(\ln \widehat{\Pi}_{s,t}(\theta, d, \tau)\right)}{\partial \tau} > 0 \Leftrightarrow \tau < q^*_{s,t} \tag{3.33}$$

so that $q^*_{s,t}$ is the unique maximizer of $\widehat{\Pi}_{s,t}(\theta, d, \cdot)$. In addition, we derive from (3.32) that

$$\begin{aligned}&\ln\left(\widehat{\Pi}_{s,t}(\theta, d, \tau)\right) - \ln\left(\widehat{\Pi}_{s,t}(\theta, d, q^*_{s,t})\right) \\ &= -\frac{\alpha^2}{2\sigma^2}\left(\tau^2 - (q^*_{s,t})^2\right) - \tau \ln \tau + q^*_{s,t} \ln q^*_{s,t} \\ &\qquad + (\tau - q^*_{s,t})\left(\ln u_s + \frac{\alpha}{\sigma^2}(r_{s,t} - c - \alpha d) - tk_s + 1\right) \\ &= -\frac{\alpha^2}{2\sigma^2}\left(\tau^2 - (q^*_{s,t})^2\right) - \tau \ln \tau + q^*_{s,t} \ln q^*_{s,t} + (\tau - q^*_{s,t})\left(\ln q^*_{s,t} + \frac{\alpha^2}{\sigma^2} q^*_{s,t} + 1\right) \\ &= -\frac{\alpha^2}{2\sigma^2}\left(\tau - q^*_{s,t}\right)^2 + \tau(\ln q^*_{s,t} - \ln \tau) + \tau - q^*_{s,t}.\end{aligned} \tag{3.34}$$

By using now the concavity of the logarithm function, we get

$$\ln q^*_{s,t} - \ln \tau \leq \frac{1}{\tau}(q^*_{s,t} - \tau). \tag{3.35}$$

Altogether (3.27), (3.34) and (3.35) yield (3.30). □

As illustrated by Fig. 3.1, the value $q^*_{s,t}$ corresponding to the maximum of function $\widehat{\Pi}_{s,t}(\theta, d, \cdot)$ is a close approximation to the maximizer of function $\Pi_{s,t}(\theta, d, \cdot)$. We show next that the above lemma is useful to derive finite

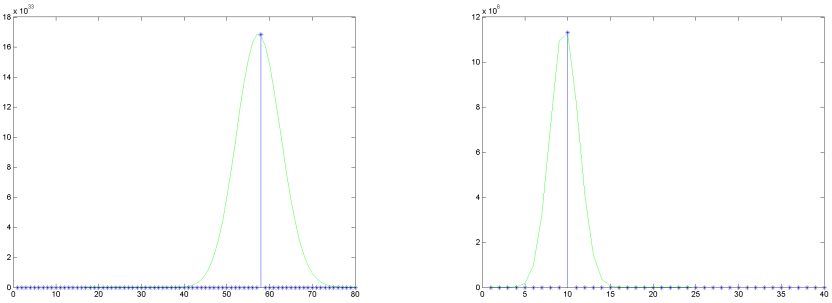

(a) $\alpha = 1$, $c = 0$, $\sigma^2 = 50$, $u_s = 100$ (b) $\alpha = 9$, $c = 0$, $\sigma^2 = 300$, $u_s = 30$

Maximum value $q^*_{s,t}$ is marked in blue while function $\Pi_{s,t}(\theta, 0, q_{s,t})$ as a function of $q_{s,t}$ for $r_{s,t} = 50$ in green.

Figure 3.1: *The value $q^*_{s,t}$ as an approximation to the maximizer of function $\Pi_{s,t}(\theta, d, \cdot)$.*

sum approximations to the series in (3.23), (3.24) and (3.25).

Proposition 3.4.2 *Let $\Delta > 0$ and set*

$$q^-_{s,t} = \lfloor q^*_{s,t} - \Delta\frac{\sigma}{\alpha} \rfloor, \quad q^+_{s,t} = \lceil q^*_{s,t} + \Delta\frac{\sigma}{\alpha} \rceil \tag{3.36}$$

where $q^*_{s,t}$ is given by (3.29) and $\lfloor\cdot\rfloor$ (resp. $\lceil\cdot\rceil$) denotes the lower (resp. upper) rounding operation. Then, $\sum_{q_{s,t}=\max(1,q^-_{s,t})}^{q^+_{s,t}} \Pi_{s,t}(\theta, d, q_{s,t})$ constitutes a lower approximation to $\sum_{q_{s,t}=1}^{+\infty} \Pi_{s,t}(\theta, d, q_{s,t})$ with maximum error value

$$\sqrt{2\pi}\frac{\sigma}{\alpha}\widehat{\Pi}_{s,t}(\theta, d, q^*_{s,t}) \left(1 - \operatorname{erf}\left(\frac{\Delta}{\sqrt{2}}\right)\right).$$

Proof. For every $q_{s,t} \in \mathbb{N}$ such that $q_{s,t} \geq q^*_{s,t}$ and, for every $\tau \in \mathbb{R}$ such that $q_{s,t} \leq \tau \leq q_{s,t} + 1$, we have

$$\exp\left(-\frac{\alpha^2}{2\sigma^2}(q_{s,t} + 1 - q^*_{s,t})^2\right) \leq \exp\left(-\frac{\alpha^2}{2\sigma^2}(\tau - q^*_{s,t})^2\right). \tag{3.37}$$

This allows us to deduce that

$$\sum_{q_{s,t}=q_{s,t}^{+}+1}^{+\infty} \exp\left(-\frac{\alpha^2}{2\sigma^2}(q_{s,t}-q_{s,t}^{*})^2\right)$$
$$\leq \int_{q_{s,t}^{+}}^{+\infty} \exp\left(-\frac{\alpha^2}{2\sigma^2}(\tau-q_{s,t}^{*})^2\right) d\tau \leq \int_{q_{s,t}^{*}+\Delta\frac{\sigma}{\alpha}}^{+\infty} \exp\left(-\frac{\alpha^2}{2\sigma^2}(\tau-q_{s,t}^{*})^2\right) d\tau$$
$$= \sqrt{2\pi}\frac{\sigma}{2\alpha}\left(1-\operatorname{erf}\left(\frac{\Delta}{\sqrt{2}}\right)\right) \tag{3.38}$$

where erf is the error function. Similarly, for every $q_{s,t} \in \mathbb{N}$ such that $q_{s,t} \leq q_{s,t}^{*} - 1$ and, for every $\tau \in \mathbb{R}$ such that $q_{s,t} \leq \tau \leq q_{s,t} + 1$, we get

$$\exp\left(-\frac{\alpha^2}{2\sigma^2}(q_{s,t}-q_{s,t}^{*})^2\right) \leq \exp\left(-\frac{\alpha^2}{2\sigma^2}(\tau-q_{s,t}^{*})^2\right), \tag{3.39}$$

which, by assuming that $q_{s,t}^{-} \geq 2$, yields

$$\sum_{q_{s,t}=1}^{q_{s,t}^{-}-1} \exp\left(-\frac{\alpha^2}{2\sigma^2}(q_{s,t}-q_{s,t}^{*})^2\right)$$
$$\leq \int_{1}^{q_{s,t}^{-}} \exp\left(-\frac{\alpha^2}{2\sigma^2}(\tau-q_{s,t}^{*})^2\right) d\tau \leq \int_{-\infty}^{q_{s,t}^{*}-\Delta\frac{\sigma}{\alpha}} \exp\left(-\frac{\alpha^2}{2\sigma^2}(\tau-q_{s,t}^{*})^2\right) d\tau$$
$$= \sqrt{2\pi}\frac{\sigma}{2\alpha}\left(1-\operatorname{erf}\left(\frac{\Delta}{\sqrt{2}}\right)\right). \tag{3.40}$$

By using now (3.30), (3.38) and (3.40), it can be concluded that

$$0 \leq \sum_{q_{s,t}=1}^{+\infty} \Pi_{s,t}(\theta,d,q_{s,t}) - \sum_{q_{s,t}=\max(1,q_{s,t}^{-})}^{q_{s,t}^{+}} \Pi_{s,t}(\theta,d,q_{s,t})$$
$$\leq \widehat{\Pi}_{s,t}(\theta,d,q_{s,t}^{*}) \left(\sum_{q_{s,t}=1}^{\max(q_{s,t}^{-}-1,0)} e^{-\frac{\alpha^2}{2\sigma^2}(q_{s,t}-q_{s,t}^{*})^2} \sum_{q_{s,t}=q_{s,t}^{+}+1}^{+\infty} e^{-\frac{\alpha^2}{2\sigma^2}(q_{s,t}-q_{s,t}^{*})^2} \right)$$
$$\leq \sqrt{2\pi}\frac{\sigma}{\alpha}\widehat{\Pi}_{s,t}(\theta,d,q_{s,t}^{*}) \left(1-\operatorname{erf}\left(\frac{\Delta}{\sqrt{2}}\right)\right). \tag{3.41}$$

□

Note that, when $\Delta = 5$, $\sqrt{2\pi}\left(1-\operatorname{erf}\left(\frac{\Delta}{\sqrt{2}}\right)\right) \simeq 1.44 \times 10^{-6}$.

Fig. 3.2 indicates that the bounds proposed in Proposition 3.4.2 given by $q_{st}^{-} = \max(0, \lfloor q_{s,t}^{*} - \Delta\frac{\sigma}{\alpha} \rfloor)$ and $q_{st}^{+} = \lceil q_{s,t}^{*} + \Delta\frac{\sigma}{\alpha} \rceil$, where $\Delta > 0$ and $q_{s,t}^{*} = \frac{\sigma^2}{\alpha^2}\mathsf{W}\left(\frac{\alpha^2}{\sigma^2}u_s e^{\frac{\alpha}{\sigma^2}(r_{s,t}-c-d\alpha)-tk_s}\right)$, are sufficiently precise in practice. We

compare them with the summation bounds proposed in [Lantéri and Theys, 2005], [Benvenuto et al., 2008] given by $q_{st}^- = 0$ and $q_{st}^+ = r_{s,t} + 4\sigma$. Those bounds are not guaranteed to include all the significant coefficients (see Fig. 3.2(a)) or to be very effective (see Fig. 3.2(b)), unlike the ones we propose.

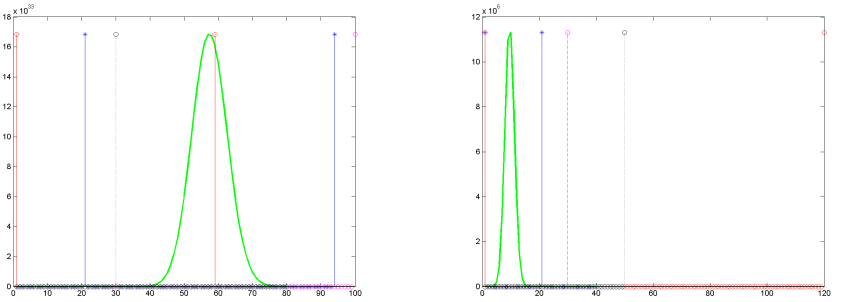

(a) $\alpha = 1$, $c = 0$, $\sigma^2 = 50$, $u_s = 100$ (b) $\alpha = 9$, $c = 0$, $\sigma^2 = 300$, $u_s = 30$

Function $\Pi_{s,t}(\theta, 0, q_{s,t})$ as a function of $q_{s,t}$ for $r_{s,t} = 50$ is marked in green, the proposed summation bounds for $\Delta = 5$ are marked in blue and the one proposed in [Benvenuto et al., 2008] in red. The black dotted line indicates $r_{s,t}$ while the pink dotted one indicates u_s.

Figure 3.2: *Infinite summation bounds.*

3.4.2 Estimation of the exponential decay rates

In the previous developments, a difficulty also arises in solving the update equation (3.13). A useful result is the following one:

Proposition 3.4.3 *For every $n \in \mathbb{N}$, $s \in \{1, \dots, S\}$ and $x \in \mathbb{R}$, let*

$$g_{n,s}(x) = \sum_{\beta=0}^{T-1} x^\beta \left((\beta+1) \sum_{t=1}^{T} \mathsf{E}_{Q|R=r,\theta^{(n)}}[Q_{s,t}] - \sum_{t=1}^{T} t \mathsf{E}_{Q|R=r,\theta^{(n)}}[Q_{s,t}] \right). \quad (3.42)$$

Then, $e^{-k_s^{(n+1)}}$ is the unique positive real root $x_{n,s}^*$ of polynomial $g_{n,s}$.

Proof. Simplifying the double root at 1 in the numerator of (3.13), we see that $e^{-k_s^{(n+1)}}$ is a root $x_{n,s}^*$ in $(0,1)$ of polynomial $g_{n,s}$. We now show that $x_{n,s}^*$ is the unique positive root of this polynomial.

For every $\beta \in \{0, \dots, T-1\}$, let $b_{n,s}^{(\beta)}$ denote the coefficient of the term of degree β in $g_{n,s}$. According to (3.42) we have:

- $b_{n,s}^{(0)} = \sum_{t=1}^{T}(1-t)\mathsf{E}_{Q|R=r,\theta(n)}[Q_{s,t}] < 0$ (Due to (3.21), (3.23) and (3.26), for every $(s,t) \in \mathbb{S}$, $u_s > 0 \Rightarrow \mathsf{E}_{Q|R=r,\theta(n)}[Q_{s,t}] > 0$.)
- $\forall \beta \in \{1,\dots,T-2\}$, $b_{n,s}^{(\beta)} = b_{n,s}^{(\beta-1)} + \sum_{t=1}^{T} \mathsf{E}_{Q|R=r,\theta^{(n)}}[Q_{s,t}]$
- $b_{n,s}^{(T-1)} = \sum_{t=1}^{T}(T-t)\mathsf{E}_{Q|R=r,\theta^{(n)}}[Q_{s,t}] > 0.$

Since the sequence $(b_{n,s}^{(\beta)})_{0\leq\beta\leq T-1}$ is an increasing arithmetic sequence, the number of sign differences between consecutive nonzero coefficients is at most 1. Moreover, since $b_{n,s}^{(T-1)} > 0$, we can conclude using Descartes' rule of signs that the maximum number of positive roots of $g_{n,s}$ is equal to 1. As $g_{n,s}^{(0)} < 0$ and $\lim_{x\to+\infty} g_{n,s}(x) = +\infty$, it can be deduced that there exists a unique positive root of $g_{n,s}$. □

In practice, we propose to compute $k_s^{(n+1)}$ by using Halley's iterative procedure [Gander, 1985]. The iterations are given by Algorithm 5, where $g'_{n,s}$ (resp. $g''_{n,s}$) denotes the first (resp. second) derivative of $g_{n,s}$.

Algorithm 5 Halley's algorithm for computing $k_s^{(n+1)}$

Init : $x_{n,s}^{(0)} = e^{-k_s^{(n)}}$
For $m = 0,\dots,M-1$

$$x_{n,s}^{(m+1)} = x_{n,s}^{(m)} - \frac{2g_{n,s}(x_{n,s}^{(m)})g'_{n,s}(x_{n,s}^{(m)})}{2(g'_{n,s}(x_{n,s}^{(m)}))^2 - g_{n,s}(x_{n,s}^{(m)})g''_{n,s}(x_{n,s}^{(m)})}$$

$k_s^{(n+1)} = -\log x_{n,s}^{(M)}$

3.4.3 Moment-based initialization

Since the EM algorithm is not guaranteed to converge to a global maximizer of the likelihood, its behavior can be improved by a judicious initialization. Usually, the choice of a good starting value is discussed in the context of specific applications [Biernacki et al., 2003], [Pereira et al., 2010], [Huda et al., 2006], [Jezierska et al., 2011a]. For the considered problem, we propose a moment-based approach. Although methods of moments are often outperformed by other estimators, their simplicity makes them popular statistical tools [Zhang, 2007].

Due to the independence assumptions made in Section 3.2, the first and second order statistics of the observations can be expressed as

- mean value: $\mathsf{E}[R_{s,t}] = \alpha e^{-k_s t}u_s + c$ (3.43)
- variance: $\mathrm{var}\,[R_{s,t}] = \alpha^2 e^{-k_s t}u_s + \sigma^2.$ (3.44)

Note that (3.43) can be re-expressed as

$$R_{s,t} = a_s e^{-k_s t} + c + E_{s,t} \tag{3.45}$$

where $a_s = \alpha u_s$ and $(E_{s,t})_{1\leq s\leq S, 1\leq t\leq T}$ are independent zero-mean random variables. This suggests adopting a nonlinear least squares approach to compute estimates $\widehat{a} = (\widehat{a}_s)_{1\leq s\leq S}$, $\widehat{k} = (\widehat{k}_s)_{1\leq s\leq S}$ and $\widehat{c}$ of the parameters:

$$(\widehat{a}, \widehat{k}, \widehat{c}) \in \operatorname*{arg\,min}_{a,k,c} \sum_{s=1}^{S} \sum_{t=1}^{T} \left(r_{s,t} - c - a_s e^{-k_s t} \right)^2 . \tag{3.46}$$

The traditional approach to address such a problem is to rewrite it as

$$\operatorname*{minimize}_{k\in(0,+\infty)^S} \ \psi(k) \tag{3.47}$$

where, for every $k = (k_s)_{1\leq s\leq S} \in (0, +\infty)^S$,

$$\psi(k) = \min_{a\in\mathbb{R}^S, c\in\mathbb{R}} \sum_{s=1}^{S} \sum_{t=1}^{T} \left(r_{s,t} - c - a_s e^{-k_s t} \right)^2 . \tag{3.48}$$

Finding the expression of ψ reduces to a linear least squares problem the solution of which can be expressed in a closed form. However, for large-size problems where S takes a high value, the minimization of ψ requires solving a large dimensional non-convex minimization problem. Alternatively, by setting $x_s = e^{-k_s}$ for every $s \in \{1, \ldots, S\}$, (3.46) can be reexpressed as the problem of finding a minimizer of a real-valued multivariate polynomial on a set defined by polynomial inequalities. Global optimization methods for such problems were introduced in [Lasserre, 2001], [Parrilo and Sturmfels, 2001]. Nevertheless, these methods do not scale well with the size of the problem.

In order to circumvent these difficulties, we propose to adopt a splitting strategy. More specifically, we reformulate the problem in the product space $\mathbb{R}^S \times \mathbb{R}^S$ as follows:

$$\operatorname*{minimize}_{\substack{(c_1,\ldots,c_S)\in\mathbb{R}^S \\ (x_1,\ldots,x_S)\in\mathbb{R}^S}} \sum_{s=1}^{S} \varphi_s(c_s, x_s) + \iota_D(c_1, \ldots, c_S) \tag{3.49}$$

where, for every $(c_s, x_s) \in \mathbb{R}^2$,

$$\varphi_s(c_s, x_s) = \begin{cases} \min\limits_{a_s\in\mathbb{R}} \sum_{t=1}^{T} \left(r_{s,t} - c_s - a_s x_s^t \right)^2 & \text{if } x_s \in [\varepsilon, 1-\varepsilon] \\ +\infty & \text{otherwise,} \end{cases} \tag{3.50}$$

$\varepsilon \in (0, 1/2)$ is a tolerance parameter, D is the vector space $\{(c_1, \ldots, c_S) \in \mathbb{R}^S \mid c_1 = \cdots = c_S\}$, and ι_D is the indicator function of D defined as

$$(\forall c = (c_1, \ldots, c_S) \in \mathbb{R}^S) \quad \iota_D(c_1, \ldots, c_S) = \begin{cases} 0 & \text{if } c \in D \\ +\infty & \text{otherwise.} \end{cases} \tag{3.51}$$

Guidelines for addressing such split optimization problems is provided in [Combettes and Pesquet, 2008] by employing proximal tools. namely algorithms involving computations of proximity operators (see Chapter 1.3.1.2). However, there is a limited number of results concerning the convergence of proximal splitting algorithms in the non-convex case. Among these algorithms, we propose to use the Douglas-Rachford algorithm which was observed to behave satisfactorily [Borwein and Sims, 2011] in a number of non-convex optimization problems.

For many functions the proximity operator has an explicit form [Combettes and Pesquet, 2011]. For instance, the proximal operator prox_{ι_D} of ι_D reduces to the projection onto D, i.e.

$$(\forall (c_s)_{1 \leq s \leq S} \in \mathbb{R}^S) \quad \text{prox}_{\iota_D}(c_1, \ldots, c_S) = \frac{c_1 + \cdots + c_S}{S}(1, \ldots, 1). \tag{3.52}$$

For every $s \in \{1, \ldots, S\}$, we have the following expression of the proximity operator of $\gamma\varphi_s$ with $\gamma \in (0, +\infty)$

$$\begin{aligned} &(\forall (\overline{c}_s, \overline{x}_s) \in \mathbb{R}^2) \qquad (\widetilde{c}_s, \widetilde{x}_s) = \text{prox}_{\gamma\varphi_s}(\overline{c}_s, \overline{x}_s) \quad \Leftrightarrow \\ &(\widetilde{c}_s, \widetilde{x}_s) = \underset{(c_s, x_s) \in \mathbb{R}^2}{\text{argmin}} \; \gamma\varphi_s(c_s, x_s) + \frac{1}{2}(c_s - \overline{c}_s)^2 + \frac{1}{2}(x_s - \overline{x}_s)^2. \end{aligned} \tag{3.53}$$

We substitute φ_s in (3.53) with (3.50). We need to solve the following problem:

$$\underset{a_s \in \mathbb{R}, x_s \in [\varepsilon, 1-\varepsilon], c_s \in \mathbb{R}}{\text{minimize}} \; \gamma \sum_{t=1}^{T} \left(r_{s,t} - c_s - a_s x_s^t \right)^2 + \frac{1}{2}(c_s - \overline{c}_s)^2 + \frac{1}{2}(x_s - \overline{x}_s)^2. \tag{3.54}$$

For any value of $x_s \in [\varepsilon, 1 - \varepsilon]$, differentiating with respect to c_s and a_s yields $\widetilde{a}_s(x_s)$ and $\widetilde{c}_s(x_s)$ as the optimal values of a_s and c_s in the above minimized quadratic function. The solution can be written in a 2×2 matrix form:

$$\begin{bmatrix} T + (2\gamma)^{-1} & \overline{\omega_s} \\ \overline{\omega_s} & \overline{\omega_s^2} \end{bmatrix} \begin{bmatrix} \widetilde{c}_s(x_s) \\ \widetilde{a}_s(x_s) \end{bmatrix} = \begin{bmatrix} (2\gamma)^{-1}\overline{c}_s + \overline{r_s} \\ \rho_s \end{bmatrix} \tag{3.55}$$

where

$$\overline{\omega_s} = \sum_{t=1}^{T} x_s^t = \chi(x_s), \quad \overline{\omega_s^2} = \sum_{t=1}^{T} x_s^{2t} = \chi(x_s^2) \tag{3.56}$$

$$\overline{r_s} = \sum_{t=1}^{T} r_{s,t}, \quad \rho_s = \sum_{t=1}^{T} r_{s,t} x_s^t \tag{3.57}$$

and

$$\forall \upsilon \in [0, +\infty), \qquad \chi(\upsilon) = \upsilon \frac{1-\upsilon^T}{1-\upsilon}. \tag{3.58}$$

The linear solution to (3.55) yields

$$\widetilde{c}_s(x_s) = \frac{\overline{\omega_s^2}((2\gamma)^{-1}\overline{c}_s + \overline{r_s}) - \overline{\omega_s}\rho_s}{(T + (2\gamma)^{-1})\overline{\omega_s^2} - (\overline{\omega_s})^2} \tag{3.59}$$

$$\widetilde{a}_s(x_s) = \frac{(T + (2\gamma)^{-1})\rho_s - \overline{\omega_s}((2\gamma)^{-1}\overline{c}_s + \overline{r_s})}{(T + (2\gamma)^{-1})\overline{\omega_s^2} - (\overline{\omega_s})^2}. \tag{3.60}$$

The solution to (3.54) thus reduces to the one-variable minimization problem:

$$\begin{aligned} \text{Find } \widetilde{x}_s = & \operatorname*{argmin}_{x_s \in [\varepsilon, 1-\varepsilon]} \gamma \sum_{t=1}^{T} \left(r_{s,t} - \widetilde{c}_s(x_s) - \widetilde{a}_s(x_s) x_s^t \right)^2 \\ & + \frac{1}{2}\left(\widetilde{c}_s(x_s) - \overline{c}_s\right)^2 + \frac{1}{2}(x_s - \overline{x}_s)^2 \\ = & \operatorname*{argmin}_{x_s \in [\varepsilon, 1-\varepsilon]} -\gamma\left(((2\gamma)^{-1}\overline{c}_s + \overline{r_s})\widetilde{c}_s(x_s) + \rho_s \widetilde{a}_s(x_s)\right) + \frac{1}{2}(x_s - \overline{x}_s)^2. \end{aligned} \tag{3.61}$$

The minimization of this rational function can be performed by various numerical methods. For instance, the global optimization method proposed in [Kostrowicki and Scheraga, 1995], [Fang et al., 2000], [Jibetean and de Klerk, 2006], [Nie et al., 2008] can be employed. We conclude that $\operatorname{prox}_{\gamma\varphi_s}(\overline{c}_s, \overline{x}_s) = (\widetilde{c}_s(\widetilde{x}_s), \widetilde{x}_s)$.

This allows us to apply the Douglas-Rachford method summarized in Algorithm 6. It is worth noticing that the computation of the proximity operators $\operatorname{prox}_{\gamma\varphi_s}$ for different values of $s \in \{1, \ldots, S\}$ can be implemented in a parallel manner.

Once estimates $\widehat{c}$ and $(\widehat{x}_s)_{1 \leq s \leq S}$ have been obtained in this fashion, the following estimates of the amplitude values can be derived from (3.50):

$$(\forall s \in \{1, \ldots, S\}) \qquad \widehat{a}_s = \frac{1}{\chi(\widehat{x}_s^2)} \sum_{t=1}^{T} (r_{s,t} - \widehat{c})\widehat{x}_s^t \tag{3.62}$$

Note that an alternative approach relying upon an alternating minimization approach was proposed in [Jezierska et al., 2012b]. However, it was observed to exhibit slower convergence.

Algorithm 6 Douglas-Rachford iterations for computing moment-based estimates of k and c.

Initialization:
Initialize $\widehat{c}^{(0)}$.
Set $\overline{c}_s^{(0)} = \widehat{c}^{(0)}$, for every $s \in \{1, \dots, S\}$.
Set initial values in $[\varepsilon, 1-\varepsilon]$ for $(\widehat{x}_s^{(0)})_{1 \leq s \leq S}$.
Main loop:
For $m = 0 \dots M-1$
  For $s = 1 \dots S$
    $(\widehat{c}_s^{(m)}, \widehat{x}_s^{(m+1)}) = \mathrm{prox}_{\gamma \varphi_s}(\overline{c}_s^{(m)}, \widehat{x}_s^{(m)})$
  $\widehat{c}^{(m+1)} = \frac{1}{S} \sum_{s=1}^{S} \widehat{c}_s^{(m)}$
  For $s = 1 \dots S$
    $\overline{c}_s^{(m+1)} = \overline{c}_s^{(m)} + 2\widehat{c}^{(m+1)} - \widehat{c}^{(m)} - \widehat{c}_s^{(m)}$
Outputs:
$\widehat{c} = \widehat{c}^{(M)}$
For $s = 1 \dots S$
  $\widehat{k}_s = -\ln\left(\widehat{x}_s^{(M)}\right)$

It remains now to deduce estimates of α, u and σ. To do so, we start by rewriting (3.44) as

$$\mathsf{E}[(R_{s,t} - \mathsf{E}[R_{s,t}])^2] = \mathsf{E}[(R_{s,t} - a_s e^{-k_s t} - c)^2] = \alpha a_s e^{-k_s t} + \sigma^2. \tag{3.63}$$

The following weighted least squares estimate for α can then be derived:

$$\widehat{\alpha} = \frac{\overline{\nu} \sum_{s=1}^{S} \nu_s \widehat{a}_s \mu_s - \sum_{s=1}^{S} \nu_s e_s \sum_{s=1}^{S} \nu_s \widehat{a}_s \overline{\omega_s}}{\overline{\nu} \sum_{s=1}^{S} \nu_s \widehat{a}_s^2 \overline{\omega_s^2} - (\sum_{s=1}^{S} \nu_s \widehat{a}_s \overline{\omega_s})^2}, \tag{3.64}$$

where $(\nu_s)_{1 \leq s \leq S}$ are positive weights, $\overline{\nu} = T \sum_{s=1}^{S} \nu_s$, and, for every $s \in \{1, \dots, S\}$,

$$\overline{\omega_s} = \chi(\widehat{x}_s), \quad \overline{\omega_s^2} = \chi(\widehat{x}_s^2), \quad e_s = \sum_{t=1}^{T} e_{s,t}, \quad \mu_s = \sum_{t=1}^{T} \widehat{x}_s^t e_{s,t}, \tag{3.65}$$

$$(\forall t \in \{1, \dots, T\}) \qquad e_{s,t} = (r_{s,t} - \widehat{a}_s \widehat{x}_s^t - \widehat{c})^2. \tag{3.66}$$

An estimate of u follows as

$$(\forall s \in \{1, \dots, S\}) \qquad \widehat{u}_s = \frac{\widehat{a}_s}{\widehat{\alpha}}. \tag{3.67}$$

Finally, the estimation process is completed by computing

$$\widehat{\sigma}^2 = \frac{\sum_{(s,t)} \nu_s \left(e_{s,t} - \widehat{\alpha} \widehat{a}_s \widehat{x}_s^t\right)}{\sum_{(s,t)} \nu_s} = \frac{\sum_{s=1}^{S} \nu_s \left(e_s - \widehat{\alpha} \widehat{a}_s \overline{\omega_s}\right)}{\overline{\nu}}. \tag{3.68}$$

The final proposed noise modeling procedure is summarized in Fig. 3.3.

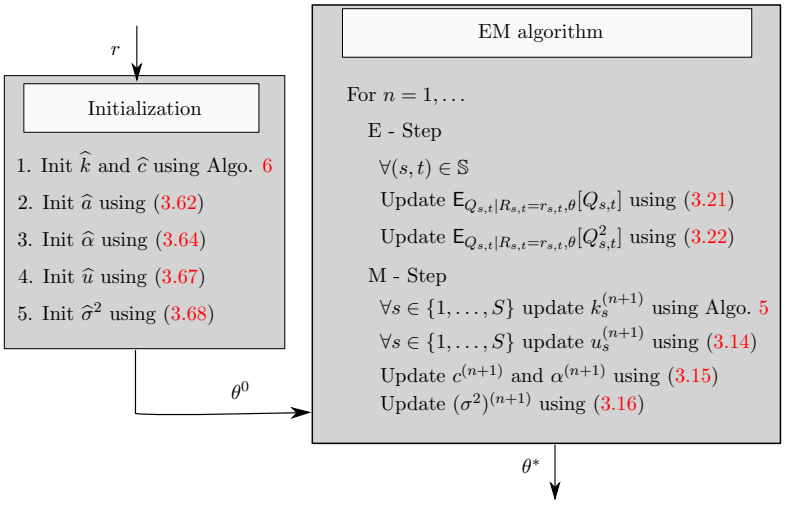

Figure 3.3: *Flowchart of the proposed parametric estimation method*

§ 3.5 Performance bounds

This section aims at deriving lower bounds on the best achievable performance in estimating the parameters of Model (3.1). These bounds will allow us to evaluate the performance of the estimator proposed in Section 3.3. A well-known lower bound on the variance of an unbiased estimator is provided by the Cramer-Rao inequality, which involves the inverse of the Fisher Information Matrix (FIM) [Rao, 1945]. The problem of computing the required FIM is addressed in Section 3.5.1, whereas the inversion of the FIM is discussed in Section 3.5.2.

3.5.1 Form of the Fisher information matrix

Recall that the FIM is expressed from the log-likelihood as follows

$$I(\theta) = \mathsf{E}_{R|\theta}\left[\frac{\partial \ln(f_R(R \mid \theta))}{\partial \theta}\left(\frac{\partial \ln(f_R(R \mid \theta))}{\partial \theta}\right)^\top\right] = \sum_{s=1}^{S}\sum_{t=1}^{T} \mathsf{E}_{R|\theta}[U_{s,t}U_{s,t}^\top] \tag{3.69}$$

where, for every $(s,t) \in \mathbb{S}$, $U_{s,t}$ is the score function defined as

$$U_{s,t} = \frac{\partial \ln(f_{R_{s,t}}(R_{s,t} \mid \theta))}{\partial \theta} \tag{3.70}$$

and the marginal pdf of $R_{s,t}$ is given by (3.20). This yields

$$\frac{\partial f_{R_{s,t}}(r_{s,t} \mid \theta)}{\partial \theta} = \sum_{q_{s,t}=0}^{+\infty} \frac{\partial p_{R_{s,t},Q_{s,t}}(r_{s,t}, q_{s,t} \mid \theta)}{\partial \theta} \tag{3.71}$$

which allows us to deduce that $U_{s,t}$ is equal to

$$\frac{\sum_{q_{s,t}=0}^{+\infty}\left\{\frac{\partial \ln(p_{R_{s,t},Q_{s,t}}(r_{s,t},q_{s,t}|\theta))}{\partial\theta}p_{R_{s,t},Q_{s,t}}(r_{s,t},q_{s,t}\mid\theta)\right\}}{\sum_{q_{s,t}=0}^{+\infty}p_{R_{s,t},Q_{s,t}}(r_{s,t},q_{s,t}\mid\theta)} = \mathsf{E}_{Q_{s,t}|R_{s,t}=r_{s,t},\theta}\left[\frac{\partial \ln(p_{R_{s,t},Q_{s,t}}(r_{s,t},Q_{s,t}\mid\theta))}{\partial\theta}\right]. \tag{3.72}$$

The components of vector $U_{s,t}$ can then be expressed from the conditional means of $Q_{s,t}$ and $Q_{s,t}^2$. Indeed, according to (3.5), we have: for every $s' \in \{1,\ldots,S\}$,

$$\mathsf{E}_{Q_{s,t}|R_{s,t}=r_{s,t},\theta}\left[\frac{\partial \ln(p_{R_{s,t},Q_{s,t}}(r_{s,t},Q_{s,t}\mid\theta))}{\partial u_{s'}}\right] = \left(\frac{1}{u_s}\mathsf{E}_{Q_{s,t}|R_{s,t}=r_{s,t},\theta}[Q_{s,t}] - e^{-k_s t}\right)\delta_{s'-s} \tag{3.73}$$

$$\mathsf{E}_{Q_{s,t}|R_{s,t}=r_{s,t},\theta}\left[\frac{\partial \ln(p_{R_{s,t},Q_{s,t}}(r_{s,t},Q_{s,t}\mid\theta))}{\partial k_{s'}}\right] = t\left(u_s e^{-k_s t} - \mathsf{E}_{Q_{s,t}|R_{s,t}=r_{s,t},\theta}[Q_{s,t}]\right)\delta_{s'-s} \tag{3.74}$$

$$\mathsf{E}_{Q_{s,t}|R_{s,t}=r_{s,t},\theta}\left[\frac{\partial \ln(p_{R_{s,t},Q_{s,t}}(r_{s,t},Q_{s,t}\mid\theta))}{\partial c}\right] = \frac{1}{\sigma^2}\left(r_{s,t} - \alpha\mathsf{E}_{Q_{s,t}|R_{s,t}=r_{s,t},\theta}[Q_{s,t}] - c\right) \tag{3.75}$$

$$\mathsf{E}_{Q_{s,t}|R_{s,t}=r_{s,t},\theta}\left[\frac{\partial \ln(p_{R_{s,t},Q_{s,t}}(r_{s,t},Q_{s,t}\mid\theta))}{\partial \alpha}\right] = \frac{1}{\sigma^2}\left((r_{s,t}-c)\mathsf{E}_{Q_{s,t}|R_{s,t}=r_{s,t},\theta}[Q_{s,t}] - \alpha\mathsf{E}_{Q_{s,t}|R_{s,t}=r_{s,t},\theta}[Q_{s,t}^2]\right) \tag{3.76}$$

$$\mathsf{E}_{Q_{s,t}|R_{s,t}=r_{s,t},\theta}\left[\frac{\partial \ln(p_{R_{s,t},Q_{s,t}}(r_{s,t},Q_{s,t}\mid\theta))}{\partial \sigma}\right] = \frac{1}{\sigma^3}\left((r_{s,t}-c)^2 - \sigma^2 + \alpha^2\mathsf{E}_{Q_{s,t}|R_{s,t}=r_{s,t},\theta}[Q_{s,t}^2] - 2\alpha(r_{s,t}-c)\mathsf{E}_{Q_{s,t}|R_{s,t}=r_{s,t},\theta}[Q_{s,t}]\right) \tag{3.77}$$

where $\delta_{s'-s} = 1$ if $s' = s$ and 0 otherwise. So, provided that $\mathsf{E}_{Q_{s,t}|R_{s,t}=r_{s,t},\theta}[Q_{s,t}]$ and $\mathsf{E}_{Q_{s,t}|R_{s,t}=r_{s,t},\theta}[Q_{s,t}^2]$ are known, the above equations allow us to deduce the expression of $U_{s,t}$. We still need to calculate the expectation with respect to R in (3.69), which is unfortunately intractable. To circumvent this difficulty, we propose to proceed similarly to the Monte Carlo approach in [Dauwels and Korl, 2006], by drawing $L \gg 1$ realizations of R and calculating, for each realization $r^{(\ell)}$ with $\ell \in \{1,\ldots,L\}$, the associated correlation matrix $\sum_{s=1}^{S}\sum_{t=1}^{T}U_{s,t}^{(\ell)}(U_{s,t}^{(\ell)})^\top$. Then, the FIM is approximated by the following consistent sample estimate

$$\widehat{I}_L(\theta) = \frac{1}{L}\sum_{\ell=1}^{L}\sum_{s=1}^{S}\sum_{t=1}^{T}U_{s,t}^{(\ell)}(U_{s,t}^{(\ell)})^\top. \tag{3.78}$$

3.5.2 Inversion of the Fisher information matrix

Let $\widehat{\theta}_i \colon \mathbb{R}^{ST} \to \mathbb{R}$ with $i \in \{1, \ldots, 2S+3\}$ be an unbiased estimator of the i-th component θ_i of vector θ. A lower bound of the mean square error $\mathsf{E}[(\widehat{\theta}_i(R) - \theta_i)^2]$ is given by the i-th diagonal term of the inverse of the FIM. It is thus of main interest to compute the diagonal terms of the inverse of matrix $I(\theta) \in \mathbb{R}^{(2S+3)\times(2S+3)}$. Note that, the FIM is assumed to be invertible as otherwise some parameters would not be identifiable. Although S may take large values, the inversion can be efficiently performed due to the sparse structure of the FIM.

More precisely, the FIM can be expressed as the following block matrix:

$$I(\theta) = \begin{bmatrix} A & B \\ B^\top & C \end{bmatrix} \tag{3.79}$$

where

• the matrix $A \in \mathbb{R}^{2S\times 2S}$ takes the following form

$$A = \begin{bmatrix} A_{1,1} & A_{1,2} \\ A_{1,2}^\top & A_{2,2} \end{bmatrix} \tag{3.80}$$

with

$$A_{1,1} = \mathsf{E}_{R|\theta}\left[\frac{\partial \ln(f_R(R \mid \theta))}{\partial u}\left(\frac{\partial \ln(f_R(R \mid \theta))}{\partial u}\right)^\top\right] \in \mathbb{R}^{S\times S} \tag{3.81}$$

$$A_{1,2} = \mathsf{E}_{R|\theta}\left[\frac{\partial \ln(f_R(R \mid \theta))}{\partial u}\left(\frac{\partial \ln(f_R(R \mid \theta))}{\partial k}\right)^\top\right] \in \mathbb{R}^{S\times S} \tag{3.82}$$

$$A_{2,2} = \mathsf{E}_{R|\theta}\left[\frac{\partial \ln(f_R(R \mid \theta))}{\partial k}\left(\frac{\partial \ln(f_R(R \mid \theta))}{\partial k}\right)^\top\right] \in \mathbb{R}^{S\times S}; \tag{3.83}$$

• the matrix B is given by

$$B^\top = [B_1 \mid B_2] \tag{3.84}$$

where

$$B_1 = \mathsf{E}_{R|\theta}\left[\frac{\partial \ln(f_R(R \mid \theta))}{\partial \widetilde{\theta}}\left(\frac{\partial \ln(f_R(R \mid \theta))}{\partial u}\right)^\top\right] \in \mathbb{R}^{3\times S} \tag{3.85}$$

$$B_2 = \mathsf{E}_{R|\theta}\left[\frac{\partial \ln(f_R(R \mid \theta))}{\partial \widetilde{\theta}}\left(\frac{\partial \ln(f_R(R \mid \theta))}{\partial k}\right)^\top\right] \in \mathbb{R}^{3\times S} \tag{3.86}$$

with $\widetilde{\theta} = [c, \alpha, \sigma]^\top$;

• $C = \mathsf{E}_{R|\theta}\left[\frac{\partial \ln(f_R(R|\theta))}{\partial \widetilde{\theta}}\left(\frac{\partial \ln(f_R(R|\theta))}{\partial \widetilde{\theta}}\right)^\top\right] \in \mathbb{R}^{3\times 3}$.

From the standard Frobenius-Schur formula for the inverse of a block matrix [Horn and Johnsone, 1990], the i-th diagonal terms of $I(\theta)^{-1}$ is given by

$$[I(\theta)^{-1}]_{i,i} = \begin{cases} [A^{-1} + A^{-1}B(C - B^\top A^{-1}B)^{-1}B^\top A^{-1}]_{i,i} & \text{if } i \leqslant 2S \\ [(C - B^\top A^{-1}B)^{-1}]_{i,i} & \text{otherwise.} \end{cases} \tag{3.87}$$

Hence, both $C - B^\top A^{-1}B \in \mathbb{R}^{3\times 3}$ and A need to be inverted. The former inversion is easy due to the small size of the matrix, but a more challenging task is to invert the latter, which is typically of large dimension. However, a closer look at (3.73) and (3.74) allows us to observe that matrices $A_{1,1}$, $A_{1,2}$ and $A_{2,2}$ in (3.81)-(3.83) are diagonal. Thus, using again the block matrix inversion formula, we get

$$A^{-1} = [A_1^{-1} \mid A_2^{-1}] \tag{3.88}$$

with $A_1^{-1} = \begin{bmatrix} (A_{1,1} - A_{1,2}A_{2,2}^{-1}A_{1,2})^{-1} \\ -A_{1,1}^{-1}A_{1,2}(A_{2,2} - A_{1,2}A_{1,1}^{-1}A_{1,2})^{-1} \end{bmatrix}$ and $A_2^{-1} = \begin{bmatrix} -A_{1,1}^{-1}A_{1,2}(A_{2,2} - A_{1,2}A_{1,1}^{-1}A_{1,2})^{-1} \\ (A_{2,2} - A_{1,2}A_{1,1}^{-1}A_{1,2})^{-1} \end{bmatrix}$, where all the required inversions are straightforward due to the diagonal structure of all the involved matrices.

In summary, the mean square error $\mathsf{E}[(\widehat{\theta}_i(R) - \theta_i)^2]$ is lower bounded by $[I(\theta)^{-1}]_{i,i}$ which is given by (3.87).

§ 3.6 Experimental results

This section illustrates the good performance of the proposed approach and shows its usefulness in a real microscopy application. The algorithm performance is measured by computing the mean square error (MSE) between the original and reconstructed noise parameters and by inspecting the difference between the variance of our estimator and the Cramer-Rao bounds (CRB). Results of a series of synthetic data simulation are provided in Section 3.6.1, while Section 3.6.2 is devoted to practical considerations, necessary details about the application and presentation of the results on a real data set.

3.6.1 Validation of the proposed approach on synthetic data

Firstly we evaluate the performance of the proposed algorithm under different working conditions. In particular the influence of the values of parameters Δ, S, T, c, α, σ^2, u_s and k_s is studied. Realizations of the observed signal $R_{s,t}$ are generated according to (3.1) for different set of parameter values for θ, S and T. Randomly chosen values of u_s and k_s are uniformly

distributed over $[\underline{u}, \overline{u}]$ and $\left[\underline{k}, \overline{k}\right]$, respectively. Poisson and Gaussian noise realizations are drawn using the random number generators proposed in Park *et al.* [Park and Miller, 1988]. The bias on the estimate of the i-th component of the parameter vector is computed as $\frac{1}{L}\sum_{\ell=1}^{L}(\theta_i - \widehat{\theta}_i^{(\ell)})$ over $L = 100$ different noise realizations. As expected, Table 3.2 illustrates that our estimator is asymptotically unbiased when $T \to +\infty$. Average values of the MSE are computed by $\frac{1}{L}\sum_{\ell=1}^{L}(\theta_i - \widehat{\theta}_i^{(\ell)})^2$. Similarly, the SNR values provided in Table 3.2 correspond to averages computed over the L realizations. The good performance of the proposed estimator is confirmed by the small difference between the MSE and the associated CRB (usually less than 50%).

Remark 3.6.1 Note that, for finite T, our estimator is biased, so that the CRB constitutes only a quality measure which is not theoretically guaranteed to provide an achievable lower bound for the MSE.

Firstly, the influence of the approximation of the infinite summations proposed in Proposition 3.4.2 is investigated. The inspection of the MSE, bias and CRB values in the provided example illustrates that 5 is an adequate choice for Δ and that any higher value does not improve the estimation results. Note that the CRB computation procedure appears to be less sensitive to the choice of Δ than the EM algorithm. Additionally, the influence of the choice of T and S on the estimation quality is assessed. As expected, the estimation performance is improved by increasing T and S, but the influence of T is more important. Finally, we provide some numerical results related to the behaviour of our algorithm for different choices of θ. The following points have been highlighted through our study:

- the accuracy of u and k estimation increases with α, while the accuracy of α, c and σ estimation decreases with α ;
- the estimation performance of our algorithm does not depend on the value of c ;
- the accuracy of c, u and k estimation decreases with σ^2, while the estimation of σ is improved ;
- σ is better estimated when low values of u_s are present in signal u ;
- the considered estimation problem becomes more difficult when the decay rate k_s is small.

One can observe that our EM estimates can be quite precise for some good choices of S, T and Δ as the estimation error can fall under 5%.

	Param.	$\widehat{\alpha}$			$\widehat{c}$			$\widehat{\sigma}$			$\widehat{u}$	$\widehat{k}$
		bias	$\overline{\text{MSE}}$	CRB	bias	$\overline{\text{MSE}}$	CRB	bias	$\overline{\text{MSE}}$	CRB	SNR	SNR
Identified noise parameters vs Δ ($\alpha = 5$, $c = 150$, $\sigma^2 = 200$, $\underline{u} = 5$, $\overline{u} = 100$, $\underline{k} = 0.0001$, $\overline{\overline{k}} = 0.01$, $S = 200$, $T = 200$)	3	-0.29	9.31×10^{-2}	4.44×10^{-3}	2.60	6.76×10^{2}	3.80×10^{0}	8.27	6.84×10^{1}	1.59×10^{-1}	27.1	12.0
	4	0.06	8.01×10^{-3}	4.44×10^{-3}	0.63	4.21×10^{0}	1.68×10^{0}	0.13	1.68×10^{-1}	1.59×10^{-1}	30.9	22.5
	5	0.06	8.40×10^{-3}	4.44×10^{-3}	0.47	3.89×10^{0}	1.68×10^{0}	0.09	1.59×10^{-1}	1.59×10^{-1}	30.9	22.5
	6	0.06	8.40×10^{-3}	4.44×10^{-3}	0.47	3.89×10^{0}	1.68×10^{0}	0.09	1.59×10^{-1}	1.59×10^{-1}	30.9	22.6
Identified noise parameters vs T ($\alpha = 5$, $c = 150$, $\sigma^2 = 1000$, $\underline{u} = 5$, $\overline{u} = 150$, $\underline{k} = 0.0001$, $\overline{\overline{k}} = 0.01$, $S = 200$)	150	0.08	2.07×10^{-2}	1.36×10^{-2}	-1.17	7.78×10^{1}	4.77×10^{1}	0.04	6.49×10^{-1}	4.49×10^{-1}	25.8	12.8
	200	0.07	1.55×10^{-2}	1.04×10^{-2}	0.85	1.73×10^{1}	1.11×10^{1}	0.13	2.21×10^{-1}	1.69×10^{-1}	30.1	19.2
	300	0.04	1.03×10^{-2}	7.14×10^{-3}	0.45	1.72×10^{0}	1.54×10^{0}	0.11	8.54×10^{-2}	5.90×10^{-2}	31.9	23.1
	350	0.04	8.80×10^{-3}	6.17×10^{-3}	0.06	8.75×10^{-1}	7.52×10^{-1}	0.08	5.54×10^{-2}	4.15×10^{-2}	32.3	23.8
Identified noise parameters vs S ($\alpha = 5$, $c = 150$, $\sigma^2 = 1000$, $\underline{u} = 5$, $\overline{u} = 150$, $\underline{k} = 0.0001$, $\overline{\overline{k}} = 0.01$, $T = 200$)	150	0.06	1.78×10^{-2}	1.36×10^{-2}	0.53	1.60×10^{1}	1.43×10^{1}	0.17	2.27×10^{-1}	2.13×10^{-1}	29.8	17.6
	200	0.07	1.55×10^{-2}	1.04×10^{-2}	0.85	1.73×10^{1}	1.11×10^{1}	0.13	2.21×10^{-1}	1.69×10^{-1}	30.1	19.2
	300	0.06	1.14×10^{-2}	6.94×10^{-3}	-0.14	9.31×10^{0}	7.69×10^{0}	0.11	1.47×10^{-1}	1.12×10^{-1}	30.8	19.7
	350	0.06	8.76×10^{-3}	6.23×10^{-3}	0.71	1.08×10^{1}	6.74×10^{0}	0.16	1.34×10^{-1}	1.02×10^{-1}	31.2	19.4
Identified noise parameters vs α ($c = 150$, $\sigma^2 = 1000$, $\underline{u} = 5$, $\overline{u} = 150$, $\underline{k} = 0.0001$, $\overline{\overline{k}} = 0.01$, $S = 200$, $T = 200$)	5	0.07	1.55×10^{-2}	1.04×10^{-2}	0.85	1.73×10^{0}	1.11×10^{1}	0.13	2.21×10^{-1}	1.69×10^{-1}	30.1	19.2
	10	0.12	2.97×10^{-2}	1.53×10^{-2}	0.99	3.08×10^{1}	2.10×10^{1}	0.16	9.98×10^{-1}	7.58×10^{-1}	32.3	23.4
	15	0.12	4.21×10^{-2}	2.47×10^{-2}	0.04	4.21×10^{1}	3.36×10^{1}	0.11	2.68×10^{0}	2.24×10^{0}	33.5	24.9
	20	0.20	7.92×10^{-2}	3.72×10^{-2}	1.00	6.22×10^{1}	4.77×10^{1}	0.28	6.14×10^{0}	5.00×10^{0}	33.3	25.6
Identified noise parameters vs c ($\alpha = 30$, $\sigma^2 = 3000$, $\underline{u} = 5$, $\overline{u} = 150$, $\underline{k} = 0.0001$, $\overline{\overline{k}} = 0.01$, $S = 200$, $T = 200$)	-10	0.32	1.95×10^{-1}	9.03×10^{-2}	1.84	1.65×10^{2}	1.20×10^{2}	0.41	1.27×10^{0}	1.00×10^{1}	33.2	25.3
	0	0.32	1.94×10^{-1}	9.03×10^{-2}	1.83	1.65×10^{2}	1.20×10^{2}	0.41	1.26×10^{0}	1.00×10^{1}	33.2	25.3
	10	0.32	1.95×10^{-1}	9.03×10^{-2}	1.84	1.65×10^{2}	1.20×10^{2}	0.41	1.26×10^{0}	1.00×10^{1}	33.2	25.3
	150	0.32	1.95×10^{-1}	9.03×10^{-2}	1.85	1.65×10^{2}	1.20×10^{2}	0.41	1.26×10^{0}	1.00×10^{1}	33.2	25.3
Identified noise parameters vs σ^2 ($\alpha = 30$, $c = 150$, $\underline{u} = 5$, $\overline{u} = 150$, $\underline{k} = 0.0001$, $\overline{\overline{k}} = 0.01$, $S = 200$, $T = 200$)	2000	0.10	1.50×10^{-1}	8.15×10^{-2}	-2.85	1.35×10^{2}	1.03×10^{2}	-0.22	1.26×10^{1}	1.18×10^{1}	33.7	25.6
	3000	0.32	1.94×10^{-1}	9.03×10^{-2}	1.83	1.65×10^{2}	1.20×10^{2}	0.41	1.26×10^{1}	1.00×10^{1}	33.2	25.3
	4000	0.33	2.10×10^{-1}	1.21×10^{-1}	2.09	1.89×10^{2}	1.04×10^{2}	0.41	1.15×10^{1}	6.80×10^{0}	33.0	24.9
	6000	0.34	2.34×10^{-1}	1.15×10^{-1}	2.46	2.28×10^{2}	1.59×10^{2}	0.42	1.01×10^{1}	7.73×10^{0}	32.7	24.2
Identified noise parameters vs $\underline{u}$ ($\alpha = 1$, $c = 150$, $\sigma^2 = 25$, $\overline{u} = 150$, $\underline{k} = 0.0001$, $\overline{\overline{k}} = 0.01$, $S = 200$, $T = 200$)	1	0.01	3.96×10^{-4}	2.61×10^{-4}	-0.03	4.46×10^{-1}	3.29×10^{-1}	0.02	6.54×10^{-3}	6.04×10^{-3}	25.2	9.4
	5	0.01	4.56×10^{-4}	2.80×10^{-4}	0.15	4.99×10^{-1}	3.36×10^{-1}	0.02	8.59×10^{-3}	6.60×10^{-3}	31.0	21.1
	15	0.01	5.29×10^{-4}	3.21×10^{-4}	0.10	3.87×10^{-1}	3.56×10^{-1}	0.02	9.48×10^{-3}	8.31×10^{-3}	31.2	24.6
	30	0.01	4.47×10^{-4}	3.66×10^{-4}	0.04	4.13×10^{-1}	3.84×10^{-1}	0.03	1.20×10^{-2}	1.11×10^{-2}	31.6	26.7
Identified noise parameters vs k ($\alpha = 30$, $c = 150$, $\sigma^2 = 10^3$, $\underline{u} = 5$, $\overline{u} = 150$, $S = 200$, $T = 200$, $\widetilde{k}_0 = 0.01$, $\widetilde{k}_{i+1} = \widetilde{k}_i/2$)	$\widetilde{k}_1, \widetilde{k}_0$	0.31	1.67×10^{-1}	7.48×10^{-2}	0.18	6.98×10^{1}	6.98×10^{1}	0.27	1.50×10^{1}	1.33×10^{1}	33.5	27.0
	$\widetilde{k}_2, k_1$	0.33	2.79×10^{-1}	8.20×10^{-2}	0.41	5.69×10^{2}	4.72×10^{2}	0.81	8.59×10^{1}	8.30×10^{1}	32.7	22.2
	$\widetilde{k}_1, \widetilde{k}_2$	0.21	1.68×10^{-1}	8.42×10^{-2}	-19.8	1.67×10^{3}	9.47×10^{2}	-5.86	1.65×10^{2}	1.65×10^{2}	32.9	16.4
	$\widetilde{k}_2, \widetilde{k}_3$	0.28	2.27×10^{-1}	8.48×10^{-2}	-34.47	5.72×10^{3}	1.33×10^{3}	-8.70	4.50×10^{2}	2.44×10^{2}	28.4	5.4

Table 3.2: *Performance of the proposed EM algorithm under different working conditions.*

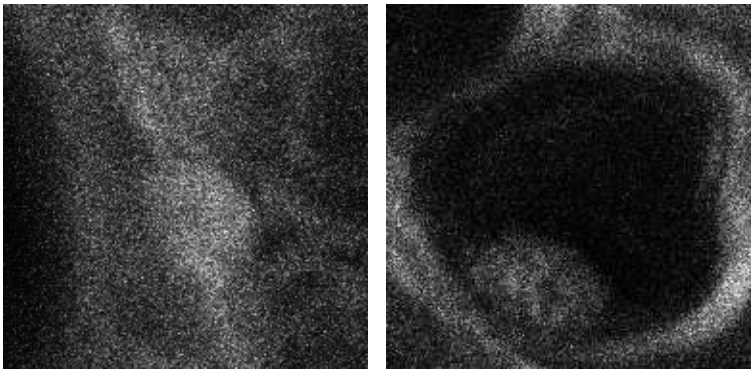

(a) $(r_{s,1})_1$ (b) $(r_{s,1})_2$

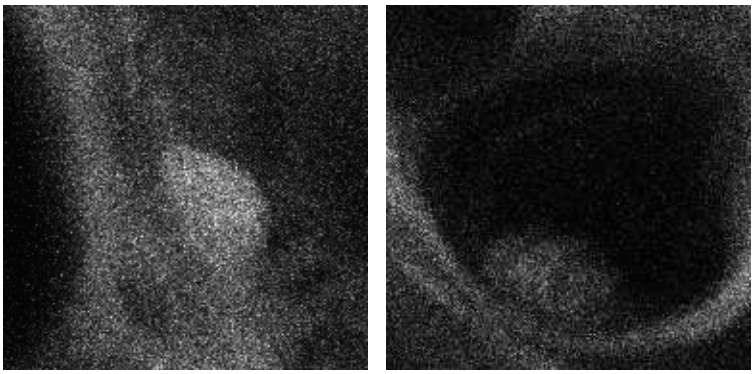

(c) $(r_{s,300})_1$ (d) $(r_{s,300})_2$

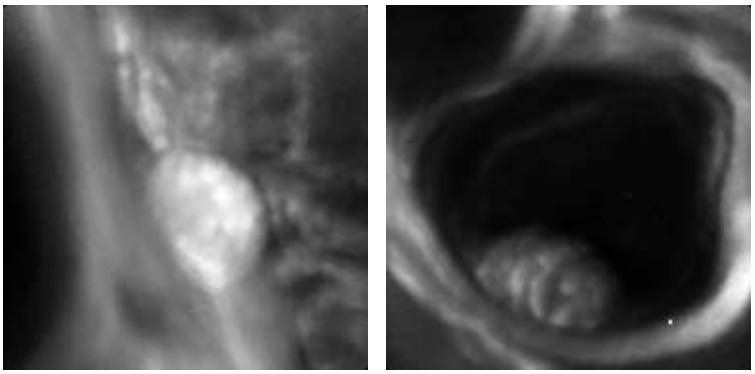

(e) reconstructed $(\widehat{u}_s)_1$ (f) reconstructed $(\widehat{u}_s)_2$

Figure 3.4: *Real data results.*

3.6.2 Application to fluorescence imaging system - macroscopy case

We have applied our algorithm to time series of real fluorescence images, acquired using a macro confocal laser scanning microscope (Leica TCS-LSI) from a cross-section through the rhizome of Convallaria majalis (Lily of the Valley). The reported signal intensities at each location within the biological sample result from natural occurring auto-fluorescence caused by different compounds like lignin and other phenolics. In microscopy practice, the

intensity decay modeled in (3.4) is due to the photobleaching effect [Song et al., 1995]. The acquired data is corrupted with noise. Thus our noise identification problem arises naturally [Zhang, 2007], [Bernas et al., 2007], [Delpretti et al., 2008], [Boulanger et al., 2008], [Paul et al., 2010], [Kedziora et al., 2011]. We evaluated our algorithm using cross validation techniques, i.e. we applied our algorithm to two subsets coming from one dataset. We can then assume that the two sequences are corrupted with the same noise model and parameters. The processed time lapse sequences consists of 300 images with 12-bit resolution of size 190×190, which translates into $T = 300$ and $S = 36100$. Fig. 3.4 (a,c) and Fig. 3.4 (b,d) illustrate the first and last images of the considered sequences 1 and 2, respectively. The visual results are presented in Fig. 3.4 (e,f). The identified models are given by $168 \times \mathcal{P}\big(\widehat{u}_s e^{-\widehat{k}_s t}\big) + \mathcal{N}(114, 64.1^2)$ and $174 \times \mathcal{P}\big(\widehat{u}_s e^{-\widehat{k}_s t}\big) + \mathcal{N}(114, 62.99^2)$ for sequence 1 and 2, respectively. One can observe that these parameter values are indeed quite close, which shows the validity of our hypotheses. The plots in Fig. 3.5 illustrate the variation of the measured and reconstructed signals along t, while s is fixed. One can observe that the bleaching curves are a good fit for the series of measured data points. The estimated $\widehat{u}_s$ values lie in $[0, 13]$. The relatively small data value range can be explained by the fact that the sampling time is only 1.2 μs.

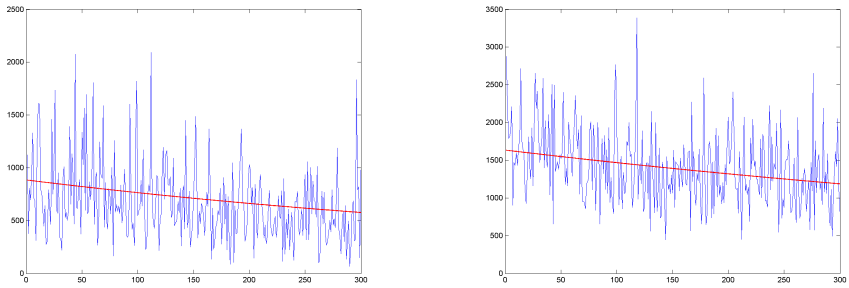

(a) $168 \times 4.5\, e^{-3.1 \times 10^{-4} t} + 114$ (b) $174 \times 9\, e^{-2.2 \times 10^{-4} t} + 114$

(a,b) illustrate time variations for fixed s for time series 1 and 2, respectively. The observed data are plotted in blue and the reconstructed ones (using formula $\widehat{\alpha}\widehat{u}_s e^{-\widehat{k}_s t} + \widehat{c}$) in red.

Figure 3.5: *Time characteristic*

§ 3.7 Conclusions

In this chapter, we have proposed a new EM-based approach for dealing with Poisson-Gaussian noise parameter estimation problems. We have pre-

sented a practical procedure for computing the corresponding Cramer-Rao bounds. We have shown that the proposed method can lead to accurate results given sufficient measurements. The numerical issues related to the computation of our estimator have been addressed. In particular, we have proposed a fast and reliable way to approximate the infinite sums arising in our estimator with a high degree of accuracy. We have proposed an improved moment based estimation method, which we used to initialize the EM algorithm. As a side result, the proposed algorithm can deliver a good estimation of the original data when the noise parameters are unknown. Finally we have shown that our approach constitutes a solution for high quality noise parameter estimation of fluorescence macroscopy data.

- Chapter 4 -

Iterative noise estimation over image segments

In the previous chapter we discussed the problem of Poisson-Gaussian noise parameter identification from multiple images. The focus of this chapter is on single image noise estimation. The problem is formulated within a mixed discrete-continuous optimization framework. The proposed approach jointly estimates the signal of interest and the noise parameters. This is achieved by introducing an adjustable regularization term in a minimization criterion, together with a data fidelity error measure. The optimal solution is sought iteratively by alternating the minimization of a label field and of a noise parameter vector. The proposed algorithm is inspired from the spatial regularization approach for vector quantization introduced in Chapter 2, while noise parameters are updated at each iteration using the results established in Chapter 3. We illustrate the usefulness of our approach on synthetic data and macroconfocal images. In the provided simulation results, we demonstrate the effectiveness of our approach.

§ 4.1 Introduction

Estimation of noise parameters is a classical problem in signal and image processing. In this context, for example, Donoho [Donoho, 1995] classically proposed to employ a robust Gaussian variance estimator from the wavelet coefficients of a single image, known as the median absolute deviation estimator (MAD). Since then, many alternative methods addressing this problem have been proposed [De Stefano et al., 2004], [Amer and Dubois, 2005], [Danielyan and Foi, 2009], [Li et al., 2010], [Pei et al., 2010], [Liu et al., 2011], [Abramov et al., 2012], [Tomaszewska, 2012] and from a Bayesian perspective, e.g. in [Dobigeon et al., 2009]. A more general problem has been investigated in [Grou-Szabo and Shibata, 2011] where the authors consider the mixture of a white Gaussian noise and a random impulsive noise.

Unfortunately, in many cases, the imaging noise is not additive. Due to the quantum nature of light, the images are degraded by shot noise, while thermal noise may play a less prominent role. Although a Gaussian approximation is well justified in some cases, one may need to consider noise mean or variance that depend on the image intensity. Consequently, studies related to image recovery in the presence of signal dependent noise constitutes an active area of research. Examples include restoration methods in the presence of Poisson [Pustelnik et al., 2011] and more recently Poisson-Gaussian noise [Luisier et al., 2011], [Jezierska et al., 2012a]. However, the associated noise identification problems have not yet been extensively studied in the literature. An intermediate step between additive stationary noise and signal dependent noise is to take advantage of variance stabilization techniques [Foi et al., 2008], [Uss et al., 2011]. Variance stabilization simplifies models by recovering the additivity and normality properties [Anscombe, 1948], [Fryzlewicz and Nason, 2004]. A review of some recent works in this direction is provided in [Foi, 2009b]. However, as already mentioned, little attention has been devoted to methods allowing us to acurately estimate the noise parameters. In this context, we should mention the contribution by Hwang *et al.* [Hwang et al., 2012] related to Poisson noise.

The present work is mainly motivated by the problem of estimating noise parameters in fluorescence macroconfocal images, which is a new tool in biomedical and pharmaceutic research. These images are characterized by a low signal-to-noise ratio. We assume that similarly to other fluorescence imaging systems, a major contribution to image noise stems from the photon counting process. However, we do not neglect other possible sources of noise resulting from electrical or thermal noise. Hence, we consider the noise to be distributed according to a Poisson-Gaussian law. Other types of images corrupted with such a noise include: hyperspectral [Acito et al., 2011], [Uss et al., 2011], computed tomography [Liao et al., 2012], radar [Lukin et al., 2008] and CCD camera [Foi et al., 2008] data.

In this chapter, we address the problem of estimating the parameters of Poisson-Gaussian noise. The problem is formulated within a variational framework. The proposed alternating optimization algorithm jointly estimates the signal of interest and the noise parameters from a single image. More precisely, the original target image x and the noise parameter vector θ are estimated from an observed image y in an inverse problem setting, by assuming that x admits a sparse gradient prior. We consider various choices of regularization functions promoting sparsity, including non-convex ones and both local and nonlocal choices of the neighborhood. The optimization proceeds iteratively by alternating the minimization of a label field and of the noise parameters.

The chapter is organized as follows. We review related works in Section 4.2. The model is introduced in Section 4.3. Then, the considered parameter estimation problem is presented in Section 4.4. Next, in Section 4.5

interesting special cases of our problem are discussed and the associated solutions are described. We provide experimental results in Section 4.6, where the performance of our approach is illustrated on both synthetic and real data. Finally, Section 4.7 concludes the chapter.

§ 4.2 Related work

In this section, we discuss existing techniques for noise parameter estimation. First, one can assume that a noise parametric model is available and that there are homogeneous regions in the image where the noise can be considered as stationary. This approach is fairly common as resulting methods are rather fast and efficient. Usually algorithms are defined as a two stage approach. The first task consists of finding the homogeneous image regions and the second performs the estimation of the parameters of the considered distribution model. The first task is performed by using either some segmentation methods [Liu et al., 2006], [Liu et al., 2008] or sliding window methods [Amer and Dubois, 2005], [Bosco et al., 2010]. The major disadvantage of this two-step approach is that the estimation performance is strongly dependent on the errors in the segmentation process. Alternatively, the assumption of a prior statistical model for the image can be exploited in addition to the noise model. For instance, in [De Stefano et al., 2004] it is assumed that the noise is Gaussian and the original image has a Laplacian distribution. The main drawback of this approach is that the image statistics are usually unknown. A simple prior model may however be defined in some transformed domain. For example, in [Donoho, 1995] it is assumed that the wavelet coefficient in the so-called HH subband are dominated by noise (the contribution from small image details being neglected). This model has been used for additive zero-mean white Gaussian noise parameter estimation [Li et al., 2010], but it was also combined with a segmentation step for the Poisson-Gaussian case [Foi et al., 2008].

The estimation of noise parameters in the presence of either multiplicative or Poisson noise is more challenging than for additive stationary Gaussian noise. Additional challenges arise from the noise non-stationarity. There have been many attempts to address this issue, for instance in the context of CCD camera [Liu et al., 2006], [Liu et al., 2008], [Foi et al., 2008], radar [Lukin et al., 2008], confocal microscopy [Bernas et al., 2007], [Delpretti et al., 2008], [Paul et al., 2010] and hyperspectral images [Aiazzi et al., 2006]. These methods are often tailored for some specific data. However, the general structure of all these approaches is similar to the model discussed above. Namely, they consist of determining pixel groups with uniform intensities [Liu et al., 2006], [Aiazzi et al., 2006], [Liu et al., 2008], [Lukin et al., 2008], [Bosco et al., 2010], [Abramov et al., 2010], [Liao et al., 2012] followed by a parameter fitting procedure.

Similarly to most of the mentioned techniques, our approach includes both a segmentation and an estimation process. However, unlike the previous works, the two main steps are repeated iteratively. At each iteration, the new partition and noise parameters are obtained by minimizing a cost function. In order to design such an optimization framework, we assume that the number of distinct intensity values present in the original image is known. Note that a similar strategy was previously introduced in [Paul et al., 2010], where the authors define a given number of histogram bins. In the following, the proposed cost function constrains the pixel values to belong to a relatively small finite set of intensities, and takes into account the spatial regularity of the associated label field. The algorithm we propose is inspired from the optimal quantization procedure described in Chapter 2. In both applications, the first step consists of finding the right partition (i.e. the sets of pixels whose intensities are assumed to be equal) provided that the size of the partition is known. The difference lies in the second step. In the quantization case, only the centroids of each class are computed while in the present case the centroids and corresponding noise parameters need to be found simultaneously.

§ 4.3 Model

Let x be the original image of size $N \times M$. Its values are assumed to belong to a finite set $\{u_1, \dots, u_K\}$ where $K \in \mathbb{N}^*$ is the number of distinct intensity values. We will denote by u the vector $[u_1, \dots, u_K]^\top \in \mathbb{R}^K$. We consider a partition $\mathbb{P} = (\mathbb{D}_k)_{1 \leqslant k \leqslant K}$ of the image support $\mathbb{X} = \{1, \dots, N\} \times \{1, \dots, M\}$, which is related to the image x through the following relation:

$$x = (u_{i_{\mathbb{P}}(\mathbf{s})})_{\mathbf{s} \in \mathbb{X}} \in \{u_1, \dots, u_K\}^{N \times M}, \tag{4.1}$$

where $\big(i_{\mathbb{P}}(\mathbf{s})\big)_{\mathbf{s} \in \mathbb{X}} \in \mathbb{I} = \{1, \dots, K\}^{N \times M}$ is a label image defined as

$$(\forall \mathbf{s} \in \mathbb{X})(\forall k \in \{1, \dots, K\}) \quad i_{\mathbb{P}}(\mathbf{s}) = k \quad \Leftrightarrow \quad \mathbf{s} \in \mathbb{D}_k. \tag{4.2}$$

Since x is a function of $i_{\mathbb{P}}$ and u, it will be denoted by $x_{i_{\mathbb{P}},u}$ throughout this paper.

The observed noisy image $y \in \mathbb{R}^{N \times M}$ is a realization of a random vector Y and is such that

$$y = \alpha\, q + w \tag{4.3}$$

where α is a positive scaling factor, and q (resp. w) are realizations of mutually independent random vectors Q (resp. $W = (W(\mathbf{s}))_{\mathbf{s} \in \mathbb{X}}$) with independent components. More precisely,

$$Q \sim \mathcal{P}(x_{i_{\mathbb{P}},u}) \tag{4.4}$$

$$(\forall \mathbf{s} \in \mathbb{X}) \quad W(\mathbf{s}) \sim \mathcal{N}(c, \sigma^2), \tag{4.5}$$

where $c \in \mathbb{R}$ and $\sigma \in (0, +\infty)$ are the mean and the standard deviation of the Gaussian noise component, respectively, and $\mathcal{P}(x)$ denotes a multivariate Poisson distribution with mean vector x.

Then, the parameter estimation problem corresponds to finding a vector of unknown noise parameters $\theta \in \mathcal{T}$, where $\theta = [c, \sigma^2, \alpha, u]^\top$ and $\mathcal{T}$ is the parameter set which is here equal to $\mathbb{R} \times (0, +\infty)^2 \times C$, C being a closed convex subset of $\mathbb{R}^K$. The unknown vector θ is related to the vector of observations y through the probability density function of Y, which has the following form: $\forall y = \big(y(\mathbf{s})\big)_{\mathbf{s}\in\mathbb{X}} \in \mathbb{R}^{N\times M}$,

$$p_Y(y; i_{\mathbb{P}}, \theta) = \prod_{k=1}^{K} \prod_{\mathbf{s}\in\mathbb{D}_k} \left(\sum_{q_{\mathbf{s}}=0}^{+\infty} \frac{e^{-u_k} \, (u_k)^{q_{\mathbf{s}}}}{q_{\mathbf{s}}!} \frac{e^{-\frac{(y(\mathbf{s})-\alpha q_{\mathbf{s}}-c)^2}{2\sigma^2}}}{\sqrt{2\pi\sigma^2}} \right). \tag{4.6}$$

§ 4.4 Problem formulation

We adopt a variational approach where the parameter vector θ is estimated by minimizing a penalized criterion. We have then to

$$\underset{(i_{\mathbb{P}},\theta)\in\mathbb{I}\times\mathcal{T}}{\text{minimize}} \quad \Phi(\theta, i_{\mathbb{P}}, y) + \rho(i_{\mathbb{P}}). \tag{4.7}$$

The above Φ is defined as the neg-log-likelihood of y:

$$\Phi(\theta, i_{\mathbb{P}}, y) = -\log\big(p_Y(y; i_{\mathbb{P}}, \theta)\big) \tag{4.8}$$

and ρ is a regularization function aiming at incorporating a-priori information about the homogeneity of the level sets of the image. Note that Problem (4.7) is non-convex due to the fact that $i_{\mathbb{P}}$ belongs to a (non-convex) set of discrete values.

We shall see that Problem (4.7) is a simple extension of the criteria, considered in Chapter 2. However, in the following instead of minimizing over vector u and $i_{\mathbb{P}}$, we minimize over θ and $i_{\mathbb{P}}$, where vector θ include values of u. Typical choices for regularization function ρ were discussed in Chapter 2. We refer the reader to (2.24), (2.25), (2.26), (2.27) for more details.

§ 4.5 Proposed approach

4.5.1 Algorithm

We propose the following alternating optimization algorithm:

Algorithm 7 Proposed algorithm

Initialization:
Fix $K \in \mathbb{N}^*$ and $\theta^{(0)} \in \mathcal{T}$.
Main loop:
For $\ell = 0, 1, \ldots$

$$i_{\mathbb{P}}^{(\ell)} \in \operatorname*{arg\,min}_{i_{\mathbb{P}} \in \mathbb{I}} \ \Phi(\theta^{(\ell)}, i_{\mathbb{P}}, y) + \rho(i_{\mathbb{P}})$$

$$\theta^{(\ell+1)} \in \operatorname*{arg\,min}_{\theta \in \mathcal{T}} \ \Phi(\theta, i_{\mathbb{P}}^{(\ell)}, y)$$

Assuming that noise parameters (α, c, σ) are known, the Algorithm 7 reduces to Algorithm 2. Consequently, the first step of the Algorithm 7, which consists of estimating $i_{\mathbb{P}}$, is unchanged with respect to the first step of Algorithm 2. Consequently the combinatorial methods discussed in Chapter 2 can be applied to this problem. Additional difficulties arise due to the second step of the proposed Algorithm 7, which is no longer convex. Hence, the previously derived PPXA+ algorithm (Algorithm 3) cannot be directly employed. However, some of the results of Chapter 3 may still be helpful. Note that there are three main differences with respect to the noise identification problem from time series discussed in the previous chapter. Firstly, the cardinalities of all partitions are not equal. Note that one can relate one time series with one partition. Previously we considered the number of samples in each time series to be equal. (The time series length in Chapter 3 was denoted by T.) Secondly, we do not here consider any signal decay within one partition. Hence, in the present chapter, we do not need to consider any exponential term. Finally, an additional challenge may stem from the constraint $u \in C$. We recall from Chapter 2 that, in the special case when ρ is defined as the anisotropic TV (2.25) with ψ given by the binary cost function defined in (2.27), then $C = \mathbb{R}^Q$. Otherwise, set C is employed to impose the total order constraint defined in (2.28).

4.5.2 Parameter update

In order to solve numerically the non-convex problem stated in the second step of Algorithm 7, we propose to employ the Expectation-Maximization (EM) algorithm [Dempster et al., 1977]. In such settings, the EM algorithm generates a sequence of estimates $(\theta^{(\ell)})_{\ell \in \mathbb{N}}$ which is given by

$$(\forall \ell \in \mathbb{N}) \qquad \theta^{(\ell+1)} = \operatorname*{argmin}_{\theta \in \mathcal{T}} \ \Phi(\theta \mid \theta^{(\ell)}) \tag{4.9}$$

where

$$\Phi(\theta \mid \theta^{(\ell)}) = \frac{1}{2\sigma^2} \sum_{\mathbf{s} \in \mathbb{S}} \mathsf{E}_{Q|Y=y,\theta^{(\ell)}}[(y(\mathbf{s}) - \alpha Q(\mathbf{s}) - c)^2] + \frac{NM}{2} \ln(\sigma^2)$$

$$+\sum_{k=1}^{K}\operatorname{card}(\mathbb{D}_k^{(\ell)})u_k-\sum_{k=1}^{K}\ln u_k\sum_{\mathbf{s}\in\mathbb{D}_k^{(\ell)}}\mathsf{E}_{Q|R=r,\theta^{(\ell)}}[Q(\mathbf{s})]. \quad (4.10)$$

and $(Q(\mathbf{s}))_{\mathbf{s}\in\mathbf{S}}$ are the components of Q as defined in (4.4) with $i_{\mathbb{P}}=i_{\mathbb{P}}^{(\ell)}$.

This leads to the following operations to be performed at each iteration ℓ:

1. Find $u^{(\ell+1)}$ as a solution of:

$$u^{(\ell+1)}\in\operatorname*{arg\,min}_{u\in C}\vartheta(u) \quad (4.11)$$

where $\vartheta(u)=\sum_{k=1}^{K}\vartheta_k(u_k)$, and, for every $k\in\{1,\dots,K\}$,

$$\vartheta_k(u_k)=\operatorname{card}(\mathbb{D}_k^{(\ell)})u_k-\ln u_k\sum_{\mathbf{s}\in\mathbb{D}_k^{(\ell)}}\mathsf{E}_{Q|R=r,\theta^{(\ell)}}[Q(\mathbf{s})]. \quad (4.12)$$

In the unconstrained case when $C=\mathbb{R}^K$, we have then

$$u^{(\ell+1)}=\frac{\sum_{\mathbf{s}\in\mathbb{D}_k^{(\ell)}}\mathsf{E}_{Q|R=r,\theta^{(\ell)}}[Q(\mathbf{s})]}{\operatorname{card}(\mathbb{D}_k^{(\ell)})}. \quad (4.13)$$

On the other hand, for some regularization terms (see Section 2.3), set C is useful to impose a total order constraint. This amounts to minimizing ϑ under the constraints that $Vu\in D=[\delta,+\infty[\times[0,+\infty[^{K-1}$ where δ is some small positive value, and V is the linear operator defined as

$$\begin{aligned}V\colon\mathbb{R}^K&\to\mathbb{R}^K\\(u_1,\dots,u_K)&\mapsto\big(u_1,u_2-u_1,\dots,u_K-u_{K-1}\big).\end{aligned} \quad (4.14)$$

2. Determine $c^{(\ell+1)}$ and $\alpha^{(\ell+1)}$ by solving the following system of linear equations:

$$\begin{bmatrix}NM & \sum_{\mathbf{s}}\mathsf{E}_{Q|Y=y,\theta^{(\ell)}}[Q(\mathbf{s})]\\ \sum_{\mathbf{s}}\mathsf{E}_{Q|Y=y,\theta^{(\ell)}}[Q(\mathbf{s})] & \sum_{\mathbf{s}}\mathsf{E}_{Q|Y=y,\theta^{(\ell)}}[Q(\mathbf{s})^2]\end{bmatrix}\begin{bmatrix}c^{(\ell+1)}\\ \alpha^{(\ell+1)}\end{bmatrix}$$
$$=\begin{bmatrix}\sum_{\mathbf{s}}y(\mathbf{s})\\ \sum_{\mathbf{s}}y(\mathbf{s})\mathsf{E}_{Q|Y=y,\theta^{(\ell)}}[Q(\mathbf{s})]\end{bmatrix}. \quad (4.15)$$

3. Compute $(\sigma^2)^{(\ell+1)}$ as

$$\frac{\sum_{\mathbf{s}} y(\mathbf{s}) \left(y(\mathbf{s}) - \alpha^{(\ell+1)} \mathsf{E}_{Q|Y=y,\theta^{(\ell)}}[Q(\mathbf{s})] - c^{(\ell+1)} \right)}{NM}. \tag{4.16}$$

Note that even when a closed form solution to Problem (4.11) does not exist, it can still be solved efficiently using proximal tools. We propose to solve numerically this problem by using a primal-dual proximal algorithm [Combettes and Pesquet, 2012].

Algorithm 8 Primal-dual algorithm for solving (4.11)

Initialization

$\gamma \in (0, +\infty)$, $u_1^{(0)} \in \mathbb{R}^K$, $v_1^{(0)} \in \mathbb{R}^K$.

Main loop

For $j = 0, \ldots$

$w_1^{(j)} = u^{(j)} - \gamma V^\top v_1^{(j)}$
$p_1^{(j)} = \mathrm{prox}_{\gamma\vartheta}(w_1^{(j)})$
$w_2^{(j)} = v_1^{(j)} + \gamma V u^{(j)}$
$p_2^{(j)} = w_2^{(j)} - \gamma P_D(\gamma^{-1} w_2^{(j)})$
$v_1^{(j+1)} = v_1^{(j)} - w_2^{(j)} + p_2^{(j)} + \gamma V p_1^{(j)}$
$u^{(j+1)} = u^{(j)} - w_1^{(j)} + p_1^{(j)} - \gamma V^\top p_2^{(j)}$

In the above algorithm, we denote the projector onto the closed convex set D by P_D. The proximity operator of $\gamma\vartheta$ with and $\gamma > 0$ admits a closed form expression [Combettes and Pesquet, 2011] and it is given by

$$\left(\forall u = (u_k)_{1\leq k\leq K} \in \mathbb{R}^K\right) \quad \mathrm{prox}_{\gamma\vartheta}(u) = \left(\mathrm{prox}_{\gamma\vartheta_k}(u_k)\right)_{1\leq k\leq K} \tag{4.17}$$

where, for every $k \in \{1, \ldots, K\}$,

$$\mathrm{prox}_{\gamma\vartheta_k}(u_k) = \frac{1}{2}\Big(u_k - \mathrm{card}(\mathbb{D}_k) + \sqrt{|u_k - \mathrm{card}(\mathbb{D}_k)|^2 + 4 \sum_{\mathbf{s}\in\mathbb{D}_k} \mathsf{E}_{Q|R=r,\theta^{(\ell)}}[Q(\mathbf{s})]}\Big). \tag{4.18}$$

The convergence of the primal-dual algorithm is guaranteed by the following result deduced from [Combettes and Pesquet, 2012, Theorem 4.2].

Theorem 4.5.1 *Under the assumptions that $\gamma \in [\epsilon, (1-\epsilon)/\beta]$ where $\epsilon \in (0, 1/(\beta+1))$ and $\beta = \|V\|$, there exists a minimizer $\widehat{u}$ of (4.11) such that the sequences $\left(u^{(j)}\right)_{j\in\mathbb{N}}$ and $\left(p_1^{(j)}\right)_{j\in\mathbb{N}}$ converge to $\widehat{u}$.*

Concerning the computation of the required conditional expectation values, it can be shown that, for every $\mathbf{s} \in \mathbb{X}$,

$$\mathsf{E}_{Q|Y=y,\theta^{(\ell)}}[Q(\mathbf{s})] = \frac{\zeta_{\mathbf{s}}^{(\ell)}}{\eta_{\mathbf{s}}^{(\ell)}} \quad \text{and} \quad \mathsf{E}_{Q|Y=y,\theta^{(\ell)}}[Q(\mathbf{s})^2] = \frac{\xi_{\mathbf{s}}^{(\ell)}}{\eta_{\mathbf{s}}^{(\ell)}} \tag{4.19}$$

where

$$\zeta_{\mathbf{s}}(\theta^{(\ell)}) = \sum_{q_{\mathbf{s}}=0}^{\infty} \Pi_{\mathbf{s}}(\theta^{(\ell)}, 1, q_{\mathbf{s}}) \tag{4.20}$$

$$\eta_{\mathbf{s}}(\theta^{(\ell)}) = \sum_{q_{\mathbf{s}}=0}^{\infty} \Pi_{\mathbf{s}}(\theta^{(\ell)}, 0, q_{\mathbf{s}}) \tag{4.21}$$

$$\xi_{\mathbf{s}}(\theta^{(\ell)}) = \sum_{q_{\mathbf{s}}=0}^{\infty} \Pi_{\mathbf{s}}(\theta^{(\ell)}, 1, q_{\mathbf{s}}) + \sum_{q_{\mathbf{s}}=0}^{\infty} \Pi_{\mathbf{s}}(\theta^{(\ell)}, 2, q_{\mathbf{s}}) \tag{4.22}$$

In these formulas, for every $(d, q_{\mathbf{s}}) \in \mathbb{N}^2$,

$$\Pi_{\mathbf{s}}(\theta, d, q_{\mathbf{s}}) = \exp\left(-\frac{(y(\mathbf{s}) - \alpha(q_{\mathbf{s}} + d) - c)^2}{2\sigma^2}\right) \frac{(u_{i_{\mathbb{P}}^{(\ell)}(\mathbf{s})})^{q_{\mathbf{s}}+d}}{q_{\mathbf{s}}!}. \tag{4.23}$$

The infinite summations in (4.20), (4.21) and (4.22) are approximated by finite sums with the following bounds:

$$q_{\mathbf{s}}^{+} = q_{\mathbf{s}}^{*} + \Delta\frac{\sigma}{\alpha}, \qquad q_{\mathbf{s}}^{-} = q_{\mathbf{s}}^{*} - \Delta\frac{\sigma}{\alpha} \tag{4.24}$$

where $q_{\mathbf{s}}^{*} = \frac{\sigma^2}{\alpha^2}\mathsf{W}\left(\frac{\alpha^2}{\sigma^2}u_{i_{\mathbb{P}}^{(\ell)}(\mathbf{s})}e^{\frac{\alpha}{\sigma^2}(y(\mathbf{s})-c-d\alpha)}\right)$. Here, W denotes the Lambert product logarithm function and $\Delta > 0$. This choice has been shown to ensure a fast decay of the approximation error as a function of Δ.

4.5.3 Patch-based initialization

Since Problem (4.7) is non-convex, the proposed approach is sensitive to initialization. In the following, we propose an initialization procedure based on image patches. Firstly, the observed image y is decomposed into non overlapping patches $\Theta y = \{\Theta y_1, \ldots, \Theta y_O\}$, where O stands for the total number of patches. Next, we compute the vectors $\mathsf{mean}\,(\Theta y) \in \mathbb{R}^O$ and $\mathrm{var}\,(\Theta y) \in \mathbb{R}^O$, whose elements are the mean and the variance over the pixels belonging to each patch, respectively. Under the assumption that the intensity of each patch is constant, the mean and variance of the patch is given by: $\forall o \in \{1, \ldots, O\}$,

$$[\mathrm{mean}\,(\Theta y)]_o = \alpha\upsilon_o + c \tag{4.25}$$

$$[\mathrm{var}\,(\Theta y)]_o = \alpha^2\upsilon_o + \sigma^2 \tag{4.26}$$

where $v_o \in \{u_1, \ldots, u_K\}$. Although, the assumption about the constant intensity of each patch is not exactly satisfied, an approximation $\theta^{(0)}$ of the parameter vector is given by

- $\alpha^{(0)} = [\text{var } (\Theta y)]_{o_1} / [\text{mean } (\Theta y)]_{o_1}$,
  where $o_1 = \arg\max_{o \in \{1,\ldots,O\}} [\text{mean } (\Theta y)]_o$

- $c^{(0)} = \min_{o \in \{1,\ldots,O\}} [\text{mean } (\Theta y)]_o$

- $\left(\sigma^2\right)^{(0)} = [\text{var } (\Theta y)]_{o_2}$,
  where $o_2 = \arg\min_{o \in \{1,\ldots,O\}} [\text{mean } (\Theta y)]_o$.

- $u_1^{(0)} = \epsilon$, where ϵ is a small value greater than 0, and $(\forall k \in \{2, \ldots, K\})$ $u_k^{(0)} = u_{k-1}^{(0)} + u_{\max}/(K-1)$. The maximum intensity value $u_{\max}$ of x is assumed to be known.

Note that in contrast with the approach proposed in Chapter 3 the EM algorithm is started iteratively. In each iteration, it is initialized with a better parameter set.

§ 4.6 Results

The aim of this section is to illustrate the performance of the proposed noise identification method with synthetic and real data examples. We experimentally evaluate the robustness of our model under different working conditions integrated into the algorithmic framework from Section 4.5. Hence, for all presented experiments in this section we fix the patch size to 12×12, $Q = 20$, $\epsilon = 0.2$ and ρ to the anisotropic total variation (2.25). Moreover, for different experiments we set the regularization parameter μ to 1.3 when ψ is the binary cost function (2.27) and to 0.8 when it is the identity.

The results presented in Fig. 4.1 indicate that in the four considered cases the reconstructed noise parameters are subject to small error with respect to the true values. In the first experiment we use a neuron phantom [Dupé, 2008] as an original image (Fig. 4.1 (a)) whose intensities range between 0.25 and 17.25. Hence, we set $u_{\max} = 20$. The image is then corrupted by noise with parameters $\alpha = 20$, $c = 100$, $\sigma^2 = 1000$ (Fig. 4.1 (b)). The noise identification procedure with ψ given by binary cost function (2.27) is applied yielding $\widehat{\alpha} = 19.8$, $\widehat{c} = 103$, $\widehat{\sigma}^2 = 1039$.

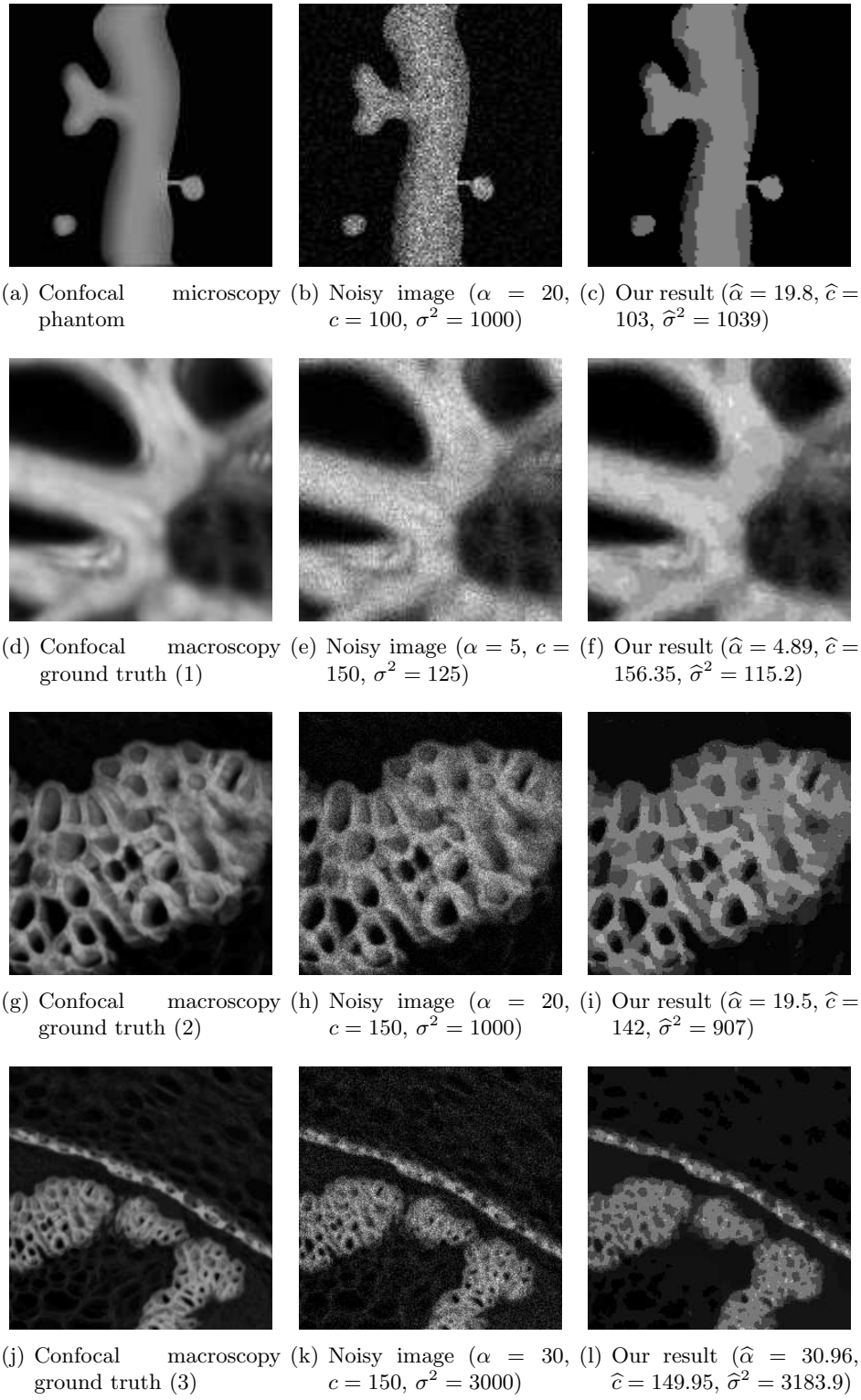

(a) Confocal microscopy phantom

(b) Noisy image ($\alpha = 20$, $c = 100$, $\sigma^2 = 1000$)

(c) Our result ($\widehat{\alpha} = 19.8$, $\widehat{c} = 103$, $\widehat{\sigma}^2 = 1039$)

(d) Confocal macroscopy ground truth (1)

(e) Noisy image ($\alpha = 5$, $c = 150$, $\sigma^2 = 125$)

(f) Our result ($\widehat{\alpha} = 4.89$, $\widehat{c} = 156.35$, $\widehat{\sigma}^2 = 115.2$)

(g) Confocal macroscopy ground truth (2)

(h) Noisy image ($\alpha = 20$, $c = 150$, $\sigma^2 = 1000$)

(i) Our result ($\widehat{\alpha} = 19.5$, $\widehat{c} = 142$, $\widehat{\sigma}^2 = 907$)

(j) Confocal macroscopy ground truth (3)

(k) Noisy image ($\alpha = 30$, $c = 150$, $\sigma^2 = 3000$)

(l) Our result ($\widehat{\alpha} = 30.96$, $\widehat{c} = 149.95$, $\widehat{\sigma}^2 = 3183.9$)

Figure 4.1: *Single image noise identification results*

The results of the time series noise identification procedure described in Chapter 3 provide a ground truth for next experiments (Fig. 4.1 (d-l)). In order to show the versatility of our model, we use ψ defined as the identity function for experiments presented in Fig. 4.1 (d-f) and Fig. 4.1 (j-l), and the binary cost function for experiment illustrated in images Fig. 4.1 (g-i). We recall that for the identity function, the constrained problem needs to be taken into account in the EM step. For these three experiments $u_{\max}$ is set to 150, 40 and 512 respectively. In the first case, image in Fig. 4.1 (d) was corrupted by noise with parameters $\alpha = 5$, $c = 150$, $\sigma^2 = 125$. The identified noise parameters are $\widehat{\alpha} = 4.89$, $\widehat{c} = 156.35$, $\widehat{\sigma}^2 = 115.2$. In the second case Fig. 4.1 (h) the estimated value of $\alpha = 20$, $c = 150$, $\sigma^2 = 1000$ are $\widehat{\alpha} = 19.5$, $\widehat{c} = 142$, $\widehat{\sigma}^2 = 907$. The corresponding visual results are presented in Fig. 4.1 (i). Finally, for $\alpha = 30$, $c = 150$, $\sigma^2 = 3000$ we get $\widehat{\alpha} = 30.96$, $\widehat{c} = 149.95$, $\widehat{\sigma}^2 = 3183.9$ (see Fig. 4.1 (h)). This experiment shows that the proposed procedure provides reliable results. The presence of a regularization parameter does not appear to be a significant disadvantage. Indeed our experiments show that for various images, similar choices of regularization parameter leads to good noise identification results.

§ 4.7 Conclusions

Noise arises in all images as an effect of the imperfectness of image acquisition systems and of the stochastic nature of light. As a consequence, it is sometimes included into image models, often in a parametric manner. One of the relevant problems in image processing is to estimate the parameters of these arising models. In the previous chapter we have presented a method for noise identification from time-series. The developed statistical framework validates the theoretical results related to approximation of Poisson-Gaussian neg-log likelihood. Here, we have shown how these results can be incorporated into a reliable, single image noise estimation method. This work also suggests to expect that the algorithmic concepts proposed in Chapter 2 can be used across a broad area of applications. Here, Algorithm 7 is developed as a simple extension of Algorithm 2. The simulation results demonstrate the usefulness of our approach on synthetic data and macro-confocal images. Finally, we identify several directions for future work. One possible extension would be to consider the single image noise estimation problem for other complex noise distributions. The estimation results also can be further improved by using a more flexible regularization term, e.g. non-local TV and a more carefully chosen initialization.

- Chapter 5 -

Image Restoration in the presence of Poisson-Gaussian noise

This chapter[1] marks the beginning of the central part of our work related to restoring data corrupted by Poisson-Gaussian noise. A Poisson-Gaussian model may accurately describes the noise present in a significant variety of imaging systems. However most existing restoration strategies rely on approximations of the Poisson-Gaussian noise statistics. We propose a convex optimization algorithm for the reconstruction of signals degraded by a linear operator and corrupted with a mixed Poisson-Gaussian noise. The originality of our approach consists of considering the exact, mixed continuous-discrete model corresponding to the data statistics. After establishing the Lipschitz differentiability and convexity of the Poisson-Gaussian neg-log likelihood, we derive a primal-dual iterative scheme for minimizing the associated penalized criterion. The proposed method is applicable to a large choice of convex penalty terms. The robustness of our scheme allows us to handle computational difficulties due to infinite sums arising from the computation of the gradient of the criterion. The proposed approach is validated on image restoration examples.

§ 5.1 Introduction

Noise in a large variety of real imaging systems can be accurately described through a mixed Poisson-Gaussian model. For example, it is frequently encountered in astronomy [Benvenuto et al., 2008], [Snyder et al., 1993], medicine [Nichols et al., 2002] and biology [Delpretti et al., 2008]. There has been a growing interest for denoising problems involving images corrupted in this fashion [Luisier et al., 2011], [Boracchi and Foi, 2008], [Begovic

[1] Published in part in Proc. of ICASSP, 2012

et al., 2011]. However, the literature involving this model together with deconvolution and reconstruction problems remains scarse. Among existing works, Benvenuto *et al.* [Benvenuto et al., 2008] proposed a scaled gradient method and more recently Gil-Rodrigo *et al.* [Gil-Rodrigo et al., 2011] developed an alternating minimization algorithm. An augmented Lagrangian method grounded on a Poisson approximation of noise characteristics was proposed in [Chakrabarti and Zickler, 2012], while a similar framework with a weighted squared ℓ_2 norm noise approximation was proposed in [Li et al., 2012].

Generally, restoration strategies are grounded on some approximations of the noise statistics, which may be detrimental to the quality of the results. The use of approximations is motivated by the mathematical difficulties raised by the Poisson-Gaussian model. Indeed, the corresponding probability distribution has a discrete-continuous nature, and the expression of the associated log-likelihood function involves an infinite sum. For simplification, one usually neglects either the Poisson or the Gaussian component, or performs an approximation of the Poisson-Gaussian model based on variance stabilization techniques [Murtagh et al., 1995], [Foi, 2009a].

In this chapter, we investigate the properties of the Poisson-Gaussian negative log-likelihood, showing that it is a convex Lipschitz differentiable function. Since the gradient of the Poisson-Gaussian neg-log likelihood requires the computation of infinite series, we propose to utilize proximal optimization methods, since their convergence is guaranteed even in the presence of summable numerical errors. Among recent approaches, only a few primal-dual splitting algorithms [Combettes and Pesquet, 2012], [Raguet et al.], [Condat, 2012], [Vu, 2011] can cope with the sum of a gradient Lipschitz term and a possibly non-smooth penalty term. Such a term can model a wide range of prior information, e.g. criteria promoting sparsity in a frame, total-variation and more generally hybrid regularization functions.

The chapter is organized as follows: Section 5.2 investigates the Poisson-Gaussian model and introduces the notation used in this work. Section 5.3 describes the proposed optimization framework. Our approach is illustrated via experiments in Section 5.4. Finally, some conclusions are drawn in Section 5.5.

§ 5.2 Degradation model

Let $y \in \mathbb{R}^Q$ be a vector of observations related to an original signal $x \in [0,+\infty)^N$ through the model $y = z(x) + w$, where $z(x) = \big(z_i(x)\big)_{1\leq i\leq Q}$ and $w = (w_i)_{1\leq i\leq Q}$ are realizations of mutually independent random vectors $Z(x) = \big(Z_i(x)\big)_{1\leq i\leq Q}$ and $W = (W_i)_{1\leq i\leq Q}$ having independent components.

It is further assumed that, for every $i \in \{1, \ldots, Q\}$,

$$Z_i(x) \sim \mathcal{P}([Hx]_i) \tag{5.1}$$
$$W_i \sim \mathcal{N}(c, \sigma^2), \tag{5.2}$$

where H is a matrix in $[0, +\infty)^{Q \times N}$ modeling the degradation process (e.g., a convolution operator) and $(c, \sigma) \in \mathbb{R} \times (0, +\infty)$ are the mean and standard deviation, respectively, of the Gaussian noise component. Hence, y is a realization of a random vector Y with probability density function

$$p_Y(y; x) = \prod_{i=1}^{Q} \left(\sum_{n=0}^{+\infty} \frac{e^{-[Hx]_i} ([Hx]_i)^n}{n!} \frac{e^{-\left(\frac{y_i - c - n}{\sqrt{2}\sigma}\right)^2}}{\sqrt{2\pi\sigma^2}} \right) \tag{5.3}$$

In the context of inverse problems, the original signal can be recovered by minimizing a penalized criterion:

$$\min_{x \in \mathbb{R}^N} \left(f(x) = \Phi(x) + \rho(x) \right), \tag{5.4}$$

where Φ is the so-called data fidelity term and ρ is a regularization function incorporating *a priori* information, so as to guarantee the stability of the solution w.r.t. the observation noise. In the Bayesian framework, this allows us to compute the *maximum a posteriori* (MAP) estimate [Demoment, 1989] of the original image. In this context, the data fidelity term is defined as the negative logarithm of $p_Y(y; x)$:

$$\begin{aligned} \Phi(x) &= -\log(p_Y(y; x)) \\ &= \sum_{i=1}^{Q} \Phi_i([Hx]_i) \end{aligned} \tag{5.5}$$

where for all $i \in \{1, \ldots, Q\}$

$$\Phi_i([Hx]_i) = -\log \left(\sum_{n=0}^{+\infty} \frac{e^{-[Hx]_i} ([Hx]_i)^n}{n!} \frac{e^{-\left(\frac{y_i - c - n}{\sqrt{2}\sigma}\right)^2}}{\sqrt{2\pi\sigma^2}} \right) \tag{5.6}$$

and the regularization term ρ corresponds to the potential of the chosen prior probability distribution.

The gradient and Hessian of Φ on the positive orthant are given by $\left(\forall x \in [0, +\infty)^N\right)$

$$\nabla \Phi(x) = H^\top (\mathbf{1} - \xi(Hx)) \tag{5.7}$$
$$\nabla^2 \Phi(x) = H^\top \operatorname{diag}\left(\eta_i([Hx]_i)\right) H \tag{5.8}$$

where, for every $z = (z_i)_{1\leq i\leq Q} \in [0,+\infty)^Q$, $\xi(z) = \big(\xi_i(z_i)\big)_{1\leq i\leq Q}$, $\eta(z) = \big(\eta_i(z_i)\big)_{1\leq i\leq Q}$ with

$$\xi_i(z_i) = s(z_i, y_i - c - 1)/s(z_i, y_i - c) \tag{5.9}$$

$$\eta_i(z_i) = \frac{\left(s(z_i, y_i - c - 1)\right)^2 - s(z_i, y_i - c)s(z_i, y_i - c - 2)}{\left(s(z_i, y_i - c)\right)^2}, \tag{5.10}$$

and, for every $(a, b) \in \mathbb{R}^2$,

$$s(a,b) = \sum_{n=0}^{+\infty} \frac{a^n}{n!} e^{-\left(\frac{b-n}{\sqrt{2}\sigma}\right)^2}. \tag{5.11}$$

We recall that proximal splitting strategy consists of decomposing f into a sum of simpler convex functions such that either an element of the sum is μ-Lipschitz differentiable or the closed form solution of the associated proximity operator exists. In view of this, the two following results become useful.

Theorem 5.2.1 *The function Φ is μ-Lipschitz differentiable on $[0,+\infty)^N$ with*

$$\mu = \|H\|^2 \left(1 - e^{-\frac{1}{\sigma^2}}\right) \exp\left(\left(2 \max_{i\in\{1,\dots,Q\}} \{y_i\} - 2c - 1\right)/\sigma^2\right). \tag{5.12}$$

Proof. The proof consists of showing that $\eta_i(z_i)$ is upper bounded over the domain $z_i \geqslant 0$ by $\eta_i(0)$. Firstly, we note that for $z_i = 0$ the infinite sum (5.11) simplifies to the first sum element, i.e. $s(0,b) = e^{-\frac{1}{2\sigma^2}(b)^2}$, where we have set $b = y_i - c$. Hence,

$$\eta_i(0) = \left(1 - e^{-\frac{1}{\sigma^2}}\right) e^{\frac{1}{\sigma^2}(2b-1)} \tag{5.13}$$

and $\forall z_i \in (0,+\infty)$,

$$\begin{aligned}
&\eta_i(0) - \eta_i(z_i) \geqslant 0 \qquad (5.14)\\
&\Leftrightarrow \left(s(z_i,b)\right)^2 \eta_i(0) - \Big(\left(s(z_i,b-1)\right)^2 - s(z_i,b)s(z_i,b-2)\Big) \geqslant 0\\
&\Leftrightarrow \sum_{m=0}^{\infty}\sum_{n=0}^{\infty} \frac{z_i^{m+n}}{m!n!} \Bigg(e^{\frac{-(b-m)^2-(b-n)^2}{2\sigma^2}} \eta_i(0) -\\
&\qquad\qquad e^{\frac{-(b-1-m)^2-(b-1-n)^2}{2\sigma^2}} + e^{\frac{-(b-m)^2-(b-2-n)^2}{2\sigma^2}} \Bigg) \geqslant 0\\
&\Leftrightarrow \sum_{m=0}^{\infty}\sum_{n=0}^{\infty} \frac{z_i^{m+n}}{m!n!} e^{\frac{-(b-n)^2-(b-m)^2+4b-2}{2\sigma^2}}\\
&\qquad\qquad \left\{\left(1 - e^{-\frac{n+m}{\sigma^2}}\right) + e^{-\frac{1}{\sigma^2}}\left(e^{-\frac{2n}{\sigma^2}} - 1\right)\right\} \geqslant 0
\end{aligned}$$

$$\Leftrightarrow \sum_{m=0}^{\infty}\sum_{n=0}^{m-1}\frac{z_i^{m+n}}{m!n!}e^{\frac{-(b-n)^2-(b-m)^2+4b-2}{2\sigma^2}} \left\{2\left(1-e^{-\frac{n+m}{\sigma^2}}\right)\left(1-e^{-\frac{1}{\sigma^2}}\right)+e^{-\frac{1}{\sigma^2}}\left(e^{-\frac{n}{\sigma^2}}-e^{-\frac{m}{\sigma^2}}\right)^2\right\}+ \sum_{m=0}^{\infty}\frac{z_i^{2m}}{(m!)^2}e^{\frac{-(b-m)^2+2b-1}{\sigma^2}}\left\{(1-e^{-\frac{2m}{\sigma^2}})(1-e^{-\frac{1}{\sigma^2}})\right\}\geqslant 0.$$

Hence the expression of the μ-Lipschitz in (5.12) is obtained by finding the maximum value of $\eta_i(0)$ for all possible values of $i \in \{1,\dots,Q\}$. □

The next convexity result can be regarded as the extension of the one presented in [Benvenuto et al., 2008].

Theorem 5.2.2 *The neg-log likelihood $\Phi^{(\beta)}$ of a mixture of Generalized-Gaussian and Poisson variables defined over the positive orthant as*

$$\Phi^{(\beta)}(x)=\sum_{i=1}^{Q}\Phi_i^{(\beta)}([Hx]_i) \tag{5.15}$$

where for all $i \in \{1,\dots,Q\}$

$$\Phi_i^{(\beta)}([Hx]_i)=-\log\left(\sum_{n=0}^{+\infty}\frac{e^{-[Hx]_i}([Hx]_i)^n}{n!}\frac{\beta}{2\sqrt{2}\sigma\Gamma(\frac{1}{\beta})}e^{-\left(\frac{|y_i-c-n|}{\sqrt{2}\sigma}\right)^{\beta}}\right) \tag{5.16}$$

is strictly convex if $\beta>1$ and convex if $\beta=1$.

Proof. The proof consists of showing that $\forall a \in (0,+\infty)$,

$$\begin{cases}\ddot{\Phi}_i^{(\beta)}(a)>0 \text{ if } \beta>1\\ \ddot{\Phi}_i^{(\beta)}(a)\geqslant 0 \text{ if } \beta=1\end{cases} \tag{5.17}$$

where

$$\ddot{\Phi}_i^{(\beta)}(a)=\frac{\left(s^{(\beta)}(a,y_i-c-1)\right)^2-s^{(\beta)}(a,y_i-c)s^{(\beta)}(a,y_i-c-2)}{\left(s^{(\beta)}(a,y_i-c)\right)^2}, \tag{5.18}$$

$\forall b \in \mathbb{R}$

$$s^{(\beta)}(a,b)=\sum_{n=0}^{+\infty}\frac{a^n}{n!}\zeta_b^{(\beta)}(n), \tag{5.19}$$

and $\zeta_b^{(\beta)}(\cdot)=e^{-\left(\frac{|\cdot-b|}{\sqrt{2}\sigma}\right)^{\beta}}$.

Thus we turn our attention to the numerator of $\ddot{\Phi}_i^{(\beta)}$. For all $a \in [0, +\infty)$, $b \in \mathbb{R}$ and positive β the following holds:

$$
\begin{aligned}
&\left(s^{(\beta)}(a, b-1)\right)^2 - s^{(\beta)}(a,b)s^{(\beta)}(a,b-2) \geqslant 0 \qquad (5.20)\\
&\Leftrightarrow \sum_{m=0}^{\infty}\sum_{n=0}^{\infty} \frac{a^{n+m}}{n!m!}\left(\zeta_b^{(\beta)}(m+1)\zeta_b^{(\beta)}(n+1) - \zeta_b^{(\beta)}(m)\zeta_b^{(\beta)}(n+2)\right) \geqslant 0\\
&\Leftrightarrow \sum_{m=0}^{\infty}\sum_{n=1}^{\infty} \frac{a^{n+m-1}}{n!m!} n\left(\zeta_b^{(\beta)}(m+1)\zeta_b^{(\beta)}(n) - \zeta_b^{(\beta)}(m)\zeta_b^{(\beta)}(n+1)\right) \geqslant 0\\
&\Leftrightarrow \sum_{m=0}^{\infty}\sum_{n=0}^{\infty} \frac{a^{n+m-1}}{n!m!} n\left(\zeta_b^{(\beta)}(m+1)\zeta_b^{(\beta)}(n) - \zeta_b^{(\beta)}(m)\zeta_b^{(\beta)}(n+1)\right) \geqslant 0\\
&\Leftrightarrow \sum_{m=0}^{\infty}\left\{\sum_{n=0}^{m} \frac{a^{n+m-1}}{n!m!} n\left(\zeta_b^{(\beta)}(m+1)\zeta_b^{(\beta)}(n) - \zeta_b^{(\beta)}(m)\zeta_b^{(\beta)}(n+1)\right) + \right.\\
&\qquad\qquad \left.\sum_{n=m}^{\infty} \frac{a^{n+m-1}}{n!m!} n\left(\zeta_b^{(\beta)}(m+1)\zeta_b^{(\beta)}(n) - \zeta_b^{(\beta)}(m)\zeta_b^{(\beta)}(n+1)\right)\right\} \geqslant 0\\
&\Leftrightarrow \sum_{m=0}^{\infty}\left\{\sum_{n=0}^{m} \frac{a^{n+m-1}}{n!m!} n\left(\zeta_b^{(\beta)}(m+1)\zeta_b^{(\beta)}(n) - \zeta_b^{(\beta)}(m)\zeta_b^{(\beta)}(n+1)\right) + \right.\\
&\qquad\qquad \left.\sum_{n=0}^{m} \frac{a^{n+m-1}}{n!m!} m\left(\zeta_b^{(\beta)}(n+1)\zeta_b^{(\beta)}(m) - \zeta_b^{(\beta)}(n)\zeta_b^{(\beta)}(m+1)\right)\right\} \geqslant 0\\
&\Leftrightarrow \sum_{m=0}^{\infty}\sum_{n=0}^{m} \frac{a^{n+m-1}}{n!m!}(m-n)\left(\zeta_b^{(\beta)}(n+1)\zeta_b^{(\beta)}(m) - \zeta_b^{(\beta)}(n)\zeta_b^{(\beta)}(m+1)\right) \geqslant 0.
\end{aligned}
$$

Next, we show that each element of the above sum is positive, i.e. $\forall a \in (0, +\infty)$, $\forall b \in \mathbb{R}$, $\forall n \in \mathbb{N}$, $\forall m \in \mathbb{N}$ and $m > n$

$$
\begin{aligned}
&\frac{a^{n+m-1}}{n!m!}(m-n)\left(\zeta_b^{(\beta)}(n+1)\zeta_b^{(\beta)}(m) - \zeta_b^{(\beta)}(n)\zeta_b^{(\beta)}(m+1)\right) \geqslant 0\\
&\Leftrightarrow \zeta_b^{(\beta)}(n+1)\zeta_b^{(\beta)}(m) - \zeta_b^{(\beta)}(n)\zeta_b^{(\beta)}(m+1) \geqslant 0\\
&\Leftrightarrow \exp\left(-\left(\frac{|b-n-1|}{\sigma}\right)^{\beta} - \left(\frac{|b-m|}{\sigma}\right)^{\beta}\right) -\\
&\qquad\qquad \exp\left(-\left(\frac{|b-n|}{\sigma}\right)^{\beta} - \left(\frac{|b-m-1|}{\sigma}\right)^{\beta}\right) \geqslant 0\\
&\Leftrightarrow |b-n|^{\beta} - |b-n-1|^{\beta} - (|b-m|^{\beta} - |b-m-1|^{\beta}) \geqslant 0. \qquad (5.21)
\end{aligned}
$$

The above inequality holds if the function

$$\begin{aligned} \pi^{(\beta)} \ &: \mathbb{R} \to \mathbb{R} \\ &u \mapsto |u|^{\beta} - |u-1|^{\beta} \end{aligned} \tag{5.22}$$

is increasing over its domain. In this way, we study the positivity of the derivative of the function $\pi^{(\beta)}$ over its domain. The singularity points, i.e. $u \in \{0,1\}$, can be excluded from the study due to the continuity of $\pi^{(\beta)}$. We firstly note that $\forall u \in \mathbb{R}$

$$\operatorname{sign}(u-1) = \begin{cases} -\operatorname{sign}(u) & \text{if } \ u \in (0,1) \\ \operatorname{sign}(u) & \text{otherwise.} \end{cases} \tag{5.23}$$

Then, for $\beta \geqslant 1$ and $u \in \mathbb{R} \setminus \{0,1\}$ the derivative is given by

$$\begin{aligned} \frac{\partial(\pi^{(\beta)}(u))}{\partial u} &= \beta \left(\operatorname{sign}(u)\,|u|^{\beta-1} - \operatorname{sign}(u-1)\,|u-1|^{\beta-1}\right) \\ &= \begin{cases} \beta \left(|u|^{\beta-1} + |u-1|^{\beta-1}\right) & \text{if } \ u \in (0,1) \\ \beta \operatorname{sign}(u)(|u|^{\beta-1} - |u-1|^{\beta-1}) & \text{if } \ u \in (-\infty,0) \cup (1,\infty) \end{cases} \end{aligned} \tag{5.24}$$

and

$$\operatorname{sign}\left(\frac{\partial(\pi^{(\beta)}(u))}{\partial u}\right) = \begin{cases} \operatorname{sign}\left(1 - |u/u-1|^{\beta-1}\right) & \text{if } \ u \in (-\infty,0) \\ \operatorname{sign}\left(|u/u-1|^{\beta-1} + 1\right) & \text{if } \ u \in (0,1) \\ \operatorname{sign}\left(|u/u-1|^{\beta-1} - 1\right) & \text{if } \ u \in (1,+\infty)\,. \end{cases} \tag{5.25}$$

Hence, it is strictly positive for $\beta > 1$ and positive for $\beta = 1$.
□

For the optimization methods that are developed in the next section, it is also important to note that the definition of the negative log-likelihood can be extended to the whole space $\mathbb{R}^N$ by setting

$$\Phi(x) = h(x) + \iota_{[0,+\infty)^N}(x), \tag{5.26}$$

where

$$h(x) = \sum_{i=1}^{Q} \varphi_i([Hx]_i) \tag{5.27}$$

$$\iota_{[0,+\infty)^N}(x) = \begin{cases} 0 & \text{if } x \in [0,+\infty)^N \\ +\infty & \text{otherwise.} \end{cases} \tag{5.28}$$

For every $i \in \{1, \dots, Q\}$ the function φ_i is a convex, twice-differentiable function, whose expression is given by

$$\begin{aligned} &\varphi_i \colon \mathbb{R} \to \mathbb{R} \\ &\quad u \mapsto \begin{cases} \Phi_i(u) & \text{if } \ u \in [0, +\infty] \\ \frac{1}{2}\eta_i(0)u^2 + (1 - \xi_i(0))u + \Phi_i(0) & \text{otherwise} \end{cases} \end{aligned} \tag{5.29}$$

where Φ_i and ξ_i are defined in (5.6) and (5.9), respectively. The expression of $\eta_i(0)$ was given in (5.13) and, in terms of $y_i - c$, reads $\eta_i(0) = \left(1 - e^{-\frac{1}{\sigma^2}}\right) e^{\frac{1}{\sigma^2}(2(y_i - c) - 1)}$. Consequently h is a convex function with a μ-Lipschitz gradient on $\mathbb{R}^N$. The positivity constraint in the original problem is imposed by (5.28).

§ 5.3 Proposed optimization method

5.3.1 Minimization problem

According to the analysis carried out in Section 5.2, the objective function takes the following form

$$f(x) = h(x) + \psi_0(x) + \sum_{r=1}^{R} \psi_r(V_r x), \tag{5.30}$$

where the regularization term is split in a sum of simpler functions. More precisely, it will be assumed that $\psi_0 \in \Gamma_0(\mathbb{R}^N)$ and, for every $r \in \{1, \dots, R\}$, $\psi_r \in \Gamma_0(\mathbb{R}^{P_r})$ and $V_r \in \mathbb{R}^{P_r \times N}$.[2] Note that (5.30) covers a large range of penalization strategies. For instance, a sparsity prior in an analysis frame with frame operator V_r is introduced by taking ψ_r equal to $\lambda_r \| \cdot \|_1$ with $\lambda_r > 0$. Block sparsity measures [Eldar et al., 2010] can also be easily addressed in the proposed framework. Another popular example in image restoration is the total variation penalization [Rudin et al., 1992a]. In this case, $P_r = 2N$, $V_r = \left[(\Delta^{\mathrm{h}})^\top \ (\Delta^{\mathrm{v}})^\top\right]^\top$, where $\Delta^{\mathrm{h}} \in \mathbb{R}^{N \times N}$ (resp. $\Delta^{\mathrm{v}} \in \mathbb{R}^{N \times N}$) corresponds to a horizontal (resp. vertical) gradient operator, and, for every $x \in \mathbb{R}^N$, $\psi_r(V_r x) = \lambda_r \sum_{n=1}^{N} \left(([\Delta^{\mathrm{h}} x]_n)^2 + ([\Delta^{\mathrm{v}} x]_n)^2\right)^{1/2}$ with $\lambda_r > 0$. Another interesting choice is the Hessian-based penalization [Geman and Reynolds, 1992], [Lefkimmiatis et al., 2012] i.e., $P_r = 3N$ and $V_r = [\left(\Delta^{\mathrm{hh}}\right)^\top \ \sqrt{2}\left(\Delta^{\mathrm{hv}}\right)^\top \ (\Delta^{\mathrm{vv}})^\top]^\top$ where $\Delta^{\mathrm{hh}} \in \mathbb{R}^{N \times N}$, $\Delta^{\mathrm{hv}} \in \mathbb{R}^{N \times N}$ and $\Delta^{\mathrm{vv}} \in \mathbb{R}^{N \times N}$ model the second-order finite difference operators between neighbooring pixels as described in [Lefkimmiatis et al., 2012, Sec.III-A] and, $\forall x \in \mathbb{R}^N$, $\psi_r(V_r x) = \lambda_r \sum_{n=1}^{N} \left(([\Delta^{\mathrm{hh}} x]_n)^2 + 2([\Delta^{\mathrm{hv}} x]_n)^2 + ([\Delta^{\mathrm{vv}} x]_n)^2\right)^{1/2}$

[2] We recall from Definition 1.3.1 that $\Gamma_0(\mathbb{R}^N)$ is the class of lower-semicontinuous, proper, convex functions from $\mathbb{R}^N$ to $(-\infty, +\infty]$.

with $\lambda_r > 0$. The above penalties can be considered individually ($R = 1$) or combined in a hybrid manner ($R > 1$) [Pustelnik et al., 2011]. Finally, following (5.26), ψ_0 should be the indicator function $\iota_{[0,+\infty)^N}$. However, to take into account the dynamic range of the expected output image, it can be more generally chosen equal to ι_C, where C is a closed convex subset of $[0,+\infty)^N$.

5.3.2 Primal-dual splitting algorithm

Problem (5.4) where f takes the form (5.30) can be efficiently addressed using proximal splitting algorithms [Combettes and Pesquet, 2008], [Briceños Arias and Combettes, 2011], [Combettes and Pesquet, 2012], [Raguet et al.]. The solution is obtained iteratively by evaluating the individual proximity operators of the functions $(\psi_r)_{0\leq r\leq R}$, provided that they have an explicit expression. A brief description of proximal-splitting methods was provided in Section 1.3.1.2. The required notion of proximity operator was introduced in Definition 1.3.3.

We are now ready to present our primal-dual splitting algorithm. The main advantage of the primal-dual splitting algorithm that we employ is that it allows us to solve (5.4) for any Lipschitz differentiable function h while allowing arbitrary linear operators $(V_r)_{1\leq r\leq R}$. This algorithm, proposed recently in [Combettes and Pesquet, 2012], is summarized in Algorithm 9.

Algorithm 9 Proposed algorithm.

Let $\gamma \in (0,+\infty)$. Let $(a_k)_{k\in\mathbb{N}}$ and $(c_k)_{k\in\mathbb{N}}$ be some sequences of elements of $\mathbb{R}^N$ corresponding to possible errors in the computation of the gradient of h.

Initialization:

Set $x_0 \in \mathbb{R}^N$, and $(\forall r \in \{1,\dots,R\})\ v_{r,0} \in \mathbb{R}^{P_r}$.

Iterations:

For $k = 0,\dots$

$y_{1,k} = x_k - \gamma\left(\nabla h(x_k) + \sum_{r=1}^R V_r^\top v_{r,k}\right) + a_k$

$p_{1,k} = \mathrm{prox}_{\gamma\psi_0}(y_{1,k})$

For $r = 1,\dots,R$

$y_{2,r,k} = v_{r,k} + \gamma V_r x_k$

$p_{2,r,k} = y_{2,r,k} - \gamma \mathrm{prox}_{\gamma^{-1}\psi_r}(\gamma^{-1} y_{2,r,k})$

$q_{2,r,k} = p_{2,r,k} + \gamma V_r p_{1,k}$

$v_{r,k+1} = v_{r,k} - y_{2,r,k} + q_{2,r,k}$

$q_{1,k} = p_{1,k} - \gamma\left(\nabla h(p_{1,k}) + \sum_{r=1}^R V_r^\top p_{2,r,k}\right) + c_k$

$x_{k+1} = x_k - y_{1,k} + q_{1,k}$

5.3.3 Convergence result

The convergence of the proposed primal-dual proximal splitting algorithm is guaranteed by the following result deduced from Theorem 5.2.1 and [Combettes and Pesquet, 2012, Theorem 4.2]:

Theorem 5.3.1 *Given the following assumptions:*

1. *f is coercive, i.e. $\lim_{\|x\|\to+\infty} f(x) = +\infty$,*
2. *for every $r \in \{1, \dots, R\}$, ψ_r is finite valued,*
3. *$\gamma \in [\epsilon, (1-\epsilon)/\delta]$ where $\epsilon \in (0, 1/(\delta+1))$ and*
$$\delta = \mu + \sqrt{\sum_{r=1}^{R} \|V_r\|^2},$$
4. *$(a_k)_{k\in\mathbb{N}}$ and $(c_k)_{k\in\mathbb{N}}$ are absolutely summable sequences,*

then there exists a minimizer $\overline{x}$ of (5.30) such that the sequences $(x_k)_{k\in\mathbb{N}}$ and $(p_{1,k})_{k\in\mathbb{N}}$ converge to $\overline{x}$.

5.3.4 Implementation issues

Note that Algorithm 9 is robust to numerical errors. This feature is essential in our problem, as the gradient of the Poisson-Gaussian negative log-likelihood given by (5.7) involves infinite sums and cannot be computed exactly. We propose to perform the sum of (5.11) between $n_{\min}$ and $n_{\max}$, to include only the significant coefficients. The approximations are obtained in a similar way to the one derived in Chapter 3.

§ 5.4 Simulation examples

We now demonstrate the practical performance of our method on image restoration experiments in the context of data corrupted by Poisson-Gaussian noise. The image resulting from the time series noise identification procedure described in Chapter 3 provides a ground truth for this experiment. The considered ground truth images, i.e. $\overline{x}_1$ of size 128×128 and $\overline{x}_2$ of size 190×190 are illustrated in Figs. 5.1 (a) and 5.2 (a).

First, a study of the influence of the data fidelity choice in terms of image restoration results intensity level is presented. For a data fidelity term h derived from Gaussian likelihood, Generalized Anscombe Transform (GAST) or given by the exact expression given in (5.5), the resulting problem involves the minimization of

$$f = h + \iota_C + \sum_{r=1}^{R} \psi_r, \tag{5.31}$$

where ι_C is the indicator function of $C = [x^-, x^+]^N$ and $(x^-, x^+) \in [0, +\infty)^2$ define the expected pixel value range. In the following x^- is set to 0. In the proposed framework, GAST is handled in a manner similar to [Dupé et al., 2009], i.e. taking advantage of Lipschitz-differentiability properties of (1.28) as described in Section 1.2.2.1.

(x^+, σ^2)		Init.	Poiss.	Gauss.	GAST	Exact
(15,9)	λ	-	0.145	0.139	0.069	0.079
	MAE	54.26	13.29	10.86	11.38	**10.60**
	SNR	6.31	18.68	19.74	19.27	**19.89**
	SSIM	0.088	0.659	0.730	0.736	**0.747**
(30,12)	λ	-	0.105	0.120	0.056	0.048
	MAE	34.81	9.60	8.46	8.71	**8.25**
	SNR	10.72	21.13	21.60	21.41	**21.85**
	SSIM	0.179	0.752	0.811	0.807	**0.812**
(60,30)	λ	-	0.076	0.069	0.032	0.032
	MAE	26.72	8.28	7.41	7.44	**7.28**
	SNR	12.34	22.23	22.67	22.67	**22.85**
	SSIM	0.255	0.783	**0.845**	0.834	0.839
(90,50)	λ	-	0.065	0.052	0.022	0.025
	MAE	22.67	7.43	6.64	6.59	**6.55**
	SNR	13.73	23.13	23.59	23.79	**23.82**
	SSIM	0.312	0.804	**0.864**	0.855	0.859
(120,60)	λ	-	0.047	0.042	0.017	0.018
	MAE	19.64	6.71	6.11	**5.92**	**5.92**
	SNR	14.85	24.01	24.39	24.62	**24.67**
	SSIM	0.367	0.829	0.876	**0.877**	**0.877**
(150,80)	λ	-	0.046	0.032	0.016	0.016
	MAE	18.17	6.61	5.94	**5.85**	**5.85**
	SNR	15.46	24.02	24.59	24.54	**24.65**
	SSIM	0.399	0.829	**0.878**	**0.878**	**0.878**

Table 5.1: *Intensity level influence on restoring image $\overline{x}_1$ degraded with a convolution operator H corresponding to a truncated Gaussian point spread function of standard deviation* 1.6 *with kernel size* 25×25 *and corrupted by Poisson-Gaussian noise.*

For a data fidelity term derived from the Poisson likelihood, we consider

$$f = \iota_C + \psi_1 + \sum_{r=2}^{R} \psi_r, \tag{5.32}$$

where ψ_1 denotes a Kullback-Leibler divergence as defined in (1.18). The observed image is generated by degrading the original image $\overline{x}_1$ with a convolution operator H, which corresponds to a truncated Gaussian point spread function of standard deviation 1.6 and kernel size 25×25. The image was further corrupted with a scaled Poisson noise and a zero-mean additive Gaussian noise. In this experiment the proposed framework is applied to NLTV restoration briefly introduced in Section 1.2.2.2. The linear operators V_r associated with NLTV are computed from image restored with a Wiener filter using code by X. Bresson [Bresson, 2009] (available at http://www.cs.cityu.edu.hk/∼ xbresson/codes.html). The prior term is weighted by parameter λ tuned so as to minimize the Mean Absolute Error (MAE). The provided relative MAE values are normalized with a factor $255/x^+$. One can observe by inspecting the evaluation scores in Table 5.1, that the exact model leads to the best result. In case of Poisson data fidelity term, the required positivity of the observation image was ensured by data truncation. The associated results provided in Table 5.1 show that this strategy leads to relatively poor performance.

Next a study of penalization strategies for low-count image is presented. As mentioned previously, the problem formulation given in (5.30) allows us to address a wide range of problems. For the sake of illustration we consider the restoration with three penalization strategies, namely TV, NLTV and hybrid regularization, which integrate TV and a Hessian prior [Lefkimmiatis et al., 2012]. The TV and Hessian denote the total variation and second order differences semi-norm defined in Section 5.3.1, respectively. We use two images: the same images as previously $\overline{x}_1$ with $x^+ = 30$ and $\overline{x}_2$ with $x^+ = 12$. The original image $\overline{x}_1$ was degraded with a convolution operator H corresponding to a truncated Gaussian point spread function of standard deviation 1.6 and kernel size 25×25, further corrupted with a Poisson noise and a zero-mean additive Gaussian noise, described by the noise variance $\sigma^2 = 12$. The original image $\overline{x}_2$ was degraded with a convolution operator H also corresponding to a truncated Gaussian point spread function of standard deviation 1.6 and kernel size 25×25, corrupted with a Poisson noise and a zero-mean additive Gaussian noise, described by the noise variance $\sigma^2 = 9$. Both examples illustrate the performance of the proposed technique for the restoration of image with fairly low initial SNR, i.e. only 10.05 dB and 2.19 dB for image given in Fig. 5.1 (b) and Fig. 5.2 (b), respectively. By inspecting the numerical evaluation scores presented in Tables 5.2 and 5.3 one can conclude that the performance gain obtained by using the exact data fidelity term is independent of the chosen regularization strategy.

		Poiss.	Gauss.	GAST	Exact
TV	λ	0.163	0.197	0.093	0.083
	MAE	10.71	9.42	9.70	**8.90**
	SNR	20.21	20.6	20.55	**21.22**
	SSIM	0.715	0.777	0.782	**0.802**
NLTV	λ	0.105	0.120	0.056	0.048
	MAE	9.60	8.46	8.71	**8.25**
	SNR	21.13	21.60	21.41	**21.85**
	SSIM	0.752	0.811	0.807	**0.812**
TV + Hessian	λ_{TV}	0.042	0.258	0.026	0.032
	λ_{H}	0.148	0.376	0.070	0.082
	MAE	8.99	7.92	8.10	**7.91**
	SNR	21.09	**21.52**	21.40	**21.52**
	SSIM	0.794	**0.854**	0.851	**0.854**

Table 5.2: *Penalization strategies for low-count image $\overline{x}_1$ ($x^+ = 30$) degradated with a convolution operator H corresponding to a truncated Gaussian point spread function of standard deviation* 1.6 *with kernel size* 25×25 *and corrupted by Poisson-Gaussian noise, described by the noise variance* $\sigma^2 = 12$ *(MAE* $= 34.81$*, SNR* $= 10.07$ *dB, SSIM* $= 0.178$*).*

		Poiss.	Gauss.	GAST	Exact
TV	λ	0.394	0.254	0.176	0.158
	MAE	11.58	9.02	10.16	**8.66**
	SNR	16.7	18.49	17.49	**18.81**
	SSIM	0.643	0.670	0.660	**0.679**
NLTV	λ	0.283	0.197	0.138	0.138
	MAE	11.80	9.33	10.35	**9.27**
	SNR	16.69	18.28	17.37	**18.29**
	SSIM	0.622	0.643	0.632	**0.644**
TV + Hessian	λ_{TV}	0.079	0.167	0.125	0.119
	λ_{H}	0.856	0.690	0.582	0.346
	MAE	10.69	7.84	9.13	**7.79**
	SNR	17.32	19.48	18.38	**19.53**
	SSIM	0.726	**0.755**	0.742	**0.755**

Table 5.3: *Penalization strategies for low-count image $\overline{x}_2$ ($x^+ = 12$) degradated with a convolution operator H corresponding to a truncated Gaussian point spread function of standard deviation* 1.6 *with kernel size* 25×25 *and corrupted by Poisson-Gaussian noise, described by the noise variance* $\sigma^2 = 9$ *(MAE* $= 61$*, SNR* $= 2.19$ *dB, SSIM* $= 0.022$*).*

(a) Original $\overline{x}_1$ ($x^+ = 30$)

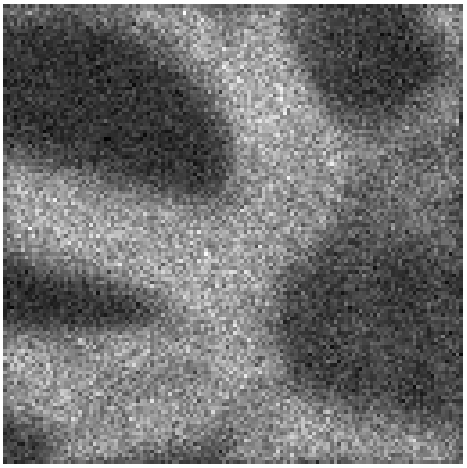

(b) Degraded (MAE = 35, SNR = 10.07 dB)

(c) Image result obtained with data fidelity term given by exact expression and Hessian-TV prior (MAE= 7.91 , SNR= 21.52 dB, ISNR = 11.44 dB, SSIM = 0.854)

Figure 5.1: *An example of macroconfocal image restored with proposed techniques. The original image (a) was degraded with* 25×25 *truncated Gaussian blur with standard deviation* 1.6 *and corrupted by Poisson-Gaussian noise* ($\sigma^2 = 12$).

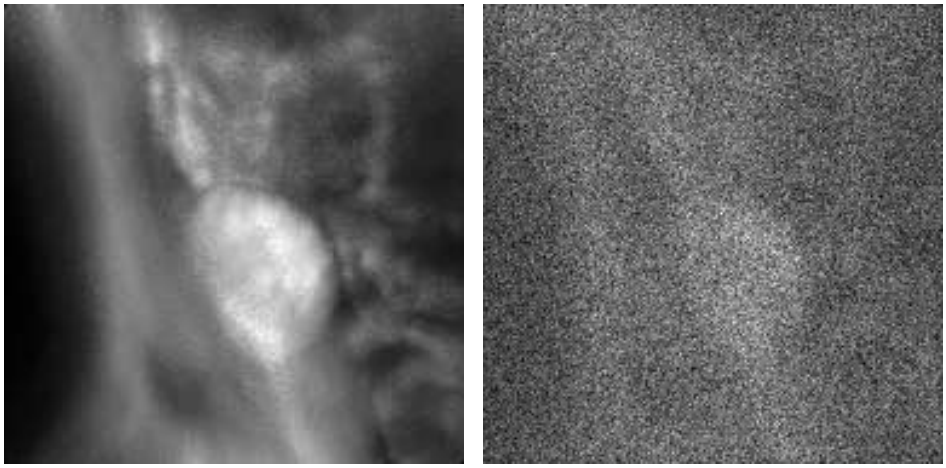

(a) Original $\overline{x}_2$ ($x^+ = 12$) (b) Degraded (MAE = 61, SNR = 2.19 dB)

(c) Result obtained with data fidelity term given by exact expression and Hessian-TV prior (MAE = 7.79 , SNR = 19.53 dB, ISNR = 17.34 dB, SSIM = 0.755)

Figure 5.2: *An example of macroconfocal image restored with proposed techniques. The original image (a) was degraded with* 25×25 *truncated Gaussian blur with standard deviation* 1.6 *and Poisson-Gaussian noise (*$\sigma^2 = 9$*).*

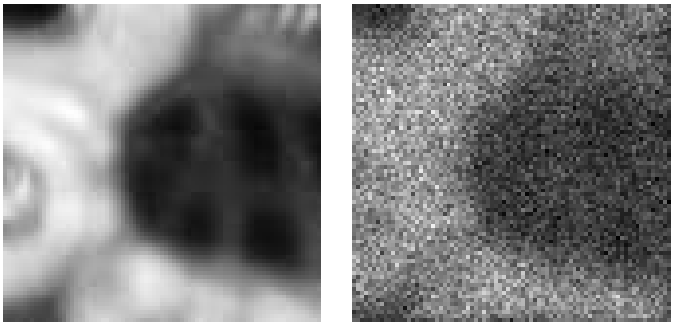

Figure 5.3: *Fragment of the original* $\overline{x}_1$ *(*$x^+ = 30$*) and its degraded version.*

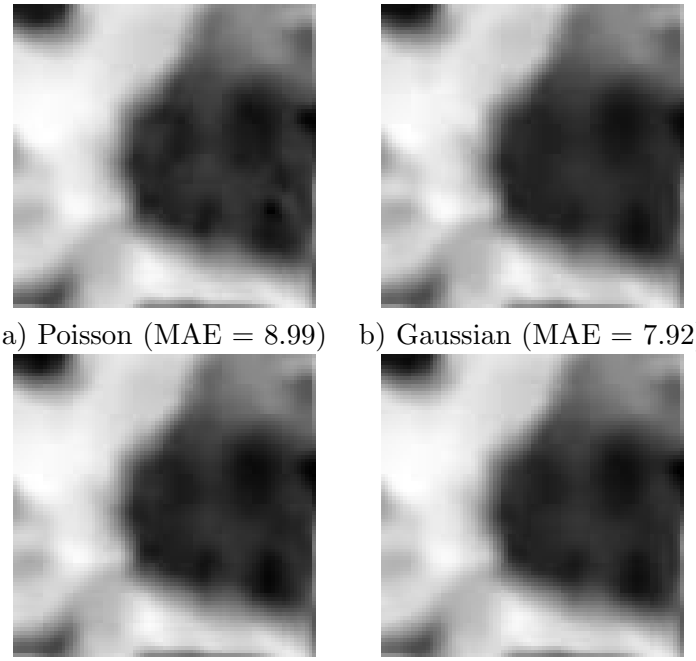

a) Poisson (MAE = 8.99) b) Gaussian (MAE = 7.92)

c) GAST (MAE = 8.10) d) Exact (MAE = 7.91)

Figure 5.4: *An influence of data fidelity term. The fragment of image* $\overline{x}_1$ *reconstructed with different data fidelity terms and Hessian-TV prior.*

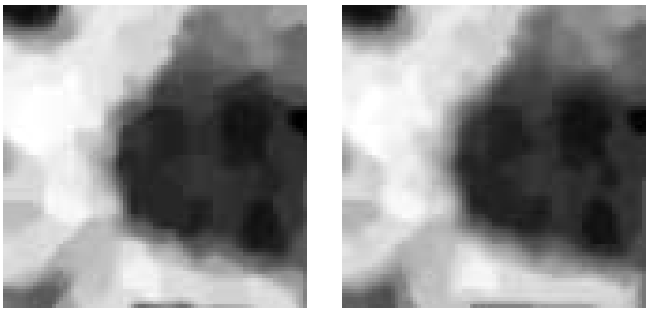

a) TV (MAE = 8.90) b) NLTV (MAE = 8.25)

Figure 5.5: *An influence of penalization strategy. The fragment of image* $\overline{x}_1$ *reconstructed with data fidelity term given by exact expression and either (a) TV or (b) NLTV prior.*

The Gaussian data fidelity term may be very competitive as illustrated in Table 5.3. However in some instances the performance gain between the exact and Gaussian data fidelity term is significant (see Table 5.2). One can observe in Fig. 5.1 (c) and Fig. 5.2 (c) that the hybrid Hessian-TV regularization strategy leads to a very good result. This can be also validated by inspecting the final MAE relative value equal to 7.91 and 7.79, ISNR equal to 11.44 dB and 17.34 dB for the first and the second image, respectively. The NLTV regularization strategy yields worse performance for the experiment presented in Table 5.3. This reflects the fact that the similarity between local image features is almost lost in initial image (Fig. 5.2 (b), SNR = 2.19 dB). Consequently, the NLTV weights were not well adjusted.

Complementary to these numerical results, Figs. 5.4 and 5.5 illustrate the visual differences resulting from various data fidelity terms and regularization strategies. One can observe that more low intensity components are lost when using a data fidelity term derived from Gaussian statistics (Fig. 5.4 (b)). The shape of low intensity component is also not well reconstructed when using a data fidelity term derived from Poisson statistics (Fig. 5.4 (a)). Most of the artifacts are corrected with GAST data fidelity term (Fig. 5.4 (c)) while even better result is obtained with the exact one (Fig. 5.4 (d)). The NLTV regularization term should be expected to reduce the undesired staircase effect visible in TV result (see Fig. 5.5 (a)) but for the considered low SNR observation images the improvement is in fact only incremental (see Fig. 5.5 (b)). In contrast, the Hessian-TV regularization seems more effective at alleviating this effect (see Fig. 5.4 (d)).

§ 5.5 Conclusion

We have shown that Poisson-Gaussian neg-log likelihood is a convex, Lipschitz-differentiable function. The provided convexity result is actually more general as it applies to the neg-log likelihood of a mixture of Generalized-Gaussian and Poisson variables. Building upon these results, we have proposed a new variational approach for solving data recovery problems in the presence of Poisson-Gaussian noise. We have observed performance gain using the exact data fidelity term instead of various approximations of it. We have also noticed that Gaussian and GAST fidelity terms approximate well the exact fidelity term for low and higher count data, respectively. We have developed a practical implementation of an efficient primal-dual algorithm, which is particularly flexible, i.e. a large range of penalization strategies are applicable. Among the ones we consider, the hybrid TV-Hessian prior was shown to produce naturally looking, high quality results for low count data restoration problem in the presence of Poisson-Gaussian noise. In the case of Gaussian noise, this regularization strategy is shown to be further improved when we use a non-convex $\ell_2 - \ell_0$ sparsity measure that

we will describe in detail in Chapter 7. In a future work we would like to extend our approach to encompass the case of Generalized Gaussian-Poisson noise and to study the performance of other regularization strategies than the ones we have considered here. Although here only TV, NLTV and hybrid TV-Hessian priors were analyzed, the versatility of our approach should allow us to address a wide range of applications by making use of various forms of convex penalty functions.

- Chapter 6 -

Discrete formulations for truncated-convex priors

This chapter[1] addresses the problem of minimizing multilabel energies with truncated convex priors. Such priors are known to be useful but difficult and slow to optimize because of their nonconvexity. We propose two novel classes of binary Graph-Cuts (GC) moves, namely the *convex move* and the *quantized move*. The moves are complementary to each other. To significantly improve efficiency, the label range is split into an even number of intervals. Quantized moves tend to efficiently put pixel labels into the correct intervals for the energy with truncated convex prior. Then the convex move assigns the labels more precisely within these intervals for the same energy. The quantized move is a modified α-expansion move, adapted to handle a generalized Potts prior, which assigns a constant penalty to arguments above some threshold. Our convex move is a graph-cut representation of the efficient Murota algorithm. We assume that the data terms are convex, since this is a requirement for Murota's algorithm. We then introduce the *Quantized-Convex Split Moves* algorithm, which minimizes energies with truncated priors by alternating both moves. This algorithm is a fast solver for labeling problems with a high number of labels and convex data terms. We illustrate its performance on image denoising problems.

§ 6.1 Introduction

We consider the well-known combinatorial optimization problem defined as follows. Let $\mathcal{G}(\mathcal{V}, \mathcal{E})$ be an undirected graph with a set of edges $\mathcal{E}$ and a set of vertices $\mathcal{V}$. The goal of our optimization problem is to restore an unknown $\widehat{x}$ based on observations y, under the condition that the components of x take values over a finite set of labels $\mathcal{L}$, representing e.g. grey level values in an image. Here we define $\mathcal{L}$ as an ordered discrete set of labels $\{0, 1, \ldots, L\}$

[1] Published in Proc. of EMMCVPR, 2011

and x_u as the label assigned to node $u \in \mathcal{V}$. The unknown $\widehat{x}$ is a minimum argument of the energy function:

$$E(x) = \sum_{u \in \mathcal{V}} \Phi(x_u) + \lambda \sum_{(u,v) \in \mathcal{E}} \rho(x_u, x_v), \tag{6.1}$$

where λ is a positive real value. $\Phi(x_u)$ is often called the data fidelity term and $\rho(x_u, x_v)$ the regularization or smoothness term. A common choice of data term Φ is a pixelwise distance $\Phi = |x_u - y_u|^p$ between the desired labeling x and a reference y, representing noisy acquired data, where p is a small positive integer, e.g. 1 or 2.

Many choices of ρ lead to useful algorithms and results. A common model is the so-called Potts model, where $\rho(x_u, x_v) = w_{uv} \min(1, |x_u - x_v|)$, and w_{uv} are spatially variant positive pairwise weights. This model corresponds to a piecewise constant prior. Other choices for ρ include $\rho(x_u, x_v) = w_{uv}|x_u - x_v|^q$, where q is typically 1 or 2 for linear and quadratic priors respectively. For $q = 1$ or $q = 2$, regularization term $\rho = w_{uv} \min(T^q, |x_u - x_v|^q)$ with threshold $T \in \mathcal{L}$ is respectively called truncated linear or truncated quadratic [Veksler, 1999]. More generally, a pairwise truncated convex prior can be formulated as:

$$\rho(x_v, x_u) = \begin{cases} f(x_u - x_v) & \text{if } |x_u - x_v| < T \\ f(T) & \text{if } |x_u - x_v| \geqslant T \end{cases} \tag{6.2}$$

where f is a convex function with $f(0) = 0$. Discrete random field models characterized by such a prior are well known and extensively discussed in the literature. Their popularity in low level vision is due to their ability to capture natural image statistics [Huang and Mumford, 1999]. Indeed, Nikolova [Nikolova, 2002] shows that the robustness of regularization terms depends on both their characteristics at $\pm\infty$, and their differentiability at zero. Non-differentiable terms at zero reconstruct sharp edges well but lead to undesirable staircase effects. In light of this "everywhere smooth" (e.g. quadratic) prior has good denoising properties with lack of staircase effect in the result, but with blurred boundaries. With respect to the behavior at $+\infty/-\infty$, truncated regularization terms imply no penalty for outliers, and so are less sensitive to them for noise removal. In this way, truncated models may combine noise suppression with edge preservation. In general, depending on the application, a sharp (e.g. truncated linear) or smooth (e.g. truncated quadratic) term might be desirable.

In the following, we introduce new GC algorithm solving optimization problem characterized by energy (6.1) and prior (6.2). In recent years, energy-based optimization methods using GC have become very popular in computer vision applications [Boykov et al., 1998], [Ishikawa, 2003], [Boykov et al., 2001]. GC optimization has been applied to e.g. stereo-vision [Woodford et al., 2008], multiview reconstruction [Sinha et al., 2007], motion analysis [Xiao and Shah, 2007], segmentation [Boykov and Jolly, 2001] and image

restoration [Darbon and Sigelle, 2006]. GC methods tend to provide optimal or near-optimal solutions to classical Markov Random Fields (MRF) problems, with some guarantees and in reasonable time. From the algorithmic point of view, GC problems can be solved when the energy is submodular, which was shown for the binary case (binary $\mathcal{L}$) in [Murota, 2000], [Kolmogorov and Zabih, 2004] and for multilabel case in [Schlesinger, 2008]. When the energy E is not submodular, some GC methods can still be used, for instance the *move* algorithms [Kolmogorov and Rother, 2007], [Veksler, 2007], [Kumar and Torr, 2008], [Lempitsky et al., 2010].

GC move algorithms have typically good theoretical quality guarantees for certain sets of regularization terms containing truncated convex functions considered in this chapter. Classical move algorithms include expansion and swap moves [Boykov et al., 2001]. More recently, improved moves have been proposed e.g. range moves and fusion moves [Veksler, 2007], [Kumar and Torr, 2008], [Veksler, 2009], [Lempitsky et al., 2010]. All are geared towards improving the quality of the solution and the speed of the algorithm. The time complexity of move algorithms usually increases steeply with the number of labels. For example, the worst-case complexity of swap moves is quadratic in the number of labels while range-moves perform even poorer. However, for problems where the number of labels is relatively low, these methods can be fast enough. Hence, move algorithms scale well with connectivity, are flexible with respect to data fidelity terms, but do not scale well with the number of labels.

It is worth noting that when ρ is convex, e.g. in the non-truncated linear or quadratic cases, the energy E of (6.1) may be optimized exactly and efficiently [Ishikawa, 2003], [Darbon and Sigelle, 2006]. Moreover, Szeliski et al. [Szeliski et al., 2008] have shown that expansion and swap moves work well in practice for the multilabel Potts model. Conversely, in the truncated linear or quadratic cases, due to non-convexity and non-differentiability (at the truncation and also at zero for truncated linear regularization term), such optimization problems remain challenging. In the multilabel case (non binary $\mathcal{L}$) the minimization problem of (6.1) is NP-hard.

The GC algorithms dedicated for energies with truncated convex priors, e.g [Veksler, 2007], [Kumar and Torr, 2008], [Kumar and Koller, 2009], have been developed to meet this challenge. We discuss them in detail in section 6.2. This group of algorithms can be extended with our *Quantized-Convex Split Moves*. This two-step approach produces results comparable to the current state-of-the-art move based algorithms and yet outperforms them by a significant factor in terms of time efficiency, especially when the number of labels is large. As these convex priors and the Potts model can be optimized efficiently with move methods, we split the label set into two parts, a regular quantized one that we optimize using a modified Potts model, and a remainder part, which we optimize using a convex framework. We propose two types of moves, which are complementary, namely the *quantized*

move and the *convex move*. Our quantized move is a modified α-expansion move, adapted to cope with a generalized Potts prior taking zero value for arguments in the range $(-T, +T)$. This move is designed to efficiently put pixel labels into the right intervals. These approximate results are corrected by the convex move, which performs finer changes with respect to the previously chosen label. A new, more precise label is found within previously chosen interval. The convex move is a GC representation of an efficient Murota's gradient descent algorithm [Murota, 2000], [Murota, 2004].

The rest of the chapter is organized as follows. The description of our method in the context of most related works is given in Section 6.2. We present our Quantized and Convex moves in Section 6.3, and the Quantized-convex split moves algorithm in Section 6.4. Then we provide experimental comparison of the different energy minimization methods in Section 6.5, and conclude with Section 6.6.

§ 6.2 Related work

In recent years, many algorithms utilizing truncated regularization terms have been proposed. Apart from GC move algorithms, the sequential tree reweighted message passing (TRW-S) [Kolmogorov, 2006] has currently the most accurate results and provides a Lagrangian approximation of the dual energy, e.g. estimates the gap between current and globally optimal energies. However, it is relatively slow [Wainwright et al., 2005] and is not well suited to highly-connected graphs [Kolmogorov and Rother, 2006]. Belief propagation (BP) [Felzenszwalb and Huttenlocher, 2004] methods, though faster than TRW, are not guaranteed to converge. GC methods were shown to outperform BP in several cases examined in [Szeliski et al., 2008]. Energies with truncated linear priors (truncated ℓ_1) may be optimized e.g. using α-expansions [Boykov et al., 2001] or Gupta and Tardos [Gupta and Tardos, 2000] algorithm. The latter offers good theoretical properties.

Veksler proposed in [Veksler, 2007] to minimize energies with truncated convex priors by splitting the problem into several subproblems that are all convex with respect to the prior. Each subproblem is defined for subsets of pixels $\widehat{u}, \widehat{v} \in \mathcal{V}$ with labels $x_{\widehat{u}} \in \mathcal{T}$ such that $\mathcal{T} \subset \mathcal{L}$ and $|x_{\widehat{u}} - x_{\widehat{v}}| \leqslant T$. According to the theorem presented in [Veksler, 2007], the original energy with labeling $\mathcal{L}$ is minimized with each subenergy having sublabeling $\mathcal{T}$. An algorithm that takes advantage of this property is the *range move*. Range move solves different subproblems for different choices of $\mathcal{T}$ iteratively using an Ishikawa-like approach [Ishikawa, 2003]. The advantage of the Ishikawa approach is that it guarantees a global minimum even with a non-convex data fidelity term, provided the prior is convex. This is particularly important for stereo-vision. In this article, we show that using what we call a *convex move* instead of the Ishikawa approach, it is possible to consider

all possible choices of $\mathcal{T} \subset \mathcal{L}$ such that $d_{\mathcal{T}} = T - 1$ simultaneously, where $d_{\mathcal{T}} = \max\{|x_{\widehat{u}} - x_{\widehat{v}}|, \{x_{\widehat{u}}, x_{\widehat{v}}\} \in \mathcal{T}\}$. This allows us to improve the time efficiency of the overall algorithm considerably. Additionally, we propose a *quantized move*, allowing for changes of x_u between $\mathcal{T}_1 \subset \mathcal{L}$ and $\mathcal{T}_2 \subset \mathcal{L}$ such that $\mathcal{T}_1 \cap \mathcal{T}_2 = \emptyset$. This further improves the time efficiency of our algorithm compared to the range move. The proposed algorithm alternates iteratively between quantized and convex moves. Note that if $\mathcal{T}_1 \cap \mathcal{T}_2 = \emptyset$, the energy (6.1) is no longer convex with respect to the prior term. For the convex move introduced in this chapter, the energy is guaranteed to decrease but the optimal solution is not secured.

More recent work by Kumar and Torr [Kumar and Torr, 2008] is better grounded theoretically than Veksler's range move. The quality of the solution is guaranteed by bounds on the converged energy for truncated ℓ_1 and ℓ_2, which are calculated with respect to $d_{\mathcal{T}}$, and equal $2 + \sqrt{2}$ if $d_{\mathcal{T}} = 2\sqrt{T}$ and $O(\sqrt{T})$ if $d_{\mathcal{T}} = \sqrt{T}$, for truncated ℓ_1 and ℓ_2, respectively. However, according to the results presented in [Kumar and Torr, 2008], the practical performance of both algorithms is similar for truncated ℓ_2 prior, although the greatest improvement is achieved for the truncated ℓ_1 prior. In terms of time efficiency, range move outperforms the approach proposed by Kumar and Torr, but not significantly. Similarly to the range move, authors use the graph construction proposed by Ishikawa, but they introduce small modifications. Namely, they adopt the Ishikawa approach for dealing with non-convex priors at the cost of not representing the energy exactly. (Here we will not analyze our algorithm as a function of $d_{\mathcal{T}}$. The convex move in our quantized-convex split moves algorithm is associated with two sets: (i) the set of all possible $\mathcal{T} \subset \mathcal{L}$ with $d_{\mathcal{T}} = T - 1$ and (ii) the set of all possible $\mathcal{T} \subset \mathcal{L}$ with $d_{\mathcal{T}} = T$).

In [Kumar and Koller, 2009], authors proposed a hierarchical approach. The original problem was replaced by a series of r-HST metric[2] labeling subproblems and obtained solutions were combined with α-expansion algorithm. The previously presented approximation bounds were improved. They are equal to $O(\ln(L))$ and $O((\gamma \ln(L))^2), \gamma \geqslant 1$ for truncated ℓ_1 and ℓ_2, respectively. However, this approach is computationally expensive.

§ 6.3 Move algorithms

Move algorithms have been developed to solve multilabeling problems. According to the definition given in [Veksler, 2007], a move algorithm is an

[2] An r-HST metric $d(\cdot, \cdot)$ is specified by a rooted tree r-HST whose edge capacity are non-negative and satisfy: (i) the edge capacity from any node to all of its children are the same; (ii) the edge capacities along any path from the root to a leaf decrease by a factor of $r > 1$. Then, $d(u, v)$ is the sum of the edge capacity on the unique path between nodes u and v.

iterative algorithm where $x^{(n+1)} \in M(x^{(n)})$ and $M(x)$ is a "moves" space of x. The local minimum with respect to a set of moves is at x if $E(x') > E(x)$ for any $x' \in M(x)$. Each move algorithm is characterized by its space of "moves" $M(x)$.

In this section we describe two moves that we develop. The quantized move is closely related to α-expansion and convex move to Murota's gradient descent algorithm. In Section 6.3, we explain why linking these moves together leads to improvement of efficiency in the context of minimization of energy functions with truncated convex prior.

6.3.1 Quantized move

The main idea behind the quantized move is to divide the label range into equal subintervals of length T and, ideally, put pixel labels into the correct intervals, thus reducing the number of categories from the original range L to L/T. This greatly accelerates the execution time of the algorithm.

The proposed move algorithm minimizes the energy E_p with an arbitrary data fidelity term Φ_p and a pairwise term defined as:

$$\rho_p(x_v, x_u) = \begin{cases} 0 & \text{if } |x_u - x_v| < T \\ f(T) & \text{if } |x_u - x_v| \geqslant T, \end{cases} \tag{6.3}$$

where T is a positive integer value. This prior is potentially interesting for other applications, but here we will use it as an intermediate step for minimizing truncated convex priors.

A *quantized move* is a new labeling where x_u is either left as x_u or moved to a new value according to the following transformation:

$$\alpha(x_u, k) = \begin{cases} t_1^k & \text{if } x_u \leqslant t_1^k \\ t_T^k & \text{if } x_u \geqslant t_T^k, \end{cases} \tag{6.4}$$

where k is an integer belonging to a regular quantization of the label set $\mathcal{L}$, i.e,: $k \in \mathcal{K} = \{k_0, k_1, \ldots, k_K\}$ such that $k_0 = 0$, $k_i = iT$, $i \in \mathbb{N}_+$, $KT \geqslant L$ and $(K-1)T < L$. Recall that L is the maximum label in $\mathcal{L}$. $\mathcal{T}^k = \{t_1^k, \ldots, t_T^k\}$ is an ordered label set, such that $t_{i+1}^k = t_i^k + 1$. The values in $\mathcal{T}^k$ change from $k - \frac{T}{2} + 1$ to $k + \frac{T}{2}$ and from $k - \frac{T}{2} + \frac{1}{2}$ to $k + \frac{T}{2} - \frac{1}{2}$ for odd and even T, respectively. The t_1^k and the t_T^k is a first and last element of set $\mathcal{T}^k$, respectively. The acceptable moves for a label depending on its current position are illustrated in Fig. 6.1.

The set of quantized moves $M_Q(x)$ is then defined as the collection of moves for all $k \in \mathcal{K}$. Quantized moves act much like expansion moves in the case of a Potts model on a quantized subset of labels. We now prove that quantized moves are graph-representable and can be optimized by GC.

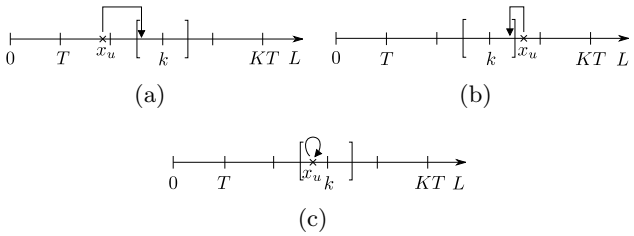

(a,b,c) illustrate the label moves when its current value is below, above, and inside the considered interval $\mathcal{T}^k$ (denoted by square brackets), respectively.

Figure 6.1: *The basic idea behind a quantized move*

Proposition 6.3.1 *For the energy in (6.1) with a regularization term given by (6.3), the optimal quantized move (i.e. giving the maximum decrease in energy) can be computed with a graph cut.*

Proof: We show that quantized move satisfies all conditions specified in [Kolmogorov and Zabih, 2004]. Let $b = \{b_u, u \in \mathcal{V}\}$ be a binary vector coding a quantized move. Then the move can be described by a transformation function $\mathcal{B}(x^{(n)}, b)$ returning a new labeling $x^{(n+1)}$, based on b and $x^{(n)}$. Here (n) is the iteration number. The transformation function $\mathcal{B}_q(x^{(n)}, b)$ for a quantized move is given by:

$$x_u^{(n+1)} = \mathcal{B}_q(x_u^{(n)}, b_u) = \begin{cases} \alpha(x_u^{(n)}, k) & \text{if } \; b_u = 1 \\ x_u^{(n)} & \text{if } \; b_u = 0 \end{cases} \tag{6.5}$$

The considered move finds $\widehat{b} = \arg\min_b E(\mathcal{B}_q(x^{(n)}, b))$, where $E(\mathcal{B}_q(x^{(n)}, b))$ is a pseudo-boolean energy, defined as $\sum_{u\in\mathcal{V}} \Phi(\mathcal{B}_q(x_u^{(n)}, b_u)) +$ $\sum_{(u,v)\in\mathcal{E}} \rho(\mathcal{B}_q(x_u^{(n)}, b_u), \mathcal{B}_q(x_v^{(n)}, b_v))$. Let us denote the pairwise term of the binary quantized move energy by $B(b_u, b_v)$, omitting $x^{(n)}$ from the notation for simplification. Then:

$$B(b_u, b_v) = \begin{cases} \rho_p(x_u^{(n)}, x_v^{(n)}) & \text{if } \; b_u = 0, b_v = 0 \\ \rho_p(x_u^{(n)}, \alpha(x_v^{(n)}, k)) & \text{if } \; b_u = 0, b_v = 1 \\ \rho_p(\alpha(x_u^{(n)}, k), x_v^{(n)}) & \text{if } \; b_u = 1, b_v = 0 \\ \rho_p(\alpha(x_u^{(n)}, k), \alpha(x_v^{(n)}, k)) & \text{if } \; b_u = 1, b_v = 1. \end{cases} \tag{6.6}$$

The pairwise term B needs to be submodular, i.e.: $B(0,0) + B(1,1) \leqslant B(1,0)+B(0,1)$. Since for all n and k we have that $\rho_p(\alpha(x_u^{(n)}, k), \alpha(x_v^{(n)}, k)) = 0$, the submodularity inequality takes the form:

$$\rho_p(x_u^{(n)}, \alpha(x_v^{(n)}, k)) + \rho_p(\alpha(x_u^{(n)}, k), x_v^{(n)}) \geqslant \rho_p(x_u^{(n)}, x_v^{(n)}), \tag{6.7}$$

or equivalently:

$$B(0,1) + B(1,0) \geqslant B(0,0). \tag{6.8}$$

The only case when $B(0,0)$ is not 0 is when neighbors x_u and x_v are at least T apart, i.e. $|x_u - x_v| \geqslant T$, in which case we have $B(0,0) = f(T)$. However, in this case either $B(0,1)$ or $B(1,0)$ or both are equal to $f(T)$, so the inequality is verified.

The problem of minimizing energy $E(\mathcal{B}_q(x^{(n)}, b))$ can be solved globally with respect to b using discrete maxflow-mincut methods [Ford and Fulkerson, 1962]. Note that when $T = 1$ our quantized move reduces to the α-expansion move.

6.3.2 Convex moves

In the previous section, we showed how to assign the pixel values into the correct intervals, and now we propose a convex algorithm to optimize these values within these intervals. To achieve this, we view the steepest descent algorithm of Murota [Murota, 2000], [Murota, 2004] as a special case of GC move. The primal and a primal-dual algorithms proposed in [Kolmogorov and Shioura, 2009] are also related to Murota's approach. It minimizes globally (6.1) for $L^\natural$-convex choice of E. Note that the solution is not guaranteed to be unique. The case of non-convex data fidelity term was not examined. This can be regarded as disadvantage compared to Ishikawa approach [Ishikawa, 2003], which guaranties a global minimum even for non-convex data fidelity. In contrast, both primal and primal-dual algorithms are more memory and time efficient than the non-iterative Ishikawa's method. The convex move is conceptually similar to the jump move [Veksler, 1999]. However, the jump move processes pixels with odd and even values differently. As a consequence, Potts functions can be represented on jump-move graphs, whereas convex functions generally cannot.

As in the previous case (section 6.3.1), a convex move is described by a binary vector b and the transformation function $\mathcal{B}_c(x^{(n)}, b)$ defined as

$$x_u^{(n+1)} = \mathcal{B}_c(x_u^{(n)}, b_u) = \begin{cases} x_u^{(n)} + s & \text{if } \; b_u = 1 \\ x_u^{(n)} & \text{if } \; b_u = 0, \end{cases} \tag{6.9}$$

where $s \in \mathcal{S}$ and $\mathcal{S}$ is a set of discrete values from $\mathbb{Z}$. The convex move space $M_C(x)$ is then defined as the collection of convex moves for all $s \in \mathcal{S}$. We call the algorithm finding $\widehat{b} = \arg\min_b E(\mathcal{B}_c(x^{(n)}, b))$ the *convex move*

algorithm. The pseudo-boolean prior term representation is given by:

$$\rho(\mathcal{B}_c(x_u^{(n)}, b_u), \mathcal{B}_c(x_v^{(n)}, b_v)) = \begin{cases} \rho_c(x_u^{(n)}, x_v^{(n)}) & \text{if } b_u = 0, b_v = 0 \\ \rho_c(x_u^{(n)}, x_v^{(n)} + s) & \text{if } b_u = 0, b_v = 1 \\ \rho_c(x_u^{(n)} + s, x_v^{(n)}) & \text{if } b_u = 1, b_v = 0 \\ \rho_c(x_u^{(n)} + s, x_v^{(n)} + s) & \text{if } b_u = 1, b_v = 1 \end{cases} \tag{6.10}$$

(6.10) is submodular as $\rho_c(x_u, x_v)$ is a $L^\natural$-convex function (since f is convex, its submodularity inequality $f(|x_u + s - x_v|) + f(|x_u - x_v - s|) \geqslant 2f(|x_u - x_v|)$ is always satisfied). The optimal convex move can be found with Murota's gradient descent algorithm [Murota, 2004]. It is worth noting that GC formulation does not impose any requirements on data fidelity term thus guaranteeing that the energy decreases. Hence, in this case energy (6.1) is guaranteed to decrease but the optimal solution of arbitrary multilabel problems is not secured.

§ 6.4 Truncated convex prior algorithm

In this section, we present an effective method combining both moves introduced in section 6.3 for minimizing energies with truncated convex prior functionals (6.2).

The convex move submodularity inequality is a function of (x_u, x_v) s.t. $(u, v) \in \mathcal{N}$ and $s \in \mathcal{S}$. The choice of $\mathcal{S}$ influences the number of pairs of neighboring pixels $u \in \mathcal{V}$ which satisfies the convex move submodularity inequality. We examine the case where $\mathcal{S} = \{-1, +1\}$ and $f(x_u, x_v)$ is defined as in (6.2). To specify the sets of pixels the convex move applies to, we define $\mathbb{T}_i$ for $0 \leqslant i \leqslant L$ to be the collection of all subsets $S_i^{\mathcal{V}}$ of $\mathcal{V}$ such that $\forall \widehat{u}, \widehat{v} \in \left(S_i^{\mathcal{V}}\right)^2, |\widehat{u} - \widehat{v}| \leqslant i$. We note that all x_u belong to at least one $S_i^{\mathcal{V}}$ irrespective of i, and so the entire image is covered by $\mathbb{T}_i$. A convex move characterized by $\mathcal{S} = \{-1, +1\}$ is a function which maps $\mathbb{T}_{T-1}$ onto $\mathbb{T}_T$, guaranteeing that the energy defined as (6.2) decreases with each move. This comes from the fact that the energy for the $\mathbb{T}_{T-1}$ is represented exactly using our convex graph and as s is equal to either 1 or -1, the solution belongs to $\mathbb{T}_T$.

Following [Kolmogorov and Zabih, 2004], we define the edge capacities of graph $\mathcal{G}(\mathcal{V}, \mathcal{E})$. The cost $c(u, v)$ between $(u, v) \in \mathcal{N}$ is set to $f(|x_u + s - x_v|) + f(|x_u - x_v - s|) - 2f(|x_u - x_v|)$ if $|x_u - x_v| < T$ and 0 otherwise. Because of the many such null connections, the final MRF is sparser which improves the time efficiency of the algorithm. The energy is guaranteed to go down, but the resulting labeling and corresponding energy are not as good as obtained by other minimizers. To improve our results, we combine this convex move with our proposed quantized move.

An arbitrary new labeling set by the quantized move part is not guaranteed to improve the energy with respect to the truncated convex prior energy (only a Potts-like energy is guaranteed to be minimized). However, we can easily impose this extra condition: the new labeling is accepted only if the proposed energy is better with respect to truncated convex prior energy, and rejected otherwise, which yields the desired effect. Since quantized move regularizes distant outliers, it is a powerful complement method for convex moves, for which $\mathcal{S} = \{-1, +1\}$ regularizes close outliers. Now, we present our two-step algorithm alternating convex and quantized move. Here, $Q(x, k)$ denotes the quantized move of image x and interval k. We also denote the convex move by $C(x, s)$, where s is the considered step and x the input image. Note that the loops indexed by n are repeated until convergence.

Algorithm 10 Quantized-convex split moves algorithm

Initialization:
Set $x^{(0)}, \mathcal{S} = \{-1, 1\}$
Iterations:
For $j = 0, 1, \ldots$
  $z^{(0)} = x^{(j)}$
  For $n = 0, 1, \ldots$
    Assign to $\overline{\mathcal{K}}$ a set of randomly ordered elements from $\mathcal{K}$
    For $i = 0, 1, \ldots, K$
      Set k_i to be the i-th element of $\overline{\mathcal{K}}$
      $z = Q(z^{(Kn+i)}, k_i)$
      if $(E(z) \leqslant E(z^{(Kn+i)}))$ then $z^{(Kn+i+1)} = z$
      else $z^{(Kn+i+1)} = z^{(Kn+i)}$
  $z^{(0)} = z^{(Kn)}$
  For $n = 0, 1 \ldots$
    Assign to $\overline{\mathcal{S}}$ a set of randomly ordered elements from $\mathcal{S}$
    For $i = 0, 1$
      Set s_i to be the i-th element of $\overline{\mathcal{S}}$
      $z^{(2n+i)} = C(z^{(2n+i-1)}, s_i)$
  $x^{(j+1)} = z^{(2n)}$

Proposition 6.4.1 *Algorithm 10 iteratively decreases energy (6.1), with ρ defined as a truncated convex function.*

Proof: This result comes straightforwardly from the previous discussion, where it was shown that all steps reduce the energy $E(x)$.

As this algorithm combines quantized and convex moves, it is important to understand what happens at the boundary between them. A difficulty

is that neighboring pairs $u, v \in \mathcal{N}$ with labels $|x_u - x_v| = T$ cannot be represented exactly on the convex graph. This comes from the fact that the convex move cannot map $\mathbb{T}_T$ to $\mathbb{T}_{T-1}$. We cope with this problem in a similar way as in [Rother et al., 2005], where α-expansions were shown to be able to minimize energies involving a truncated prior, as long as the number of pairs x_u, x_v not satisfying the submodularity inequality is relatively small. This is the reason why we limited the convex moves to $\mathcal{S} = \{-1, +1\}$. We represent truncated priors on convex move graph in a similar spirit.

§ 6.5 Results

We implemented our proposed algorithm in the framework of the Middlebury MRF vision code (http://vision.middlebury.edu/MRF/code/), based on [Szeliski et al., 2008], so we could compare our approach with the following methods: Iterated Conditional Modes (ICM) [Besag, 1986], α-expansion and swap moves [Boykov and Kolmogorov, 2004], [Boykov et al., 2001], Max-ProdBP, BP-S (using software provided by Marshall Tappen [Tappen and Freeman, 2008]), and TRW-S [Wainwright et al., 2005], [Kolmogorov, 2006]. We also endeavoured to compare it with the range move, but range move did not work in our tests because the value of T was too large. The tests were performed single-threaded on an Intel Xeon 2.5GHz with 32GB of RAM running RedHat Enterprise Linux 5.5. All algorithms were run either until full convergence for GC algorithms, ICM, and ours, or until the first oscillation for the other algorithms.

We evaluated our proposed algorithm only in the context of image denoising for different prior functions, namely truncated ℓ_2 and truncated ℓ_1-ℓ_2, defined as $\sqrt{\epsilon + x^2}$. In each case, we also examined the influence of parameter T. The grey scale images ($L = 255$) of size 512×512 (for ℓ_2) and 256×256 (for ℓ_1-ℓ_2) were corrupted with additive zero mean, white Gaussian noise with standard deviation 25.3 corresponding to initial SNR values 13.75 dB, 15.09 dB, and 14.26 dB for images `gold rec`, `elaine`, and `barbara`, respectively. Consequently, all experiments were performed with an ℓ_2 data fidelity term, which is most appropriate for this noise distribution. All the algorithms were initialized with an empty zero image. The algorithm accuracy is evaluated in terms of absolute error defined as $err = (E(\widehat{x}) - E(x_{\mathrm{TRW}-S_l}))/E(x_{\mathrm{TRW}-S_l})$, where $E(x_{\mathrm{TRW}-S_l})$ is the lower bound value reported by TRW-S and $E(\widehat{x})$ is an energy corresponding to the solution obtained by the algorithm. The restoration quality is evaluated in terms of SNR. The mean time, the energy, SNR, and the error presented in Table 6.1 and Table 6.2 are computed from 3 different realizations of the noise added to 3 considered images. The performance of our algorithm is also illustrated by energy vs. time plots (Fig. 6.2).

	$T = 25$, $\lambda = 2$			$T = 35$, $\lambda = 2$			$T = 50$, $\lambda = 1$		
	$\overline{\text{time}}$	$\overline{\text{err}}$	$\overline{\text{SNR}}$	$\overline{\text{time}}$	$\overline{\text{err}}$	$\overline{\text{SNR}}$	$\overline{\text{time}}$	$\overline{\text{err}}$	$\overline{\text{SNR}}$
ICM	39.8	$3.02.10^{-2}$	20.11	39.06	$1.71.10^{-2}$	21.70	**25.4**	$5.25.10^{-3}$	21.53
BP-S	1807.8	$\mathbf{8.29.10^{-4}}$	20.82	1658.7	$\mathbf{5.10.10^{-4}}$	21.74	1641.8	$\mathbf{7.21.10^{-5}}$	21.52
BP	153.0	$1.05.10^{-3}$	20.80	154.5	$7.21.10^{-4}$	**21.76**	153.3	$1.17.10^{-4}$	21.52
TRW-S	154.9	$1.36.10^{-3}$	20.85	154.6	$7.55.10^{-4}$	21.72	172.2	$8.53.10^{-3}$	**21.54**
α-exp	307.6	$1.98.10^{-2}$	20.53	294.6	$2.01.10^{-2}$	21.61	240.3	$1.98.10^{-2}$	21.28
$\alpha\beta$ swap	360.1	$2.57.10^{-2}$	20.33	362.3	$1.48.10^{-2}$	21.75	359.5	$4.26.10^{-3}$	21.53
Proposed	**27.1**	$1.57.10^{-2}$	**21.53**	**28.6**	$6.30.10^{-3}$	21.71	29.2	$3.28.10^{-3}$	21.51

Table 6.1: *Truncated ℓ_2 prior results on 512×512 images. The SNR is given in dB, and the time in seconds. Best results are in bold. TRW-S and BP were stopped after 15 iterations (after this, the energy did not improve significantly).*

	$T = 35$, $\lambda = 55$			$T = 50$, $\lambda = 45$			$T = 60$, $\lambda = 30$		
	$\overline{\text{time}}$	$\overline{\text{err}}$	$\overline{\text{SNR}}$	$\overline{\text{time}}$]	$\overline{\text{err}}$	$\overline{\text{SNR}}$	$\overline{\text{time}}$	$\overline{\text{err}}$	$\overline{\text{SNR}}$
ICM	104.4	$2.69.10^{-2}$	19.51	84.4	$8.67.10^{-3}$	20.57	46.8	$2.39.10^{-3}$	20.88
BP-S	4871.9	$7.28.10^{-4}$	20.08	5069.9	$1.34.10^{-4}$	20.68	3866.7	$1.42.10^{-5}$	20.97
BP	13950.0	$9.40.10^{-4}$	20.12	16048.7	$2.10.10^{-4}$	20.69	14902.3	$4.31.10^{-5}$	20.97
TRW-S	2508.9	$\mathbf{2.54.10^{-4}}$	20.06	2259.0.4	$\mathbf{4.30.10^{-5}}$	20.66	2852.2	$\mathbf{5.08.10^{-6}}$	20.97
α-exp	61.8	$7.96.10^{-3}$	20.10	50.3	$7.36.10^{-3}$	20.72	50.9	$7.37.10^{-3}$	20.80
$\alpha\beta$ swap	200.4	$1.12.10^{-2}$	19.94	178.9	$4.31.10^{-3}$	20.63	112.7	$1.19.10^{-3}$	20.95
Proposed	**9.4**	$1.16.10^{-2}$	**20.37**	**9.3**	$4.00.10^{-3}$	**20.86**	**7.9**	$1.51.10^{-3}$	**21.19**

Table 6.2: *Truncated ℓ_1-ℓ_2 prior results with $\epsilon = 10$ on 256×256 images. The SNR is given in dB, and the time in seconds. Best results are in bold.*

The quality of the results is also verified by inspecting the mean SNR value, which is not further improved by other algorithms in comparison to ours. Indeed, our algorithm appears to perform better at removing isolated noisy pixels compared with other algorithms (see Fig. 6.3 (i)). Since our *Quantized-convex split moves* algorithm leads to very good results (Fig. 6.3), is fast and less memory expensive than other algorithms, it appears to be well suited for image denoising application. In Table 6.2, our *quantized-convex split moves* algorithm outperforms all other GC based algorithms in terms of minimum energy and time efficiency for truncated ℓ_2 prior. However, the best final energy is obtained by the BP (contrary to what was found in [Szeliski et al., 2008]) and TRW-S algorithms, the latter converging faster than the former. One can observe in Fig. 6.2 (a) that in the case of truncated ℓ_2, TRW-S offers a speed/energy compromise comparable with our *quantized-convex split moves* algorithm when it is stopped early, for instance after two iterations. However, for truncated ℓ_1-ℓ_2 prior, our algorithm is significantly faster (Fig. 6.2 (b)), while still achieving energies comparable with other algorithms (Table 6.2).

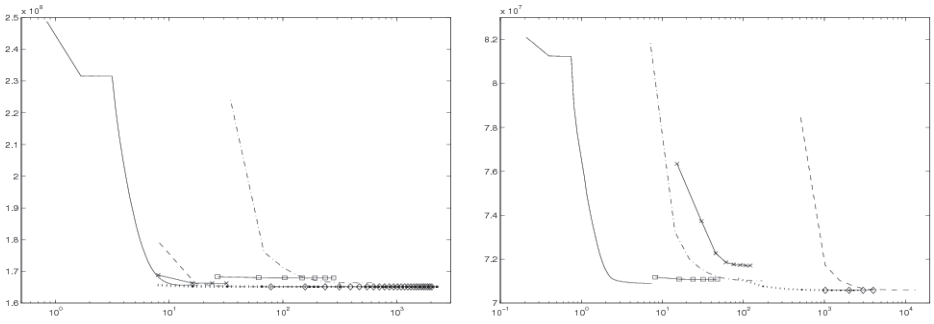

(a) (b)

Energy versus log time characteristics of convergence for algorithm comparison: ICM (solid line with crosses), BP-S (solid line with diamonds), BP (dashed line), TRW-S (dotted line), $\alpha\beta$ swap (dash-dot line), α-exp (solid line with squares), ours (solid line). (a,b) illustrates the case of ℓ_2 and ℓ_1-ℓ_2 prior, respectively.

Figure 6.2: *Algorithm comparison*

§ 6.6 Conclusion

In this chapter, we have presented a novel move-based algorithm to solve GC problems with truncated convex priors in the context of image denoising. Our move is split in two parts, a first Potts-like move that denoises a quantized version of the image, and a second move that processes the result of the

(a) Original (b) Noisy $\mathcal{N}(0, 25.3)$ (c) ICM 20.11 dB

(d) BP-S 20.16 dB (e) BP 20.15 dB (f) TRW-S 20.16 dB

(g) α-exp 20.14 dB (h) $\alpha\beta$ swap 20.15 dB (i) Ours 20.35 dB

Figure 6.3: *The image restoration results for truncated ℓ_1-ℓ_2 prior with threshold $T = 50$, ℓ_2 data fidelity term, and $\lambda = 2$.*

first move according to a fully convex prior. We have shown that combining these moves corresponds to denoising with a truncated convex prior. For a convex prior truncated at threshold T and for an image with L labels, the Potts-like denoising operates on L/T labels and the convex part on T labels only. This results in two optimization procedures over a much reduced set of labels for most useful values of T, and therefore it translates into large savings in computing time. Because only submodular moves are effected, the algorithm is guaranteed to converge in finite time. The result of these moves appears better in terms of energy than all moves, and depending on the problems, our algorithm is at least 5 times and up to several orders of magnitude faster than current state-of-the-art algorithms. We believe this constitutes an interesting compromise between efficiency and precision.

Since our algorithm uses versions of Potts and discrete convex optimization methods that are close to the original, future progress in this area will also translate into improvements for the proposed method. In particular, future work will include analyzing primal-dual methods for convex optimization. Precision can also be improved by using more sophisticated Potts-like moves. We will also explore the behaviour of our algorithm with non-convex data terms and consider other applications, such as stereo-vision.

- Chapter 7 -

$\ell_2 - \ell_0$ sparsity measures for imaging

In this chapter[1], we consider a class of differentiable criteria for sparse image computing problems, where a non-convex regularization is applied to an arbitrary linear transform of the target image. As special cases, it includes edge preserving measures or frame analysis potentials commonly used in image processing. As shown by our asymptotic results, the $\ell_2 - \ell_0$ penalties we consider may be employed to provide approximate solutions to ℓ_0-penalized optimization problems. One of the advantages of the proposed approach is that it allows us to derive an efficient Majorize-Minimize subspace algorithm. The convergence of the algorithm is investigated by using recent results in non-convex optimization. The fast convergence properties of the proposed optimization method are illustrated through image processing examples. In particular, its effectiveness is demonstrated on several data recovery problems.

§ 7.1 Introduction

The objective of this chapter is to show that, for a wide range of variational problems in image processing, an estimation $\widehat{x} \in \mathbb{R}^N$ of the target image can be efficiently obtained by using a class of non-convex, regularizing criteria that promote sparsity. More specifically, we focus on the following penalized optimization problem:

$$\underset{x \in \mathbb{R}^N}{\text{minimize}} \ \big(F_\delta(x) = \Phi(Hx - y) + \Psi_\delta(x)\big), \tag{7.1}$$

where $H \neq \mathbf{0}$ is a matrix in $\mathbb{R}^{Q \times N}$, y is a vector in $\mathbb{R}^Q$, $\Phi \colon \mathbb{R}^Q \to \mathbb{R}$ and $\Psi_\delta \colon \mathbb{R}^N \to \mathbb{R}$ are functions, and δ is a positive scalar. We are mainly interested in the case when Φ is a differentiable function. This includes the classical squared Euclidean norm. The problem then reduces to a penalized least

[1] The content of this chapter is to appear in SIAM Journal on Imaging Sciences

squares (PLS) problem [Tikhonov and Arsenin, 1977], [Titterington, 1985]. Another case of interest is when Φ is the separable Huber function [Huber, 1981, Example 5.4] which is useful for limiting the influence of outliers in some observed data. Other examples shall be mentioned subsequently.

Note that the considered optimization problem is frequently encountered in the field of inverse problems. Then, y is some vector of observations related to the original image $\overline{x} \in \mathbb{R}^N$ through a linear model of the form

$$y = H\overline{x} + w, \tag{7.2}$$

where H models the measurement process (e.g. a convolution operator or a projection operator), w is an additive noise vector, Φ is a data-fidelity term and Ψ_δ is a regularization term.

An efficient strategy to promote images formed by smooth regions separated by sharp edges, is to use regularization functions of the form

$$(\forall x \in \mathbb{R}^N) \qquad \Psi_\delta(x) = \sum_{s=1}^{S} \psi_{s,\delta}(\|V_s x - c_s\|) + \|V_0 x\|^2, \tag{7.3}$$

where $\|\cdot\|$ denotes the Euclidean norm, and, for every $s \in \{1,\dots,S\}$, $c_s \in \mathbb{R}^{P_s}$, $V_s \in \mathbb{R}^{P_s \times N}$ and $\psi_{s,\delta}\colon \mathbb{R} \to \mathbb{R}$. An important example of such a framework is when, for every $s \in \{1,\dots,S\}$, $P_s = 1$ and $c_s = 0$, and $\mathcal{V} = \left\{V_s^\top, s \in \{1,\dots,S\}\right\} \subset \mathbb{R}^N$ constitutes a frame of $\mathbb{R}^N$, leading to a so-called frame-analysis regularization [Elad et al., 2007]. For every $s \in \{1,\dots,S\}$, V_s may also be a matrix serving to compute discrete gradients (or higher-order differences), useful for edge preservation. In particular, if $S = N$ and, for every $s \in \{1,\dots,N\}$, $P_s = 2$, $c_s = \mathbf{0}$ and $V_s = [\Delta_s^{\mathrm{h}} \;\; \Delta_s^{\mathrm{v}}]^\top$ where $\Delta_s^{\mathrm{h}} \in \mathbb{R}^N$ (resp. $\Delta_s^{\mathrm{v}} \in \mathbb{R}^N$) corresponds to a horizontal (resp. vertical) gradient operator, and $(\forall t \in \mathbb{R})$ $\psi_{s,\delta}(t) = \lambda|t|$ with $\lambda > 0$, the first term in the right hand side of (7.3) corresponds to a discrete version of the isotropic total variation semi-norm [Rudin et al., 1992b]. Note that other choices of V_s lead to different penalization strategies. For instance, one can use nonlocal mean regularization, which has been recently studied in the context of edge preserving functions in [Peter et al., 2010].

In order to preserve significant coefficients in $\mathcal{V}$, one may require the functions $(\psi_{s,\delta})_{1\leq s\leq S}$ to have a slower-than-parabolic growth, as this limits the cost associated with these components. Two of the main families of such functions known in the literature are:

1. $\ell_2 - \ell_1$ functions, i.e. convex, continuously differentiable, asymptotically linear functions with a quadratic behavior near 0 [Allain et al., 2006], [Charbonnier et al., 1997], [Lange, 1990], [Zibulevsky and Elad, 2010]. Typical examples are the functions $(\forall s \in \{1,\dots,S\})$ $(\forall t \in \mathbb{R})$ $\psi_{s,\delta}(t) = \lambda\sqrt{t^2 + \delta^2}$ with $\lambda > 0$. In the limit case when $\delta \to 0$, the classical ℓ_1 penalty is obtained.

2. $\ell_2-\ell_0$ functions, i.e. asymptotically constant functions with a quadratic behavior near 0 [Fornasier and Solombrino, 2012], [Hebert and Leahy, 1992], [Nikolova et al., 2008], [Veksler, 2007], [Zhang and Kingsbury, 2010]. Typical examples are the truncated quadratic functions $(\forall s \in \{1,\ldots,S\})\ (\forall t \in \mathbb{R})\ \psi_{s,\delta}(t) = \lambda \min(t^2/(2\delta^2), 1)$ with $\lambda > 0$. When $\delta \to 0$, an ℓ_0 penalty is obtained.

The last quadratic penalty term $x \mapsto \|V_0 x\|^2$ in (7.3) plays a role similar to the elastic net regularization introduced in [Zou and Hastie, 2005]. It allows us to guarantee some properties of the minimizers and minimization algorithms, when H is not injective (e.g. an ideal low-pass filtering operator).

The $\ell_2 - \ell_0$ approach has been shown in the literature to be advantageous in many applications, for instance sparse component analysis [Mohimani et al., 2009], compressive sensing [Hyder and Mahata, 2009], matrix completion [Malek-Mohammadi et al., 2011], robust regression [Meer et al., 1991], segmentation [Rivera and Marroquin, 2003], and image recovery [Delaney and Bresler, 1998], [Peter et al., 2010]. This chapter mainly addresses the latter problem, where $\ell_2 - \ell_0$ is recognized for its ability to preserve edges between homogeneous regions [Nikolova, 2005]. The non-convexity and sometimes non-differentiability of the potential function lead however to a difficult optimization problem. In this chapter, we consider a class of non-convex differentiable potential functions, which can be viewed as smoothed versions of a truncated quadratic penalty function.

An effective approach for the minimization of differentiable criteria is to consider a subspace descent algorithm [Elad et al., 2006], [Zibulevsky and Elad, 2010]. For such methods, at each iteration, a stepsize vector representing an optimized combination of several search directions is computed through a multidimensional search. Recently, an original stepsize strategy based on a Majorize-Minimize (MM) recursion was introduced in [Chouzenoux et al., 2011]. This latter approach leads to a closed-form algorithm whose practical efficiency has been demonstrated in the context of image restoration, when using convex penalized least squares criteria.

Our main contributions in this chapter are:

- to establish conditions under which a solution to an ℓ_0 penalized criterion can be asymptotically obtained by using the considered class of penalty functions;
- to extend the approach in [Chouzenoux et al., 2011] to non necessarily convex minimization problems of the form (7.1);
- to provide a proof of convergence of the proposed subspace MM algorithm;
- to illustrate the good practical performance of the proposed method for image denoising and deblurring.

It must be stressed that the convergence proofs in this chapter rely on recent results demonstrating the prominent role played by the Kurdyka-Łojasiewicz inequality [Attouch and Bolte, 2008], [Attouch et al., 2010], [Attouch et al., 2011], [Bolte et al., 2010] in the study of the convergence of various iterative optimization methods. Our results constitute a significant improvement over those in [Chouzenoux et al., 2011]. In this previous article, the analysis was restricted to showing that the gradient of the objective function converges to zero.

The rest of the chapter is organized as follows: properties of the considered optimization problem are first investigated in section 7.2. Then, we introduce in section 7.3 a minimization strategy based on an MM subspace scheme. In section 7.4, we investigate the general convergence properties for the proposed algorithm. Finally, section 7.5 illustrates the performance of our algorithm through a set of comparisons and experiments in image processing.

§ 7.2 Considered class of objective functions

In this section, we briefly mention some useful properties of Problem (7.1).

7.2.1 Existence of a minimizer

First, we provide a preliminary result concerning the existence of a solution to the problem under the following assumption on the functions in (7.1) and on the nullspaces $\operatorname{Ker} H$ and $\operatorname{Ker} V_0$ of H and V_0, respectively:

Assumption 7.2.1

1. *Φ is continuous and coercive (that is $\lim_{\|\boldsymbol{z}\|\to+\infty} \Phi(\boldsymbol{z}) = +\infty$).*
2. *For every $\delta > 0$ and $s \in \{1, \ldots, S\}$, $\psi_{s,\delta}$ is continuous and takes nonnegative values.*
3. $\operatorname{Ker} H \cap \operatorname{Ker} V_0 = \{\mathbf{0}\}$.

Proposition 7.2.2 *Suppose that Assumption 7.2.1 holds. Then, for every $\delta > 0$,*

1. *F_δ is coercive;*
2. *the set of minimizers of F_δ is nonempty and compact.*

Proof. Let $\delta > 0$. Since, for every $s \in \{1, \cdots, S\}$, $\psi_{s,\delta} \geq 0$, we have

$$(\forall x \in \mathbb{R}^N) \qquad F_\delta(x) \geq \Phi(Hx - y) + \|V_0 x\|^2 = \underline{F}(x). \tag{7.4}$$

This implies that, for every $\eta \in \mathbb{R}$, [2]

$$\operatorname{lev}_{\leq \eta} F_\delta \subset \operatorname{lev}_{\leq \eta} \underline{F}. \tag{7.5}$$

As Φ is continuous and coercive, $\inf \Phi > -\infty$. For every $x \in \mathbb{R}^N$ and $\eta \in \mathbb{R}$, if $x \in \operatorname{lev}_{\leq \eta} \underline{F}$, then

$$\Phi(Hx - y) \leq \eta \tag{7.6}$$

$$\|V_0 x\|^2 \leq \eta - \inf \Phi. \tag{7.7}$$

Then, as a consequence of (7.6) and the coercivity of Φ, there exists $\zeta > 0$ such that, for every $x \in \operatorname{lev}_{\leq \eta} \underline{F}$,

$$\|Hx\| \leq \zeta. \tag{7.8}$$

The combination of (7.7) and (7.8) shows that there exists $\zeta' > 0$ such that, for every $x \in \operatorname{lev}_{\leq \eta} \underline{F}$, $\|\boldsymbol{A}x\| \leq \zeta'$ where

$$\boldsymbol{A} = \begin{bmatrix} H \\ V_0 \end{bmatrix}. \tag{7.9}$$

It can be deduced that, for every $x \in \operatorname{lev}_{\leq \eta} \underline{F} \cap (\operatorname{Ker} \boldsymbol{A})^\perp$,

$$\underline{\nu}\|x\| \leq \zeta' \tag{7.10}$$

where $\underline{\nu}$ is the minimum non-zero singular value of $\boldsymbol{A}$ (the existence of which is guaranteed since $\boldsymbol{A} \neq \boldsymbol{0}$). In addition, $\operatorname{Ker} \boldsymbol{A} = \operatorname{Ker} H \cap \operatorname{Ker} V_0 = \{\boldsymbol{0}\}$, which implies that $(\operatorname{Ker} \boldsymbol{A})^\perp = \mathbb{R}^N$. Hence, $\underline{F}$ is a level-bounded function, that is, for every $\eta \in \mathbb{R}$, $\operatorname{lev}_{\leq \eta} \underline{F}$ is bounded (and possibly empty). Using (7.5), we can conclude that F_δ is a level-bounded function (or equivalently, it is coercive [Rockafellar and Wets, 1997, Proposition 11.11]). As F_δ is also continuous, 2 follows from [Rockafellar and Wets, 1997, Theorem 1.9]. □

Remark 7.2.3

1. In the particular case when H is injective, Assumption 7.2.1 (3) is satisfied if $V_0 = \boldsymbol{0}$. The injectivity of H obviously holds when $H = \boldsymbol{I}$ in (7.2), which typically corresponds to denoising applications.

2. When $V_0 = \boldsymbol{0}$, the existence of a minimizer of F_δ with $\delta > 0$ can also be guaranteed under other useful conditions. For example, this property holds under Assumptions 7.2.1 (1 - 2), if $\operatorname{Ker} H \cap \bigcap_{s=1}^{S} \operatorname{Ker} V_s = \{0\}$, and when for every $s \in \{1, \ldots, S\}$, $\psi_{s,\delta}^{-1}(0)$ is a nonempty bounded set.

[2] Operator lower level set is defined as $\operatorname{lev}_{\leq \eta} F_\delta := \{x \in \mathbb{R}^N \mid F_\delta(x) \leq \eta\}$ [Rockafellar and Wets, 1997, Chapter 1]

7.2.2 Non-convex regularization functions

In the remainder of this work, we will be interested in potentials satisfying the following additional property:

Assumption 7.2.4

1. $(\forall s \in \{1, \dots, S\})\ (\forall (\delta_1, \delta_2) \in (0, +\infty)^2)\ \delta_1 \leq \delta_2 \Rightarrow (\forall t \in \mathbb{R})\ \psi_{s,\delta_1}(t) \geq \psi_{s,\delta_2}(t)$.
2. *There exists* $\lambda > 0$ *such that*

$$(\forall s \in \{1, \dots, S\})(\forall t \in \mathbb{R}) \qquad \lim_{\substack{\delta \to 0 \\ \delta > 0}} \psi_{s,\delta}(t) = \lambda \chi_{\mathbb{R}\setminus\{0\}}(t) \tag{7.11}$$

where $\chi_{\mathbb{R}\setminus\{0\}}(t) = \begin{cases} 0 & \text{if } t = 0 \\ 1 & \text{otherwise.} \end{cases}$

The latter condition shows that a binary penalty function is asymptotically obtained. Examples of functions $\psi_{s,\delta}$ with $s \in \{1, \dots, S\}$ and $\delta > 0$ satisfying Assumptions 7.2.1 (2) and 7.2.4 are provided below:

Example 7.2.5

1. Truncated quadratic potential [Veksler, 1999]:

$$(\forall t \in \mathbb{R}) \qquad \psi_{s,\delta}(t) = \lambda \min\left(\frac{t^2}{2\delta^2}, 1\right), \quad \lambda > 0.$$

2. Geman-McClure potential [Geman and McClure, 1985]:

$$(\forall t \in \mathbb{R}) \qquad \psi_{s,\delta}(t) = \frac{\lambda t^2}{2\delta^2 + t^2}, \quad \lambda > 0.$$

3. Welsch potential [Dennis and Welsch, 1978]:

$$(\forall t \in \mathbb{R}) \qquad \psi_{s,\delta}(t) = \lambda\Big(1 - \exp(-\frac{t^2}{2\delta^2})\Big), \quad \lambda > 0.$$

4. Hyberbolic tangent potential:

$$(\forall t \in \mathbb{R}) \qquad \psi_{s,\delta}(t) = \lambda \tanh\left(\frac{t^2}{2\delta^2}\right), \quad \lambda > 0.$$

5. Tukey biweight potential [Black et al., 1998]:

$$(\forall t \in \mathbb{R}) \qquad \psi_{s,\delta}(t) = \begin{cases} \lambda\left(1 - (1 - \frac{t^2}{6\delta^2})^3\right) & \text{if} \quad |t| \leq \sqrt{6}\delta \\ \lambda & \text{otherwise} \end{cases}, \quad \lambda > 0.$$

The latter four functions are such that $\psi_{s,\delta}(t) \sim \lambda t^2/(2\delta^2)$ as $t \to 0$. They can thus be viewed as smoothed versions of the one-variable truncated quadratic function in Example 7.2.5 (1) (see Fig. 7.1).

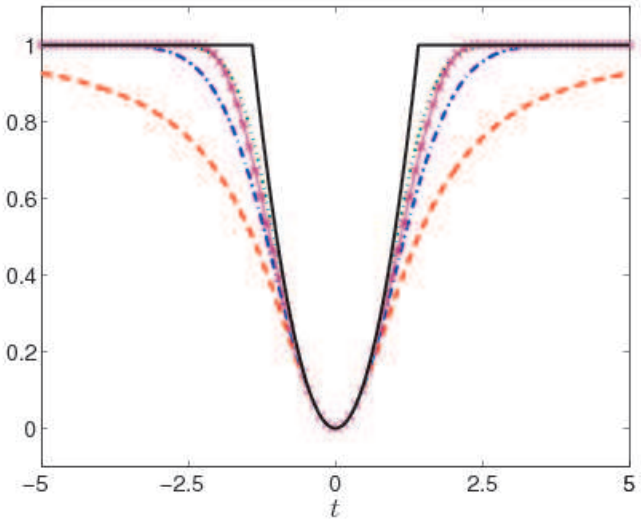

Truncated quadratic penalty in Example 7.2.5 (1) (black, full) and its smooth approximations $\psi_{s,\delta}(t)$ as defined in Examples 7.2.5 (2) (red, dashed), 7.2.5 (3) (blue, dash-dot), 7.2.5 (4) (green, dot), and 7.2.5 (5) (magenta, cross), for parameters $\lambda = 1$ and $\delta = 1$.

Figure 7.1: *Examples of smoothed versions of the one-variable truncated quadratic function.*

7.2.3 Asymptotic convergence to ℓ_0 criterion

The asymptotic behavior of the considered class of potentials can now be derived by showing the epi-convergence of F_δ to the following block (or group) ℓ_0-penalized objective function:

$$F_0 \colon x \mapsto \Phi(Hx - y) + \lambda \ell_0(Vx - c) + \|V_0 x\|^2, \tag{7.12}$$

where $V = \left[V_1^\top \mid \ldots \mid V_S^\top\right]^\top$, $c = \left[c_1^\top, \ldots, c_S^\top\right]^\top$, and ℓ_0 denotes the so-called 'block ℓ_0 cost' [Eldar et al., 2010] defined as

$$(\forall t = [t_1^\top, \ldots, t_S^\top]^\top \in \mathbb{R}^{P_1 + \cdots + P_S}) \qquad \ell_0(t) = \sum_{s=1}^{S} \chi_{\mathbb{R}\setminus\{0\}}(\|t_s\|), \tag{7.13}$$

where, for every $s \in \{1, \ldots, S\}$, $t_s \in \mathbb{R}^{P_s}$. When $P_1 = \ldots = P_S = 1$, (7.13) provides the standard expression of the ℓ_0 cost of $\mathbb{R}^S$.

Proposition 7.2.6 *Suppose that Assumptions 7.2.1 and 7.2.4 hold. Let $(\delta_n)_{n\in\mathbb{N}}$ be a decreasing sequence of positive real numbers converging to 0. Then,*

1. $\inf F_{\delta_n} \to \inf F_0$ *as* $n \to +\infty$.

2. *If* $(\forall n \in \mathbb{N})$ $\widehat{x}_n$ *is a minimizer of* F_{δ_n}, *then the sequence* $(\widehat{x}_n)_{n\in\mathbb{N}}$ *is bounded and all its cluster points are minimizers of* F_0.

3. *If* F_0 *has a unique minimizer* $\widetilde{x}$, *then* $\widehat{x}_n \to \widetilde{x}$ *as* $n \to +\infty$.

Proof. First, note that, according to Assumption 7.2.4 (1), for every $n \in \mathbb{N}$, $F_{\delta_{n+1}} \geq F_{\delta_n}$. In addition, for every $n \in \mathbb{N}$, F_{δ_n} is a continuous function as a consequence of Assumptions 7.2.1 (1 - 2). Then it can be deduced from [Rockafellar and Wets, 1997, Theorem 7.4(d)] that $(F_{\delta_n})_{n\in\mathbb{N}}$ epi-converges to $\sup_{n\in\mathbb{N}} F_{\delta_n}$. The latter function is equal to F_0 by virtue of Assumption 7.2.4 (2). In addition, $(F_{\delta_n})_{n\in\mathbb{N}}$ is eventually level-bounded[3] as a consequence of [Rockafellar and Wets, 1997, Ex. 7.32(a)], the lower bound in (7.4) and the fact that $\underline{F}\colon x \mapsto \Phi(Hx - y) + \|V_0 x\|^2$ is level-bounded (as shown in the proof of Proposition 7.2.2). We complete the proof by noticing that F_0 is lower semicontinuous and proper, and by applying [Rockafellar and Wets, 1997, Theorem 7.33]. □

The above proposition guarantees that a minimizer of F_0 can be well-approximated by choosing a small enough δ. Note that the existence / uniqueness of a minimizer of F_0 is discussed in the literature on compressed sensing under some specific assumptions [Candès, 2008], [Davenport et al., 2012], [Donoho, 2005].

We will now turn our attention to numerical methods allowing us to efficiently solve Problem (7.1) when all the involved functions are smooth.

§ 7.3 Proposed optimization method

7.3.1 Subspace algorithm

A classical strategy to minimize the criterion F_δ consists of building a sequence $(x_k)_{k\in\mathbb{N}}$ of $\mathbb{R}^N$ such that

$$(\forall k \in \mathbb{N}) \qquad F_\delta(x_{k+1}) \leq F_\delta(x_k). \tag{7.14}$$

This can be performed by translating the current solution x_k at each iteration $k \in \mathbb{N}$ along a suitable direction $d_k \in \mathbb{R}^N$:

$$x_{k+1} = x_k + \alpha_k d_k, \tag{7.15}$$

[3] $(F_{\delta_n})_{n\in\mathbb{N}}$ is eventually level-bounded if, for every $\eta \in \mathbb{R}$, there exists some subset $\mathcal{N}$ of $\mathbb{N}$ such that $\mathbb{N} \setminus \mathcal{N}$ is finite and $\cup_{n\in\mathcal{N}} \operatorname{lev}_{\leq\eta} F_{\delta_n}$ is bounded.

where $\alpha_k > 0$ is the *stepsize*, and d_k is a *descent direction*. When F_δ is differentiable, this direction is chosen such that $g_k^\top d_k \leq 0$ where g_k denotes the gradient of F_δ at x_k.

A significant practical improvement regarding the convergence rate is achieved by performing subspace acceleration, i.e. by considering a set of M search directions $\{d_k^1, \ldots, d_k^M\} \subset \mathbb{R}^N$ and by defining the new iteration as

$$x_{k+1} = x_k + D_k \epsilon_k, \tag{7.16}$$

where $D_k = [d_k^1, \ldots, d_k^M] \in \mathbb{R}^{N \times M}$ is the search direction matrix and $\epsilon_k \in \mathbb{R}^M$ is a multivariate stepsize, which is computed so as to minimize

$$f_{k,\delta} \colon \epsilon \mapsto F_\delta(x_k + D_k \epsilon). \tag{7.17}$$

The memory gradient subspace algorithm, initially proposed in the late 1960's by Miele and Cantrell [Miele and Cantrell, 1969], corresponds to:

$$(\forall k \geq 1) \qquad D_k = [-g_k \mid x_k - x_{k-1}]. \tag{7.18}$$

When the objective function is quadratic, this algorithm is equivalent to the linear conjugate gradient algorithm [Cantrell, 1969]. More recently, several other subspace algorithms have been proposed, where, at each iteration $k \in \mathbb{N}$, D_k usually includes a descent direction (e.g. gradient, Newton, truncated Newton directions) and a short history of previous directions (see [Chouzenoux et al., 2011, Tab.1] for a general review).

In addition, the subspace scheme (7.16) was shown to outperform standard descent algorithms such as nonlinear conjugate gradient over a set of PLS minimization problems in [Chouzenoux et al., 2011], [Zibulevsky and Elad, 2010]. The convergence of Algorithm (7.16) however requires the design of a proper strategy to determine the stepsizes $(\epsilon_k)_{k \in \mathbb{N}}$, which we discuss in the next section.

7.3.2 Majorize-Minimize stepsize

At each iteration $k \in \mathbb{N}$, the minimization of $f_{k,\delta}$ using the Majorization-Minimization (MM) principle is approximately performed by successive minimizations of tangent majorant functions for $f_{k,\delta}$. Let $q_k \colon \mathbb{R}^M \times \mathbb{R}^M \to \mathbb{R}$ and let $\epsilon' \in \mathbb{R}^M$. We recall from Section 1.3.1.1 that the function $q_k(., \epsilon')$ is said to be a tangent majorant for $f_{k,\delta}$ at ϵ' if $(\forall \epsilon \in \mathbb{R}^M) \quad q_k(\epsilon, \epsilon') \geq f_{k,\delta}(\epsilon)$ and $q_k(\epsilon', \epsilon') = f_{k,\delta}(\epsilon')$.

From this point forward, we assume that $f_{k,\delta}$ is differentiable. Following [Chouzenoux et al., 2011], we propose to employ a convex quadratic tangent majorant function of the form:

$$(\forall \epsilon \in \mathbb{R}^M) \quad q_k(\epsilon, \epsilon') = f_{k,\delta}(\epsilon') + \nabla f_{k,\delta}(\epsilon')^\top (\epsilon - \epsilon') + \frac{1}{2} (\epsilon - \epsilon')^\top B_{k,\epsilon'} (\epsilon - \epsilon'), \tag{7.19}$$

where $\nabla f_{k,\delta}(\epsilon')$ denotes the derivative of $f_{k,\delta}$ at ϵ', and $B_{k,\epsilon'}$ is an $M \times M$ symmetric positive semi-definite matrix that ensures the fulfillment of majorization properties (1.38) and (1.39). The initial minimization of $f_{k,\delta}$ is replaced by a sequence of easier subproblems, corresponding to the MM update rule summarized in Algorithm 11. Note that for $M = 1$, this reduces

Algorithm 11 General form of MM stepsize procedure

Initialization:
$\epsilon_k^0 = \mathbf{0}$
Iterations:
For $j = 0, \ldots, J$
$\epsilon_k^j \in \underset{\epsilon \in \mathbb{R}^M}{\text{Argmin}} \; q_k(\epsilon, \epsilon_k^{j-1})$

to the scalar MM line search [Labat and Idier, 2008].

7.3.3 Construction of the majorizing approximation

We now make the following assumption:

Assumption 7.3.1

1. *Φ is differentiable with an L-Lipschitzian gradient, i.e.*

$$(\forall \boldsymbol{z} \in \mathbb{R}^Q)(\forall \boldsymbol{z}' \in \mathbb{R}^Q) \; \|\nabla\Phi(\boldsymbol{z}) - \nabla\Phi(\boldsymbol{z}')\| \leq L\|\boldsymbol{z} - \boldsymbol{z}'\|. \tag{7.20}$$

2. *For every $s \in \{1, \cdots, S\}$, $\psi_{s,\delta}$ is a differentiable function.*

3. *For every $s \in \{1, \cdots, S\}$, $\psi_{s,\delta}(\sqrt{.})$ is concave on $[0, +\infty)$.*

4. *For every $s \in \{1, \cdots, S\}$, there exists $\overline{\omega_s} \in [0, +\infty)$ such that $(\forall t \in (0, +\infty))$ $0 \leq \dot{\psi}_{s,\delta}(t) \leq \overline{\omega_s} t$ where $\dot{\psi}_{s,\delta}$ is the derivative of $\psi_{s,\delta}$. In addition, $\lim_{\substack{t \to 0 \\ t \neq 0}} \dot{\psi}_{s,\delta}(t)/t \in \mathbb{R}$.*

We emphasize the fact that Assumptions 7.3.1 (2-4) hold for the ℓ_2-ℓ_0 penalties in Examples 7.2.5 (2-5). Morever, Tab. 7.1 presents several examples of functions fulfilling Assumption 7.3.1 (1).

By defining

$$(\forall s \in \{1, \ldots, S\})(\forall t \in \mathbb{R}) \quad \omega_{s,\delta}(t) = \dot{\psi}_{s,\delta}(t)/t, \tag{7.21}$$

(the function $\omega_{s,\delta}$ is extended by continuity at 0), a tangent majorant can be built as described below:

$\Phi(\boldsymbol{z})$ $\boldsymbol{z} = (z_q)_{1\leq q\leq Q} \in \mathbb{R}^Q$	L
Least squares	
$\frac{1}{2}\boldsymbol{z}^\top \Lambda \boldsymbol{z}$, $\Lambda \in \mathbb{R}^{Q\times Q}$ -symmetric positive semi-definite	$\|\Lambda\|$
Huber [Huber, 1981]	
$\sum_{q=1}^Q \phi_q(z_q)$ $(\forall t \in \mathbb{R})$ $\phi_q(t) = \begin{cases} \rho_q t^2 & \text{if } \|t\| \leq \nu_q \\ \rho_q \nu_q (2\|t\| - \nu_q) & \text{if } \|t\| > \nu_q \end{cases}$ $\nu_q > 0$, $\rho_q > 0$	$2\max_{1\leq q\leq Q} \rho_q$
Cauchy [Antoniadis et al., 2002]	
$\sum_{q=1}^Q \phi_q(z_q)$ $(\forall t \in \mathbb{R})$ $\phi_q(t) = \ln(\rho_q + t^2)$, $\rho_q > 0$	$\max_{1\leq q\leq Q}(\frac{2}{\rho_q})$
Squared distance to a closed convex set B [Bauschke and Combettes, 2011]	
$\frac{1}{2} d_B^2(\boldsymbol{z})$	1
Smoothed max [Ben-Tal and Teboulle, 1989]	
$\rho \ln(\sum_{q=1}^Q e^{z_q/\rho})$, $\rho > 0$	$1/\rho$
Inf-convolution [Bauschke and Combettes, 2011]	
$\inf_{\boldsymbol{z}_1+\boldsymbol{z}_2=\boldsymbol{z}} \Phi_1(\boldsymbol{z}_1) + \Phi_2(\boldsymbol{z}_2)$ $\Phi_1 \in \Gamma_0(\mathbb{R}^Q)$, $\Phi_2 \in \Gamma_0(\mathbb{R}^Q)$ Φ_2 ρ-Lipschitz differentiable, $\rho > 0$, such that $\lim_{\|\boldsymbol{z}\|\to+\infty} \frac{\Phi_2(\boldsymbol{z})}{\|\boldsymbol{z}\|} = +\infty$	ρ

Table 7.1: *Some examples of functions Φ with an L-Lipschitzian gradient. ($\|\Lambda\|$ denotes the spectral norm of Λ and $\Gamma_0(\mathbb{R}^Q)$ denotes the class of proper lower-semicontinuous convex functions from $\mathbb{R}^Q$ to $(-\infty, +\infty]$.)*

Lemma 7.3.2 [Allain et al., 2006] *For every $x \in \mathbb{R}^N$, let*

$$A(x) = \mu H^\top H + 2V_0^\top V_0 + V^\top \mathrm{Diag}\{b(x)\} V, \tag{7.22}$$

where $\mu \in [L, +\infty)$ and $b(x) = \big(b_i(x)\big)_{1\leq i\leq SP} \in \mathbb{R}^{SP}$ with $P = \sum_{s=1}^S P_s$ is such that

$$(\forall s \in \{1, \ldots, S\})\,(\forall p \in \{1, \ldots, P_s\}) \quad b_{P_1+\cdots+P_{s-1}+p}(x) = \omega_{s,\delta}(\|V_s x - c_s\|).$$

Let $\epsilon' \in \mathbb{R}^M$ and $k \in \mathbb{N}$. Then, under Assumption 7.3.1, $q_k(\cdot, \epsilon')$ with

$$B_{k,\epsilon'} = D_k^\top A(x_k + D_k \epsilon') D_k, \tag{7.23}$$

is a convex quadratic tangent majorant of $f_{\delta,k}$ *at* ϵ'.

Hence, according to (7.19) and procedure summarized in Algorithm 11, the optimality condition for the choice of the stepsize in the MM iteration is given by:

$$(\forall k \in \mathbb{N})(\forall j \in \{1, \dots, J\}) \quad B_{k,\epsilon_k^{j-1}}(\epsilon_k^j - \epsilon_k^{j-1}) + \nabla f_{k,\delta}(\epsilon_k^{j-1}) = \mathbf{0}. \quad (7.24)$$

This yields the explicit stepsize formula

$$\epsilon_k^j = \epsilon_k^{j-1} - B^{-1}_{k,\epsilon_k^{j-1}} \nabla f_{k,\delta}(\epsilon_k^{j-1}), \quad (7.25)$$

where $B^{-1}_{k,\epsilon_k^{j-1}}$ is the pseudo-inverse of $B_{k,\epsilon_k^{j-1}} \in \mathbb{R}^{M\times M}$. One of the main advantages of this approach is that the computational cost of the required inversion is low, provided that the number M of search directions remains small. The resulting MM subspace algorithm is summarized in Algorithm 12.

Algorithm 12 MM subspace algorithm

Initialization:
Set $x_0 \in \mathbb{R}^N$
Iterations:
For $k = 0, \dots$
  $\epsilon_k^0 = \mathbf{0}$,
  For $j = 1, \dots, J$
    $B_{k,\epsilon_k^{j-1}} = D_k^\top A(x_k + D_k\epsilon_k^{j-1})D_k$
    $\epsilon_k^j = \epsilon_k^{j-1} - B^{-1}_{k,\epsilon_k^{j-1}} D_k^\top \nabla F_{k,\delta}(x_k + D_k\epsilon_k^{j-1})$
  $x_{k+1} = x_k + D_k\epsilon_k^J$

§ 7.4 Convergence result

We first provide some preliminary technical lemmas before stating the main convergence result. In the following, for every $k \in \mathbb{N}$ and $j \in \{0, \dots, J\}$, we define

$$x_k^j = x_k + D_k\epsilon_k^j, \quad (7.26)$$
$$g_k^j = \nabla F_\delta(x_k^j), \quad (7.27)$$

(thus, $x_k^J = x_{k+1}$ and $g_k^J = g_{k+1}$). Moreover, we assume that the set of directions $(D_k)_{k\in\mathbb{N}}$ fulfills the following condition:

Assumption 7.4.1 *For every $k \in \mathbb{N}$, the matrix of directions D_k is of size $N \times M$ with $1 \leq M \leq N$ and the first subspace direction d_k^1 is gradient-related i.e.,*

$$g_k^\top d_k^1 \leq -\gamma_0 \|g_k\|^2, \tag{7.28}$$

$$\|d_k^1\| \leq \gamma_1 \|g_k\|, \tag{7.29}$$

with $\gamma_0 > 0$ and $\gamma_1 > 0$.

As emphasized in [Bertsekas, 1999, Sec.1.2] and [Chouzenoux et al., 2011, Sec.III-D], conditions (7.28) and (7.29) hold for a large family of descent directions, such as the steepest descent direction or the truncated Newton direction.

7.4.1 Preliminary results

Lemma 7.4.2 *Under Assumptions 7.3.1 and 7.4.1, there exists a constant $\nu > 0$ such that, for every $k \in \mathbb{N}$ and $j \in \{1, \ldots, J\}$, $F_\delta(x_k) - F_\delta(x_k^j) \geq \frac{\gamma_0^2}{\gamma_1^2} \nu^{-1} \|g_k\|^2$.*

Proof. According to Assumption 7.3.1 (4) and (7.21), for every $s \in \{1, \cdots, S\}$, $\omega_{s,\delta}$ is upper-bounded on $(0, +\infty)$. Hence, there exists $\nu > 0$ such that, for every $x \in \mathbb{R}^N$ and $V \in \mathbb{R}^N$, $V^\top A(x) V \leq \nu \|V\|^2/2$. The result then follows from [Chouzenoux et al., 2011, Theorem 1]. □

Lemma 7.4.3 *Under Assumptions 7.2.1 and 7.3.1, the MM subspace iterates are such that*

$$(\forall k \in \mathbb{N})(\forall j \in \{0, \ldots, J-1\}) \qquad F_\delta(x_k^j) - F_\delta(x_k^{j+1}) \geq \frac{\eta}{2} \|x_k^{j+1} - x_k^j\|^2 \tag{7.30}$$

where $\eta > 0$ is the smallest eigenvalue of $\mu H^\top H + 2 V_0^\top V_0$.

Proof. Let $k \in \mathbb{N}$ and $j \in \{0, \ldots, J-1\}$. According to (7.19) and the definition of ϵ_k^{j+1},

$$f_{k,\delta}(\epsilon_k^j) - q_k(\epsilon_k^{j+1}, \epsilon_k^j) = -\frac{1}{2} \nabla f_{k,\delta}(\epsilon_k^j)^\top (\epsilon_k^{j+1} - \epsilon_k^j). \tag{7.31}$$

Furthermore, $q_k(\epsilon_k^{j+1}, \epsilon^j) \geq f_{k,\delta}(\epsilon_k^{j+1})$. Thus,

$$f_{k,\delta}(\epsilon_k^j) - f_{k,\delta}(\epsilon_k^{j+1}) \geq -\frac{1}{2} \nabla f_{k,\delta}(\epsilon^j)^\top (\epsilon_k^{j+1} - \epsilon_k^j). \tag{7.32}$$

The last inequality also reads

$$F_\delta(x_k^j) - F_\delta(x_k^{j+1}) \geq -\frac{1}{2}\nabla f_{k,\delta}(\epsilon^j)^\top(\epsilon_k^{j+1} - \epsilon_k^j). \tag{7.33}$$

So, using (7.23) and (7.24),

$$F_\delta(x_k^j) - F_\delta(x_k^{j+1}) \geq \frac{1}{2}\big(D_k(\epsilon_k^{j+1} - \epsilon_k^j)\big)^\top A(x_k^j) D_k(\epsilon_k^{j+1} - \epsilon_k^j) \tag{7.34}$$

$$\geq \frac{\eta}{2}\|D_k(\epsilon_k^{j+1} - \epsilon_k^j)\|^2. \tag{7.35}$$

In the latter inequality, we make use of the fact that, since $\mathrm{Ker}H \cap \mathrm{Ker}V_0 = \{\mathbf{0}\}$, η is positive, and

$$(\forall x \in \mathbb{R}^N)(\forall V \in \mathbb{R}^N) \qquad V^\top A(x) V \geq \eta\|V\|^2. \tag{7.36}$$

□

Lemma 7.4.4 *Under Assumptions 7.2.1 and 7.3.1, the MM subspace iterates are such that*

$$(\forall k \in \mathbb{N})(\forall j \in \{0, \ldots, J-1\}) \qquad \eta\|x_k^{j+1} - x_k^j\| \leq \|g_k^j\|, \tag{7.37}$$

where $\eta > 0$ is the same constant as in Lemma 7.4.3.

Proof. According to (7.24), we have, for every $k \in \mathbb{N}$ and $j \in \{0, \ldots, J-1\}$,

$$D_k^\top g_k^j + D_k^\top A(x_k^j) D_k(\epsilon_k^{j+1} - \epsilon_k^j) = \mathbf{0}. \tag{7.38}$$

Hence,

$$\big(D_k(\epsilon_k^{j+1} - \epsilon_k^j)\big)^\top g_k^j + \big(D_k(\epsilon_k^{j+1} - \epsilon_k^j)\big)^\top A(x_k) D_k(\epsilon_k^{j+1} - \epsilon_k^j) = \mathbf{0}. \tag{7.39}$$

By using (7.36), (7.39) leads to

$$-\big(D_k(\epsilon_k^{j+1} - \epsilon_k^j)\big)^\top g_k^j \geq \eta\|D_k(\epsilon_k^{j+1} - \epsilon_k^j)\|^2. \tag{7.40}$$

In addition, the Cauchy-Schwarz inequality leads to

$$-\big(D_k(\epsilon_k^{j+1} - \epsilon_k^j)\big)^\top g_k^j \leq \|g_k^j\|\|D_k(\epsilon_k^{j+1} - \epsilon_k^j)\|. \tag{7.41}$$

Thus, the latter two inequalities yield:

$$\eta\|D_k(\epsilon_k^{j+1} - \epsilon_k^j)\|^2 \leq \|g_k^j\|\|D_k(\epsilon_k^{j+1} - \epsilon_k^j)\|. \tag{7.42}$$

Substituting with (7.26), obtaining the desired result is straightforward. □

7.4.2 Convergence theorem

Based on the two previous lemmas, classical results in the optimization literature [Ortega and Rheinboldt, 1970] may allow us to deduce the convergence of the sequence $(x_k)_{k\in\mathbb{N}}$ generated by the MM subspace algorithm, but these results require restrictive conditions on the critical points of the objective function F_δ. We propose here a more general approach based on recent results in non-convex optimization [Attouch and Bolte, 2008], [Attouch et al., 2010], [Attouch et al., 2011]. We first recall the following definition from [Łojasiewicz, 1963]:

Definition 7.4.5 A differentiable function $G\colon \mathbb{R}^N \to \mathbb{R}$ satisfies the Kurdyka-Łojasiewicz inequality if, for every $\widetilde{x} \in \mathbb{R}^N$ and every bounded neighborhood E of $\widetilde{x}$, there exist three constants $\kappa > 0$, $\zeta > 0$ and $\theta \in [0, 1)$ such that

$$\|\nabla G(x)\| \geq \kappa |G(x) - G(\widetilde{x})|^\theta, \tag{7.43}$$

for every $x \in E$ such that $|G(x) - G(\widetilde{x})| < \zeta$.

The interesting point is that this inequality is satisfied for a wide class of functions. In particular, it holds for real analytic functions, semi-algebraic functions as well as many others [Łojasiewicz, 1963], [Kurdyka and Parusinski, 1994] [Bolte et al., 2006], [Bolte et al., 2007]. Recall that a function $G\colon \mathbb{R}^N \to \mathbb{R}$ is semi-algebraic if its graph $\{(x, \eta) \in \mathbb{R}^N \times \mathbb{R} \mid \eta = G(x)\}$ is a semi-algebraic set, i.e. it can be expressed as a finite union of subsets of $\mathbb{R}^N \times \mathbb{R}$ defined by a finite number of polynomial inequalities. The semi-algebraicity property is stable under various operations (sum, product, inversion, composition,...). Examples of semi-algebraic functions include $x \mapsto \|Hx - y\|^2$, Ψ_δ when the functions $(\psi_{s,\delta})_{1\leq s\leq S}$ are given by Example 7.2.5 (2) or 7.2.5 (5), the squared distance to a closed convex semi-algebraic set. In turn, examples of real-analytic functions include $x \mapsto \|Hx - y\|^2$ and Ψ_δ when the functions $(\psi_{s,\delta})_{1\leq s\leq S}$ are given by Examples 7.2.5 (2-4). Note that a more general local version of inequality (7.43) can also be found in the literature [Bolte et al., 2007].

Let us now state our main convergence result:

Theorem 7.4.6 *Assume that F_δ satisfies the Kurdyka-Łojasiewicz inequality. Under Assumptions 7.2.1, 7.3.1 and 7.4.1, the MM subspace algorithm given by (12) generates a sequence $(x_k)_{k\in\mathbb{N}}$ converging to a critical point $\widetilde{x}$ of F_δ. Moreover, this sequence has a finite length in the sense that*

$$\sum_{k=0}^{+\infty} \|x_{k+1} - x_k\| < +\infty. \tag{7.44}$$

Proof. As $\mathrm{lev}_{\leq F_\delta(x_0)} = \{x \in \mathbb{R}^N | F_\delta(x) \leq F_\delta(x_0)\}$ is a bounded set (by virtue of Proposition 7.2.2 (1)) and $(F_\delta(x_k))_{k\in\mathbb{N}}$ is a decreasing sequence, the sequence $(x_k)_{k\in\mathbb{N}}$ belongs to a compact subset E of $\mathbb{R}^N$. Hence, there exists

a subsequence $(x_{k_i})_{i\in\mathbb{N}}$ of $(x_k)_{k\in\mathbb{N}}$ converging to a vector $\widetilde{x}$ of $\mathbb{R}^N$. Besides, since F_δ is a continuous function, $(F_\delta(x_{k_i}))_{i\in\mathbb{N}}$ converges to $F_\delta(\widetilde{x})$. As $(F_\delta(x_k))_{k\in\mathbb{N}}$ is decreasing, and Proposition 7.2.2 (1) shows that it is bounded from below, we deduce that $(F_\delta(x_k) - F_\delta(\widetilde{x}))_{k\in\mathbb{N}}$ is a nonnegative sequence converging to 0.

Now, by invoking Lemma 7.4.2 (with $j = J$), we have that, for every $k \in \mathbb{N}$,

$$\frac{\gamma_0^2}{\gamma_1^2}\nu^{-1}\|g_k\|^2 \leq F_\delta(x_k) - F_\delta(x_{k+1}) = F_\delta(x_k) - F_\delta(\widetilde{x}) - \big(F_\delta(x_{k+1}) - F_\delta(\widetilde{x})\big). \tag{7.45}$$

According to the Łojasiewicz property, there exist constants $\kappa > 0$, $\zeta > 0$ and $\theta \in [0, 1)$ such that

$$\|\nabla F_\delta(x)\| \geq \kappa |F_\delta(x) - F_\delta(\widetilde{x})|^\theta, \tag{7.46}$$

for every $x \in E$ such that $|F_\delta(x) - F_\delta(\widetilde{x})| < \zeta$. Let us now apply to the convex function $\varphi\colon [0, +\infty) \to [0, +\infty)\colon u \mapsto u^{1/(1-\theta)}$ the gradient inequality

$$(\forall (u, v) \in [0, +\infty)^2) \qquad \varphi(v) \geq \varphi(u) + \dot{\varphi}(u)(v - u) \tag{7.47}$$

which, after a change of variables, can be rewritten as

$$(\forall (u, v) \in [0, +\infty)^2) \qquad u - v \leq (1 - \theta)^{-1} u^\theta (u^{1-\theta} - v^{1-\theta}). \tag{7.48}$$

Combining the latter inequality with (7.45) leads to

$$F_\delta(x_k) - F_\delta(\widetilde{x}) - \big(F_\delta(x_{k+1}) - F_\delta(\widetilde{x})\big) \leq (1 - \theta)^{-1}(F_\delta(x_k) - F_\delta(\widetilde{x}))^\theta \Delta_k \tag{7.49}$$

where

$$\Delta_k = \big(F_\delta(x_k) - F_\delta(\widetilde{x})\big)^{1-\theta} - \big(F_\delta(x_{k+1}) - F_\delta(\widetilde{x})\big)^{1-\theta}. \tag{7.50}$$

Thus,

$$\|g_k\|^2 \leq \frac{\gamma_1^2}{\gamma_0^2}\nu(1 - \theta)^{-1}(F_\delta(x_k) - F_\delta(\widetilde{x}))^\theta \Delta_k. \tag{7.51}$$

Since $(F_\delta(x_k))_{k\in\mathbb{N}}$ converges to $F_\delta(\widetilde{x})$, there exists $k^* \in \mathbb{N}$, such that, for every $k \geq k^*$, $0 \leq F_\delta(x_k) - F_\delta(\widetilde{x}) < \zeta$. By applying the Łojasiewicz inequality,

$$(\forall k \geq k^*) \qquad \|g_k\|^2 \leq \frac{\gamma_1^2}{\gamma_0^2}\nu\kappa^{-1}(1 - \theta)^{-1}\|g_k\|\Delta_k. \tag{7.52}$$

This allows us to deduce that

$$\sum_{k=k^*}^{+\infty} \|g_k\| \leq \frac{\gamma_1^2}{\gamma_0^2}\nu\kappa^{-1}(1 - \theta)^{-1}\big(F_\delta(x_{k^*}) - F_\delta(\widetilde{x})\big)^{1-\theta}. \tag{7.53}$$

Furthermore, according to (7.26),

$$\frac{\eta}{2}\|x_{k+1}-x_k\|^2 = \frac{\eta}{2}\Big\|\sum_{j=0}^{J-1}(x_k^{j+1}-x_k^j)\Big\|^2 \tag{7.54}$$

which, by using Lemma 7.4.3 and the convexity of the squared norm, yields for every $k \in \mathbb{N}$,

$$\begin{aligned}\frac{\eta}{2}\|x_{k+1}-x_k\|^2 &\leq \frac{\eta J}{2}\sum_{j=0}^{J-1}\|x_k^{j+1}-x_k^j\|^2 \\ &\leq J\sum_{j=0}^{J-1}F_\delta(x_k^j)-F_\delta(x_k^{j+1}) = J\big(F_\delta(x_k)-F_\delta(x_{k+1})\big).\end{aligned} \tag{7.55}$$

By proceeding similarly to the derivation of (7.52), we obtain: for every $k \geq k^*$,

$$\frac{\eta}{2}\|x_{k+1}-x_k\|^2 \leq J(1-\theta)^{-1}\big(F_\delta(x_k)-F_\delta(\widetilde{x})\big)^\theta\Delta_k \leq J\kappa^{-1}(1-\theta)^{-1}\|g_k\|\Delta_k. \tag{7.56}$$

By using the fact that, for every $(u,v) \in [0,+\infty)^2$, $(uv)^{1/2} \leq u + \frac{v}{4}$, and taking $u = J\eta^{-1}\kappa^{-1}(1-\theta)^{-1}\Delta_k$ and $v = 2\|g_k\|$, (7.56) leads to

$$\|x_{k+1}-x_k\| \leq J\eta^{-1}\kappa^{-1}(1-\theta)^{-1}\Delta_k + \frac{1}{2}\|g_k\|. \tag{7.57}$$

By summing now over k and using (7.50) and (7.53), we finally obtain

$$\sum_{k=k^*}^{+\infty}\|x_{k+1}-x_k\| \leq \kappa^{-1}(1-\theta)^{-1}(J\eta^{-1}+\frac{\gamma_1^2}{\gamma_0^2}\frac{\nu}{2})\big(F_\delta(x_{k^*})-F_\delta(\widetilde{x})\big)^{1-\theta}. \tag{7.58}$$

This gives us the desired finite length property. In addition, since this condition implies that $(x_k)_{k\in\mathbb{N}}$ is a Cauchy sequence, it converges towards a single point, which is necessarily $\widetilde{x}$. Finally, due to the continuity of F_δ and Lemma 7.4.2, $(g_k)_{k\in\mathbb{N}}$ converges to zero. As $(x_k, F_\delta(x_k)) \to (\widetilde{x}, F_\delta(\widetilde{x}))$, the closedness property of the gradient implies that $\nabla F_\delta(\widetilde{x}) = \mathbf{0}$, i.e. $\widetilde{x}$ must be a critical point of F_δ.
□

Note that the inexact gradient methods that are studied in [Attouch et al., 2011] are distinct from the subspace algorithms we consider.

§ 7.5 Simulation results

The aim of this section is to illustrate and analyze the performance of the proposed algorithm in the context of Problem (7.1). We also show the non-convex penalization functions in Example 7.2.5 to be appropriate for image processing applications. In the following, denoising and deblurring image processing problems are considered. Our algorithm has also been applied to other image processing tasks, i.e. segmentation and tomographic image reconstruction, in [Chouzenoux et al., 2012]. However these applications are not in the main scope of this thesis. For each of the presented problems, the produced image $\widehat{x} \in \mathbb{R}^N$ is defined as a minimizer of the function F_δ, where Φ, H, y and V depend on the considered application. For the elastic net regularization term, we choose $V_0 = \tau \boldsymbol{I}$, $\tau \geq 0$. For deblurring, the linear operator H is not necessarily injective. Thus, we set τ equal to a small positive value in order to fulfill Assumption 7.2.1 (3). In the two other cases, τ is set to zero.

For every $s \in \{1, \ldots, S\}$, we have set $c_s = \mathbf{0}$. For the potential function $\psi_{s,\delta}$, we have tested the smooth convex $\ell_2 - \ell_1$ function $\psi_{s,\delta} \colon t \mapsto \lambda(\sqrt{1 + t^2/\delta^2} - 1)$ with $\lambda > 0$ (SC) and the smooth non-convex functions in Example 7.2.5 (2) (SNC2), Example 7.2.5 (3) (SNC3), Example 7.2.5 (4) (SNC4) and Example 7.2.5 (5) (SNC5). Moreover, in the case of denoising example, we provide optimization results for four state-of-the-art combinatorial optimization algorithms, namely the α-expansion [Boykov et al., 2001] (α-EXP), Quantized-Convex Move Splitting [Jezierska et al., 2011b] (QCSM), Tree-Reweighted (TRW) [Kolmogorov, 2006] and Belief Propagation (BP) [Felzenszwalb and Huttenlocher, 2004] algorithms, for which the nonsmooth non-convex truncated quadratic function in Example 7.2.5 (1) (NSNC) is considered. When the linear degradation operator is not the identity matrix, we do not provide comparisons with the combinatorial algorithms. Indeed, although a few algorithms [Raj and Zabih, 2005], [Raj et al., 2007] are applicable to inverse problems involving a linear degradation operator, these methods are well-founded only for a sparse convolution operator H. Moreover, they rely on an adaptation of the graph cut α-expansion algorithm, which is shown in our segmentation and denoising examples to be outperformed by our proposed approach.

The computation of the proposed MM subspace algorithm requires specifying the direction set D_k, for every $k \in \mathbb{N}$, and the number of MM subiterations J. First, the memory-gradient direction matrices,

$$(\forall k \geq m) \qquad D_k = [-g_k \mid x_k - x_{k-1} \mid \cdots \mid x_{k-m+1} - x_{k-m}] \in \mathbb{R}^{N \times (m+1)}, \tag{7.59}$$

with memory parameter $m \geq 0$, is considered. Moreover, in all our experiments, we set $J = 1$. This choice was observed to yield the best results in terms of convergence profile in the context of MM-based stepsize compu-

tation [Chouzenoux et al., 2011], [Labat and Idier, 2008]. In the following, we compare our proposed subspace algorithm, denoted hereafter by 3MG-m (for Majorize-Minimize Memory Gradient) with three other iterative first order descent methods. The methods we compare against are namely the nonlinear conjugate gradient (NLCG) algorithm [Hager and Zhang, 2006], the L-BFGS algorithm [Liu and Nocedal, 1989] with the memory parameter set to 3, and the fast version of half quadratic (HQ) algorithm [Allain et al., 2006]. For each descent algorithm, the MM scalar line search with $J = 1$ is employed for the computation of the stepsize. In the case of HQ, the inner optimization problems are solved partially with conjugate gradient iterations. Note that this algorithm has been previously studied in the context of non-convex regularization functions in [Delaney and Bresler, 1998], [Rivera and Marroquin, 2003]. In order to limit the influence of possible local minima in the non-convex case, the result of 10 iterations of convex minimization using an $\ell_2 - \ell_1$ penalty is employed as an initialization. In the convex case, minimization is started with the constant null image. The computational complexity is evaluated in terms of iteration number and computational time necessary to achieve the global stopping rule $\|g_k\|/\sqrt{N} < 10^{-4}$. C++ codes were compiled with the Intel C++ compiler icpc (version 12.1.0) and were run on an Intel(R) Xeon(R) CPU X5570 at 2.93GHz, in a single thread.

7.5.1 Image denoising

The first problem considered in this section corresponds to the recovery of an image $\overline{x}$ from noisy observations $u = \overline{x} + w$ where w is a realization of a zero-mean white Gaussian noise. The vector $\overline{x}$ here corresponds to `Word` image of size $N = 128 \times 128$ pixels. The variance of the noise was adjusted to correspond to a signal-to-noise ratio (SNR) of 15 dB (Fig. 7.2). The recovery of the original image is performed by solving (7.1) where $Q = 2N$,

$$H = \begin{bmatrix} \boldsymbol{I} \\ \boldsymbol{I} \end{bmatrix} \qquad y = \begin{bmatrix} u \\ \boldsymbol{0} \end{bmatrix}, \tag{7.60}$$

and

$$(\forall \boldsymbol{z} = (z_q)_{1 \leq q \leq 2N}) \qquad \Phi(\boldsymbol{z}) = \frac{1}{2} \left(\sum_{q=1}^{N} z_q^2 + \beta \sum_{q=N+1}^{2N} d_B^2(z_q) \right), \tag{7.61}$$

where d_B denotes the distance to the closed convex interval $B = [0, 255]$ and $\beta > 0$ is a weighting factor. Then, Φ is Lipschitz differentiable with Lipschitz constant $L = \max(1, \beta)$. In the sequel, we choose $\beta = 1$ so that we have $L = 1$. Moreover, the penalization term (7.3) is used, with $\tau = 0$ and an anisotropic penalization on neighboring pixels i.e., $S = 2N$, and for every $s \in \{1, \ldots, N\}$ (resp. $s \in \{N+1, \ldots, 2N\}$), $P_s = 1$ and V_s corresponds

to a horizontal (resp. vertical) gradient operator. This anisotropic term is chosen so as to compare more fairly our approach with the combinatorial methods.

Parameters λ and δ were automatically chosen to maximize the SNR between the original image and its reconstructed version. In Fig. 7.3, the reconstructed images are displayed and the corresponding SNR and MSSIM [Wang et al., 2004] values are provided. Morever, the absolute values of the reconstruction errors $\widehat{x} - \overline{x}$ are illustrated. It should be noticed that the non-convex regularization strategy with penalty function SNC2 leads to the best results in terms of reconstruction quality.

7.5.1.1 Influence of memory size

We first analyze the effect of the memory size m on the performance of our algorithm. We recall that the detailed performance analysis of 3MG algorithm with respect to the size of the memory was provided in [Chouzenoux et al., 2011], but it was restricted to the convex case. The results in Tab. 7.2 illustrate that the choice of a memory equal to one, which corresponds to a subspace with size 2, leads to the best results in terms of computational time. Hence, our experiments confirm the conclusions drawn in [Chouzenoux et al., 2011] for the convex case. Consequently, the setting $m = 1$, i.e. $D_k = [-g_k \mid x_k - x_{k-1}]$ for all $k \geq 1$ was retained for the remaining experiments presented in the chapter, and the shorter notation 3MG is employed for denoting the 3MG-1 algorithm.

7.5.1.2 Comparison with NLCG algorithm

The NLCG algorithm is based on the following iterations:

$$(\forall k \geq 1) \qquad x_{k+1} = x_k + \alpha_k(-g_k + \beta_k(x_k - x_{k-1})), \tag{7.62}$$

where $\alpha_k > 0$ is the stepsize and $\beta_k \in \mathbb{R}$ is the conjugacy parameter. Tab. 7.3 summarizes the performances of NLCG for five different conjugacy strategies described in [Hager and Zhang, 2006]. Contrary to the convex case, in the non-convex case the conjugacy formula has a major influence on the convergence speed (see Tab. 7.3 results related to NLCG in rows 1-6 and 7-30). In particular the conjugacy strategies FR and DY do not appear well-adapted to the non-convex problems. On the other hand, the HS, LS and PRP+ conjugacy parameters yield a good numerical performance. Thus, they have been selected for the numerical experiments in the following. For comparison, we include in Tab. 7.3 the results of 3MG for $m = 1$. Although the superiority of 3MG versus NLCG is not established theoretically, these experimental results are very promising. They show that 3MG algorithm is faster than the considered non-linear conjugate gradient algorithms.

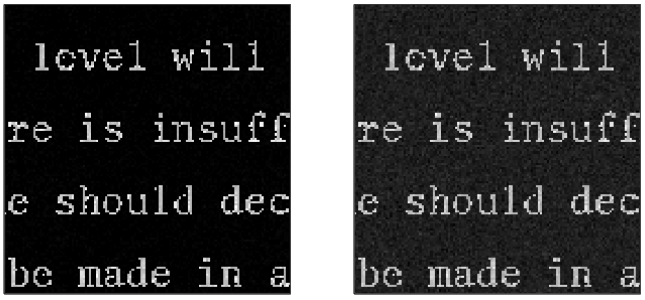

(*a*) Original 128×128

(*b*) Noisy $\mathcal{N}(0, 100)$
SNR= 15 dB
MSSIM = 0.66

Figure 7.2: *Denoising test image.*

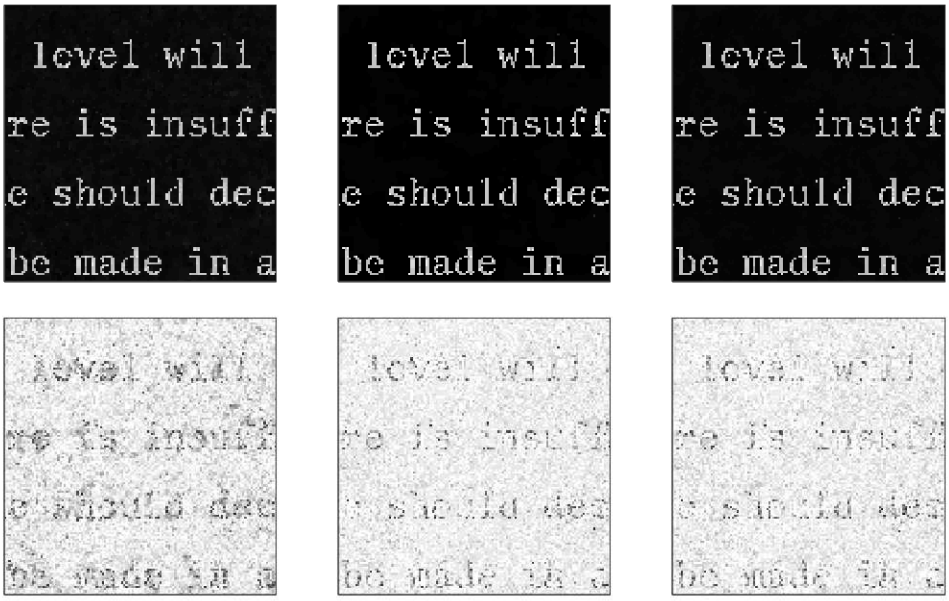

(*a*) 3MG SC
$\lambda = 0.3$
$\delta = 0.07$
SNR = 20.41 dB
MSSIM = 0.89

(*b*) TRW
$\lambda = 350$
$\delta = 3.5$
SNR = 22.8 dB
MSSIM = 0.93

(*c*) 3MG SNC2
$\lambda = 280$
$\delta = 7.25$
SNR = 22.74 dB
MSSIM = 0.92

Figure 7.3: *Denoising results and absolute reconstruction error.*

$\psi_{s,\delta}(\cdot)$ (λ, δ)	Algorithm	Iteration	Time (s)	F_δ	SNR (dB)
SNC2 $(280, 7.25)$	3MG-0	998	1.08	$1.54 \cdot 10^6$	22.74
	3MG-1	270	0.35	$1.54 \cdot 10^6$	22.74
	3MG-2	247	0.38	$1.54 \cdot 10^6$	22.74
	3MG-3	248	0.44	$1.54 \cdot 10^6$	22.74
	3MG-4	243	0.51	$1.54 \cdot 10^6$	22.74
	3MG-5	239	0.59	$1.54 \cdot 10^6$	22.74
SNC3 $(301, 8.76)$	3MG-0	536	0.66	$1.59 \cdot 10^6$	22.55
	3MG-1	101	0.21	$1.59 \cdot 10^6$	22.55
	3MG-2	159	0.28	$1.59 \cdot 10^6$	22.55
	3MG-3	158	0.32	$1.59 \cdot 10^6$	22.55
	3MG-4	156	0.36	$1.59 \cdot 10^6$	22.55
	3MG-5	155	0.41	$1.59 \cdot 10^6$	22.55
SNC4 $(381, 10)$	3MG-0	287	0.61	$1.8 \cdot 10^6$	22.47
	3MG-1	69	0.16	$1.8 \cdot 10^6$	22.47
	3MG-2	70	0.19	$1.8 \cdot 10^6$	22.47
	3MG-3	67	0.21	$1.8 \cdot 10^6$	22.47
	3MG-4	66	0.22	$1.8 \cdot 10^6$	22.47
	3MG-5	67	0.28	$1.8 \cdot 10^6$	22.47
SNC5 $(386, 9)$	3MG-0	202	0.42	$1.8 \cdot 10^6$	22.48
	3MG-1	49	0.11	$1.8 \cdot 10^6$	22.48
	3MG-2	51	0.13	$1.8 \cdot 10^6$	22.48
	3MG-3	51	0.16	$1.8 \cdot 10^6$	22.48
	3MG-4	52	0.17	$1.8 \cdot 10^6$	22.48
	3MG-5	52	0.21	$1.8 \cdot 10^6$	22.48

Table 7.2: *Denoising problem with* `word` *image. Influence of memory parameter m in 3MG algorithm.*

$\psi_{s,\delta}(\cdot)$ (λ, δ)	Algorithm	Iteration	Time (s)	F_δ	SNR (dB)
SC $(0.3, 0.07)$	NLCG-HS	138	0.84	$2.7 \cdot 10^6$	20.41
	NLCG-FR	305	1.86	$2.7 \cdot 10^6$	20.41
	NLCG-PRP+	143	0.87	$2.7 \cdot 10^6$	20.41
	NLCG-LS	158	0.96	$2.7 \cdot 10^6$	20.41
	NLCG-DY	223	1.35	$2.7 \cdot 10^6$	20.41
	3MG	122	0.22	$2.7 \cdot 10^6$	20.41
SNC2 $(280, 7.25)$	NLCG-HS	1250	2.34	$1.54 \cdot 10^6$	22.74
	NLCG-FR	> 10000	–	–	–
	NLCG-PRP+	292	0.55	$1.54 \cdot 10^6$	22.74
	NLCG-LS	320	0.79	$1.54 \cdot 10^6$	22.74
	NLCG-DY	> 10000	–	–	–
	3MG	270	0.35	$1.54 \cdot 10^6$	22.74
SNC3 $(301, 8.76)$	NLCG-HS	112	0.26	$1.59 \cdot 10^6$	22.55
	NLCG-FR	> 10000	–	–	–
	NLCG-PRP+	179	0.42	$1.59 \cdot 10^6$	22.55
	NLCG-LS	210	0.54	$1.59 \cdot 10^6$	22.55
	NLCG-DY	> 10000	–	–	–
	3MG	101	0.21	$1.59 \cdot 10^6$	22.55
SNC4 $(381, 10)$	NLCG-HS	102	1.1	$1.8 \cdot 10^6$	22.47
	NLCG-FR	3289	36.3	$1.8 \cdot 10^6$	22.47
	NLCG-PRP+	79	0.9	$1.8 \cdot 10^6$	22.47
	NLCG-LS	90	1	$1.8 \cdot 10^6$	22.47
	NLCG-DY	3342	36.8	$1.8 \cdot 10^6$	22.47
	3MG	69	0.16	$1.8 \cdot 10^6$	22.47
SNC5 $(386, 9)$	NLCG-HS	52	0.15	$1.8 \cdot 10^6$	22.48
	NLCG-FR	> 10000	–	–	–
	NLCG-PRP+	55	0.16	$1.8 \cdot 10^6$	22.48
	NLCG-LS	56	0.16	$1.8 \cdot 10^6$	22.48
	NLCG-DY	> 10000	–	–	–
	3MG	49	0.11	$1.8 \cdot 10^6$	22.48

Table 7.3: *Denoising problem with* `word` *image. Influence of conjugacy parameter* β_k *in NLCG algorithm.*

7.5.1.3 Summary

We summarize the results by comparing the performance of continuous and discrete algorithms with SC, SNC and NSNC potential functions (see Tab. 7.4). One can observe that the considered discrete optimization algorithms lead to a SNR which is very similar to that obtained with smooth non-convex regularization. However, they are more demanding in terms of computational time than 3MG. Thus, we can conclude that the 3MG algorithm behaves well in comparison with the considered continuous and discrete algorithms.

7.5.2 Image deblurring

Our second experiment corresponds to the problem of restoring an image $\overline{x}$ from observations u corrupted by noise and blur R. The recovery of the original image is performed by solving (7.1) where $Q = 2N$

$$H = \begin{bmatrix} R \\ \boldsymbol{I} \end{bmatrix} \qquad y = \begin{bmatrix} u \\ \mathbf{0} \end{bmatrix}, \tag{7.63}$$

and

$$(\forall \boldsymbol{z} = (z_q)_{1 \leq q \leq 2N}) \qquad \Phi(\boldsymbol{z}) = \frac{1}{2} \left(\sum_{q=1}^{N} z_q^2 + \beta \sum_{q=N+1}^{2N} d_B^2(z_q) \right), \tag{7.64}$$

where d_B denotes the distance to the closed convex interval $B = [0, 255]$ and $\beta = 0.01$. Furthermore, function Ψ_δ is given by (7.3) with $\tau = 10^{-10}$ and $S = 2N$. We consider, for every $s \in \{1, \ldots, N\}$, an isotropic regularization between neighbooring pixels, i.e., $P_s = 2$ and $V_s = [\Delta_s^{\mathrm{h}} \;\; \Delta_s^{\mathrm{v}}]^\top$ where $\Delta_s^{\mathrm{h}} \in \mathbb{R}^N$ (resp. $\Delta_s^{\mathrm{v}} \in \mathbb{R}^N$) corresponds to a horizontal (resp. vertical) gradient operator, and, for every $s \in \{N+1, \ldots, 2N\}$, the Hessian-based penalization from [Lefkimmiatis et al., 2012] i.e., $P_s = 3$ and $V_s = [\Delta_s^{\mathrm{hh}} \;\; \sqrt{2}\Delta_s^{\mathrm{hv}} \;\; \Delta_s^{\mathrm{vv}}]^\top$ where $\Delta_s^{\mathrm{hh}} \in \mathbb{R}^N$, $\Delta_s^{\mathrm{hv}} \in \mathbb{R}^N$ and $\Delta_s^{\mathrm{vv}} \in \mathbb{R}^N$ model the second-order finite difference operators between neighbooring pixels, as described in [Lefkimmiatis et al., 2012, Sec.III-A]. For $s \in \{N+1, \ldots, 2N\}$ we consider the $\ell_2 - \ell_1$ function $\psi_{s,\delta} \colon t \mapsto \rho(\sqrt{1 + t^2/(\theta\delta)^2} - 1)$, where ρ and θ take positive values. We illustrate the performance of our algorithm on the image `montage` of size 256×256, which represents different cases of natural and artificial images, in the case of the Gaussian noise i.e. $u = R\overline{x} + w$ where w is a realization of a zero-mean white Gaussian noise. Tab. 7.5 presents the results for SC and SNC2 regularization of the image gradient (i.e. $\psi_{s,\delta}$ for $s \in \{1, \ldots, N\}$). Parameters $(\rho, \theta, \lambda, \delta)$ are tuned to maximize the SNR of the restored image. In both cases, the 3MG algorithm outperforms the three considered descent algorithms in terms of time efficiency.

$\psi_{s,\delta}(\cdot)$ (λ, δ)	Algorithm	Iteration	Time (s)	F_δ	SNR (dB)
SC $(0.3, 0.07)$	3MG	122	0.22	$2.7 \cdot 10^6$	20.41
	NLCG-HS	138	0.35	$2.7 \cdot 10^6$	20.41
	NLCG-PRP+	143	0.37	$2.7 \cdot 10^6$	20.41
	NLCG-LS	158	0.96	$2.7 \cdot 10^6$	20.41
	L-BFGS	209	0.73	$2.7 \cdot 10^6$	20.41
	HQ	670	3.03	$2.7 \cdot 10^6$	20.41
SNC2 $(280, 7.25)$	3MG	270	0.35	$1.54 \cdot 10^6$	22.74
	NLCG-HS	1250	2.34	$1.54 \cdot 10^6$	22.74
	NLCG-PRP+	292	0.55	$1.54 \cdot 10^6$	22.74
	NLCG-LS	320	0.79	$1.54 \cdot 10^6$	22.74
	L-BFGS	332	0.96	$1.54 \cdot 10^6$	22.73
	HQ	1025	3.84	$1.54 \cdot 10^6$	22.74
SNC3 $(301, 8.76)$	3MG	101	0.21	$1.59 \cdot 10^6$	22.55
	NLCG-HS	112	0.26	$1.59 \cdot 10^6$	22.55
	NLCG-PRP+	179	0.42	$1.59 \cdot 10^6$	22.55
	NLCG-LS	210	0.54	$1.59 \cdot 10^6$	22.55
	L-BFGS	351	1.08	$1.59 \cdot 10^6$	22.55
	HQ	604	2.53	$1.59 \cdot 10^6$	22.54
SNC4 $(381, 10)$	3MG	69	0.16	$1.8 \cdot 10^6$	22.47
	NLCG-HS	102	0.27	$1.8 \cdot 10^6$	22.47
	NLCG-PRP+	79	0.21	$1.8 \cdot 10^6$	22.47
	NLCG-LS	90	1	$1.8 \cdot 10^6$	22.47
	L-BFGS	94	0.32	$1.8 \cdot 10^6$	22.46
	HQ	287	1.36	$1.8 \cdot 10^6$	22.47
SNC5 $(386, 9)$	3MG	49	0.11	$1.8 \cdot 10^6$	22.48
	NLCG-HS	52	0.15	$1.8 \cdot 10^6$	22.48
	NLCG-PRP+	55	0.16	$1.8 \cdot 10^6$	22.48
	NLCG-LS	56	0.16	$1.8 \cdot 10^6$	22.48
	L-BFGS	80	0.25	$1.8 \cdot 10^6$	22.48
	HQ	202	1.1	$1.8 \cdot 10^6$	22.48
NSNC $(350, 3.5)$	α-EXP	4	4.67	$1.31 \cdot 10^6$	22.69
	QCSM	2	1.25	$1.31 \cdot 10^6$	22.60
	TRW	5	1.65	$1.31 \cdot 10^6$	22.80
	BP	18	5.33	$1.31 \cdot 10^6$	22.73

Table 7.4: *Results for the denoising problem.*

(a) Original 256×256

(b) Degraded $\mathcal{N}(0, 16)$
3×3 uniform blur
SNR= 18.65 dB
MSSIM = 0.82

Figure 7.4: *Deblurring test image.*

(a) 3MG SC
$\rho = 0.56$, $\theta = 0.18$
$\lambda = 0.042$, $\delta = 4.19$
SNR = 26.90 dB
MSSIM = 0.94

(b) 3MG SNC2
$\rho = 41.55$, $\theta = 0.86$
$\lambda = 3.68$, $\delta = 18.65$
SNR = 27.69 dB
MSSIM = 0.94

Figure 7.5: *Deblurring results.*

$\psi_{s,\delta}(\cdot)$ $(\rho, \theta, \lambda, \delta)$	Algorithm	Iteration	Time (s)	F_δ	SNR (dB)
SC $(0.56, 0.18, 0.042, 4.19)$	3MG	121	<u>8.36</u>	$8.22 \cdot 10^6$	26.90
	NLCG-HS	121	8.92	$8.22 \cdot 10^6$	26.90
	NLCG-PRP+	129	9.32	$8.22 \cdot 10^6$	26.90
	NLCG-LS	131	9.51	$8.22 \cdot 10^6$	26.90
	L-BFGS	162	12.42	$8.22 \cdot 10^6$	26.90
	HQ	418	94.3	$8.22 \cdot 10^6$	26.90
SNC2 $(41.55, 0.86, 3.68, 18.65)$	3MG	196	<u>11.58</u>	$7.92 \cdot 10^6$	27.69
	NLCG-HS	243	15.93	$7.92 \cdot 10^6$	27.69
	NLCG-PRP+	221	14.41	$7.92 \cdot 10^6$	27.69
	NLCG-LS	246	15.62	$7.92 \cdot 10^6$	27.69
	L-BFGS	216	14.78	$7.92 \cdot 10^6$	27.69
	HQ	616	104.9	$7.92 \cdot 10^6$	27.69

Table 7.5: *Results for the deblurring problem.*

Additionally, the non-convex strategy leads to better results in terms of SNR (see Fig. 7.4). One can also observe that in this case the staircasing effect is reduced (see some image details in Fig. 7.4).

§ 7.6 Conclusion

In this chapter, we have considered a class of smooth non-convex regularization functions and we have proposed an efficient minimization strategy for solving the associated variational problems in imaging applications. Connections with ℓ_0 penalized problems were exhibited asymptotically. In addition, a novel convergence proof of the proposed subspace MM algorithm relying on the Kurdyka-Łojasiewicz inequality was given. Numerical experiments were carried out to compare the proposed approach with other state-of-the art continuous optimization methods (both for non-convex and convex penalizations) and with discrete optimization approaches dealing with a truncated quadratic penalization. In the presented image processing examples, we argue that the proposed approach constitutes an appealing alternative to the existing methods in terms of recovered image quality and computational time.

- Chapter 8 -

Conclusion

As we have seen, there is an increasing interest for high resolution 3D confocal macroscopy images. However, human understanding and automatic assessment of an observed scene is still limited due to noise and blur. In low-count discrete photon imaging systems the spatial distribution of only a few photons per pixel may encode important information about the shape of an observed object. In order to retrieve these informations, the associated methods need to be carefully tailored to cover the specificity of low-count images, their noise distribution and the characteristics of their blur. The physics-driven design of such approaches requires learning noise parameters and blur operator model. This thesis contributed into the development of such tools. Our next step was to restore the degraded image. Our goal was to improve over existing restoration methods taking into account more realistic models.

§ 8.1 Contributions

Poisson-Gaussian noise parameter estimation: The parameters of signal dependent noise are particularly difficult to estimate. Concerning confocal data, when one attempts to identify noise parameters from time series, the data is nonstationary in time and in space. The time nonstationarity is essentially due to the bleaching problem. In this thesis an EM-based approach was proposed to handle this problem. The high accuracy of the proposed method was illustrated through the comparison between obtained estimates and associated Cramer-Rao bounds. In the case of parameter estimation from a single image, a selection procedure of pixels with similar values is required. While most published approaches incorporate two steps i.e. segmentation and identification, we proposed an iterative noise parameter

estimation algorithm over image segments. The proposed minimization method alternates between discrete and continuous optimization procedures. The first aims at finding group of pixels with similar values by enforcing a spatial regularity in the considered image, while the latter estimates new noise parameters by employing an EM approach. As shown by our simulation results, our proposed approach leads to promising results.

Restoration of Poisson-Gaussian data: So far the usage of a mixed continuous-discrete model corresponding to Poisson-Gaussian noise statistics was limited due to the lack of theoretical advances in this area. Given a Poisson-Gauss noise model, only approximative restoration methods have been proposed so far. In contrast, we have provided restoration models based on the true Poisson-Gaussian neg-log likelihood. In this thesis we have proved that the Poisson-Gaussian neg-log likelihood is a convex, Lipschitz-differentiable function. The provided convexity result is in fact more general as it concerns the neg-log likelihood of a mixture of Generalized-Gaussian and Poisson variables. Numerical difficulties related to the computation of the infinite sums arising in the computation of the gradient of the Poisson-Gaussian neg-log likelihood function have been addressed. In light of these theoretical results, we have proposed a new variational approach for solving data recovery problems in the presence of Poisson-Gaussian noise. We have developed the first implementation of the primal-dual algorithm presented in [Combettes and Pesquet, 2012]. We have shown that it is of great practical value and flexibility, since it can be used with a large range of penalization strategies. Our results indicate the performance gain using the exact data fidelity term instead of various approximation for low photon count images. This work was recognized by the European Organization for Nuclear Research (CERN), and presented during an invited talk in June 2012.

Non-convex sparsity measures: In the context of image restoration, the most common assumption is that the signal of interest has a sparse representation with respect to preassigned operator. According to [Donoho et al., 1995], an ideal measure of sparsity is the ℓ_0 measure. However, due to the non-convexity of ℓ_0, different measures of sparsity have been proposed. Among them the ℓ_1 measure is the most popular, because it is convex. In this thesis we examined the $\ell_2 - \ell_0$ measure. Firstly we proposed a fast discrete optimization algorithm for denoising with sparsity measures given by truncated convex function. One limitation of this approach is that it cannot be easily extended to handle general restoration problem (e.g. with a convolution kernel). One advantage is that it does not require data fidelity term to be Lips-

chitz differentiable. Building on this, we have proposed alternative continuous optimization algorithm for restoration problem. This work was the result of a collaboration with Emilie Chouzenoux. We have considered a class of smooth non-convex regularization functions. Convergence to ℓ_0 penalized problems have been shown asymptotically. In addition, contributions to a novel convergence proof of the proposed subspace MM algorithm relying on the Kurdyka-Łojasiewicz inequality were given. In the presented image restoration examples, we argue that our proposed approaches constitute an appealing alternative to existing methods in terms of recovered image quality and computational time.

Mixed discrete-continuous optimization methods: Continuous and discrete optimization methods increasingly inspire and depend on each other. In the context of image processing, approaches often cross the boundary between discrete and continuous optimization. In this thesis we have proposed an optimization framework featuring both continuous and combinatorial techniques. Our approach address problems, in which all of the variables take values from an unknown discrete set. The discrete set is described by its cardinality and is known to be an inclusion of a given continuous set. We have shown a vector quantization and a single image noise parameter estimation problem to be naturally formulated in such framework. The associated discrete-continuous optimization algorithms have led to interesting and promising results.

§ 8.2 Perspectives

Restoration of Generalized Poisson-Gaussian data: The convexity result presented here allows us to address the problem of denoising data corrupted by Generalized Gaussian-Poisson noise in the framework proposed in Chapter 6. In such case the convergence speed is independent of the Lipschitz constant. Provided that we use convex regularization term, the convex move is guaranteed to converge in a number of iterations lower or equal to the number of labels. For truncated convex sparsity measures the convergence is also fast, although not guaranteed by any theoretical results. However, the problem of data restoration in the presence of Generalized Gaussian-Poisson noise is more difficult, as the associated neg-log likelihood function has not been shown to be a Lipschitz differentiable function. Having this result, we may extend our proposed algorithm in Chapter 5 to the case of Generalized Gaussian-Poisson data.

Non-convex regularization strategies for Poisson-Gaussian data: As mentioned in the previous point the Poisson-Gaussian data denois-

ing problem can be adopted in the framework proposed in Chapter 6. However, in order to handle the restoration problem with $\ell_2 - \ell_0$ sparsity measures using algorithm developed in Chapter 7, we need an extra theoretical result, that is to show that the objective function with data fidelity term derived from Poisson-Gaussian likelihood satisfies the Kurdyka-Łojasiewicz inequality.

Comparison with other Primal-Dual algorithms: The algorithm proposed in Chapter 5 was formulated in the framework introduced in [Combettes and Pesquet, 2012]. However, the problem (5.30) can also be addressed using a primal-dual extension of the forward-backward algorithm proposed independently in [Vu, 2011] and [Condat, 2012]. This algorithm offers the same flexibility of incorporating regularization terms as Algorithm 9. However in the algorithm proposed by [Vu, 2011], [Condat, 2012] a gradient descent term needs to be computed only once per iteration, while in our proposed algorithm it needs to be computed twice. In future work we will compare both algorithms for our problem in terms of time efficiency.

Robustness of restoration algorithm to noise parameters: In this thesis we have proposed two Poisson-Gaussian noise parameters identification approaches and associated restoration algorithm. In light of these contributions, a study related to the restoration algorithm robustness to the precision of the provided noise parameters is missing. The main difficulty would be to separate the impact of the noise parameter choice on the final results from the other factors, e.g. regularization parameter choice. A possibility could be to try to reformulate the Poisson-Gaussian restoration problem into epigraphical projection framework [Chierchia et al., 2012], [Harizanov et al., 2012].

Inter-channel prior for confocal images: The problem of multichannel confocal macroscopy images restoration has not been addressed in this thesis. Some multi-channel image restoration techniques do exist. However most of them are adapted to natural color images [Aujol and Kang, 2006], [Joshi et al., 2009]. As far as we are concerned, modeling inter-channel dependency for confocal macroscopy images is an open problem. Thus, the simplest solution is to restore each channel independently. However, enforcing inter-channel constraints should lead to an improvement of the quality of the restored images. One goal could be to extend the proposed primal-dual algorithm to multi-channel problems incorporating inter-channel regularization term adapted to confocal macroscopy images.

Confocal macroscopy optical PSF estimation: One subject that has not yet been fully studied in this work is the estimation of confocal

macroscopy PSFs. PSF determination is a crucial preliminary step to image restoration. Even if one resorts to blind deconvolution schemes, a priori knowledge related to the PSF is desired [Thiébaut, 2002], [Bolte et al., 2010], [Soulez et al., 2012]. This knowledge can be acquired either by studying PSF theoretical properties or experimental data. In the context of fluorescence imaging, the theoretical approach usually relies on diffraction-limited PSF model [Kirshner et al., 2012]. Experimental PSFs may be measured using calibration beads [Yoo et al., 2006] or directly from the image by extracting small point-like objects [Von Tiedemann et al., 2006]. Such PSFs can be used for instance to validate theoretical parametric PSF model or to assess the aberration of point spread function in given imaging systems [Pankajakshan et al., 2012].

The PSF modeling problem becomes more complex if the PSF is spatially variant. The space variation model usually relies on one of the following strategies. Firstly, assuming that the PSF variation is smooth, the PSF can be represented as a weighted sum of basis functions [Arigovindan et al., 2010]. The efficiency can be further improved by applying interpolation methods [Denis et al., 2011]. Alternatively an image can be segmented into regions inside which PSFs are assumed to be invariant [Reràbek and Pàta, 2008]. In fluorescence microscopy, the aberrations increase as a function of depth from the coverslip [Aguet et al., 2008], [Pawley, 2006, Chapter 23]. A scheme illustrating an effect of spherical aberration is illustrated in Fig. 8.1 (a). One can observe that the peripheral rays passing through a lens are focused closer to the lens than paraxial rays. In microscopy, the strength of the spherical aberration depends on refractive index of specimen medium. Consequently, the effect of spherical aberration may manifest itself in a non-homogenous way due to refractive index gradient in a sample. This is a common phenomenon observed in microscopy, and the main reason for PSF depth variation. In Fig. 8.1 (b) one can observe the characteristic effect of growing PSF size with depth. This effect is accompanied with a decrease of image intensity [Ben Hadj and Blanc-Féraud, 2012].

One goal related to confocal macroscopy images would be to assess experimentally the PSF depth variation by imaging sample with point sources (beads) placed at different depths by using the experimental set up illustrated in Fig. 8.2. This is a similar experimental setup as the one proposed in [Hanser et al., 2004] (see Fig. 8.1 (b)) but adapted to observe several PSF distributed over the field in different depths.

The sections of prepared specimen illustrate the PSF depth variation for two choices of objectives (see Fig. 8.3 (a)). One can observe that the high magnitude depth PSF variation for 20 $\times$ objective lens are

no longer visible for 10 × objective lens and conclude that the depth intensity variation of PSF decreases with objective magnification.

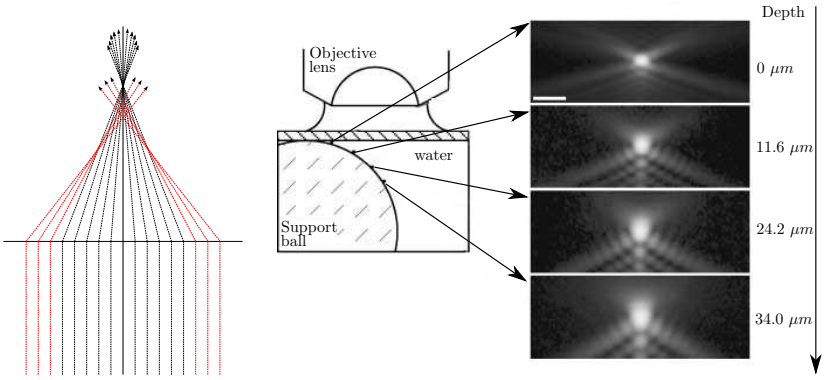

(a) Spherical aberration. Peripheral rays (red lines) passing through a spherically shaped lens are focused closer to the lens than paraxial rays (those rays entering the objective closest to the optical axes).

(b) PSF depth variation due to the depth dependent spherical aberration in widefield microscope (redrawn from [Hanser et al., 2004]). The experiment set up for locating beads at a variety of well-characterized depths below the cover slip. Beads are applied onto a support ball (1-mm-diameter sapphire ball lens, Edmund Industrial Optics, Barrington, NJ, U.S.A.) immobilized in near contact with the cover glass surface. The space between the support ball and the cover glass is filled with water.

Figure 8.1: *PSF depth variation due to the spherical aberration*

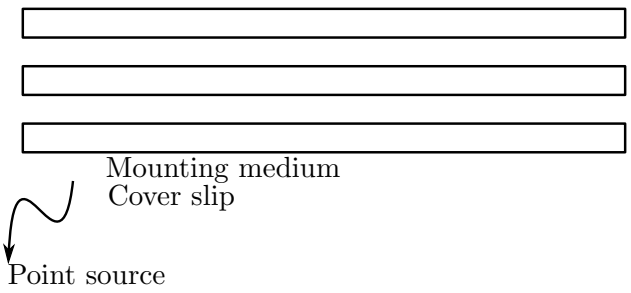

Figure 8.2: *Proposed experimental setup.*

Consequently, we should expect a confocal macroscope system, working with 5 × objective under very low numerical aperture not to suffer from the depth intensity variation observed in the microscope system. Indeed the results presented in Fig. 8.3 (b) indicate that the typical intensity decrease for confocal microscopy are not present in macroscopy

imaging modality.

The confocal macroscopy PSF varies in the field of view, i.e. the optical aberrations increase towards the margins (Fig. 8.4). Similar phenomena occur in the context of astronomy [Denis et al., 2011], but for 2D-PSF. In macroscopy the problem of field aberration is coupled with the problem of out-of-focus blur, in the depth-direction, due to the diffraction-limited nature of the lens. An associated 3D-PSF model was proposed in [Pankajakshan et al., 2010].

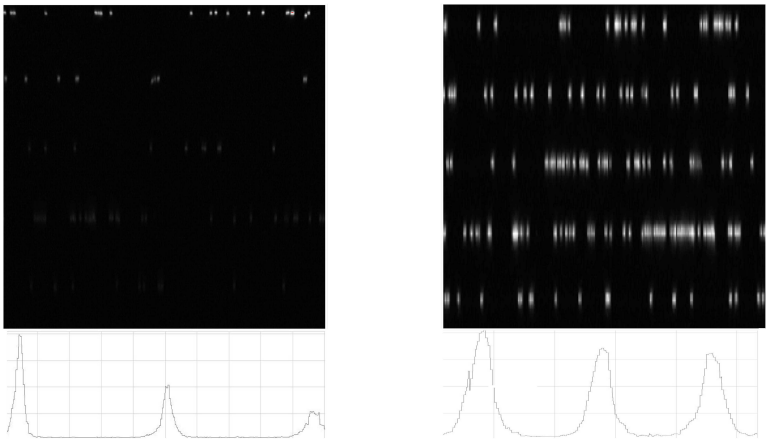

(a) Microscope. Confocal microscope PSF radial projection (author: *Gilbert Engler*). The observed sample consists of point sources (beads) mounted on 5 different depth. The right and left image illustrate the confocal microscope PSF radial projection and depth intensity profile for 20 × (left) and 10 × (right) objective lens

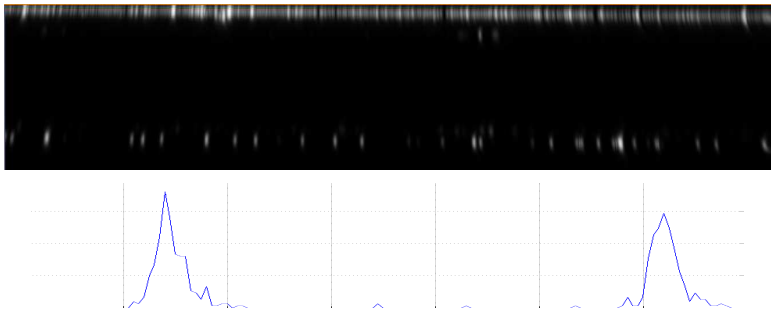

(b) Macroscope. Confocal macroscope PSF radial projection and depth intensity profile for 5 × objective lens (author: *Gilbert Engler*). The observed sample consists of point sources (beads) mounted on 2 different depth.

Figure 8.3: *An example illustrating PSF depth variation*

One limitation of the proposed PSF model is that it requires two pa-

rameters to be estimated at each pixel position. Certainly, the problem is untractable without any prior knowledge about unknown parameters. Conclusions derived in this previous work were based on experiments with beads mounted only one depth. Hence, it is not stated clearly if field aberrations vary with depth. The PSFs symmetry also needs to be investigated. We would assume that the principal axes of the PSFs observed around each bead converge to one point, called the optical center. More specifically, we would aim at comparing the optical center coordinates identified using the PSFs originating from different depth. In [Pankajakshan et al., 2012] the authors observed that the PSFs are symmetrical around the optical center but a procedure for optical center identification is missing.

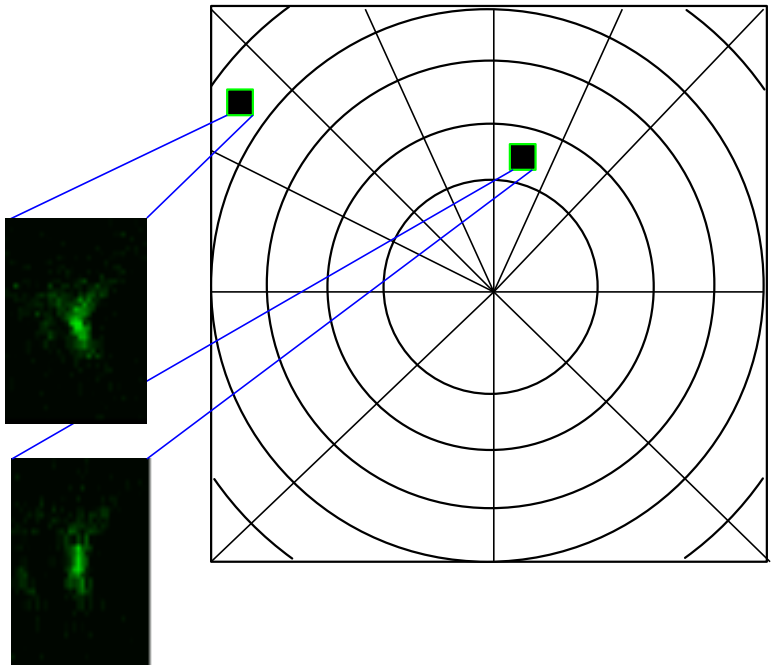

Regions of invariant macroscopy PSFs in the presence of field aberrations. The top and bottom images illustrate the radial projection of PSFs cropped from the periphery and center of the field, respectively.

Figure 8.4: *An example illustrating macroscope PSF field variation*

In order to achieve this goal, we have performed some first tests. The experiment was designed to detect the signal originating from point sources distributed over sample as illustrated in Fig. 8.2. The reported signal was expected to consist of PSFs distributed over the 3D image in field and depth. The distribution in field was as uniform as possible, while in depth each PSF took one position from a discrete set of num-

bers, associated with beads layers. The PSF was assumed to be 3D. Further we expected the principal axes of the PSFs to all converge to one point (the optical center). Hence, the idea of the experiment was to segment all the PSF in the acquired image and then to detect their center and their principal axes. To this aim, we proposed the following two step procedure. (1) Find the discrete finite set of ellipsoids in an image, which we assumed to be related by injection with PSFs. (2) Compute the grey-level statistics of each independent ellipsoid. Next, we briefly discuss the proposed implementation of each step.

Difficulties that can arise in the process of identifying the signal of interest associated with PSF stem from noise, beads sticking together in the original sample or very low image SNR. To overcome them, we proposed the following simple implementation using morphological tools. First, the noise was reduced by anisotropic Gaussian blurring. Then small maxima were suppressed by volume opening [Vincent, 1993], which had the effect of suppressing small objects. A top-hat operator was then used to remove low frequency variations in the background [Serra, 1982]. Next, segmentation was performed by thresholding, resulting in a binary image where 1 correspond to the signal of interest and 0 the background. Finally we extended the volume of each detected nonzero ellipsoid using the Watershed algorithm [Beucher and Lantuéjoul, 1979], i.e. we searched for the maximum region around each volume under the constraint that the regions of any two PSFs may not intersect. The size of resulting volume was also limited by maximum length, width and height. In the second step we computed the grey-level statistics of each independent ellipsoid. More specifically we used principal component analysis [Eckart and Young, 1936] to find the center and principal axes of each ellipsoid.

An example of the results of the above described procedure is illustrated in Fig. 8.5. In the experimental sample, the beads were distributed over two layers. Images were acquired using a macro confocal laser scanning microscope (Leica TCS-LSI). Measurements were done on images taken according to the following settings: pinhole 1.0 airy, 400 Hz scan speed, excitation line 405/532 nm, and emission range 534 nm-690nm. In the processed 12 bit precision image stack of size $2048 \times 2048 \times 350$ we have identified 967 PSFs, within 930 lay in the first layer and only 37 in the second one. The nonuniform distribution of PSFs in two layers can be also observed in Fig. 8.4. This is clearly an undesired effect. Nevertheless, as expected the results presented in Fig. 8.5 indicates that the collection of lines associated with couples (the PSF center, principal axes of the PSF) form a cone like shape, which is in agreement with our assumption that the principal axes of the PSFs all converge to one point. The cross-section over the PSFs

cone in the the x, y plane close to the optical center is illustrated in the zoomed image in Fig. 8.5. Ideally, one should expect only a point in this plane. However, the acquired data are noisy and there are many outliers.

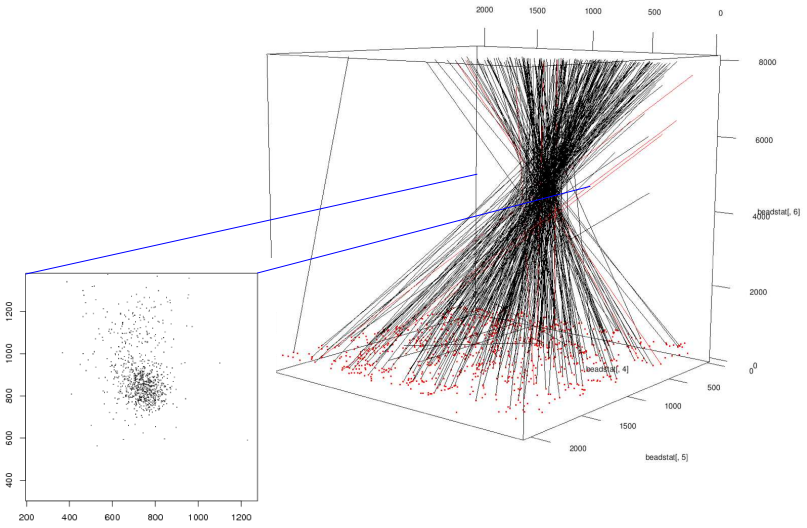

Figure 8.5: *An example illustrating PSFs the convergence of the main direction of some measured PSFs.*

The further study would start from the experimental setting presented here . The principal goal would be to identify the optical center using all PSFs, and PSFs originating from each layer separately, thus allowing us to to acquire more prior information about field aberration in a confocal macroscopy imaging system.

List of Figures

List of Tables

Bibliography

S. Abramov, V. Zabrodina, V. Lukin, B. Vozel, K. Chehdi, and J. Astola. Improved method for blind estimation of the variance of mixed noise using weighted LMS line fitting algorithm. In *Proceedings of 2010 IEEE International Symposium on Circuits and Systems (ISCAS)*, pages 2642–2645, Paris, 2010. doi: 10.1109/ISCAS.2010.5537084. 68, 70, 95

S. Abramov, V. Abramova, V. Lukin, and K. Egiazarian. Robust local scale estimators for blind evaluation of noise variance in images. In *5th International Symposium on Communications Control and Signal Processing (ISCCSP)*, pages 1 –4, May 2012. doi: 10.1109/ISCCSP.2012.6217835. 93

A. Abrams, S. Ganzell, H. Landau, Z. Landau, J. Pommersheim, and E. Zaslow. Optimal estimators for threshold-based quality measures. *Journal of Probability and Statistics*, 2010(4), 2010. Article ID 752750. 23

N. Acito, M. Diani, and G. Corsini. Signal-dependent noise modeling and model parameter estimation in hyperspectral images. *IEEE Trans. on Geoscience and Remote Sensing*, 49(8):2957–2971, 2011. 68, 94

M. Afonso, J. Bioucas-Dias, and M. Figueiredo. A fast algorithm for the constrained formulation of compressive image reconstruction and other linear inverse problems. In *Proc. Int. Conf. Acoust., Speech Signal Process.*, Dallas, USA, Mar. 2010a. 50

M. V. Afonso, J. M. Bioucas-Dias, and M. A. T. Figueiredo. Fast image recovery using variable splitting and constrained optimization. *IEEE Trans. Image Process.*, 19:2345–2356, 2010b. ISSN 1057-7149. doi: 10.1109/TIP.2010.2047910. 50

F. Aguet, D. Van De Ville, and M. Unser. An accurate PSF model with few parameters for axially shift-variant deconvolution. In *Proc. IEEE Int. Symp. Biomedical Imaging (ISBI)*, pages 157–160. IEEE, 2008. 171

B. Aiazzi, L. Alparone, A. Barducci, S. Baronti, P. Marcoionni, I. Pippi, and M. Selva. Noise modelling and estimation of hyperspectral data from

airborne imaging spectrometers. *Annals of Geophysics*, 49(1):1–9, 2006. ISSN 2037-416X. 95

M. Allain, J. Idier, and Y. Goussard. On global and local convergence of half-quadratic algorithms. *IEEE Trans. Image Process.*, 15(5):1130–1142, 2006. 140, 149, 157

L. Alvarez and J. Esclarín. Image quantization using reaction-diffusion equations. *SIAM J. Appl. Math.*, 57(1):153–175, 1997. ISSN 0036-1399. 42, 48

A. Amer and E. Dubois. Fast and reliable structure-oriented video noise estimation. *IEEE Trans. Circuits Syst. for Video Technology*, 15(1):113–118, 2005. 93, 95

A. A. Amini, T. E. Weymouth, and R. C. Jain. Using dynamic programming for solving variational problems in vision. *IEEE Trans. Pattern Anal. Mach. Int.*, 12:855–867, 1990. ISSN 0162-8828. doi: http://doi.ieeecomputersociety.org/10.1109/34.57681. 33

F. J. Anscombe. The transformation, of Poisson, binomial and negative-binomial data. *Biometrika*, 35(3/4):246–254, Dec. 1948. 16, 70, 94

A. Antoniadis, D. Leporini, and J.-C. Pesquet. Wavelet thresholding for some classes of non-Gaussian noise. *Statist. Neerlandica*, 56:434–453, 2002. 149

B. Appleton and H. Talbot. Globally minimal surfaces by continuous maximal flows. *IEEE Trans. Pattern Anal. Mach. Int.*, 28(1):106–118, 2006. 40

M. Arigovindan, J. Shaevitz, J. McGowan, J. W. Sedat, and D. A. Agard. A parallel product-convolution approach for representing the depth varying Point Spread Functions in 3D widefield microscopy based on principalcomponent analysis. *Opt. Express*, 18(7):6461–6476, Mar 2010. doi: 10.1364/OE.18.006461. 171

V. Arya, A. Mittal, and R. C. Joshi. An efficient coding method for teleconferencing and medical image sequences. In *International Conference on Intelligent Sensing and Information Processing*, pages 8–13, Los Alamitos, CA, USA, 2005. IEEE Computer Society. ISBN 0-7803-9588-3. doi: http://doi.ieeecomputersociety.org/10.1109/ICISIP.2005.1619405. 42

H. Attouch and J. Bolte. On the convergence of the proximal algorithm for nonsmooth functions involving analytic features. *Math. Prog.*, 116:5–16, Jun. 2008. 142, 153

H. Attouch, J. Bolte, P. Redont, and A. Soubeyran. Proximal alternating minimization and projection methods for nonconvex problems. An approach based on the Kurdyka-Łojasiewicz inequality. *Math. Oper. Res.*, 35(2):438–457, 2010. 142, 153

H. Attouch, J. Bolte, and B. Svaiter. Convergence of descent methods for semi-algebraic and tame problems: proximal algorithms, forward-backward splitting, and regularized Gauss-Seidel methods. *Math. Programm.*, 137:1–39, 2011. ISSN 0025-5610. doi: 10.1007/s10107-011-0484-9. 33, 142, 153, 155

J.-F. Aujol and S. H. Kang. Color image decomposition and restoration. *J. Visual Communication and Image Representation*, 17(4):916–928, 2006. 170

F. R. Bach, R. Jenatton, J. Mairal, and G. Obozinski. Optimization with sparsity-inducing penalties. *Foundations and Trends in Machine Learning*, 4(1):1–106, 2012. 31, 33

M. L. Balinski. Notes–on a selection problem. *Management Science*, 17(3): 230–231, 1970. 33

M. S. Bartlett. The square root transformation in analysis of variance. *Supplement to the Journal of the Royal Statistical Society*, 3(1):68–78, 1936. ISSN 14666162. 16

H. H. Bauschke and P. L. Combettes. *Convex analysis and monotone operator theory in Hilbert spaces*. Springer, New York, 2011. ISBN 9781441994660. 26, 32, 33, 149

B. Begovic, V. Stankovic, and L. Stankovic. Contrast enhancement and denoising of Poisson and Gaussian mixture noise for solar images. In *Proc. Int. Conf. Image Process.*, Brussels, Belgium, Sep. 2011. 68, 105

S. Ben Hadj and L. Blanc-Féraud. Modeling and removing depth variant blur in 3D fluorescence microscopy. In *Proc. Int. Conf. Acoust., Speech Signal Process.*, pages 689–692. IEEE, 2012. ISBN 978-1-4673-0046-9. 171

A. Ben-Tal and M. Teboulle. A smoothing technique for nondifferentiable optimization problems. In *Optimization*, volume 1405 of *Lecture Notes in Mathematics*, pages 1–11. Springer Berlin, 1989. ISBN 978-3-540-51970-6. 149

F. Benvenuto, A. La Camera, C. Theys, A. Ferrari, H. Lantéri, and M. Bertero. The study of an iterative method for the reconstruction of images corrupted by Poisson and Gaussian noise. *Inverse Problems*, 24(3), 2008. 20 pp. 18, 68, 70, 78, 105, 106, 109

T. Bernas, D. Barnes, E. K. Asem, J. P. Robinson, and B. Rajwa. Precision of light intensity measurement in biological optical microscopy. *Journal of Microscopy*, 226(2):163–174, 2007. ISSN 1365-2818. doi: 10.1111/j.1365-2818.2007.01764.x. 91, 95

D. Bertsekas. Incremental proximal methods for large scale convex optimization. *Math. Programm.*, 129:163–195, 2011. ISSN 0025-5610. doi: 10.1007/s10107-011-0472-0. 29

D. P. Bertsekas. *Nonlinear Programming*. Athena Scientific, Belmont, MA, USA, second edition, 1999. ISBN ISBN 1-886529-00-0. 151

D. Bertsimas, D. B. Brown, and C. Caramanis. Theory and applications of robust optimization. *CoRR*, abs/1010.5445:464–501, 2010. 25

J. Besag. On the statistical analysis of dirty pictures. *J. Royal Stat. Soc. B*, 48(3):259–302, 1986. 33, 133

S. Beucher and C. Lantuéjoul. Use of watersheds in contour detection. In *Int. Workshop on Image Processing*, Rennes, France, Sep. 1979. CCETT/IRISA. 175

C. Biernacki, G. Celeux, and G. Govaert. Choosing starting values for the EM algorithm for getting the highest likelihood in multivariate Gaussian mixture models. *Computational Statistics & Data Analysis*, 41(3-4):561–575, 2003. 79

M. J. Black, G. Sapiro, D. H. Marimont, and D. Heeger. Robust anisotropic diffusion. *IEEE Trans. Image Process.*, 7(3):421–432, Mar. 1998. 144

J. Bolte, A. Daniilidis, and A. Lewis. The Łojasiewicz inequality for nonsmooth subanalytic functions with applications to subgradient dynamical systems. *SIAM J. Optim.*, 17:1205–1223, 2006. 153

J. Bolte, A. Daniilidis, A. Lewis, and M. Shiota. Clarke subgradients of stratifiable functions. *SIAM J. Optim.*, 18(2):556–572, 2007. 153

J. Bolte, P. L. Combettes, and J.-C. Pesquet. Alternating proximal algorithm for blind image recovery. In *Proc. Int. Conf. Image Process.*, pages 1673–1676. IEEE, 2010. ISBN 978-1-4244-7994-8. 142, 171

G. Boracchi and A. Foi. Multiframe raw-data denoising based on block-matching and 3-D filtering for low-light imaging and stabilization. In *The 2008 International Workshop on Local and Non-Local Approximation in Image Processing*, Lausanne, Switzerland, Aug. 2008. ISBN 9789521520044. 105

E. Boros and P. L. Hammer. Pseudo-boolean optimization. *Discrete Applied Mathematics*, 123(1-3):155–225, 2002. 38

J. M. Borwein and B. Sims. The Douglas-Rachford algorithm in the absence of convexity. In H. H. Bauschke, R. S. Burachik, P. L. Combettes, V. Elser, D. R. Luke, and H. Wolkowicz, editors, *Fixed-Point Algorithms for Inverse Problems in Science and Engineering*, volume 49 of *Springer Optimization and Its Applications*, pages 93–109. Springer New York, 2011. ISBN 978-1-4419-9569-8. 81

A. Bosco, A. Bruna, D. Giacalone, S. Battiato, and R. Rizzo. Signal-dependent raw image denoising using sensor noise characterization via multiple acquisitions. In F. H. Imai, N. Sampat, and F. Xiao, editors, *Digital Photography*, volume 7537 of *SPIE Proceedings*, page 753705. SPIE, 2010. ISBN 978-0-8194-7930-3. 68, 95

J. Boulanger, J. B. Sibarita, C. Kervrann, and P. Bouthemy. Non-parametric regression for patch-based fluorescence microscopy image sequence denoising. In *Proc. IEEE Int. Symp. Biomedical Imaging (ISBI)*, pages 748–751, Paris, 2008. doi: 10.1109/ISBI.2008.4541104. 68, 91

G. E. P. Box and D. R. Cox. An analysis of transformations. *J. Royal Stat. Soc. B*, 26(2):211–252, 1964. ISSN 00359246. 16

S. Boyd and L. Vandenberghe. *Convex Optimization*. Cambridge University Press, Cambridge, England, Mar. 2004. 26, 46, 50

Y. Boykov and M.-P. Jolly. Interactive graph cuts for optimal boundary & region segmentation of objects in N-D images. In *Proc. IEEE Int. Conf. Comput. Vis.*, pages 105–112, Vancouver, BC , Canada, 2001. doi: 10.1109/ICCV.2001.937505. 33, 124

Y. Boykov and V. Kolmogorov. An experimental comparison of min-cut/max-flow algorithms for energy minimization in vision. *IEEE Trans. Pattern Anal. Mach. Int.*, 26(9):1124–1137, Sep. 2004. doi: 10.1109/TPAMI.2004.60. 37, 60, 133

Y. Boykov, O. Veksler, and R. Zabih. Markov random fields with efficient approximations. In *Proc. IEEE Comput. Soc. Conf. Comput. Vision and Pattern Recogn. (CVPR)*, pages 648–655, 1998. 124

Y. Boykov, O. Veksler, and R. Zabih. Fast approximate energy minimization via graph cuts. *IEEE Trans. Pattern Anal. Mach. Int.*, 23(11):1222–1239, Nov. 2001. doi: 10.1109/34.969114. 39, 55, 124, 125, 126, 133, 156

X. Bresson. A short note for nonlocal TV minimization. Technical report, Jun. 2009. 116

L. M. Briceños Arias and P. L. Combettes. A monotone + skew splitting model for composite monotone inclusions in duality. *SIAM J. Optim.*, 21 (4):1230–1250, Oct. 2011. 113

J. D. Bruce. Optimum quantization. Technical Report 429, Massachusetts Institute of Technology, Research Laboratory of Electronics, Cambridge, Massachusetts, Mar. 1965. 46

A. Buades, B. Coll, and J.-M. Morel. A non-local algorithm for image denoising. In *Proc. IEEE Comput. Soc. Conf. Comput. Vision and Pattern Recogn. (CVPR)*, pages 60–65. IEEE Computer Society, 2005. ISBN 0-7695-2372-2. 20

Z. L. Budrikis. Visual fidelity criterion and modeling. *Proceedings of the IEEE*, 60(7):771 – 779, Jul. 1972. ISSN 0018-9219. doi: 10.1109/PROC.1972.8776. 24

E. J. Candès. *Ridgelets: Theory and Applications*. PhD thesis, Stanford University, 1998. 22

E. J. Candès. The restricted isometry property and its implications for compressed sensing. *C. R. Math.*, 346(9–10):589–592, 2008. 146

E. J. Candès and D. L. Donoho. Curvelets and curvilinear integrals. *Journal of Approximation Theory*, 113(1):59–90, 2001. 22

J. Cantrell. Relation between the memory gradient method and the Fletcher-Reeves method. *J. Optim. Theory Appl.*, 4(1):67–71, 1969. 147

A. Chakrabarti and T. Zickler. Image restoration with signal-dependent camera noise. *CoRR*, abs/1204.2994, 2012. 18, 68, 106

A. Chambolle. An algorithm for total variation minimization and applications. *J. Math. Imaging Vis.*, 20(1–2):89–97, 2004. 58

A. Chambolle and J. Darbon. On total variation minimization and surface evolution using parametric maximum flows. *Int. J. Comput. Vision*, 84 (3):288 – 307, 2009. ISSN 0920-5691. doi: http://dx.doi.org/10.1007/s11263-009-0238-9. 58

A. Chambolle and T. Pock. A first-order primal-dual algorithm for convex problems with applications to imaging. *Journal of Mathematical Imaging and Vision*, 40(1):120–145, 2011. 32

D. M. Chandler and S. S. Hemami. VSNR: A wavelet-based visual signal-to-noise ratio for natural images. *IEEE Trans. Image Process.*, 16(9):2284 –2298, Sep. 2007. ISSN 1057-7149. doi: 10.1109/TIP.2007.901820. 24

J. Chanussot and P. Lambert. Bit mixing paradigm for multivalued morphological filters. In *Sixth International Conference on Image Processing and Its Applications*, volume 2, pages 804–808, Dublin, Jul. 1997. 48

P. Charbonnier, L. Blanc-Féraud, G. Aubert, and M. Barlaud. Deterministic edge-preserving regularization in computed imaging. *IEEE Trans. Image Process.*, 6:298–311, 1997. 140

C. Chaux, P. L. Combettes, J.-C. Pesquet, and V. R. Wajs. A variational formulation for frame based inverse problems. *Inverse Problems*, 23:1495–1518, Jun. 2007. 51

G. Chierchia, N. Pustelnik, J.-C. Pesquet, and B. Pesquet-Popescu. Epigraphical projection and proximal tools for solving constrained convex optimization problems: Part I. *CoRR*, abs/1210.5844, 2012. 170

E. Chouzenoux, J. Idier, and S. Moussaoui. A majorize-minimize strategy for subspace optimization applied to image restoration. *IEEE Trans. Image Process.*, 20(6):1517 –1528, Jun. 2011. ISSN 1057-7149. doi: 10.1109/TIP.2010.2103083. 8, 29, 141, 142, 147, 151, 157, 158

E. Chouzenoux, A. Jezierska, J.-C. Pesquet, and H. Talbot. A majorize-minimize subspace approach for l2-l0 image regularization. accepted to SIAM Journal on Imaging Science, 2012. 156

S. Chretien and A. O. Hero. Acceleration of the EM algorithm via proximal point iterations. In *IEEE International Symposium on Information Theory*, page 444, Aug. 1998. doi: 10.1109/ISIT.1998.709049. 32

S. Chretien and A. O. Hero. On EM algorithms and their proximal generalizations. *ESAIM: Probability and Statistics*, 12:308–326, 2008. 32

K. Chuang, H. Tzeng, S. Chen, J. Wu, and T. Chen. Fuzzy C-means clustering with spatial information for image segmentation. *Comput. Med. Imag. Graph.*, 30:9–15, 2006. 42

P. L. Combettes and J.-C. Pesquet. A Douglas-Rachford splitting approach to nonsmooth convex variational signal recovery. *IEEE J. Selected Topics Signal Process.*, 1(4):564–574, Dec. 2007. doi: 10.1109/JSTSP.2007.910264. 69

P. L. Combettes and J.-C. Pesquet. A proximal decomposition method for solving convex variational inverse problems. *Inverse Problems*, 24(6):065014, Dec. 2008. doi: 10.1088/0266-5611/24/6/065014. 50, 81, 113

P. L. Combettes and J.-C. Pesquet. Proximal splitting methods in signal processing. In H. H. Bauschke, R. S. Burachik, P.L. Combettes, V. Elser, D. R. Luke, and H. Wolkowicz, editors, *Fixed-Point Algorithms for Inverse Problems in Science and Engineering*, Springer Optimization and Its Applications, pages 185–212. Springer New York, 2011. 31, 33, 50, 81, 100

P. L. Combettes and J.-C. Pesquet. Primal-dual splitting algorithm for solving inclusions with mixtures of composite, Lipschitzian, and parallel-sum type monotone operators. *Set-Valued and Variational Analysis*, 20:307–330, 2012. ISSN 1877-0533. doi: 10.1007/s11228-011-0191-y. 10.1007/s11228-011-0191-y. 32, 100, 106, 113, 114, 168, 170

L. Condat. A primal-dual splitting method for convex optimization involving Lipschitzian, proximable and linear composite terms. *Journal of Optimization Theory and Applications*, pages 1–20, Dec. 2012. 32, 106, 170

P. C. Cosman, R. M. Gray, and R. A. Olshen. Evaluating quality of compressed medical images: SNR. subjective rating, and diagnostic accuracy. *PROCEEDINGS- IEEE*, 82(6):919 – 932, Jun. 1994. ISSN 0018-9219. doi: 10.1109/5.286196. 23

C. Couprie, L. Grady, L. Najman, and H. Talbot. Power watersheds: A new image segmentation framework extending graph cuts, random walker and optimal spanning forest. In *Proc. IEEE Int. Conf. Comput. Vis.*, pages 731–738, Kyoto, Japan, 2009. 58

C. Couprie, L. Grady, H. Talbot, and L. Najman. Combinatorial Continuous Maximum Flows. *SIAM J. Imaging Sciences*, 4(3):905–930, 2011. 40

H. Cramer. *Mathematical methods of statistics*. Princeton University Press, Princeton, 1946. ISBN 0691080046. 12

S. R. Cranmer. New views of the solar wind with the Lambert W function. *American Journal of Physics*, 72(11):16, 2004. 75

A. Danielyan and A. Foi. Noise variance estimation in nonlocal transform domain. In *International Workshop on Local and Non-Local Approximation in Image Processing*, pages 41–45, Aug. 2009. 93

A. Danielyan, V. Katkovnik, and K. Egiazarian. BM3D frames and variational image deblurring. *IEEE Trans. Image Process.*, 21(4):1715–1728, 2012. 22

J. Darbon and M. Sigelle. Image restoration with discrete constrained total variation Part II: Levelable functions, convex priors and non-convex cases. *J. Math. Imag. Vision*, 26(3):277 – 291, Dec. 2006. 33, 58, 125

J. Dauwels and S. Korl. A numerical method to compute Cramer-Rao-Type bounds for challenging estimation problems. In *Proc. Int. Conf. Acoust., Speech Signal Process.*, Toulouse, 2006. doi: 10.1109/ICASSP.2006.1661376. 85

M. Davenport, M. F. Duarte, Y. C. Eldar, and G. Kutyniok. *Introduction to compressed sensing*, chapter 1, pages 1–68. Cambridge University Press, 2012. 146

A. De Stefano, P. R. White, and W. B. Collis. Training methods for image noise level estimation on wavelet components. *EURASIP J. Adv. Sig. Proc.*, 2004(16):2400–2407, 2004. 93, 95

A. H. Delaney and Y. Bresler. Globally convergent edge-preserving regularized reconstruction: an application to limited-angle tomography. *IEEE Trans. Image Process.*, 7(2):204 –221, Feb. 1998. 141, 157

A. Delong and Y. Boykov. A scalable graph-cut algorithm for N-D grids. In *Proc. IEEE Comput. Soc. Conf. Comput. Vision and Pattern Recogn. (CVPR)*. IEEE Computer Society, 2008. 37

S. Delpretti, F. Luisier, S. Ramani, T. Blu, and M. Unser. Multiframe sure-let denoising of timelapse fluorescence microscopy images. In *Proc. IEEE Int. Symp. Biomedical Imaging (ISBI)*, pages 149–152, Paris, 2008. doi: 10.1109/ISBI.2008.4540954. 68, 70, 91, 95, 105

G. Demoment. Image reconstruction and restoration: Overview of common estimation structure and problems. *IEEE Trans. Acous., Speech Signal Process.*, 37(12):2024–2036, Dec. 1989. 107

A. P. Dempster, N. M. Laird, and D. B. Rubin. Maximum likelihood from incomplete data via the EM algorithm. *J. Royal Stat. Soc. B*, 39(1):1–38, 1977. 68, 72, 98

L. Denis, E. Thiébaut, and F. Soulez. Fast model of space-variant blurring and its application to deconvolution in astronomy. In B. Macq and P. Schelkens, editors, *Proc. Int. Conf. Image Process.*, pages 2817–2820. IEEE, 2011. ISBN 978-1-4577-1304-0. 171, 173

J. E. Dennis and R. E. Welsch. Techniques for nonlinear least squares and robust regression. *Communications in Statistics - Simulation and Computation*, 7(4):345–359, 1978. doi: 10.1080/03610917808812083. 144

N. Dobigeon, A. O. Hero, and J.-Y. Tourneret. Hierarchical Bayesian sparse image reconstruction with application to MRFM. *IEEE Trans. Image Process.*, 18(9):2059–2070, 2009. 93

D. Donoho. Denoising by soft-thresholding. *IEEE Trans. Inform. Theory*, 41:613–627, 1995. 93, 95

D. L. Donoho. Neighborly polytopes and sparse solutions of underdetermined linear equations. Technical report, University of Stanford, 2005. 146

D. L. Donoho, I. M. Johnstone, G. Kerkyacharian, and D. Picard. Wavelet shrinkage: Asymptopia? *J. Royal Stat. Soc. B*, 57(2):301–337, 1995. 19, 168

U. Drepper. What every programmer should know about memory. 2007. 25

Q. Du, M. Emelianenko, and L. Ju. Convergence of the Lloyd algorithm for computing centroidal voronoi tessellations. *SIAM J. Numer. Anal.*, 44(1): 102–119, Feb. 2006. 42

F. X. Dupé. Deconvolution under Poisson noise using proximal thresholding iteration, 2008. http://fxdupe.free.fr/software.html. 102

F.-X. Dupé, J. M. Fadili, and J.-L. Starck. A proximal iteration for deconvolving Poisson noisy images using sparse representations. *IEEE Trans. Image Process.*, 18(2):310–321, Feb. 2009. ISSN 1057-7149. doi: 10.1109/TIP.2008.2008223. 16, 23, 115

C. Eckart and G. Young. The approximation of one by another of lower rank. *Psychometrika*, 1(3):211–218, Sep. 1936. 48, 175

J. Eckstein and D. P. Bertekas. On the Douglas-Rachford splitting methods and the proximal point algorithm for maximal monotone operators. *Math. Programm.*, 55(3):293–318, 1992. 69

M. Elad, B. Matalon, and M. Zibulevsky. Coordinate and subspace optimization methods for linear least squares with non-quadratic regularization. *Appl. Comput. Harmon. Anal.*, 23:346–367, 2006. 141

M. Elad, P. Milanfar, and R. Rubinstein. Analysis versus synthesis in signal priors. *Inverse Prob.*, 23(3):947–968, 2007. 140

Y. C. Eldar, P. Kuppinger, and H. Bolcskei. Block-sparse signals: uncertainty relations and efficient recovery. *IEEE Trans. Signal Process.*, 58(6): 3042 –3054, Jun. 2010. ISSN 1053-587X. doi: 10.1109/TSP.2010.2044837. 112, 145

P. Elias, A. Feinstein, and C. Shannon. A note on the maximum flow through a network. *IEEE Trans. Inform. Theory*, 2(4):117–119, 1956. ISSN 0018-9448. 37

R. R. Ernst, G. Bodenhausen, and A. Wokaun. *Principles of nuclear magnetic resonance in one and two dimensions*. International Series of Monographs on Chemistry. Clarendon Press Oxford University Press, Oxford Oxfordshire New York, 1991. 68

D. Fairbairn, K. L. O'Neill, and M. D. Standing. Application of confocal laser scanning microscopy to analysis of H2O2-induced DNA damage in

human cells. *Scanning*, 15(3):136–139, 1993. ISSN 1932-8745. doi: 10.1002/sca.4950150305. 1

W. Fang, T. Wu, and J. Chen. An algorithm of global optimization for rational functions with rational constraints. *Journal of Global Optimization*, 18:211–218, 2000. ISSN 0925-5001. 10.1023/A:1008318925663. 82

P. F. Felzenszwalb and D. P. Huttenlocher. Pictorial structures for object recognition. *International Journal of Computer Vision*, 61(1):55–79, 2005. 33

P. F. Felzenszwalb and D. R. Huttenlocher. Efficient belief propagation for early vision. In *Proc. IEEE Comput. Soc. Conf. Comput. Vision and Pattern Recogn. (CVPR)*, pages 261–268, 2004. doi: 10.1109/CVPR.2004.1315041. 33, 126, 156

P. F. Felzenszwalb and R. Zabih. Dynamic programming and graph algorithms in computer vision. *IEEE Trans. Pattern Anal. Mach. Int.*, 33(4):721–740, 2011. 33

J. A. Fessler and A. O. Hero. Space-alternating generalized expectation-maximization algorithm. *IEEE Trans. Signal Process.*, 42(10):2664–2677, 1994. ISSN 1053-587X. doi: 10.1109/78.324732. 27, 68

J. A. Fessler and A.O. Hero. Penalized maximum-likelihood image reconstruction using space-alternating generalized EM algorithms. *IEEE Trans. Image Process.*, 4(10):1417–1429, 1995. 29, 72

J. Fischer and K. Kersting. Scaled CGEM: A fast accelerated EM. In N. Lavrac, D. Gamberger, L. Todorovski, and H. Blockeel, editors, *ECML*, volume 2837 of *Lecture Notes in Computer Science*, pages 133–144. Springer, 2003. ISBN 3-540-20121-1. 29

A. Foi. Clipped noisy images: Heteroskedastic modeling and practical denoising. *Signal Process.*, 89:2609–2629, Dec. 2009a. ISSN 0165-1684. doi: 10.1016/j.sigpro.2009.04.035. 68, 106

A. Foi. Optimization of variance-stabilizing transformations. Preprint, 2009b. 94

A. Foi, M. Trimeche, V. Katkovnik, and K. Egiazarian. Practical Poissonian-Gaussian noise modeling and fitting for single-image raw-data. *IEEE Trans. Image Process.*, 17:1737–1754, 2008. ISSN 1057-7149. doi: 10.1109/TIP.2008.2001399. 68, 70, 94, 95

J. L. R. Ford and D. R. Fulkerson. *Flows in Networks*. Princeton University Press, Princeton, NJ, 1962. 37, 54, 130

M. Fornasier and F. Solombrino. Linearly constrained nonsmooth and nonconvex minimization. Technical report, Jan. 2012. http://arxiv.org/abs/1201.6069. 141

M. Fortin and R. Glowinski. Augmented Lagrangian methods: Applications to the numerical solution of boundary-value problems. *ZAMM - Journal of Applied Mathematics and Mechanics / Zeitschrift fur Angewandte Mathematik und Mechanik*, 65(12):622–622, 1985. ISSN 1521-4001. doi: 10.1002/zamm.19850651211. 31

J. T. Fredrich, B. Menendez, and T.-F. Wong. Imaging the pore structure of geomaterials. *Science*, 268:276–279, 1995. doi: 10.1126/science.268.5208.276. 2

P. Fryzlewicz and G. Nason. A Haar-Fisz algorithm for Poisson intensity estimation. *Journal of Computational and Graphical Statistics*, 13(3):621–638, 2004. 16, 94

P. Furrer and R. Gurny. Recent advances in confocal microscopy for studying drug delivery to the eye: Concepts and pharmaceutical applications. *European Journal of Pharmaceutics and Biopharmaceutics*, 74(1):33 – 40, 2010. ISSN 0939-6411. doi: 10.1016/j.ejpb.2009.09.002. 1

W. Gander. On Halley's iteration method. *The American Mathematical Monthly*, 92(2):131–134, 1985. ISSN 00029890. 79

D. Geman and G. Reynolds. Constrained restoration and the recovery of discontinuities. *IEEE Trans. Pattern Anal. Mach. Int.*, 14(3):367–383, 1992. 20, 112

S. Geman and D. Geman. Stochastic relaxation, Gibbs distributions, and the Bayesian restoration of images. *IEEE Trans. Pattern Anal. Mach. Int.*, 6:721–741, 1984. 20

S. Geman and D. E. McClure. Bayesian image analysis: An application to single photon emission tomography. In *In Proc. Statist. Comput. Sect.*, pages 12–18. American Statistical Association, 1985. 144

A. Gersho and R. M. Gray. *Vector Quantization and Signal Compression*. Kluwer Academic Publishers, MA, US, 1992. 41

E. Gil-Rodrigo, J. Portilla, D. Miraut, and R. Suarez-Mesa. Efficient joint Poisson-Gauss restoration using multi-frame ℓ_2-relaxed-ℓ_0 analysis-based sparsity. In *Proc. Int. Conf. Image Process.*, Brussels, Belgium, Sep. 2011. 68, 70, 106

G. Gilboa and S. Osher. Nonlocal operators with applications to image processing. *Multiscale Modeling and Simulation*, 7(3):1005–1028, 2008. 20

A. V. Goldberg and R. E. Tarjan. A new approach to the maximum-flow problem. *J. ACM*, 35(4):921–940, 1988. 37

T. Goldstein and S. Osher. The split Bregman method for L1-regularized problems. *SIAM J. Imaging Sciences*, 2(2):323–343, Apr. 2009. 50

R. L. Graham and L. Lovász. *Handbook of combinatorics. 1.* Handbook of Combinatorics. North-Holland, 1995. ISBN 9780444823465. 26, 36, 37

D. M. Greig, B. T. Porteous, and A. H. Seheult. Exact maximum a posteriori estimation for binary images. *J. Royal Stat. Soc. B*, 51(2):271–279, 1989. ISSN 00359246. 33, 37

R. Grou-Szabo and T. Shibata. A dominant-noise discrimination system for images corrupted by content-independent noises without a priori references. In *International Conference on Signal Processing and Communication Systems (ICSPCS)*, pages 1 –6, Dec. 2011. doi: 10.1109/ICSPCS.2011.6140861. 93

A. Gupta and E. Tardos. A constant factor approximation algorithm for a class of classification problems. In *In Proceedings of the 43rd Annual IEEE Symposium on Foundations of Computer Science*, pages 333–342, 2000. 126

J. Hadamard. Sur les problèmes aux dérivés partielles et leur signification physique. *Princeton University Bulletin*, 13:49–52, 1902. 11

W. W. Hager and H. Zhang. A survey of nonlinear conjugate gradient methods. *Pacific J. Optim.*, 2(1):35–58, jan. 2006. 157, 158

B. M. Hanser, M. G. L. Gustafsson, D. A. Agard, and J. W. Sedat. Phase-retrieved pupil functions in wide-field fluorescence microscopy. *Journal of Microscopy*, 216(1):32–48, 2004. ISSN 1365-2818. doi: 10.1111/j.0022-2720.2004.01393.x. 171, 172

S. Harizanov, J.C. Pesquet, and G. Steidl. Epigraphical projection for solving least squares Anscombe transformed constrained optimization problems. Technical report, 2012. 170

S. Hauser and G. Steidl. Convex multiclass segmentation with shearlet regularization. *International Journal of Computer Mathematics*, 90(1):62–81, 2013. doi: 10.1080/00207160.2012.688960. 22, 65

Y. He, M. Y. Hussaini, J. Ma, B. Shafei, and G. Steidl. A new fuzzy C-means method with total variation regularization for segmentation of images with noisy and incomplete data. *Pattern Recognition*, 45(9):3463 – 3471, 2012. ISSN 0031-3203. doi: 10.1016/j.patcog.2012.03.009. 42

G. E. Healey and R. Kondepudy. Radiometric CCD camera calibration and noise estimation. *IEEE Trans. Pattern Anal. Mach. Int.*, 16:267–276, 1994. ISSN 0162-8828. doi: 10.1109/34.276126. 68

T. J. Hebert and R. Leahy. Statistic-based MAP image reconstruction from poisson data using Gibbs priors. *IEEE Trans. Signal Process.*, 40(9): 2290–2303, Sep. 1992. 141

P. Heckbert. Color image quantization for frame buffer display. *SIGGRAPH Comput. Graph.*, 16(3):297–307, Jul. 1982. ISSN 0097-8930. doi: http://doi.acm.org/10.1145/965145.801294. 60

B. Hill, Th. Roger, and F. W. Vorhagen. Comparative analysis of the quantization of color spaces on the basis of the CIELAB color-difference formula. *ACM Trans. Graph.*, 16(2):109–154, 1997. ISSN 0730-0301. doi: http://doi.acm.org/10.1145/248210.248212. 48

J. B. Hiriart-Urruty and C. Lemaréchal. *Convex Analysis and Minimization Algorithms*. Grundlehren 305, 306. Springer Verlag, 1993. 50

D. S. Hochbaum. 50th anniversary article: Selection, provisioning, shared fixed costs, maximum closure, and implications on algorithmic methods today. *Management Science*, 50(6):709–723, 2004. 33

R. Horn and C. R. Johnsone. *Matrix analysis*. Cambridge University Press, Cambridge England New York, 1990. 87

J. P. Hornak. The basics of MRI, 2008. URL http://www.cis.rit.edu/htbooks/mri/index.html. 68

J. Huang and D. Mumford. Statistics of natural images and models. In *Proc. IEEE Comput. Soc. Conf. Comput. Vision and Pattern Recogn. (CVPR)*, Fort Collins, CO , USA, 1999. doi: 10.1109/CVPR.1999.786990. 124

P. J. Huber. *Robust Statistics*. Wiley, J., New York, NY, USA, 1981. 140, 149

W. Hubner, G. P. McNerney, P. Chen, B. M. Dale, R. E. Gordon, F. Y. S. Chuang, X.-D. Li, D. M. Asmuth, T. Huser, and B. K. Chen. Quantitative 3D video microscopy of HIV transfer across T cell virological synapses. *Science*, 323(5922):1743–1747, 2009. doi: 10.1126/science.1167525. 2

S. Huda, R. Ghosh, and J. Yearwood. A variable initialization approach to the EM algorithm for better estimation of the parameters of hidden Markov model based acoustic modeling of speech signals. In P. Perner, editor, *Advances in Data Mining. Applications in Medicine, Web Mining, Marketing, Image and Signal Mining*, volume 4065 of *Lecture Notes in Computer Science*, pages 416–430. Springer Berlin / Heidelberg, 2006. ISBN 978-3-540-36036-0. 10.1007/11790853_33. 79

Y. Hwang, J.-S. Kim, and I.S. Kweon. Difference-based image noise modeling using skellam distribution. *IEEE Trans. Pattern Anal. Mach. Int.*, 34 (7):1329–1341, Jul. 2012. ISSN 0162-8828. doi: 10.1109/TPAMI.2011.224. 94

M. Hyder and K. Mahata. An approximate ℓ_0 norm minimization algorithm for compressed sensing. In *Proc. Int. Conf. Acoust., Speech Signal Process.*, pages 3365 –3368, Taipei, Taiwan, Apr. 2009. 141

H. Ishikawa. Exact optimization for Markov random fields with convex priors. *IEEE Trans. Pattern Anal. Mach. Int.*, 25(10):1333–1336, Oct. 2003. doi: 10.1109/TPAMI.2003.1233908. 39, 55, 124, 125, 126, 130

H. Ishikawa. Higher-order clique reduction in binary graph cut. In *Proc. IEEE Comput. Soc. Conf. Comput. Vision and Pattern Recogn. (CVPR)*, pages 2993–3000, Miami, FL, 2009. doi: 10.1109/CVPR.2009.5206689. 58

H. Ishikawa and D. Geiger. Mapping image restoration to a graph problem. In *IEEE-EURASIP Workshop Nonlinear Signal Image Process.*, pages 189–193, Antalya, Turkey, Jun. 1999. 52, 54

M. W. Jacobson and J. A. Fessler. An expanded theoretical treatment of iteration-dependent Majorize-Minimize algorithms. *IEEE Trans. Image Process.*, 16(10):2411–2422, 2007. 27, 28, 29

K.-H. Jeong, J. Kim, and L. P. Lee. Biologically inspired artificial compound eyes. *Science*, 312(5773):557–561, 2006. doi: 10.1126/science.1123053. 2

A. Jezierska, C. Chaux, J.-C. Pesquet, and H. Talbot. An EM approach for Poisson-Gaussian noise modeling. In *Proc. Eur. Sig. and Image Proc. Conference*, pages 2244–2248, Barcelona, Aug. 2011a. 70, 79

A. Jezierska, H. Talbot, O. Veksler, and D. Wesierski. A fast solver for truncated-convex priors: quantized-convex split moves. In Y. Boykov, F. Kahl, V. Lempitsky, and F. Schmidt, editors, *Proc. IEEE Int. Conf. Energy Minimization Methods Comput. Vision and Pattern Recogn. (EMMCVPR)*, volume 6819 of *Lecture Notes in Computer Science*, pages 45–58. Springer Berlin / Heidelberg, 2011b. 156

A. Jezierska, E. Chouzenoux, J.-C. Pesquet, and H. Talbot. A primal-dual proximal splitting approach for restoring data corrupted with Poisson-Gaussian noise. In *Proc. Int. Conf. Acoust., Speech Signal Process.*, Kyoto, Mar. 2012a. 68, 94

A. Jezierska, H. Talbot, C. Chaux, J.-C. Pesquet, and G. Engler. Poisson-Gaussian noise parameter estimation in fluorescence microscopy imaging. In *Proc. IEEE Int. Symp. Biomedical Imaging (ISBI)*, Barcelona, May 2012b. 82

D. Jibetean and E. de Klerk. Global optimization of rational functions: a semidefinite programming approach. *Math. Programm.*, 106(1):93–109, 2006. 82

N. Joshi, C. L. Zitnick, R. Szeliski, and D. J. Kriegman. Image deblurring and denoising using color priors. In *Proc. IEEE Comput. Soc. Conf. Comput. Vision and Pattern Recogn. (CVPR)*, pages 1550–1557. IEEE, 2009. ISBN 978-1-4244-3992-8. 170

S. Kadioglu, Y. Malitsky, A. Sabharwal, H. Samulowitz, and M. Sellmann. Algorithm selection and scheduling. volume 6876 of *Lecture Notes in Computer Science*, pages 454–469. Springer, 2011. ISBN 978-3-642-23785-0. 24

A. Kaplan and R. Tichatschke. Proximal point methods and nonconvex optimization. *Journal of Global Optimization*, 13:389–406, 1998. ISSN 0925-5001. 32

I. Katsavounidis, C.-C. J. Kuo, and Z. Zhang. A new initialization technique for generalized Lloyd iteration. *Statist. Probab. Lett.*, 1(10):144–146, Oct. 1994. 60

R. Kawada, A. Koike, and Y. Nakajima. Prefilter control scheme for low bitrate TV distribution. In *IEEE International Conference on Multimedia and Expo*, pages 769–772, Toronto, Ont., 2006. IEEE Computer Society. ISBN 1-4244-0366-7. doi: http://doi.ieeecomputersociety.org/10.1109/ICME.2006.262952. 42

K. M. Kedziora, J. H.M. Prehn, J. Dobrucki, and T. Bernas. Method of calibration of a fluorescence microscope for quantitative studies. *Journal of Microscopy*, 244(1):101–111, 2011. ISSN 1365-2818. doi: 10.1111/j.1365-2818.2011.03514.x. 91

H. Kirshner, F. Aguet, D. Sage, and M. Unser. Least-square PSF fitting for localization microscopy. In *Second Swiss Single Molecule Localization Microscopy Symposium (SSMLMS'12)*, Lausanne VD, Switzerland, Aug. 2012. 171

P. Kohli, A. Shekhovtsov, C. Rother, V. Kolmogorov, and P. H. S. Torr. On partial optimality in multi-label MRFs. In W. W. Cohen, A. McCallum, and S. T. Roweis, editors, *ICML*, volume 307 of *ACM International Conference Proceeding Series*, pages 480–487. ACM, 2008. ISBN 978-1-60558-205-4. 38

V. Kolmogorov. Convergent tree-reweighted message passing for energy minimization. *IEEE Trans. Pattern Anal. Mach. Int.*, 28:1568–1583, 2006. ISSN 0162-8828. doi: 10.1109/TPAMI.2006.200. 33, 126, 133, 156

V. Kolmogorov. A note on the primal-dual method for semi-metric labeling problem. Technical report, UCL, 2007. 65

V. Kolmogorov and C. Rother. Comparison of energy minimization algorithms for highly connected graphs. In *Proc. European Conf. Comput. Vision (ECCV)*, volume II, pages 1–15, 2006. 126

V. Kolmogorov and C. Rother. Minimizing nonsubmodular functions with graph cuts-a review. *IEEE Trans. Pattern Anal. Mach. Int.*, 29(7):1274–1279, Jul. 2007. ISSN 0162-8828. doi: 10.1109/TPAMI.2007.1031. 38, 125

V. Kolmogorov and A. Shioura. New algorithms for convex cost tension problem with application to computer vision. *Discrete Optimization*, 6 (4):378–393, 2009. 65, 130

V. Kolmogorov and R. Zabih. What energy functions can be minimized via graph cuts? *IEEE Trans. Pattern Anal. Mach. Int.*, 26(2):147–159, 2004. ISSN 0162-8828. doi: http://dx.doi.org/10.1109/TPAMI.2004.1262177. 38, 55, 56, 57, 125, 129, 131

N. Komodakis and G. Tziritas. Approximate labeling via graph cuts based on linear programming. *IEEE Trans. Pattern Anal. Mach. Int.*, 29 (8):1436–1453, 2007. ISSN 0162-8828. doi: http://dx.doi.org/10.1109/TPAMI.2007.1061. 58

N. Komodakis, G. Tziritas, and N. Paragios. Performance vs computational efficiency for optimizing single and dynamic MRFs: Setting the state of the art with primal-dual strategies. *Computer Vision and Image Understanding*, 112(1):14–29, 2008. 58, 65

J. Kostrowicki and H. A. Scheraga. Simple global minimization algorithm for one-variable rational functions. *Journal of Global Optimization*, 6: 293–311, 1995. ISSN 0925-5001. 10.1007/BF01099466. 82

M. P. Kumar and D. Koller. MAP estimation of semi-metric MRFs via hierarchical graph cuts. In *Proceedings of the Twenty-Fifth Conference on Uncertainty in Artificial Intelligence*, UAI '09, pages 313–320, Arlington, Virginia, United States, 2009. AUAI Press. ISBN 978-0-9749039-5-8. 125, 127

M. P. Kumar and P. H. S. Torr. Improved moves for truncated convex models. In *Proceedings of Advances in Neural Information Processing Systems*, 2008. 125, 127

K. Kurdyka and A. Parusinski. w_f-stratification of subanalytic functions and the Łojasiewicz inequality. *C.R. Acad. Sci., Ser. I: Math.*, 318(2): 129–133, 1994. 153

C. Labat and J. Idier. Convergence of conjugate gradient methods with a closed-form stepsize formula. *J. Optim. Theory Appl.*, 136(1):43–60, Jan. 2008. 148, 157

K. Lange. Convergence of EM image reconstruction algorithms with Gibbs smoothing. *IEEE Trans. Med. Imaging*, 9(4):439–446, 1990. 140

K. Lange. A quasi-newton acceleration of the EM algorithm. *Statistica sinica*, 5(1):1–18, 1995. 29

K. Lange. *Optimization*. Springer, New York, 2004. ISBN 9780387203324. 29

K. Lange. *Numerical analysis for statisticians*. Springer, New York, 2010. ISBN 9781441959447. 26, 27, 28

H. Lantéri and C. Theys. Restoration of astrophysical images - the case of Poisson data with additive Gaussian noise. *EURASIP J. Appl. Signal Process.*, 2005(15):2500–2513, 2005. 68, 78

J. B. Lasserre. Global optimization with polynomials and the problem of moments. *SIAM J. Optim.*, 11(3):796–817, 2001. 80

D. Lawunmi. A theoretical analysis of exponentially decaying time series. *Measurement Science and Technology*, 8(7):703, 1997. 71

D. Lawunmi. Extracting useful information from noisy exponentially decaying signal, 2004. URL http://arxiv.org/abs/cond-mat/0408044. 71

S. Lefkimmiatis, A. Bourquard, and M. Unser. Hessian-based norm regularization for image restoration with biomedical applications. *IEEE Trans. Image Process.*, 21(3):983–995, Mar. 2012. 20, 112, 116, 162

J. Lellmann, J. Kappes, J. Yuan, F. Becker, and C. Schnörr. Convex multi-class image labeling by simplex-constrained total variation. In *SSVM '09: Proceedings of the Second International Conference on Scale Space and Variational Methods in Computer Vision*, pages 150–162, Berlin, Heidelberg, 2009. Springer-Verlag. ISBN 978-3-642-02255-5. doi: http://dx.doi.org/10.1007/978-3-642-02256-2_13. 58

V.S. Lempitsky, C. Rother, S. Roth, and A. Blake. Fusion moves for Markov Random Field optimization. *IEEE Trans. Pattern Anal. Mach. Int.*, 32 (8):1392–1405, 2010. 64, 125

J. Li, Z. Shen, R. Jin, , and X. Zhang. A reweighted ℓ_2 method for image restoration with Poisson and mixed Poisson-Gaussian noise. UCLA Preprint, 2012. 68, 106

T. Li, M. Wang, and T. Li. Estimating noise parameter based on the wavelet coefficients estimation of original image. In *2010 International Conference on Challenges in Environmental Science and Computer Engineering (CESCE)*, volume 1, pages 126 –129, Mar. 2010. doi: 10.1109/CESCE.2010.247. 93, 95

Y. Li and D. P. Huttenlocher. Sparse long-range random field and its application to image denoising. In *Proc. European Conf. Comput. Vision (ECCV)*, pages 344–357, 2008. 20

Z Liao, S. Hu, M. Li, and W. Chen. Noise estimation for single-slice sinogram of low-dose X-Ray computed tomography using homogenous patch. *Mathematical Problems in Engineering*, 2012, 2012. 94, 95

Y. Linde, A. Buzo, and R. Gray. An algorithm for vector quantizer design. *IEEE Trans. Commun.*, 28(1):84–95, Jan. 1980. 42

P. L. Lions and B. Mercier. Splitting algorithms for the sum of two nonlinear operators. *SIAM Journal on Numerical Analysis*, 16(6):964–979, 1979. ISSN 00361429. 31, 69

C. Liu, D. Rubin, and Y. Wu. Parameter expansion to accelerate EM: The PX-EM algorithm. *Biometrika*, 85(4):755–770, 1998. 29

C. Liu, W. T. Freeman, R. Szeliski, and S. B. Kang. Noise estimation from a single image. In *Proc. IEEE Comput. Soc. Conf. Comput. Vision and Pattern Recogn. (CVPR)*, pages 901–908, 2006. doi: 10.1109/CVPR.2006.207. 95

C. Liu, R. Szeliski, S. B. Kang, C. L. Zitnick, and W. T. Freeman. Automatic estimation and removal of noise from a single image. *IEEE Trans. Pattern Anal. Mach. Int.*, 30(2):299–314, 2008. 95

D. C. Liu and J. Nocedal. On the limited memory BFGS method for large scale optimization. *Math. Prog.*, 45(3):503–528, 1989. 157

W. Liu, T. Liu, M. Rong, R. Wang, and H. Zhang. A fast noise variance estimation algorithm. In *Microelectronics and Electronics (PrimeAsia), 2011 Asia Pacific Conference on Postgraduate Research in*, pages 61 –64, Oct. 2011. doi: 10.1109/PrimeAsia.2011.6075071. 93

S. Lloyd. Least squares quantization in PCM. *IEEE Trans. Inform. Theory*, 28(2):129–137, Mar. 1982. 42, 60

S. Łojasiewicz. *Une propriété topologique des sous-ensembles analytiques réels*, pages 87–89. Editions du centre National de la Recherche Scientifique, 1963. 153

F. Luisier, T. Blu, and M. Unser. Image denoising in mixed PoissonGaussian noise. *IEEE Trans. Image Process.*, 20(3):696–708, Mar. 2011. ISSN 1057-7149. 68, 70, 94, 105

V. V. Lukin, N. N. Ponomarenko, S. K. Abramov, B. Vozel, K. Chehdi, and J. T. Astola. Filtering of radar images based on blind evaluation of noise characteristics. *Image and Signal Processing for Remote Sensing XIV*, 7109(1):71090R, 2008. doi: 10.1117/12.799396. 94, 95

M. Makitalo and A. Foi. Optimal inversion of the Anscombe transformation in low-count Poisson image denoising. *IEEE Trans. Image Process.*, 20 (1):99 –109, Jan. 2011. ISSN 1057-7149. doi: 10.1109/TIP.2010.2056693. 16

M. Makitalo and A. Foi. Optimal inversion of the generalized Anscombe transformation for Poisson-Gaussian noise. *IEEE Trans. Image Process.*, PP(99):1, 2012. ISSN 1057-7149. doi: 10.1109/TIP.2012.2202675. 18

M. Malek-Mohammadi, M. Babaie-Zadeh, and C. Jutten. SRF: matrix completion based on smoothed rank function. In *Proc. Int. Conf. Acoust., Speech Signal Process.*, pages 3672–3675, Praque, Czech Republic, May 2011. 141

S. Mallat. *A wavelet tour of signal processing (2. ed.)*. Academic Press, San Diego, 1999. ISBN 978-0-12-466606-1. 22

J. Max. Quantizing for minimum distortion. *IRE Trans. on Inform. Theory*, 6(1):7–12, Mar. 1960. doi: 10.1109/TIT.1960.1057548. 41

P. Meer, D. Mintz, A. Rosenfeld, and D. Y. Kim. Robust regression methods for computer vision: a review. *Int. J. Computer Vision*, 6:59–70, 1991. 141

A. Miele and J. W. Cantrell. Study on a memory gradient method for the minimization of functions. *J. Optim. Theory Appl.*, 3(6):459–470, 1969. 147

M. Minsky. Microscopy apparatus, Nov. 1957. 1

H. Mohimani, M. Babaie-Zadeh, and C. Jutten. A fast approach for overcomplete sparse decomposition based on smoothed ℓ_0 norm. *IEEE Trans. Signal Process.*, 57(1):289 –301, Jan. 2009. 141

J. J. Moreau. Proximité et dualité dans un espace hilbertien. *Bull. Soc. Math. France*, 93:273–299, 1965. 31, 50

K. Murota. Algorithms in discrete convex analysis. *IEICE TRANSACTIONS on Information and Systems*, E83-D(3):344–352, 2000. 125, 126, 130

K. Murota. On steepest descent algorithms for discrete convex functions. *SIAM J. Optim.*, 14(3):699–707, 2004. 39, 126, 130, 131

K. Murota and A. Tamura. Proximity theorems of discrete convex functions. *Math. Programm.*, 99(3):539–562, Apr. 2004. ISSN 0025-5610. 38

F. Murtagh, J.-L. Starck, and A. Bijaoui. Image restoration with noise suppression using a multiresolution support. *Astronomy and Astrophysics Supplement*, 112:179–189, 1995. 18, 106

T. E. Nichols, J. Qi, E. Asma, and R. M. Leahy. Spatiotemporal reconstruction of list-mode PET data. *IEEE Transactions on Medical Imaging*, 21 (4):396–404, Apr. 2002. ISSN 0278-0062. doi: 10.1109/TMI.2002.1000263. 68, 105

J. Nie, J. Demmel, and M. Gu. Global minimization of rational functions and the nearest gcds. *Journal of Global Optimization*, 40(4):697–718, 2008. 82

M. Nikolova. Minimizers of cost-functions involving non-smooth data-fidelity terms. Application to the processing of outliers. *SIAM J. on Numerical Analysis*, 40(3):965–994, 2002. 124

M. Nikolova. Analysis of the recovery of edges in images and signals by minimizing nonconvex regularized least-squares. *Multiscale Model. Simul.*, 4(3):960–991, 2005. 141

M. Nikolova, S. Esedoglu, and T. F. Chan. Algorithms for finding global minimizers of image segmentation and denoising models. *SIAM Journal of Applied Mathematics*, 66(5):1632–1648, 2006. 39

M. Nikolova, M. K. Ng, S. Zhang, and W.-K. Ching. Efficient reconstruction of piecewise constant images using nonsmooth nonconvex minimization. *SIAM J. Imag. Sci.*, 1:2–25, Mar. 2008. 141

Y. Ohno. CIE fundamentals for color measurements. In *IS&T NIP16 Conference*, Vancouver, Canada, Oct. 2000. 61

J. M. Ortega and W. C. Rheinboldt. *Iterative solution of nonlinear equations in several variables*. Academic Press, New York, USA, 1970. 153

P. Pankajakshan, Z. Kam, A. Dieterlen, G. Engler, L. Blanc-Féraud, J. Zerubia, and J. C. Olivo-Marin. Point-spread function model for fluorescence MACROscopy imaging. In *Proc. Asilomar Conference on Signals, Systems and Computers*, pages 1364–1368, Chicago, USA, Nov. 2010. 173

P. Pankajakshan, A. Dieterlen, G. Engler, Z. Kam, L. Blanc-Féraud, J. Zerubia, and J. C. Olivo-Marin. Wavefront sensing for aberration modeling in fluorescence MACROscopy. In *Proc. IEEE Int. Symp. Biomedical Imaging (ISBI)*, Chicago, USA, Apr. 2011. 5

P. Pankajakshan, Z. Kam, A. Dieterlen, and J.-C. Olivo-Marin. Characterizing the 3-D field distortions in low numerical aperture fluorescence zooming microscope. *Optics Express*, 20(9):9876–9889, 2012. 171, 174

C. H. Papadimitriou and K. Steiglitz. *Combinatorial Optimization: Algorithms and Complexity*. Prentice-Hall, 1982. ISBN 0-13-152462-3. 26, 34, 36, 37

J. Park, P. Mroz, Michael R. Hamblin, and A. N. Yaroslavsky. Dye-enhanced multimodal confocal microscopy for noninvasive detection of skin cancers in mouse models. *Journal of Biomedical Optics*, 15(2):026023–026023–5, 2010. doi: 10.1117/1.3394301. 1

S. Park and K. Miller. Random number generators: Good ones are hard to find. *Communications of the ACM*, 31(10):1–10, Oct. 1988. 88

P. A. Parrilo and B. Sturmfels. Minimizing polynomial functions. In S. Basu and L. Gonzlez-Vega, editors, *Algorithmic and Quantitative Aspects of Real Algebraic Geometry in Mathematics and Computer Science*, pages 83–100. American Mathematical Society, 2001. ISBN 0-8218-2863-0. 80

P. Paul, H. Duessmann, T. Bernas, H. Huber, and D. Kalamatianos. Automatic noise quantification for confocal fluorescence microscopy images. *Computerized Medical Imaging and Graphics*, 34(6):426–434, Sep. 2010. doi: 10.1016/j.compmedimag.2010.04.001. 91, 95, 96

J. Pawley. *Handbook of Biological Confocal Microscopy*. Language of science. Springer, 2006. ISBN 9780387259215. 1, 2, 5, 68, 171

J. B. Pawley. Sources of noise in three-dimensional microscopical data sets. In J. Stevens, L. Mills, and J. Trogadis, editors, *Three-Dimensional Confocal Microscopy: Volume Investigation of Biological Specimens*, pages 47–94. Academic Press, San Diego, CA., 1994. ISBN 978-0126683301. 68

Z. Pei, Q. Tong, Wang. L., and J. Zhang. A median filter method for image noise variance estimation. In *2010 Second International Conference on Information Technology and Computer Science (ITCS)*, pages 13 –16, Jul. 2010. doi: 10.1109/ITCS.2010.11. 93

J. Pereira, R. Celso, L. Marques, and J. Justino da Costa. An empirical comparison of EM initialization methods and model choice criteria for mixtures of skew-normal distributions. In *19 SINAPE - Simpósio Nacional de Probabilidade e Estatística*, 2010. 79

Z. Peric and J. Nikolic. An effective method for initialization of Lloyd-Max's algorithm of optimal scalar quantization for Laplacian source. *Informatica*, 18(2):279–288, 2007. 60

J.-C. Pesquet and N. Pustelnik. A parallel inertial proximal optimization methods. *Pacific Journal of Optimization*, 8(2):273–305, Apr. 2012. 50, 51

J.-C. Pesquet, A. Benazza-Benyahia, and C. Chaux. A SURE approach for digital signal/image deconvolution problems. *IEEE Trans. Signal Process.*, 57(12):4616 –4632, Dec. 2009. ISSN 1053-587X. doi: 10.1109/TSP.2009.2026077. 13

D. J. Peter, V. K. Govindan, and A. T. Mathew. Nonlocal-means image denoising technique using robust M-estimator. *J. Comput. Sci. Technol.*, 25 (3):623–631, May 2010. ISSN 1000-9000. doi: 10.1007/s11390-010-9351-z. 140, 141

G. Peyré. A review of adaptive image representations. *J. Sel. Topics Signal Processing*, 5(5):896–911, 2011. 19

J-C. Picard. Maximal closure of a graph and applications to combinatorial problems. *Management Science*, 22(11):1268–1272, 1976. 33

T. Pock, D. Cremers, H. Bischof, and A. Chambolle. Global solutions of variational models with convex regularization. *SIAM J. Imaging Sciences*, 3(4):1122–1145, 2010. 25, 40

B. T. Polyak. *Introduction to optimization*. Optimization Software, Publications Division, New York, 1987. ISBN 0911575146. 32

N. Pustelnik, C. Chaux, and J.-C. Pesquet. Parallel proximal algorithm for image restoration using hybrid regularization. *IEEE Trans. Image Process.*, 20(9):2450–2462, Sep. 2011. ISSN 1057–7149. 31, 94, 113

H. Raguet, J. Fadili, and G. Peyré. Generalized forward-backward splitting. *To appear in SIAM Journal on Imaging Sciences*. URL http://hal.archives-ouvertes.fr/hal-00613637/. 106, 113

A. Raj and R. Zabih. A graph cut algorithm for generalized image deconvolution. In *Proc. IEEE Int. Conf. Comput. Vis.*, pages 1048–1054, Beijing, China, 2005. 156

A. Raj, G. Singh, R. Zabih, B. Kressler, Y. Wang, N. Schuff, and M. Weiner. Bayesian parallel imaging with edge-preserving priors. *Magn. Reson. Med.*, 57(1):8–21, 2007. 156

C. R. Rao. Information and the accuracy attainable in the estimation of statistical parameters. *Bulletin of Cal. Math. Soc.*, 37(3):81–91, 1945. 12, 84

R. A. Redner and H. F. Walker. Mixture densities, maximum likelihood and the EM algorithm. *SIAM Review*, 26(2):195–239, 1984. ISSN 00361445. 67

M. Reràbek and P. Pàta. The space variant PSF for deconvolution of wide-field astronomical images. *Acta Polytechnica*, 48(3):79–83, 2008. 171

M. Rivera and J. Marroquin. Efficient half-quadratic regularization with granularity control. 21(4):345–357, Apr. 2003. 141, 157

S. J. Roberts, D. Husmeier, I. Rezek, and W. D. Penny. Bayesian approaches to Gaussian mixture modeling. *IEEE Trans. Pattern Anal. Mach. Int.*, 20(11):1133–1142, 1998. 67

R. T. Rockafellar. Monotone Operators and the Proximal Point Algorithm. *SIAM J. Control Optim.*, 14(5):877–898, 1976. 30, 31

R. T. Rockafellar and R. J.-B. Wets. *Variational analysis*. Springer-Verlag, first edition, 1997. 143, 146

R. T. Rockafellar and R. J.-B. Wets. *Variational Analysis*. Springer, Oxford Oxfordshire, 2004. 30, 47

C. Rother, S. Kumar, V. Kolmogorov, and A. Blake. Digital tapestry [automatic image synthesis]. In *Proc. IEEE Comput. Soc. Conf. Comput. Vision and Pattern Recogn. (CVPR)*, pages 589–596, Jun. 2005. doi: 10.1109/CVPR.2005.130. 133

D. M. Rouse and S. S. Hemami. Analyzing the role of visual structure in the recognition of natural image content with multi-scale SSIM. In *Proc. SPIE 6806, Human Vision and Electronic Imaging XIII*, pages 680615–680615–14, 2008. doi: 10.1117/12.768060. 24

L. I. Rudin, S. Osher, and E. Fatemi. Nonlinear total variation based noise removal algorithms. *Journal Physica D*, 60:259–268, 1992a. 20, 112

L. I. Rudin, S. Osher, and E. Fatemi. Nonlinear total variation based noise removal algorithms. *Physica D*, 60:259–268, 1992b. 140

K. Sampathkumar and C. Arun. Poisson noise removal from fluorescence images using optimized variance-stabilizing transformations and standard gaussian denoising strategies. *European Journal of Scientific Research*, 84 (3):336–344, 2012. ISSN 1450-216X. 16

B. Schlesinger, D.and Flach. Transforming an arbitrary minsum problem into a binary one. Technical report, Dresden University of Technology, 2008. 125

J. Serra. *Image analysis and mathematical morphology*. Academic Press, 1982. 175

S. Setzer, G. Steidl, and T. Teuber. Deblurring Poissonian images by split Bregman techniques. *J. Vis. Comm. Image Repr.*, 21(3):193–199, 2010. ISSN 1047-3203. 50

H. R. Sheikh, A. C. Bovik, and G. de Veciana. An information fidelity criterion for image quality assessment using natural scene statistics. *IEEE Trans. Image Process.*, 14(12):2117 –2128, Dec. 2005. ISSN 1057-7149. doi: 10.1109/TIP.2005.859389. 24

S. N. Sinha, P. Mordohai, and M. Pollefeys. Multi-view stereo via graph cuts on the dual of an adaptive tetrahedral mesh. In *Proc. IEEE Int. Conf. Comput. Vis.*, pages 1–8, Rio de Janeiro, 2007. doi: 10.1109/ICCV.2007.4408997. 33, 124

K. Smith-Miles. Cross-disciplinary perspectives on meta-learning for algorithm selection. *ACM Comput. Surv.*, 41(1):6:1–6:25, 2008. 24

D. L. Snyder, A. M. Hammoud, and R. L. White. Image recovery from data acquired with a charge-coupled-device camera. *J. Opt. Soc. Am. A*, 10 (5):1014–1023, May 1993. doi: 10.1364/JOSAA.10.001014. 68, 105

L. Song, E. Hennink, I. Young, and H. Tanke. Photobleaching kinetics of fluorescein in quantitative fluorescence microscopy. *Biophysical Journal*, 68(6):2588–2600, Jun. 1995. ISSN 00063495. doi: 10.1016/S0006-3495(95)80442-X. 91

F. Soulez, L. Denis, Y. Tourneur, and E. Thièbaut. Blind deconvolution of 3D data in wide field fluorescence microscopy. In *Proc. IEEE Int. Symp. Biomedical Imaging (ISBI)*, pages 1735–1738. IEEE, 2012. ISBN 978-1-4577-1858-8. 171

S. Sra. Nonconvex proximal splitting: batch and incremental algorithms. http://arxiv.org/abs/1109.0258, 2012. 33

J.-L. Starck and F. Murtagh. Automatic noise estimation from the multiresolution support. *Publications of the Astronomical Society of the Pacific*, 110(744):193–199, 1998. ISSN 00046280. 68

C. M. Stein. Estimation of the mean of a multivariate normal distribution. *The Annals of Statistics*, 9(6):1135–1151, 1981. ISSN 00905364. 13

D. W. J. Stein. Detection of random signals in Gaussian mixture noise. *IEEE Trans. Inform. Theory*, 41:1788–1801, 1994. ISSN 0018-9448. doi: 10.1109/18.476307. 68

Jr. Stockham, T. G. Image processing in the context of a visual model. *Proceedings of the IEEE*, 60(7):828 – 842, Jul. 1972. ISSN 0018-9219. doi: 10.1109/PROC.1972.8782. 24

P. Strandmark and F. Kahl. Pseudo-boolean optimization: Theory and applications in vision, 2012. 38

P. Strandmark, F. Kahl, and T. Schoenemann. Parallel and distributed vision algorithms using dual decomposition. *Comput. Vis. Image Underst.*, 115(12):1721–1732, Dec. 2011. ISSN 1077-3142. doi: 10.1016/j.cviu.2011.06.012. 37

G. Strang. Maximal flow through a domain. *Math. Programm.*, 26:123–143, 1983. ISSN 0025-5610. doi: 10.1007/BF02592050. 39

G. Strang. Maximum flows and minimum cuts in the plane. *J. Global Optimization*, 47(3):527–535, 2010. 40

R. A. Sweet, K. N. Fish, and D. A. Lewis. Mapping synaptic pathology within cerebral cortical circuits in subjects with schizophrenia. *Frontiers in Human Neuroscience*, page 44 pages, 2010. doi: 10.3389/fnhum.2010.00044. 1

R. Szeliski, R. Zabih, D. Scharstein, O. Veksler, V. Kolmogorov, A. Agarwala, M. Tappen, and C. Rother. A comparative study of energy minimization methods for Markov Random Fields with smoothness-based priors. *IEEE Trans. Pattern Anal. Mach. Int.*, 30:1068–1080, 2008. ISSN 0162-8828. doi: 10.1109/TPAMI.2007.70844. 125, 126, 133, 135

H. Talbot, C. Evans, and R. Jones. Complete ordering and multivariate mathematical morphology. In *ISMM '98: Proceedings of the fourth international symposium on Mathematical morphology and its applications to image and signal processing*, pages 27–34, Norwell, MA, USA, 1998. Kluwer Academic Publishers. ISBN 0-7923-5133-9. 48

M. F. Tappen and W. T. Freeman. Comparison of graph cuts with belief propagation for stereo, using identical MRF parameters. In *Proc. IEEE Int. Conf. Comput. Vis.*, pages 900–906, Nice, France, 2008. doi: 10.1109/ICCV.2003.1238444. 133

N. A. Tatton and H. J. Rideout. Confocal microscopy as a tool to examine DNA fragmentation, chromatin condensation and other apoptotic changes in Parkinson's disease. *Parkinsonism and Related Disorders*, 5(4):179 – 186, 1999. ISSN 1353-8020. doi: 10.1016/S1353-8020(99)00035-8. 1

E. Thiébaut. Optimization issues in blind deconvolution algorithms. *Astronomical Data Analysis II*, 4847:174–183, 2002. doi: 10.1117/12.461151. 171

A. Tikhonov and V. Arsenin. *Solutions of Ill-Posed Problems*. Winston, Washington, DC, USA, 1977. 140

D. M. Titterington. General structure of regularization procedures in image restoration. *Astron. Astrophys.*, 144:381–387, 1985. 140

A. Tomaszewska. Blind noise level detection. In A. Campilho and M. Kamel, editors, *Image Analysis and Recognition*, volume 7324 of *Lecture Notes in Computer Science*, pages 107–114. Springer Berlin / Heidelberg, 2012. ISBN 978-3-642-31294-6. 93

W. Trobin, T. Pock, D. Cremers, and H. Bischof. Continuous energy minimization via repeated binary fusion. In *Proc. European Conf. Comput. Vision (ECCV)*, Part IV, pages 677–690, Marseille, France, Oct. 2008. 58

P. Tseng. A modified forward-backward splitting method for maximal monotone mappings. *SIAM J. Control Optim.*, 38(2):431–446, 2000. 31

P. Tseng. An analysis of the EM algorithm and entropy-like proximal point methods. *Math. Oper. Res.*, 29(1):27–44, 2004. 32

M. Uss, B. Vozel, V. V. Lukin, and K. Chehdi. Local signal-dependent noise variance estimation from hyperspectral textural images. *J. Sel. Topics Signal Processing*, 5(3):469–486, 2011. 70, 94

O. Veksler. *Efficient graph-based energy minimization methods in computer vision*. PhD thesis, Cornell University, Ithaca, NY, USA, 1999. 47, 56, 57, 124, 130, 144

O. Veksler. Graph cut based optimization for MRFs with truncated convex priors. In *Proc. IEEE Comput. Soc. Conf. Comput. Vision and Pattern Recogn. (CVPR)*, pages 1–8, Minneapolis, MN, 2007. doi: 10.1109/CVPR.2007.383249. 58, 125, 126, 127, 141

O. Veksler. Multi-label moves for MRFs with truncated convex priors. In *Proc. IEEE Int. Conf. Energy Minimization Methods Comput. Vision and Pattern Recogn. (EMMCVPR)*, pages 1–8, Aug. 2009. 125

C. Vertan, V. Popescu, and V. Buzuloiu. Morphological like operators for color images. In *Proc. Eur. Sig. and Image Proc. Conference*, Trieste, Italy, Sep. 1996. 48

L. Vincent. Grayscale area openings and closings, their efficient implementation and applications. In *Proceedings of the conference on mathematical morphology and its applications to signal processing*, pages 22–27, Barcelona, Spain, May 1993. 175

M. Von Tiedemann, A. Fridberger, M. Ulfendahl, and J. Boutet De Monvel. Image adaptive point-spread function estimation and deconvolution for in vivo confocal microscopy. *Microscopy Research and Technique*, 69(1): 10–20, 2006. ISSN 1097-0029. doi: 10.1002/jemt.20261. 171

B. C. Vu. A splitting algorithm for dual monotone inclusions involving cocoercive operators. *Advances in Computational Mathematics*, pages 1–15, 2011. ISSN 1019-7168. doi: 10.1007/s10444-011-9254-8. 32, 106, 170

M. J. Wainwright, T. S. Jaakkola, and A. S. Willsky. MAP estimation via agreement on trees: message-passing and linear programming. *IEEE Trans. Inform. Theory*, 51:3697–3717, 2005. ISSN 0018-9448. doi: 10.1109/TIT.2005.856938. 126, 133

Z. Wang, A. C. Bovik, and L. Lu. Why is image quality assessment so difficult? In *Proc. Int. Conf. Acoust., Speech Signal Process.*, volume 4, pages IV–3313 –IV–3316, May 2002. doi: 10.1109/ICASSP.2002.5745362. 24

Z. Wang, A.C. Bovik, H.R. Sheikh, and E.P. Simoncelli. Image quality assessment: from error visibility to structural similarity. *IEEE Trans. Image Process.*, 13(4):600 –612, Apr. 2004. ISSN 1057-7149. doi: 10.1109/TIP.2003.819861. 24, 158

E. B. Wilson and M. M. Hilferty. The distribution of Chi-squared. *Proceedings of the National Academy of Sciences of the United States of America*, 17(12):684–688, 1931. 16

O. J. Woodford, P. H. S. Torr, I. D. Reid, and A. W. Fitzgibbon. Global stereo reconstruction under second order smoothness priors. In *Proc. IEEE Comput. Soc. Conf. Comput. Vision and Pattern Recogn. (CVPR)*, 2008. 33, 124

C. F. J. Wu. On the convergence properties of the EM algorithm. *The Annals of Statistics*, 11(1):95–103, 1983. 29

X. Wu. On initialization of Max's algorithm for optimum quantization. *IEEE Trans. on Communications*, 38(10):1653–1656, Oct. 1990. doi: 10.1109/26.61431. 60

X. Wu. Optimal quantization by matrix searching. *Journal of algorithms*, 12(4):663–673, 1991. 46

X. Wu. Color quantization by dynamic programming and principal analysis. *ACM Transactions on Graphics*, 11(4):348–372, 1992a. ISSN 0730-0301. doi: http://doi.acm.org/10.1145/146443.146475. 60

X. Wu. On convergence of Lloyd's method I. *IEEE Trans. Inform. Theory*, 38(1):171–174, Jan. 1992b. doi: 10.1109/18.108266. 42

X. Wu and J. Rokne. An $O(KN \log N)$ algorithm for optimum K-level quantization on histograms of N points. In *ACM Annual Computer Science Conference*, pages 339 – 343, Louisville, Kentucky, Jul. 1989. 46

J. Xiao and M. Shah. Motion layer extraction in the presence of occlusion using graph cuts. *IEEE Trans. Pattern Anal. Mach. Int.*, 27:1644–1659, 2007. ISSN 0162-8828. doi: 10.1109/TPAMI.2005.202. 33, 124

H. Yoo, I. Song, and D.-G. Gweon. Measurement and restoration of the point spread function of fluorescence confocal microscopy. *Journal of Microscopy*, 221(3):172–176, 2006. ISSN 1365-2818. doi: 10.1111/j.1365-2818.2006.01556.x. 171

G. Yu, G. Sapiro, and S. Mallat. Solving inverse problems with piecewise linear estimators: From Gaussian mixture models to structured sparsity. *IEEE Trans. Image Process.*, 21(5):2481–2499, 2012. 22

J. Yuan, E. Bae, and X.-C. Tai. A study on continuous max-flow and min-cut approaches. In *Proc. IEEE Comput. Soc. Conf. Comput. Vision and Pattern Recogn. (CVPR)*, pages 2217–2224. IEEE, 2010. 40

A. L. Yuille and A. Rangarajan. The concave-convex procedure. *Neural Computation*, 15(4):915–936, 2003. 29

C. Zach and P. Kohli. A convex discrete-continuous approach for Markov Random Fields. In A. W. Fitzgibbon, S. Lazebnik, P. Perona, Y. Sato, and C. Schmid, editors, *ECCV (6)*, volume 7577 of *Lecture Notes in Computer Science*, pages 386–399. Springer, 2012. ISBN 978-3-642-33782-6. 25, 40

C. Zach, M. Niethammer, and J.-M. Frahm. Continuous maximal flows and Wulff shapes: Application to MRFs. In *Proc. IEEE Comput. Soc. Conf. Comput. Vision and Pattern Recogn. (CVPR)*, pages 1911–1918, Miami, FL, 2009. doi: 10.1109/CVPR.2009.5206565. 58

B. Zalesky. Efficient determination of Gibbs estimators with submodular energy functions. http://arxiv.org/abs/math/0304041, 2003. 58

B. Zhang. *Contributions à la microscopie à fluorescence en imagerie biologique : modélisation de la PSF, restauration d'images et détection super-résolutive*. Phd thesis, TELECOM Paris, Nov. 2007. 68, 79, 91

Y. Zhang and N. Kingsbury. Restoration of images and 3D data to higher resolution by deconvolution with sparsity regularization. In *Proc. Int. Conf. Image Process.*, pages 1685 –1688, Hong Kong, Sep. 2010. 141

M. Zibulevsky and M. Elad. ℓ_2-ℓ_1 optimization in signal and image processing. *IEEE Signal Process. Mag.*, 27(3):76–88, May 2010. 140, 141, 147

H. Zou and T. Hastie. Regularization and variable selection via the elastic net. *J. R. Statist. Soc. B*, 67(2):301–320, 2005. 141